



IDO1

**Targeting amino acid-metabolizing
enzymes for cancer immunotherapy and
treatment of Parkinson's disease**

Yvonne Grobben

TDO

ARG1

**Targeting amino acid-metabolizing
enzymes for cancer immunotherapy and
treatment of Parkinson's disease**

Yvonne Grobбен

Targeting amino acid-metabolizing enzymes for cancer immunotherapy and treatment of Parkinson's disease | Yvonne Grobбен

ISBN: 978-94-6473-277-1
DOI: <https://doi.org/10.33540/2034>
Layout and design: Yvonne Grobбен
Printed by: Ipskamp Printing

For reasons of consistency within this thesis, some terms have been standardized throughout the text. As a consequence, the text may differ in this respect from the articles that have been published.

Copyright © 2023 by Yvonne Grobбен

All rights reserved. No part of this thesis may be reproduced, distributed, stored in a retrieval system, or transmitted in any form or by any means, without prior written permission of the author.

Targeting amino acid-metabolizing enzymes for cancer immunotherapy and treatment of Parkinson's disease

**Aminozuur-metaboliserende enzymen als
aangrijpingspunten voor kankerimmunotherapie
en de behandeling van de ziekte van Parkinson**

(met een samenvatting in het Nederlands)

Proefschrift

ter verkrijging van de graad van doctor aan de
Universiteit Utrecht
op gezag van de
rector magnificus, prof.dr. H.R.B.M. Kummeling,
ingevolge het besluit van het college voor promoties
in het openbaar te verdedigen op

maandag 18 december 2023 des ochtends te 10.15 uur

door

Yvonne Grobben

geboren op 20 september 1994
te Nieuwegein

Promotoren:

Prof. dr. A.D. Kraneveld

Prof. dr. J. Garssen

Copromotoren:

Dr. G.J.R. Zaman

Dr. R.C. Buijsman

Beoordelingscommissie:

Prof. dr. J.H. Beijnen

Prof. dr. C.R. Berkers

Prof. dr. R.H. Medema

Dr. M. Slijper

Prof. dr. A.B. Smit

Contents

Chapter 1	General introduction and outline of the thesis	7
Chapter 2	Targeting amino acid-metabolizing enzymes for cancer immunotherapy	15
Chapter 3	Amino acid-metabolizing enzymes in advanced high-grade serous ovarian cancer patients: value of ascites as biomarker source and role for IL4I1 and IDO1	59
Chapter 4	Structural insights into human arginase 1 pH dependence and its inhibition by the small molecule inhibitor CB-1158	103
Chapter 5	High-throughput fluorescence-based activity assay for arginase 1	135
Chapter 6	Targeting indoleamine 2,3-dioxygenase 1 (IDO1) in cancer models using the novel small molecule inhibitor NTRC 3883-0	151
Chapter 7	Pharmacological validation of tryptophan 2,3-dioxygenase (TDO) as a target for Parkinson's disease	187
Chapter 8	Summarizing discussion	231
Appendices	Nederlandse samenvatting	251
	Curriculum vitae	259
	List of publications	260
	Dankwoord	263



Chapter 1

General introduction and
outline of the thesis





General introduction

Altered amino acid metabolism in disease

In all living systems, the internal environment is tightly regulated to ensure optimal physiological function and survival. This process, known as homeostasis, is coordinated by a complex network of feedback mechanisms that strives for a stable physical and chemical balance within all levels of organization—*i.e.*, within organelles, cells, tissues, organs, organ systems and organisms as a whole. However, both intrinsic and extrinsic factors, such as aging, genetics, nutrient deficiency and exposure to toxins, can cause disruption of normal homeostasis. When maintained, such homeostatic imbalance can ultimately result in disease development and its progression.

The regulation of amino acid metabolism is an essential aspect of maintaining homeostasis, as amino acids are fundamental building blocks of life and serve as key metabolic intermediates in various biosynthetic and energetic pathways. Amongst others, these include pathways involved in the synthesis of proteins, signaling molecules, nucleotides, polyamines, glutathione, creatin and heme. To ensure sufficient production of these molecules, amino acids and their metabolic rates are to be kept at adequately high levels. Concurrently, overproduction of metabolites must be prevented, as these may exert deleterious effects when present at supraphysiological concentrations.

Altered amino acid metabolism has been implicated in the pathogenesis of a variety of conditions, including neoplastic, neurodegenerative, cardiovascular and autoimmune diseases. In this thesis, two types of these diseases are studied, being cancer and Parkinson's disease. Although these diseases are seemingly unrelated, both can be categorized as age-related pathologies and frequently involve immune dysregulation. Moreover, both can potentially be treated with drugs targeting amino acid-metabolizing enzymes, as is explored and discussed throughout this thesis.

Role of amino acid-metabolizing enzymes in tumor immune escape

Cancer is one of the leading causes of death worldwide, accounting for almost 10 million deaths in 2020.¹ Cancer is a heterogeneous and dynamic disease arising from a complex interplay of genetic, epigenetic and environmental factors, culminating in the disruption of tissue homeostasis.² Although cancer development can in principle be controlled by the immune system, tumor cells develop diverse strategies to evade immune elimination, which is considered one of the hallmarks of cancer.³ In order to combat cancer, this hallmark trait serves as an abundant source of potential targets that can be modulated to reinvigorate the anti-tumor immune response. Among these targets are different amino acid-metabolizing enzymes, including enzymes that metabolize glutamine, arginine

or tryptophan. Aberrant induction of these enzymes in tumor or tumor-infiltrating cells can lead to disturbance of amino acid homeostasis in immune cells as well as to their suppression by accumulating amino acid-derived metabolites.⁴⁻⁸ Targeting of these enzymes with small molecule inhibitors is therefore considered a promising immunotherapeutic approach for cancer treatment, and will serve as the main topic of this thesis.

Tryptophan metabolism in Parkinson's disease

Compared to cancer, Parkinson's disease has a considerably lower prevalence worldwide, although still over 6 million individuals are living with this disease.⁹ Parkinson's disease is a severe, progressive neurodegenerative disorder, with patients presenting with both debilitating motor deficits and various non-motor symptoms. Principal pathological hallmarks of Parkinson's disease are brain region-specific neuronal loss, α -synuclein inclusion formation, neuroinflammation and oxidative stress, which are thought to arise from an interplay of aging, genetics and environmental factors.¹⁰ Moreover, an imbalance in tryptophan metabolism is considered to contribute to the pathology of Parkinson's disease.¹¹ This is supported by altered metabolite levels found in patient samples.¹²⁻¹⁴ Furthermore, in invertebrate models of Parkinson's disease, beneficial effects are observed upon modulation of tryptophan metabolism by genetic or pharmacological inhibition of relevant enzymes.^{15,16} Targeted modulation of tryptophan metabolism using small molecules therefore holds promise for the treatment of Parkinson's disease, and may additionally be extended to the treatment of other neurodegenerative disorders.¹⁶⁻¹⁸

Outline of the thesis

This thesis aims to contribute to the drug discovery process of inhibitors targeting amino acid-metabolizing enzymes in cancer and Parkinson's disease. To accomplish this objective, research has been performed that provides support for various stages of this process, including target validation, hit generation, lead identification and optimization, and *in vivo* studies.

In chapters of this thesis focused around cancer research, different amino acid-metabolizing enzymes with a known role in tumor immune escape are studied. These include the glutamine-metabolizing enzyme glutaminase 1 (GLS1), the arginine-metabolizing enzymes arginase 1 (ARG1) and inducible nitric oxide synthase (iNOS), the tryptophan-metabolizing enzymes indoleamine 2,3-dioxygenase 1 (IDO1) and tryptophan 2,3-dioxygenase (TDO), and the aromatic amino acid-metabolizing enzyme interleukin 4 induced 1 (IL4I1). For Parkinson's disease, the presented research is focused specifically on only one of these enzymes, *i.e.*, TDO, based on its implication in the disease pathogenesis.

In **chapter 2**, the current body of knowledge on the role of amino acid-metabolizing enzymes in cancer immune escape and their potential as immunotherapeutic targets is reviewed.

In **chapter 3**, it is explored whether any of the discussed amino acid-metabolizing enzymes may serve a role in a specific subtype of cancer, *i.e.*, high-grade serous ovarian cancer. This cancer is characterized by a highly immunosuppressive tumor microenvironment,¹⁹ and immunotherapies approved for treatment of other cancer types have demonstrated only limited efficacy in this indication.²⁰ The potential contribution of amino acid-metabolizing enzymes to the immune environment in ovarian cancer is therefore investigated by measurement of amino acid and corresponding metabolite levels in liquid biopsies of patients and healthy donors, and by correlation of these findings with patient characteristics.

In **chapter 4**, the mechanism of inhibition of ARG1 by known small molecule inhibitors of the enzyme is studied from a biochemical, biophysical and structural perspective, with the aim to support ongoing and future drug discovery initiatives. In this chapter, three frequently studied ARG1 inhibitors are compared side-by-side in different biochemical and biophysical assays. Moreover, the effect of pH on the structure and inhibition of ARG1 is studied and the binding mode of a clinical-stage ARG1 inhibitor is visualized for the first time.

In **chapter 5**, an innovative biochemical assay is presented to enable the discovery of novel small molecule ARG1 inhibitors by high-throughput screening (HTS). HTS is an automated process that allows for the rapid screening of large compound libraries to identify new starting points ("hits") for drug discovery. The ARG1 assay developed and optimized in this chapter is validated by comparison with an established, non-HTS-compatible assay and by its application in an HTS campaign.

In **chapter 6**, the focus is shifted towards IDO1, for which the development of a potent, selective and orally bioavailable inhibitor is described from HTS hit towards optimized lead compound. This novel small molecule inhibitor is compared to the clinical-stage IDO1 inhibitor epacadostat in various biochemical and cell-based assays, with the aim to determine its differentiation from epacadostat and to demonstrate proof-of-activity in a co-culture model of *IDO1*-overexpressing cells with immune cells. Moreover, the modulation of IDO1 activity by this inhibitor is studied both *in vivo* in murine cancer models and *ex vivo* in primary cell cultures established from ovarian cancer patient samples.

In **chapter 7**, TDO inhibition is investigated as a potential therapeutic strategy for the treatment of Parkinson's disease. This study builds on previous work in the nematode *Caenorhabditis elegans*,¹⁵ indicating a role for TDO in ageing-related proteotoxicity via α -synuclein, a neuronal protein that has been genetically and neuropathologically linked

to Parkinson's disease.²¹ With the aim to study the role of TDO in Parkinson's disease, a novel, brain-penetrable, small molecule TDO inhibitor is assessed for its ability to reduce both motor and non-motor symptoms as well as the underlying pathologies in a murine model of the disease.

Finally, in **chapter 8**, the main findings of this thesis are summarized and discussed, and perspectives for future research are provided.

References

1. Sung, H. *et al.* Global cancer statistics 2020: GLOBOCAN estimates of incidence and mortality worldwide for 36 cancers in 185 countries. *CA. Cancer J. Clin.* **71**, 209–49 (2021).
2. Stratton, M. R., Campbell, P. J. & Futreal, P. A. The cancer genome. *Nature* **458**, 719–24 (2009).
3. Hanahan, D. & Weinberg, R. A. Hallmarks of cancer: the next generation. *Cell* **144**, 646–74 (2011).
4. Peñarando, J., Aranda, E. & Rodríguez-Ariza, A. Immunomodulatory roles of nitric oxide in cancer: tumor microenvironment says “NO” to antitumor immune response. *Transl. Res.* **210**, 99–108 (2019).
5. Grzywa, T. M. *et al.* Myeloid cell-derived arginase in cancer immune response. *Front. Immunol.* **11**, 938 (2020).
6. Opitz, C. A. *et al.* The therapeutic potential of targeting tryptophan catabolism in cancer. *Br. J. Cancer* **122**, 30–44 (2020).
7. Sadik, A. *et al.* IL4I1 Is a metabolic immune checkpoint that activates the AHR and promotes tumor progression. *Cell* **182**, 1252–70.e34 (2020).
8. Wang, Z. *et al.* Targeting glutaminolysis: new perspectives to understand cancer development and novel strategies for potential target therapies. *Front. Oncol.* **10**, 589508 (2020).
9. GBD 2016 Parkinson's Disease Collaborators. Global, regional, and national burden of Parkinson's disease, 1990–2016: a systematic analysis for the Global Burden of Disease Study 2016. *Lancet. Neurol.* **17**, 939–53 (2018).
10. Antony, P. M. A., Diederich, N. J., Krüger, R. & Balling, R. The hallmarks of Parkinson's disease. *FEBS J.* **280**, 5981–93 (2013).
11. Platten, M., Nollen, E. A. A., Röhrig, U. F., Fallarino, F. & Opitz, C. A. Tryptophan metabolism as a common therapeutic target in cancer, neurodegeneration and beyond. *Nat. Rev. Drug Discov.* **18**, 379–401 (2019).
12. Ogawa, T. *et al.* Kynurenine pathway abnormalities in Parkinson's disease. *Neurology* **42**, 1702–6 (1992).
13. Widner, B., Leblhuber, F. & Fuchs, D. Increased neopterin production and tryptophan degradation in advanced Parkinson's disease. *J. Neural Transm.* **109**, 181–9 (2002).
14. Sorgdrager, F. J. H. *et al.* Age- and disease-specific changes of the kynurenine pathway in Parkinson's and Alzheimer's disease. *J. Neurochem.* **151**, 656–68 (2019).
15. van der Goot, A. T. *et al.* Delaying aging and the aging-associated decline in protein homeostasis by inhibition of tryptophan degradation. *Proc. Natl. Acad. Sci. U. S. A.* **109**, 14912–7 (2012).
16. Breda, C. *et al.* Tryptophan-2,3-dioxygenase (TDO) inhibition ameliorates neurodegeneration by modulation of kynurenine pathway metabolites. *Proc. Natl. Acad. Sci. U. S. A.* **113**, 5435–40 (2016).
17. Campesan, S. *et al.* The kynurenine pathway modulates neurodegeneration in a *Drosophila* model of Huntington's disease. *Curr. Biol.* **21**, 961–6 (2011).
18. Zwilling, D. *et al.* Kynurenine 3-monooxygenase inhibition in blood ameliorates neurodegeneration. *Cell* **145**, 863–74 (2011).
19. Rodriguez, G. M., Galpin, K. J. C., McCloskey, C. W. & Vanderhyden, B. C. The tumor microenvironment of epithelial ovarian cancer and its influence on response to immunotherapy. *Cancers (Basel)* **10**, 242 (2018).
20. Gaillard, S. L., Secord, A. A. & Monk, B. The role of immune checkpoint inhibition in the treatment of ovarian cancer. *Gynecol. Oncol. Res. Pract.* **3**, 11 (2016).
21. Stefanis, L. α -Synuclein in Parkinson's disease. *Cold Spring Harb. Perspect. Med.* **2**, a009399 (2012).



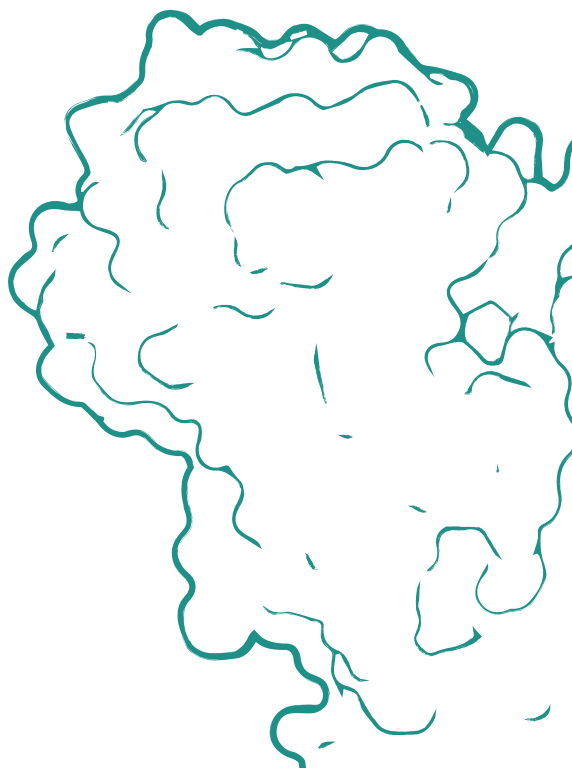
Chapter 2

Targeting amino acid-metabolizing enzymes
for cancer immunotherapy

Yvonne Grobben

Oncolines B.V., Oss, The Netherlands

Manuscript in preparation



Abstract

Despite the immune system's role in the detection and eradication of abnormal cells, cancer cells often evade elimination by exploitation of various immune escape mechanisms. Among these mechanisms is the ability of cancer cells to upregulate amino acid-metabolizing enzymes, or to induce these enzymes in tumor-infiltrating immunosuppressive cells. Amino acids are fundamental cellular nutrients required for a variety of physiological processes, and their inadequacy can severely impact immune cell function. Amino acid-derived metabolites can additionally dampen the anti-tumor immune response by means of their immunosuppressive activities, whilst some can also promote tumor growth directly. Based on their evident role in tumor immune escape, the amino acid-metabolizing enzymes glutaminase 1 (GLS1), arginase 1 (ARG1), inducible nitric oxide synthase (iNOS), indoleamine 2,3-dioxygenase 1 (IDO1), tryptophan 2,3-dioxygenase (TDO) and interleukin 4 induced 1 (IL4I1) each serve as a promising target for immunotherapeutic intervention. This review summarizes and discusses the involvement of these enzymes in cancer, their effect on the anti-tumor immune response and the recent progress made in the preclinical and clinical evaluation of inhibitors targeting these enzymes.

Introduction

Cancer arises from the accumulation of genetic and epigenetic alterations, conferring selective growth advantage to transformed cells.^{1,2} Associated with these alterations is generally a diverse set of tumor-expressed antigens, including aberrantly expressed self-antigens and neoantigens resulting from somatic mutations.³ Although this antigenic diversity provides the immune system with ample opportunity to recognize and destroy cancerous cells, an effective antitumor immune response is absent in many human cancers.⁴ Mechanisms facilitating the immune escape of tumor cells include the downregulation or loss of tumor antigens or antigen-presenting machinery, the impairment of T-cell trafficking and infiltration into tumors, and the induction of immunosuppressive factors and cells in the tumor microenvironment (TME).^{5,6}

Over the recent decades, cancer immunotherapy has emerged as a revolutionary approach to reinvigorate host antitumor immunity.⁷ By alleviating negative regulation of T-cell activation, antibodies targeting inhibitory immune checkpoint proteins, including programmed death 1 (PD-1), its ligand PD-L1, and cytotoxic T-lymphocyte-associated protein 4 (CTLA-4), have produced durable clinical responses in a subset of cancer patients.^{8,9} Other immunotherapeutic treatment modalities, such as cytokine therapy, cancer vaccines and adoptive cell transfer, have additionally been developed to amplify pre-existing immune reactivity in patients, or generate new tumor-specific immune responses.^{7,10} However, while cancer immunotherapies represent attractive alternatives to conventional and targeted therapies in terms of efficacy and tolerability, many patients experience primary or acquired resistance,^{11,12} necessitating the development of alternative strategies or combinatorial therapies.

A critical hurdle for successful immunotherapeutic treatment of cancer patients is the complex and heterogeneous nature of the TME.¹³ Within this environment, tumor-induced accumulation of immunosuppressive cells, such as regulatory T cells and myeloid-derived suppressor cells (MDSCs), can promote profound tolerance to cancerous cells.¹⁴ Molecular mechanisms employed by these suppressive populations as well as by tumor cells themselves include the expression of inhibitory receptors or their ligands,⁸ and the secretion of immunosuppressive cytokines.⁶ In addition, upregulation of metabolic enzymes by any of these participants can deprive the TME of nutrients essential to proliferating T cells, or expose them to high levels of immunosuppressive metabolites.¹⁵ Finally, the frequently hypoxic and acidic conditions surrounding tumor-infiltrating T cells can further attenuate their function.¹⁶

In this review, the role of a specific group of metabolic enzymes—*i.e.*, those metabolizing amino acids—in the escape of tumor cells from immune surveillance will be summarized; advances in the therapeutic targeting of these enzymes will be highlighted, and current challenges and opportunities in this field will be discussed.

Amino acid-metabolizing enzymes involved in tumor immune escape

Amino acids are integral to cellular homeostasis and proliferation, serving as precursors for protein synthesis and constituting key metabolic intermediates in energy production and various biosynthetic pathways. In naïve T cells, only minimal uptake of amino acids is required to maintain homeostasis, which is attributable to the metabolically quiescent state of these cells.¹⁷ However, upon cognate antigen engagement and co-stimulation, T cells drastically alter their metabolism to meet the energetic and anabolic needs of rapid growth and proliferation.¹⁸ Being auxotrophic for most amino acids,¹⁹ this requires activated T cells to strongly increase both essential and non-essential amino acid uptake.²⁰ In the case of tumor-infiltrating T cells, this has to be achieved amidst the highly competitive and dynamic settings of the TME.

Within the tumor landscape, metabolic reprogramming is not a unique feature of activated T cells, as highly proliferative cancer cells have similar metabolic requirements. Cancer cells often avidly consume energetic nutrients, particularly glucose and glutamine,²¹ causing them to outcompete T cells for respiratory fuel. This voracious phenotype is governed by the upregulation of transporter proteins as well as metabolic enzymes, including the glutamine-metabolizing enzyme glutaminase 1 (GLS1).²² Expression of other amino acid-metabolizing enzymes can additionally be exploited by either tumor or infiltrating immunosuppressive cells. These enzymes include arginase 1 (ARG1),²³ inducible nitric oxide synthase (iNOS),²⁴ indoleamine 2,3-dioxygenase 1 (IDO1), tryptophan 2,3-dioxygenase (TDO)²⁵ and interleukin 4 induced 1 (IL4I1).²⁶ Whereas the activities of these enzymes may also directly serve to potentiate tumor malignant properties through different mechanisms, their main common denominator is the ability to promote tumor growth through suppression of T-cell responses.^{23–26}

A common mechanism of immunosuppression exerted by different amino acid-metabolizing enzymes relies on the amino acid dependency of activated T cells. As in all eukaryotic cells, the intracellular availability of amino acids in T cells is continuously monitored through at least two distinct pathways, involving either the general control nonderepressible 2 (GCN2) kinase²⁷ or the mammalian target of rapamycin

complex 1 (mTORC1).²⁸ Activation of the GCN2 pathway occurs upon accumulation of uncharged tRNAs consequent to amino acid withdrawal,²⁷ whereas T-cell receptor (TCR)-induced mTORC1 signaling is inhibited upon insufficiency of selected amino acids.²⁸ Through independent mechanisms, either perturbation induces a global reduction in translation initiation concomitant with the selective induction of genes aiding in cellular recovery.^{27,28} As a consequence, amino acid deprivation can severely impact the functionality of T cells.²⁹

A second suppressive mechanism shared by distinct amino acid-metabolizing enzymes is the accumulation of immunosuppressive metabolites within the TME. Among the different metabolites generated by these enzymes, activation of the aryl hydrocarbon receptor (AhR) is the most represented mechanism of immunosuppression.^{25,26} The AhR is a ligand-activated transcription factor expressed by most human cell types, including various cells of the immune system, in which it regulates the transcription of numerous target genes. Through sensing of a broad range of exogenous and endogenous ligands, including amino acid metabolites, the AhR controls various physiological processes, including cell cycle progression, cellular motility and immune cell function.^{30,31}

In the following sections, each of the amino acid-metabolizing enzymes involved in tumor immune escape will be discussed separately, as this allows for the depth of review to be adequately coordinated with the extent of knowledge available. As an exception, IDO1 and TDO will be discussed jointly, as these enzymes demonstrate highly overlapping mechanisms of action.

The glutamine-metabolizing enzyme GLS1

Glutamine is the most abundant amino acid in humans, both in circulation and in the intracellular environment.³² It is considered conditionally essential, as it can be adequately obtained from *de novo* synthesis and protein turnover in healthy individuals, but requires dietary supplementation during certain pathophysiological conditions.³³ Aside from its key role in protein synthesis, glutamine contributes to numerous biosynthetic pathways, including those directed towards synthesis of nucleotides, non-essential amino acids, fatty acids and glutathione.³⁴ Moreover, glutamine can serve as a significant source of energy in cells with high energetic demands.²¹ In non-proliferating cells, this role is primarily reserved for glucose, which is efficiently used in glycolysis, the tricarboxylic acid (TCA) cycle and oxidative phosphorylation for generation of ATP and biosynthetic precursors.³⁵ In contrast, energy production in most cancer cells is shifted towards the inefficient use of glucose in aerobic glycolysis (“the Warburg effect”), achieved through

re-programming of metabolic pathways.³⁶ This altered metabolism yields important glycolytic intermediates required for various anabolic processes, but concurrently restricts entry of glucose into the TCA cycle.³⁵ To compensate for this metabolic shift, cancer cells often become addicted to exogenous glutamine, which can replenish TCA cycle intermediates through its downstream metabolite α -ketoglutarate in a process called glutaminolysis.²¹

Conversion of glutamine into α -ketoglutarate is initiated by glutaminase (GLS) enzymes, which catalyze the deamidation of glutamine to glutamate and act as the rate-limiting enzymes for glutamine entry into the TCA cycle. In mammalian cells, GLS is encoded by two genes, *GLS1* (or kidney-type glutaminase; KGA) and *GLS2* (or liver-type glutaminase; LGA). Expression of *GLS1* occurs ubiquitously across human extrahepatic tissues,^{37,38} and is regulated by the c-Myc oncoprotein, which coordinately controls cellular glutamine uptake.^{39,40} Elevated tumoral *GLS1* expression is found across a variety of cancer types, and is frequently correlated with poor patient prognosis.²² In contrast, *GLS2* is identified as a target gene of the tumor suppressor protein p53,^{41,42} with expression restricted primarily to the liver, pancreas, brain and pituitary gland.^{37,38} Along with its decreased expression in various cancer types,^{43,44} *GLS2* is therefore generally regarded to have a tumor-suppressive function. This may be related to its role in the promotion of an iron-dependent form of cell death termed ferroptosis,⁴⁵ or its ability to act as a binding protein independent of its glutaminase activity.⁴⁶ In contrast, expression of *GLS2* can also be promoted by the oncogenic n-Myc protein,⁴⁷ and upregulated *GLS2* expression in breast cancer tissues is found to be correlated with poor patient prognosis,^{48,49} indicating that the function of *GLS2* may not be strictly suppressive.

Following the discovery that glutamine is an indispensable nutrient for the growth and survival of many cancer cells, several glutamine metabolism-targeting strategies have been evaluated as potential targeted anti-cancer therapies. These include the broad-spectrum, irreversible inhibition of glutamine-utilizing enzymes using 6-diazo-5-oxo-L-norleucine (DON)^{50,51} or either of its pro-drug successors, JHU-083⁵² and sirpiglenastat (DRP-104),⁵³ the selective inhibition of *GLS1* using bis-2-(5-phenylacetamido-1,2,4-thiadiazol-2-yl)ethyl sulfide (BPTES),⁵⁴ its successor telaglenastat (CB-839)⁵⁵ or IACS-6274 (IPN60090),⁵⁶ and the inhibition of glutamine uptake using V-9302.⁵⁷ Already in the mid-1950s, clinical testing of the first of these strategies commenced. However, although DON demonstrated promising anti-tumor activity in these trials, it was withdrawn from further clinical development due to significant toxicities.⁵⁸ Since then, telaglenastat has entered clinical evaluation in 2014 and is currently studied in several phase I and II trials, whereas sirpiglenastat (ClinicalTrials.gov identifier: NCT04471415) and IACS-6274 (NCT05039801) only more recently entered clinical-stage development. Importantly,

although the mentioned therapeutic strategies were initially solely perceived to exploit the dependence of tumors on glutamine, it has been increasingly recognized that their effects extend beyond those affecting the cancer cells, as will be discussed below.

In addition to directly supporting cancer cell proliferation, excessive tumoral metabolism of glutamine may also deprive tumor-infiltrating immune cells of an important nutrient. Similar to cancer cells, activated T cells enhance glutamine uptake and glutaminolysis to accommodate the demands of rapid proliferation.^{59,60} Moreover, sufficient levels of intracellular glutamine are required for activation of TCR-induced mTORC1 signaling,^{61,62} as glutamine serves as a counter-substrate for import of the essential amino acid leucine.⁶³ Accordingly, glutamine-depriving conditions compromise the growth and proliferation of activated T cells *in vitro*,^{59,60} whereas restoration of tumor interstitial glutamine levels by tumor-specific GLS1 knockout increases T-cell infiltration and activity *in vivo*.⁶⁴ However, since different subsets of T cells engage distinct metabolic programs,^{18,65} their dependency on glutamine availability also diverges. In particular, limitation of glutamine uptake inhibits the differentiation of naïve CD4⁺ T cells under Th1- and Th17-skewing conditions,⁶² while glutamine deprivation promotes their differentiation into CD4⁺CD25⁺FoxP3⁺ regulatory T cells.⁶⁵⁻⁶⁷ These effects may at least partially be due to compromised *de novo* synthesis of glutathione,⁶⁸ nucleotides⁶⁷ or α -ketoglutarate.⁶⁶ In contrast to T cells, natural killer (NK) cells do not require glutamine to fuel their metabolism, although glutamine deprivation does impair NK-cell growth and functional responses due to its role in the regulation of c-Myc expression.⁶⁹

Based on the evident role of GLS1 in cancer development, selective targeting of this enzyme presents an attractive therapeutic anti-cancer approach. This is supported by the direct anti-proliferative effect exerted by different GLS1 inhibitors on cancer cells of diverse origin in *in vitro* studies.^{55,70,71} However, inhibition of GLS1 may also indirectly affect tumor growth through the combined effect of elevated glutamine availability and inhibition of glutaminolysis on immune cell function. Notably, although both tumor cells and activated T cells upregulate glutaminolysis to fuel their proliferation,^{21,59} the metabolism and proliferative ability of these cells is not equally disrupted by GLS1 inhibition.^{55,72} More specifically, different subsets of T cells are differentially dependent on functional glutaminolysis, as genetic GLS1 disruption suppresses CD4⁺ T-cell differentiation into Th17 cells, but promotes CD4⁺ Th1 and cytotoxic CD8⁺ T-cell differentiation and function. This is associated with the altered epigenetic regulation of gene expression caused by modulation of α -ketoglutarate levels.⁶⁵ Furthermore, restoration of glutamine availability upon GLS1 inhibition restores NK-cell cytotoxicity, which is not abolished by abrogation of NK-cell glutaminolysis.⁶⁹ In contrast, selective inhibition of GLS1 suppresses the differentiation and immunosuppressive function of immature myeloid cells as well as

the polarization of macrophages towards an anti-inflammatory phenotype, which is analogous to the effect of tumor-induced glutamine deprivation.⁷³⁻⁷⁵

Despite the complementary anti-proliferative effect exerted by GLS1 inhibitors on tumor cells and their stimulatory effect on the immune cell compartment, monotherapy with BPTES or telaglenastat has demonstrated variable efficacy in *in vivo* models.^{55,71,72,74,76} Moreover, only limited single-agent activity has been observed for telaglenastat in clinical trials,⁷⁷ which may be due to upregulation of compensatory metabolic pathways in the targeted cancer cells.^{76,78,79} Inhibition of glutamine uptake or broader blockade of glutamine-utilizing enzymes may at least partially resolve these issues, although they would logically also disrupt the metabolism of immune cells. Nonetheless, inhibition of glutamine uptake by V-9302 induces a marked reduction of tumor growth *in vivo*, which is accompanied by enhanced activation and functionality of effector T cells. Compensatory upregulation of an alternative glutamine transporter by T cells, but not tumor cells, is suggested to explain the unanticipated effective immune response.⁶⁴ Moreover, inhibition of glutamine-utilizing enzymes by JHU-083 or sirpiglenastat does not disable the *in vivo* anti-tumor immune response, but instead conditions T cells towards a more proliferative, less exhausted phenotype.^{52,53} This is attributed to the remarkable flexibility of T cells, but not tumor cells, to use glucose for replenishment of TCA cycle intermediates when glutamine metabolism is blocked.⁵² Furthermore, broad inhibition of glutamine-utilizing enzymes promotes anti-tumor immunity by inducing apoptosis of MDSCs, stimulating the conversion of immunosuppressive macrophages and MDSCs into pro-inflammatory macrophages, and inhibiting the expression of IDO1 in both myeloid and tumor cells.⁸⁰

Alternatively, the effectiveness of GLS1 inhibition may be limited by the exhaustion of T cells *in vivo*, as GLS1 deficiency over time induces expression of PD-1 on T cells.⁶⁵ Moreover, inhibition of GLS1, as well as glutamine deprivation or inhibition of glutamine uptake, results in upregulation of tumoral PD-L1 expression.^{81,82} These observations indicate that dual targeting of glutamine metabolism and the PD-1/PD-L1 interaction may improve the therapeutic anti-tumor response. Accordingly, α -PD-1 or α -PD-L1 treatment, as well as blockade of CTLA-4, enhances the efficacy of inhibitors targeting GLS1, glutamine uptake or glutamine-utilizing enzymes *in vivo*.^{52,53,72,74,81,83,84} Moreover, inhibition of GLS1 or glutamine-utilizing enzymes enhances the response to immune checkpoint inhibitors in immune checkpoint blockade-resistant mouse models.^{74,80} In a phase II clinical trial, telaglenastat combined with the PD-1 inhibitor nivolumab showed a modest objective response rate in α -PD-1/PD-L1-refractory melanoma patients based on preliminary results (NCT02771626).⁸⁵ In contrast, a phase II study of telaglenastat in combination with pembrolizumab (α -PD-1) and chemotherapy in patients with metastatic non-small

cell lung cancer (NCT04265534) was recently terminated due to lack of clinical benefit. Clinical results of the ongoing phase I/II trial of sirpiglenastat combined with atezolizumab (α -PD-L1) in patients with advanced solid tumors (NCT04471415) may provide further clarity on the effectiveness of combining glutamine metabolism-targeting strategies with immune checkpoint blockade.

In conclusion, GLS1 inhibition and other glutamine metabolism-targeting strategies have presented themselves as promising approaches for cancer treatment, both through direct targeting of glutamine-addicted tumor cells and through enhancement of the anti-tumor immune response. The latter effect appears to be at least partially owed to the plasticity of T cells to accommodate perturbations in their glutamine metabolism, although further efforts are required to completely understand the mechanisms underlying this favorable phenomenon. Moreover, as the discussed approaches have yet to demonstrate convincing efficacy in clinical trials, a rational exploration of the drug combination space may prove valuable for future clinical endeavors.

The arginine-metabolizing enzyme ARG1

Similar to glutamine, arginine is classified as a conditionally essential amino acid, as it must be provided through nutrition during conditions of stress as well as during fetal and neonatal development.⁸⁶ It is a highly versatile amino acid, serving as a precursor for the synthesis of proteins, other amino acids and a variety of biologically important metabolites, including nitric oxide (NO), creatine, agmatine and polyamines. The metabolic fate of arginine is determined by the coordinated action of a diverse set of highly regulated enzymes and arginine transporters.⁸⁷ Among these are the arginase (ARG) enzymes, catalyzing the hydrolysis of arginine into the non-proteinogenic amino acid ornithine and the waste product urea. This metabolic conversion presents the final step of the urea cycle for ammonia detoxification and provides ornithine as a substrate for polyamine synthesis and interconversion into proline or glutamate.⁸⁷

In humans, ARG is expressed as two isoforms differing in subcellular localization and distribution among cell and tissue types.⁸⁸ ARG1 is a cytosolic enzyme predominantly and abundantly expressed in the liver as a key enzyme of the urea cycle, although it is also expressed by cells of the myeloid lineage to regulate immune responses.⁸⁹ In contrast, mitochondrial ARG2 has a more ubiquitous, extrahepatic expression pattern,⁸⁹ and is suggested to primarily function as a regulator of arginine availability.⁹⁰ Similar to ARG1, it is also expressed by various immune cells,²³ but its role in the immune system is still largely elusive. In accordance with their physiological tissue distribution,

expression of ARG1 by tumors is mainly limited to hepatocellular carcinoma,^{91,92} while ARG2, although largely understudied compared to ARG1, is found in the neoplastic cells of several human cancer types.^{93–96} Importantly, however, and in contrast to the GLS1 enzyme, the main immunosuppressive activity exerted by ARG enzymes does not stem from their expression by tumor cells, but rather from ARG1 expressed by tumor-infiltrating immune cells.

A role for ARG1 in the immune system was first identified based on its Th2-type cytokine-inducible expression in various murine myeloid cell types, including macrophages and dendritic cells.^{97,98} However, the cell-type specificity and inducibility of ARG1 expression in myeloid cells differs considerably between humans and mice,²³ complicating the translation from murine studies to human subjects. In contrast to its murine counterpart, human ARG1 is strictly and mostly constitutively expressed by granulocytes, including neutrophils, granulocytic MDSCs (G-MDSCs) and eosinophils.^{99,100} For this reason, murine ARG1-expressing myeloid cells other than granulocytes will not receive focus in this review. However, this is not where the discrepancies end, as murine myeloid cells mostly regulate extracellular arginine levels through its uptake and subsequent ARG1-mediated degradation,¹⁰¹ whereas human granulocytes store ARG1 in their granules to become active only upon exocytosis.^{99,102,103} Moreover, murine G-MDSCs have been found to release ARG1 in small extracellular vesicles,¹⁰⁴ which is a phenomenon currently only observed for ARG1-expressing tumor cells in the human setting.¹⁰⁵

In patients with various cancer types, high ARG1 expression and activity is found in both circulating and tumor-infiltrating myeloid cells, with G-MDSCs as its major source.^{91,106–109} Notably, granulocytes of glioblastoma patients are found to be in a degranulated state, while plasma ARG1 levels of these patients are significantly increased.¹¹⁰ Furthermore, tumor-infiltrating granulocytes in patients with non-small cell lung cancer or renal cell carcinoma have decreased ARG1 levels compared to their non-tumor-infiltrating counterparts,^{100,111} despite having increased ARG1 mRNA expression.¹⁰⁰ These findings indicate the tumor-associated release of granule-stored ARG1 in cancer patients, which is in line with the elevated ARG1 levels and activity, as well as decreased arginine levels, found in the plasma of patients with diverse tumor types.^{91,100,106,111} Importantly, since the release of ARG1 occurs upon tumor infiltration,¹¹¹ arginine levels in the TME may be even further reduced. In murine pancreatic tumors, near-complete depletion of arginine is detected in tumor interstitial fluids, whereas ornithine levels are increased compared to those in plasma samples.¹¹² Although ARG1 expression and its mode of action differs between the murine and human myeloid compartment, this suggests that myeloid cell-expressed ARG1 can efficiently deprive the TME of a valuable nutrient.

Enhanced activity of ARG1 in the TME may directly support tumor growth by supplying tumor cells with ornithine or ornithine-derived polyamines, which are essential for their growth and proliferation,^{113,114} and by decreasing cytotoxic NO production.¹¹⁴ However, these are not the sole mechanisms through which ARG1 promotes tumor growth, as its activity can also adversely affect the activation and function of tumor-infiltrating immune cells. In activated T cells, arginine is not only required to keep up with the fast rate of activation-induced protein synthesis, but it is also rapidly metabolized by virtue of the upregulation of ARG2 and that of other enzymes determining its downstream fate.¹¹⁵ To meet the high demand for arginine, activated T cells mostly depend on its enhanced uptake, which is achieved through upregulation of arginine transporter expression.^{115,116} When extracellular arginine is superfluous, activated T cells shift their metabolism from aerobic glycolysis towards oxidative phosphorylation. While this limits their differentiation, it instead favors the generation of central memory-like T cells with greater survival capacity and enhanced *in vivo* anti-tumor responses.¹¹⁵ In contrast, when extracellular levels of arginine are depleted, intracellular arginine levels become insufficient, despite attempts of T cells to restore them by increasing the import of its precursor citrulline and upregulating the expression of the arginine biosynthetic enzyme argininosuccinate synthetase.^{117,118}

Arginine-depriving conditions or ARG1-expressing cells profoundly inhibit the activation-induced proliferation of T cells.^{100,119,120} Over the years, a number of mechanisms underlying this inhibitory effect have already been elucidated. A prime mechanism is the reversible reduction of CD3 ζ chain expression, which blocks re-expression of the TCR after its antigen-induced internalization and thus compromises T-cell signaling.^{119,121} Accordingly, decreased CD3 ζ expression is found in the peripheral or tumor-infiltrating T cells of cancer patients with high myeloid ARG1 expression.^{101,106} Arginine starvation also disrupts the cell cycle progression of activated T cells, arresting them in the G₀/G₁ phase and thereby hampering their proliferation.¹²² Cell cycle arrest is caused by arginine deprivation-induced activation of the GCN2 pathway, which blocks the upregulation of critical cell cycle progression regulators by promoting a global arrest in *de novo* protein synthesis.^{122,123} Amino acid sensing by mTORC1 may additionally be involved in the effects of arginine starvation on T-cell proliferation.^{124,125} Finally, the actin-depolymerizing factor cofilin is inhibited in T cells cultured under arginine-depriving conditions. This impairs formation of the immunological synapse between T cells and antigen-presenting cells due to stiffening of the actin cytoskeleton and thereby hampers effective T-cell activation and thus proliferation.¹²⁶

Besides affecting T-cell proliferation, arginine depletion also inhibits the T-cell production of several cytokines, including IFN γ , IL-5 and IL-10,^{119,127} and the secretion of the cytotoxic protease granzyme B.¹²⁷ In contrast, T-cell chemotaxis and the antigen-specific cytotoxicity

of CD8⁺ T cells are largely preserved.^{127,128} Moreover, the viability of T cells remains unaltered upon arginine depletion,^{119–121} allowing these cells to re-gain their proliferative and cytokine secretory potential upon arginine replenishment and re-stimulation.¹²⁰ Arginine deprivation also induces the generation of CD4⁺CD25⁺FoxP3⁺ regulatory T cells, either from naïve CD4⁺ T cells or from a pre-existing natural CD4⁺CD25⁺FoxP3⁻ regulatory T cell population.^{124,129–131} This may require or be potentiated by TGF-β^{124,131} and involves the mTORC1 signaling pathway.¹²⁴ However, ARG1-expressing MDSCs may also promote Th17 differentiation of naïve CD4⁺ T cells,¹³² indicating a complex role for arginine in T-cell differentiation. Depletion of arginine additionally impairs NK-cell proliferation and IFNγ secretion, while effects on NK-cell viability and cytotoxicity are still unclear based on the existence of contradictory reports.^{91,133–135} Moreover, arginine deprivation promotes the expansion of immunosuppressive G-MDSCs in mice,¹³⁶ while it does not affect the activation, phagocytic functions or cytokine production of murine macrophages.¹³⁷

In an effort to constrain the immunosuppressive effects exerted by ARG1-expressing myeloid cells, several ARG-targeting small molecule inhibitors have been developed. These are limited to only dual inhibitors of ARG1 and ARG2, as the highly conserved active sites of these enzymes encumber the development of isoform-specific variants.¹³⁸ The extensively studied (2S)-2-amino-6-boronohexanoic acid (ABH) and N^ω-hydroxy-nor-L-arginine (nor-NOHA) were among the first inhibitors to be identified,^{139,140} but poor pharmacokinetic properties have limited their clinical application.^{141,142} More recently, inhibitors with considerably improved pharmacokinetic profiles have been developed, which include CB-1158 (INCB001158; numidargistat)⁹¹ and OATD-02 (OAT-1746).¹⁴³ Whereas OATD-02 can inhibit both intracellular and secreted ARG enzymes,¹²⁸ CB-1158 acts only extracellularly due to its inefficient ability to cross the cell membrane.⁹¹ Notably, this spares not only the activity of crucial liver-expressed ARG1, but also that of ARG2, which appears to function only within the cell. However, consequences of ARG2 inhibition may be limited based on the phenotype of ARG2-deficient mice.¹⁴⁴ Furthermore, *in vitro* studies indicate that inhibition of ARG2 may even be beneficial for the anti-tumor T cell response,^{145,146} whereas it may also directly inhibit the growth of ARG2-expressing tumors.¹⁴⁷ Alternative approaches to directly or indirectly inhibit ARG activity have also been reported, which include isoform-specific ARG antibodies^{148,149} and therapeutic peptide vaccines.^{150,151}

ARG inhibition or myeloid cell ARG1 knock-out inhibits tumor growth in various syngeneic mouse models, which has compellingly been associated with changes of the TME immune cell composition towards a tumor-hostile environment.^{91,101,128,147,152,153} Moreover, in different murine tumor models, inhibition of ARG enhances the therapeutic efficacy of α-PD-1 treatment.^{91,128,154} Based on these promising results, CB-1158 has entered a number of phase I/II clinical trials over the last several years. These include two completed trials in

patients with advanced solid tumors in which CB-1158 was studied as monotherapy and in combination with the PD-1 inhibitor pembrolizumab (NCT02903914) or retifanlimab (NCT03910530). Preliminary phase I data reported for the former demonstrate a slight improvement in the objective response rate of colorectal carcinoma patients treated with CB-1158 mono- or combination therapy compared to historical control data, and an increased number of intratumoral CD8⁺ T cells in post-treatment biopsies.¹⁵⁵ However, further clinical results will have to be awaited to draw any firm conclusions on the benefit of ARG inhibition for cancer treatment. The clinical evaluation of OATD-02, which has just recently entered its first phase I trial in patients with advanced and/or metastatic solid tumors (NCT05759923), should also contribute to this quest.

Taken together, the growing body of research on the role of myeloid cell-expressed ARG1 in cancer immune escape underscores the promise of this enzyme as a target for cancer immunotherapy. To date, this is mostly supported by *in vitro* studies performed on human immune cells and *in vivo* studies with syngeneic mouse models. Importantly, however, it remains to be determined whether the differential expression of ARG1 between mice and men poses any problem for the translation of this approach towards cancer patients. For this, data from clinical trials is pivotal, and these data should also provide insight as to whether extracellularly-restricted ARG inhibitors may be more beneficial for cancer treatment compared to inhibitors acting also intracellularly, or *vice versa*.

The arginine-metabolizing enzyme iNOS

A different metabolic fate of arginine is its conversion into the important signaling molecule NO. This reaction is catalyzed by nitric oxide synthase (NOS) enzymes and yields citrulline as a by-product that can be recycled back into its precursor arginine. Three distinct isoforms of NOS are encoded by the mammalian genome, which are neuronal NOS (nNOS or NOS1), inducible NOS (iNOS or NOS2) and endothelial NOS (eNOS or NOS3).¹⁵⁶ Both nNOS and eNOS are constitutively expressed enzymes that can be triggered by calcium influx to transiently produce nanomolar concentrations of NO. A calcium-independent increase in eNOS activity can additionally be elicited by eNOS phosphorylation.¹⁵⁷ Under physiological conditions, nNOS plays a fundamental role in neurotransmission, while eNOS is a critical regulator of various cardiovascular functions, including vasodilation.¹⁵⁶ Distinctively, expression of iNOS can be induced in a variety of cell types upon exposure to a broad range of factors, including pro-inflammatory cytokines and hypoxia,¹⁵⁸ while it is concurrently subject to intricate regulation by NO levels and arginine availability.^{159–161} iNOS is capable of calcium-independently producing sustained micromolar levels of NO,¹⁵⁷ through which it primarily supports pathogen killing and regulation of immune responses.¹⁶²

NO, the primary product of NOS activity, is a short-lived, highly diffusible free radical (frequently denoted as $\cdot\text{NO}$) capable of freely crossing cellular membranes. While NO is relatively unreactive towards most biomolecules, it can very rapidly form reactive nitrogen species (RNS) by reacting with molecules having unpaired electrons, such as other free radicals and transition metal ions.¹⁶³ An important reaction partner of NO is superoxide anion ($\text{O}_2^{\cdot-}$), which is formed by NOS enzymes upon depletion of the substrate arginine or co-factor tetrahydrobiopterin (BH_4), but can also be generated by other sources.¹⁶⁴ Reaction of NO with superoxide anion yields the powerful, but short-lived oxidant peroxynitrite (ONOO^-), which can efficiently nitrate protein tyrosine residues upon its decomposition.¹⁶³ Other NO-derived RNS (*i.e.*, N_2O_3 and NO^+) can readily react with the thiol side chain of cysteine residues to yield protein S-nitrosylation.¹⁶⁵ Both nitration and S-nitrosylation are highly selective processes, and have the potential to greatly alter the structure and function of target proteins.^{164,165} In addition to protein modification, NO-derived RNS can cause DNA damage by modifying nucleic acids,¹⁶⁶ and can generate nitrolipids capable of activating cell-signaling pathways.¹⁶⁷ Moreover, NO can coordinate to transition metals bound by enzymes and transcription factors, thereby altering their activity.¹⁶⁸ As a relevant exemplar, coordination of NO to the heme-bound iron of soluble guanylate cyclase (sGC) induces production of the second messenger cyclic guanosine monophosphate (cGMP), which serves to regulate various physiological processes.¹⁶⁹

It is broadly acknowledged that NO plays an important role in both cancer development and subsequent progression. NO-producing NOS enzymes are aberrantly expressed in a variety of human tumors,¹⁷⁰ with effects of elevated NO levels being dependent on its cellular source, concentration, local chemical environment and cellular target.¹⁷¹ Among the three isoforms, iNOS has most extensively been studied in cancer based on its frequent detection in tumor cells, tumor-infiltrating immune cells and tumor-associated fibroblasts. Overexpression of eNOS has additionally been found in the vascular endothelial cells of a myriad of cancer types.¹⁷⁰ Although the elevated expression of NOS enzymes, particularly iNOS, has recurrently been associated with tumor malignancy and poor patient prognosis, it is increasingly recognized that the role of NO in cancer is inherently complex owing to its diverse spectrum of cellular sources and biological effects.¹⁷¹ Notably, NO acts as a double-edged sword in cancer by predominantly exerting pro-tumorigenic effects at relatively low concentrations, such as inducing DNA damage, tumor cell metabolic reprogramming and neovascularization, while suppressing tumor growth at higher concentrations by inducing apoptosis.^{170,172} Furthermore, dependent on its concentration, NO can either stimulate or suppress the anti-tumor immune response, as will be discussed below.

Early research has indicated that NO promotes an effective immune response when present at low, physiological concentrations. This is for instance achieved through the

cGMP-dependent induction of Th1- and Th17-cell differentiation,^{173,174} the suppression of regulatory T-cell generation,¹⁷⁵ and the inhibition of T-cell apoptosis through caspase S-nitrosylation.¹⁷⁶ However, within the TME, the production of NO is often considerably enhanced due to the presence of iNOS-expressing tumor cells, macrophages and MDSCs, resulting in NO concentrations capable of significantly hampering immune responses. At elevated concentrations, NO inhibits T-cell activation and proliferation by impeding activation-induced protein tyrosine phosphorylation, which may occur through nitration or S-nitrosylation of crucial protein residues, or through a cGMP-dependent pathway.^{177–182} In addition, these and other NO-dependent mechanisms can prime T cells to undergo apoptosis.^{179,183,184} High concentrations of NO also suppress the *in vitro* polarization of CD4⁺ T cells towards both Th1 and Th17 phenotypes,^{185–188} while an effective immune response may further be precluded by the NO-induced generation of CD4⁺CD25⁺FoxP3⁻ regulatory T cells.¹⁸⁹ Moreover, besides affecting the functionality of T cells, high concentrations of NO can impair effector functions of NK cells through nitration of crucial signaling proteins,¹⁹⁰ and induce phenotypic and metabolic reprogramming of macrophages and dendritic cells.^{191–193}

An effective immune response also relies on the ability of T cells to infiltrate tumor tissues and to successfully recognize their cognate tumor antigens. While low concentrations of NO stimulate the expression of cellular adhesion molecules mediating the migration of T cells from blood vessels into the tumor stroma,¹⁹⁴ high concentrations act suppressive, thereby hampering the infiltration of T cells into tumor tissues.^{194–196} Moreover, NO-induced nitration of the chemoattractant CCL2 can cause successfully migrated T cells to remain trapped in the tumor stroma.¹⁹⁷ In contrast, nitrated CCL2 has an unaltered ability to recruit MDSCs into the tumor core,¹⁹⁷ while accumulation and induction of MDSCs is further promoted by iNOS-dependent upregulation of vascular endothelial growth factor (VEGF) secretion.¹⁹⁸ NO-mediated nitration can also abrogate the recognition of tumor antigens by T cells, as nitration of even a single tyrosine residue in major histocompatibility complex (MHC)-presented peptides can hinder their interaction with the TCR.^{199,200} Moreover, MDSCs from peripheral lymphoid organs can induce nitration of TCR and CD8 molecules on T cells upon antigen-specific cell–cell contact, rendering them insensitive to stimulation by the presented antigen.^{201,202} Tumor-infiltrating MDSCs, which greatly upregulate iNOS expression in response to the hypoxic TME, can additionally affect nearby cells without requiring antigen-specific interaction.²⁰³ This allows them to nitrate MHC class I molecules on neighboring tumor cells, thereby disturbing their peptide presentation and allowing them to become resistant to antigen-specific cytotoxic T cells.²⁰⁴ Finally, through inducing the downregulation of MHC class II gene transcription, NO can also negatively affect the function of antigen-presenting cells.²⁰⁵

Based on the pivotal role of NO in cancer development, different therapeutic strategies aimed at the modulation of NO levels have already been considered for cancer treatment. Noteworthy in this context is the clear dichotomy presented by the assessment of both NO-donating molecules and NOS inhibitors. NO donors are studied for their ability to directly induce the apoptosis of tumor cells or to sensitize them to other therapies,²⁰⁶ but will evidently frustrate the immune system as well. In contrast, NOS inhibitors may serve as targeted therapies to revert the pro-tumorigenic effects of NO on tumor cells,²⁰⁷ while they may also reinvigorate anti-tumor immune responses. During the recent decades, a large number of NOS inhibitors has already been developed and evaluated in clinical trials for various disease indications.²⁰⁸ These include both pan- and isozyme-selective inhibitors of the NOS enzymes.²⁰⁸ In murine cancer models, treatment with either type of inhibitor has been shown to reduce tumor growth,^{207,209–211} but availability of *in vivo* data on the contribution of the immune system to this effect is still very limited.^{210,212} Since peroxynitrite may be the major NO-derived effector molecule responsible for T-cell dysfunction, peroxynitrite neutralization or blockade of its formation may also present an attractive therapeutic strategy, which has already demonstrated efficacy in murine models.^{182,197} Only recently, the first phase I/II clinical trial evaluating the use of an NOS inhibitor for anti-cancer therapy has been completed (NCT02834403). Results from this trial demonstrate a promising efficacy for the pan-NOS inhibitor L-N^G-monomethyl-arginine (L-NMMA) in combination with docetaxel chemotherapy in triple-negative breast cancer patients, and show modest differences in circulating immune cell composition between responders and non-responders.²¹³ Moreover, L-NMMA is currently being evaluated in a phase I trial in combination with pembrolizumab (α -PD-1) in patients with different solid tumors (NCT03236935), which may yield further clarification on the effects of NOS inhibition on the anti-tumor immune response.

Overall, there is accumulating evidence that the complex, multifaceted role of iNOS in cancer includes the facilitation of tumor immune escape. Distinctive from the action of other amino acid-metabolizing enzymes, this may not only involve the direct suppression of T-cell responses, but also the impediment of their tumor infiltration and antigen recognition. However, as *in vivo* data on the effect of NOS inhibitors on the anti-tumor immune response are currently still largely lacking, attention should be directed towards studying these inhibitors in more complex models. Simultaneously, such studies can contribute to our understanding of whether the use of either pan- or isozyme-selective NOS inhibitors should be the preferred approach for future clinical trials.

The tryptophan-metabolizing enzymes IDO1 and TDO

Unlike glutamine and arginine, tryptophan is an essential amino acid that is exclusively obtained by humans through dietary intake.²¹⁴ In addition to serving as a fundamental protein building block, tryptophan is a precursor for various bioactive compounds. These include metabolites generated along the serotonin pathway and indoles produced by the gut microbiota or by host cells.^{215,216} However, the vast majority of tryptophan degradation occurs through the kynurenine pathway, which is initiated and rate-limited by the paralogous enzymes IDO1 and IDO2, and the evolutionarily unrelated TDO. Each of these enzymes catalyzes the oxidation of tryptophan to yield *N*-formylkynurenine, which is then rapidly hydrolyzed to kynurenine and can be further metabolized into an array of downstream molecules.²¹⁵

Expression of IDO1, the most extensively studied enzyme of the kynurenine pathway, is highly inducible across a broad range of cell and tissue types, with IFN γ serving as its main inducer.^{217,218} While initially recognized for its role in the defense against infectious pathogens,²¹⁹ IDO1 is now widely acknowledged as a critical regulator of immune responses. Existence of the closely related enzyme IDO2 was not discovered until two decades later,^{220,221} and its physiological relevance is still to be fully elucidated.^{222,223} Although it is expressed in a number of human tissues,²²¹ IDO2 displays only low tryptophan-metabolizing activity²²⁴ and frequently suffers from genetic polymorphisms compromising or ablating its activity.²²¹ Nonetheless, studies performed with IDO2-deficient mice have indicated a role for the enzyme in controlling inflammation.²²⁵ Finally, expression of TDO is mainly restricted to the liver and the brain, where it constitutively regulates systemic and brain tryptophan homeostasis.^{226,227} In addition, TDO has been implicated in the maintenance of brain morphology and the regulation of brain function.²²⁷

The immunoregulatory function of IDO1 is one also commonly exploited by tumors, and has additionally been ascribed to TDO expressed in the context of cancer. While normally silenced in many tissues, IDO1 is highly expressed in the tumor cells of a wide range of human cancer types.²²⁸ This constitutive or inducible expression can be initiated by loss of the tumor suppressor protein Bin1,²²⁹ or gain-of-function mutation of the *KIT* proto-oncogene.²³⁰ Moreover, constitutive IDO1 expression can further be maintained by autocrine signaling involving the cyclooxygenase-2 (COX-2)/prostaglandin E2 (PGE2) pathway²³¹ or a self-sustaining autocrine loop involving activation of the AhR by tryptophan metabolites.²³² Besides its presence in tumor cells, IDO1 is also expressed by various cells residing in the TME or tumor-draining lymph nodes, including dendritic cells, MDSCs, macrophages, endothelial cells, fibroblasts and mesenchymal stem cells.^{233–238} Across different tumor types, expression of IDO1 is inversely correlated with infiltrating CD3⁺ and

CD8⁺ T cells as well as NK cells, while being positively correlated with regulatory T-cell frequency.^{239–244} In addition, elevated IDO1 expression correlates with tumor progression as well as poor survival in both solid and hematological cancers.^{245,246}

Expression of TDO can be detected in cancers of various tissue origins as well,^{247,248} despite normally being confined to only specific tissue types. Constitutive expression of TDO in tumor cells can be regulated similarly to that of IDO1, involving signaling via the COX-2/PGE2 and AhR pathways,^{249,250} while other TDO-regulating pathways have been described as well.^{251,252} Upregulated expression of TDO is additionally (or even predominantly) found in the stroma of various tumor types,^{253,254} which includes its expression by pericytes and fibroblasts.^{253,255} Elevated TDO expression is correlated with decreased survival in a number of human cancer types,^{256–259} and inversely correlates with CD8⁺ T-cell infiltration in human glioma tissues.²⁴⁷ In contrast to both IDO1 and TDO, gene expression of IDO2 is limited in human tumor tissues,²⁶ and tryptophan-metabolizing activity fully resides with co-present IDO1 in IDO2-expressing tumors.²⁶⁰ Furthermore, although IDO2 is also expressed by dendritic cells,²²¹ it remains unclear what role it serves in these cells.^{261,262}

Elevated metabolism of tryptophan by either IDO1 or TDO can adversely affect T-cell responses through both depletion of tryptophan levels and accumulation of its metabolites. While tryptophan depletion may act by activation of the GCN2 kinase pathway or repression of mTORC1 activity,^{263,264} kynurenine and its downstream derivatives can operate as agonists of the AhR.^{247,265–267} IDO1-expressing cells inhibit the proliferation of activated T cells^{233,268,269} and induce CD8⁺ T-cell anergy,²⁷⁰ which is at least partially ascribed to tryptophan depletion-induced GCN2 activation.²⁶³ Underlying molecular mechanisms affecting the T cells include their arrest in the mid-G₁ cell cycle phase²⁶⁸ and the GCN2-dependent downregulation of CD3 ζ expression in the CD8⁺ subset, which impairs their cytotoxic effector function.²⁷¹ Notably, tryptophan metabolites may also contribute to suppression of T-cell proliferation as well as induce T-cell apoptosis,^{272–274} with AhR activation and kynurenine-induced depletion of fatty acids as recently proposed apoptosis-inducing mechanisms.^{257,275} Furthermore, elevated tryptophan metabolism upregulates PD-1 expression on CD8⁺ T cells through activation of the kynurenine–AhR signaling pathway,^{276–278} and concurrently inhibits the production of IFN γ by these cells.^{271,279} On the other hand, IDO1-expressing cells promote the activity of immunosuppressive T cells through GCN2-dependent activation of resting regulatory T cells and inhibition of their reprogramming into Th17-like effector cells.^{280–282} Moreover, tryptophan depletion and metabolite accumulation promote the conversion of naïve CD4⁺ T cells into CD4⁺CD25⁺FoxP3⁺ regulatory T cells, which can involve modulation of the GCN2, mTORC1 or AhR signaling pathway.^{124,266,271}

The tryptophan-metabolizing activities of IDO1 and TDO can also have detrimental consequences for NK cells, which are mostly attributed to the action of kynurenine or its downstream metabolites. Effects exerted by these molecules include the inhibition of NK-cell proliferation and the induction of NK-cell apoptosis.^{273,274} Moreover, kynurenine downregulates the expression of activating NK-cell receptors,²⁸³ as well as NK receptor ligand on tumor cells,²⁸⁴ with consequential inhibition of NK-cell cytotoxic activity and IFN γ production.^{283,285} The generation of an immunosuppressive microenvironment can further be driven by the effects of excessive tryptophan metabolism on dendritic cells, macrophages and MDSCs. In particular, through modulation of the GCN2 pathway, tryptophan depletion enhances the tolerogenicity of dendritic cells²⁸⁶ and polarizes macrophages towards a suppressive phenotype.²⁸⁷ The latter effect can also be induced through kynurenine-dependent AhR signaling,^{277,288} which additionally promotes chemokine-mediated recruitment of these macrophages by tumors.²⁸⁸ Furthermore, IDO1 promotes the expansion and suppressive capacity of MDSCs,²⁸⁹ and indirectly recruits them to the tumor through the action of IDO1-induced regulatory T cells.²⁴⁴

In contrast to different immune cells, tumor cells can rather efficiently adapt to tryptophan-deprived conditions. While activation of the GCN2 pathway in malignant cells downregulates protein synthesis, it concurrently upregulates tryptophan transport²⁹⁰ and tryptophanyl-tRNA synthetase expression,²⁹¹ allowing the cells to readily utilize any incoming tryptophan for proliferation. Notably, even upon sustained tryptophan deprivation, tumor cells continue protein synthesis, which was recently shown to result in the generation of frame-shifted and tryptophan-to-phenylalanine-substituted proteins.^{292,293} Consequences of these aberrant proteins for cellular physiology are, however, still unclear and tumor cell presentation of resultant aberrant peptides may even elicit immunogenic responses.^{292,293} Tryptophan metabolism can also directly promote the survival and proliferation of tumor cells through accumulation of kynurenine,^{247,294,295} which additionally stimulates their migratory ability.^{249,296} Moreover, the activity of IDO1 is involved in promoting neovascularization, thereby further supporting tumor growth,^{289,297} while expression of TDO by tumor-associated pericytes suggests a similar role for TDO.²⁵³

Despite the abundant *in vitro* evidence indicating a tumor-promoting role for IDO1, elucidation of the effects exerted by IDO1 *in vivo* have been complicated by the expression of IDO1 in both tumor cells and non-malignant host cells of cancer patients, of which contributions vary among cancer types.²⁵⁴ This encumbers the reproduction of tumors and their TME in syngeneic mouse models, which is further obstructed by the scarcity of murine cell lines naturally expressing IDO1,²⁹⁸ as is also the case for TDO.²⁹⁹ However, using IDO1-deficient mice, host IDO1 has been found to play a role in promoting tumor growth, MDSC accumulation and expression of PD-1 by CD8⁺ T cells in a model of Lewis

lung carcinoma.³⁰⁰ In murine models of colon, skin and brain cancer, however, host IDO1 deficiency does not diminish tumor growth,^{301–303} although it modestly enhances the efficacy of immune checkpoint blockade therapies³⁰² or decreases regulatory T-cell infiltration.³⁰³ Notably, ablation of host IDO1 expression also induces loss of IDO1 inhibitor efficacy in different tumor models, which would be suggestive of a suppressive role for host IDO1, although IDO1 deficiency itself paradoxically does not alter tumor growth in these models.^{304,305} On the other hand, tumor cell-specific knockdown of IDO1 can inhibit tumor growth, decrease regulatory T-cell accumulation and improve survival in murine cancer models.^{301,306} An important role for tumor-expressed IDO1 is further corroborated by the effective IDO1 inhibitor-mediated suppression of tumor growth in IDO1-deficient hosts.³⁰⁷ Moreover, IDO1 overexpression in tumor cells promotes tumor growth *in vivo*,^{228,244} which is associated with decreased infiltration of effector T cells, and increased numbers of regulatory T cells and MDSCs.²⁴⁴ Based on *in vivo* models, tumor cell-expressed IDO1 thus appears to considerably contribute to the promotion of tumor growth, whereas a role for host IDO1 remains to be further substantiated.

Since discovery of the immunosuppressive role of IDO1 in tumor development, a great number of IDO1 inhibitors has been developed.^{308,309} Preclinical evaluation of promising inhibitors has demonstrated their lymphocyte-dependent monotherapeutic efficacy in different murine tumor models.^{107,244,305,307,310} Moreover, IDO1 inhibition enhances the *in vivo* efficacy of α -CTLA-4 and α -PD-L1 therapy,^{302,311–313} which may in part be related to the induction of IDO1 observed upon immune checkpoint blockade.^{310,311} Similar induction of IDO1 also appears to occur in patients, as indicated by the elevation of systemic kynurenine-to-tryptophan ratios in α -PD-1-treated sarcoma, melanoma and renal cell carcinoma patients.^{314,315} Contrary to inhibitors of IDO1, only relatively few selective TDO inhibitors have been reported.³¹⁶ Development of TDO inhibitors is complicated by the small size and lipophilicity of the TDO active site, explaining the general suffering of TDO inhibitors from limited potency or drug-likeness.³¹⁶ Nonetheless, inhibitors such as the orally bioavailable LM10 and PF06845102/EOS200809 have enabled evaluation of the immunosuppressive effect of TDO in murine tumor models.^{248,299} While TDO overexpression in tumor cells can promote tumor growth through suppression of the anti-tumor immune response,^{247,248} inhibition of TDO can restore tumor suppression²⁴⁸ and enhance the efficacy of CTLA-4 blockade therapy.²⁹⁹ Preclinical and clinical development of several dual IDO1/TDO inhibitors is currently also ongoing,^{317,318} which may serve a role for tumors co-expressing IDO1 and TDO or those upregulating TDO upon IDO1 inhibition.

While clinical evaluation of selective TDO inhibitors for cancer treatment is still to be awaited, various IDO1 inhibitors have already entered clinical testing, frequently in combination with immune checkpoint blockade.³⁰⁹ Epacadostat (INCB024360) was the

first IDO1 inhibitor to advance into a phase III clinical trial (ECHO-301/KEYNOTE-252) after showing promising efficacy in advanced melanoma patients when combined with α -PD-1 antibodies in two nonrandomized, uncontrolled phase II trials.^{319,320} However, the phase III trial failed to demonstrate an improved progression-free survival for the combination of epacadostat with pembrolizumab (α -PD-1) compared to pembrolizumab alone.³²¹ Thereupon, several other phase III trials were terminated early, withdrawn or downscaled to randomized phase II trials, along with the suspension of several phase I and II evaluations (ClinicalTrials.gov database). Nonetheless, various phase I and II trials have also been initiated since the failure of ECHO-301 (ClinicalTrials.gov database), and the IDO1 inhibitor linrodostat (BMS-986205) has even entered a phase III trial in patients with muscle invasive bladder cancer (NCT03661320).³²²

Extensive discussion about factors underlying the disappointing clinical results has also since arisen.^{25,323,324} Concerns have been raised as to whether the dosing of epacadostat in the ECHO-301 trial was sufficient to obtain adequate intratumoral and intracellular concentrations required for maximal IDO1 inhibition.²⁵ Based on results of a phase I dose escalation, the chosen dose of 100 mg twice daily yields an appreciable, though sub-maximal, reduction in plasma kynurenine levels.³²⁵ Considering the reported association of immune checkpoint blockade with induction of IDO1,^{310,311,314,315} dosing based on its monotherapeutic profile could thus have proven to be insufficient. Regrettably, the degree of IDO1 inhibition was evaluated in neither plasma nor tumor biopsies of patients enrolled in the ECHO-301 trial. The same argument of therapy-induced IDO1 induction should also question α -PD-1 antibodies as preferred combination partners for IDO1 inhibitors. Moreover, restriction of kynurenine-mediated PD-1 induction in tumor-infiltrating T cells upon IDO1 inhibition may even cause PD-1 blockade to be redundant.^{276–278} Selection or stratification of patients based on IDO1 expression or activity could also have improved the chance of observing a clinical benefit upon IDO1 inhibition, but this is still only rarely applied in clinical trials.^{25,324}

IDO1 can also exert immunosuppressive effects independent of its enzymatic activity,^{326–328} which can involve a non-catalytic signaling function of the enzyme^{326,327} that is likely not inhibited by active site-targeting inhibitors. Such effects were recently suggested to partially account for the IDO1-dependent immune suppression observed in human glioma,³²⁸ but it remains to be determined whether they also serve a role in different tumor types. Other possible explanations for the outcome of the ECHO-301 trial include a potential compensatory induction of TDO or IDO2 expression,³²³ and activation of AhR signaling by IDO1 inhibitors themselves.^{324,329} Although these mechanisms are unlikely to account for the disappointing results,³²⁴ only thorough evaluation of clinical samples will allow their unequivocal rejection. Finally, a recent study performed with treatment-

naïve ovarian cancer patients demonstrates that IDO1 inhibition by epacadostat induces overproduction of tumoral NAD⁺, which reduces T-cell proliferation and functionality *in vitro* and mitigates IDO1 inhibitor efficacy *in vivo*.³³⁰ Blockade of NAD⁺ generation or signaling may therefore present a promising combination strategy for IDO1 inhibition.³³⁰ Alternatively, patients may benefit from the direct targeting of downstream effector pathways of tryptophan metabolism, such as AhR or GCN2 signaling,^{277,331} or the selective depletion of kynurenine by kynureninase treatment,³³² rather than inhibition of upstream IDO1 or TDO. Moreover, peptide vaccines are being developed to target IDO1-expressing cells rather than the enzyme itself.³³³ However, these strategies remain to be validated in preclinical or clinical studies.

Collectively, the extensive prognostic, preclinical and early-phase clinical evidence linking deranged tryptophan metabolism to immunosuppression and tumor growth once positioned IDO1 inhibitors at the forefront of experimental immunotherapy. While this perception has since been challenged by the failure of the ECHO-301 trial, it remains evident that tryptophan metabolism holds promise as a targetable pathway for cancer treatment. Nonetheless, this development urges for a deeper understanding to be attained of both the mechanisms underlying IDO1-mediated immunosuppression and the effects of tryptophan metabolic pathway inhibition, to which the examination of clinical samples may strongly contribute. Moreover, the improved design of clinical trials using patient stratification and monitoring of target engagement could contribute to further validation of the target, whereas alternative or combinatorial strategies should also still offer hope for cancer patients.

The aromatic amino acid-metabolizing enzyme IL4I1

The final amino acid-metabolizing enzyme with a proposed role in tumor immune escape is IL4I1, which is a secreted L-amino acid oxidase (LAAO) first characterized by its interleukin 4-inducible expression in murine and human B cells.^{334,335} IL4I1 catalyzes the conversion of L-amino acids into their respective α -keto acids with concomitant release of hydrogen peroxide (H₂O₂) and ammonia (NH₃), and has a preference for aromatic substrates, specifically phenylalanine, tyrosine and tryptophan.^{26,336–338} Although five isoforms of IL4I1 are encoded by the human genome, expression of only two isoforms has been found in humans.^{334,339} These isoforms diverge in their secretory signal peptide sequence, but yield identical proteins upon signal peptide cleavage.³³⁹ Expression of the first IL4I1 isoform is chiefly found in lymphoid tissues,^{335,340} while the second isoform is highly expressed in the testis and can also be found in specific cells of the brain.³³⁹ Within human lymphoid tissues, IL4I1 expression is primarily restricted to professional

antigen-presenting cells,^{335,337,341} with considerably higher levels found in macrophages and dendritic cells compared to those in B cells.³⁴² Moreover, IL411 is expressed by human Th17 and Th17-like cells^{343–345} and is found in MDSCs of tumor-bearing mice.^{346,347}

Elevated expression of IL411 has been detected in various human cancer types, including both solid tumors and lymphomas.^{26,340,341} Among solid and non-B-cell malignancies, IL411 is only rarely expressed by tumor cells, but instead can often be found in tumor-associated macrophages.^{341,348} Contrarily, although IL411 expression by macrophages is a common feature of B-cell lymphomas as well, several subtypes also frequently express IL411 in neoplastic cells, in keeping with its natural expression in B cells.³⁴¹ Moreover, whereas high IL411 expression appears to portend a poor prognosis in several solid tumor types,^{26,349–353} high levels of IL411 are correlated with superior outcome in follicular and diffuse large B-cell lymphoma.^{341,354} This suggests a dichotomous role for IL411 in solid tumors compared to B-cell lymphomas, which may be related to the physiological regulatory role of IL411 in B-cell activation,³⁵⁵ but requires further substantiating evidence.

Similar to other amino acid-metabolizing enzymes, IL411 is capable of inhibiting the proliferation of activated human T cells.³³⁷ This effect was initially solely ascribed to the IL411-mediated generation of H₂O₂, since phenylpyruvate, the α-keto acid product of major substrate phenylalanine, only affects T cells at very high concentrations.³³⁷ Treatment of human T cells with H₂O₂ results in the downmodulation of CD3ζ expression, IFNγ production and cytotoxic activity.^{337,356,357} Moreover, at higher concentrations or prolonged exposure, H₂O₂ can induce T-cell apoptosis,^{358,359} which preferentially targets effector rather than regulatory T cells.³⁶⁰ IL411 activity additionally promotes the differentiation of naïve CD4⁺ T cells into CD4⁺CD25⁺FoxP3⁺ regulatory T cells, which has been suggested to involve phenylalanine deficiency-induced inhibition of mTORC1 signaling.³⁶¹ Based on the relatively low affinity of IL411 for phenylalanine,³⁶² however, it seems unlikely that IL411 is capable of depleting this amino acid, indicating that another mechanism may underly the observed effect. Finally, IL411 is capable of raising the activation threshold of CD8⁺ T cells while restraining their differentiation into memory T cells,³⁶³ and promoting the polarization of macrophages towards a suppressive phenotype.³⁶⁴

More recently, IL411 has additionally been recognized for its ability to generate AhR ligands upon degradation of one of its other substrates.²⁶ Metabolism of tryptophan yields the α-keto acid indole-3-pyruvic acid, which can subsequently be converted into indole-3-lactic acid, indole-3-acetic acid, indole-3-aldehyde and kynurenic acid.^{26,365} Each of these metabolites has previously, albeit generally not consistently, been associated with AhR agonism,^{26,265,365–368} with indole-3-pyruvic acid serving as its most potent activator.²⁶ Addition of indole-3-pyruvic acid, but not the α-keto acid derivative of phenylalanine or

tyrosine, to human T cells induces the expression of AhR target genes, and reproduces the inhibition of their proliferation observed with supernatants of IL4I1-expressing cells.²⁶ IL4I1 is also reported to inhibit TCR activation through a mechanism independent of its enzymatic activity,³⁶⁹ but an effect of IL4I1-mediated tryptophan metabolism was not considered in this study and may underly these observations. The activity of IL4I1 can additionally directly affect tumor cells, as evidenced by the enhanced proliferation, motility and invasive capacity of IL4I1-expressing tumor cells of different tissue origin,^{26,353,370} which may at least in part be due to indole-3-pyruvic acid-mediated activation of the AhR pathway.²⁶ Similarly, AhR signaling may be involved in the IL4I1-induced suppression of tumor cell ferroptosis.³³⁸

Across human cancer types, IL4I1 gene expression associates more strongly with a pan-tissue AhR activation signature compared to that of either IDO1 or TDO, indicating IL4I1-generated metabolites as key AhR activators in cancer.²⁶ While this is corroborated by the ability of IL4I1 to activate the AhR in various models and the high expression of IL4I1 in cancer tissues,²⁶ it is argued by another study demonstrating only poor correlation between the expression of IL4I1 and individual AhR target genes in a number of tumor types.³⁶² Moreover, IL4I1 demonstrates a roughly 50-fold lower affinity for tryptophan compared to IDO1,³⁶² whereas its expression is on average only moderately higher than that of IDO1 across different tumor types.²⁶ Although this may partially be compensated for by the considerably higher AhR-activating potency of indole-3-pyruvic acid compared to IDO1-generated metabolites,²⁶ it remains unclear whether IL4I1 is capable of achieving significant AhR activation in most tumor types. Nonetheless, as IL4I1 is relieved from competition with IDO1 upon inhibition of the latter, IL4I1-mediated AhR activation presents a potential mechanism of resistance against IDO1 inhibition.²⁶ While this remains to be validated in specimens of patients treated with an IDO1 inhibitor, it may argue for the treatment of patients with a combination of IDO1 and IL4I1 inhibitors, or with an AhR inhibitor.

The *in vivo* effect of IL4I1 expression on tumor growth and the anti-tumor immune response has currently been studied in only a limited number of models. In melanoma-challenged mice, IL4I1 expression by tumor cells facilitates their outgrowth, which is mediated by suppression of the tumor antigen-specific CD8⁺ T-cell response.³⁷¹ Moreover, in a model of spontaneous melanoma, host IL4I1 deficiency enhances tumor control and associates with reduced tumor infiltration of G-MDSCs and macrophages, while it improves CD4⁺ T-cell, CD8⁺ T-cell and B-cell infiltration.³⁷² Similarly, IL4I1-deficient mice challenged with chronic lymphocytic leukemia present with reduced tumor burden, which is accompanied by enhanced CD8⁺ T-cell functionality and reduced frequency of total and activated regulatory T cells.²⁶ Overall, these results corroborate the findings of enhanced MDSC and regulatory T-cell infiltration and reduced CD8⁺ T-cell infiltration in cancer patients with high

IL4I1 expression.^{26,350} Noteworthy, similar as observed for IDO1, α -PD-1 treatment can also induce IL4I1 upregulation in cancer patients, and IL4I1 is suggested to potentially constitute a resistance mechanism to immune checkpoint blockade.²⁶ Whereas only few inhibitors of IL4I1 have yet been disclosed,³⁷³⁻³⁷⁶ the preclinical inhibitor CB-668 has demonstrated both monotherapeutic efficacy and favorable combinatorial efficacy with α -PD-L1 therapy in tumor-bearing mice.³⁷⁷

Taken together, although the field studying the role of IL4I1 in cancer immune escape is still in its relative infancy compared to that of IDO1, the pharmacological targeting of IL4I1 offers new prospects for the treatment of cancer patients. A more comprehensive understanding of the consequences of IL4I1 expression and its inhibition in cancer is, however, required to determine whether this enzyme indeed constitutes an effective immunotherapeutic target. As the development of IL4I1 inhibitors is currently ongoing, disclosure of complementary studies addressing these aspects may be expected in the near future.

Concluding remarks

Cancer immunotherapy has revolutionized the treatment of malignant tumors, with immune checkpoint blockade as major breakthrough therapy being approved for an ever-expanding list of clinical indications. However, despite the impressive durable responses observed in a subset of cancer patients, diverse resistance mechanisms limit the effectiveness of immunotherapeutic interventions. Amino acid-metabolizing enzymes can serve as important mediators of tumor immune evasion, as activated T cells and other immune cells have a high need for amino acids and can be adversely affected by accumulation of amino acid-derived metabolites. Inhibition of tumor- or immunosuppressive cell-expressed GLS1, ARG1, iNOS, IDO1, TDO and/or IL4I1 therefore constitutes a promising approach to alleviate tumor-induced immune suppression, either as monotherapy or in combination with other treatment modalities.

Clinical successes of inhibitors of amino acid-metabolizing enzymes are, however, still limited to date, indicating that our understanding of the involved complex pathways remains incomplete. This urges for both the extension of preclinical research as well as the thorough investigation of samples collected during clinical studies. As various clinical trials are currently also still ongoing, valuable insight into the efficacy of different inhibitors is also still to be expected. However, identification of novel targets such as IL4I1, exploration of alternative strategies such as targeting of downstream pathways (e.g., the AhR pathway) and rational selection of combination therapies should additionally receive adequate focus, as these may well serve to overcome the current limitations of cancer immunotherapies.

References

1. Flavahan, W. A., Gaskell, E. & Bernstein, B. E. Epigenetic plasticity and the hallmarks of cancer. *Science* **357**, eaal2380 (2017).
2. Vogelstein, B. *et al.* Cancer genome landscapes. *Science* **339**, 1546–58 (2013).
3. Coullie, P. G., Van den Eynde, B. J., van der Bruggen, P. & Boon, T. Tumour antigens recognized by T lymphocytes: at the core of cancer immunotherapy. *Nat. Rev. Cancer* **14**, 135–46 (2014).
4. Gajewski, T. F., Schreiber, H. & Fu, Y.-X. Innate and adaptive immune cells in the tumor microenvironment. *Nat. Immunol.* **14**, 1014–22 (2013).
5. Beatty, G. L. & Gladney, W. L. Immune escape mechanisms as a guide for cancer immunotherapy. *Clin. Cancer Res.* **21**, 687–92 (2015).
6. Vinay, D. S. *et al.* Immune evasion in cancer: mechanistic basis and therapeutic strategies. *Semin. Cancer Biol.* **35**, S185–98 (2015).
7. Waldman, A. D., Fritz, J. M. & Lenardo, M. J. A guide to cancer immunotherapy: from T cell basic science to clinical practice. *Nat. Rev. Immunol.* **20**, 651–68 (2020).
8. Pardoll, D. M. The blockade of immune checkpoints in cancer immunotherapy. *Nat. Rev. Cancer* **12**, 252–64 (2012).
9. Chen, D. S. & Mellman, I. Elements of cancer immunity and the cancer-immune set point. *Nature* **541**, 321–30 (2017).
10. Berraondo, P. *et al.* Cytokines in clinical cancer immunotherapy. *Br. J. Cancer* **120**, 6–15 (2019).
11. Sharma, P., Hu-Lieskovan, S., Wargo, J. A. & Ribas, A. Primary, adaptive, and acquired resistance to cancer immunotherapy. *Cell* **168**, 707–23 (2017).
12. O'Donnell, J. S., Teng, M. W. L. & Smyth, M. J. Cancer immunoeediting and resistance to T cell-based immunotherapy. *Nat. Rev. Clin. Oncol.* **16**, 151–67 (2019).
13. Binnewies, M. *et al.* Understanding the tumor immune microenvironment (TIME) for effective therapy. *Nat. Med.* **24**, 541–50 (2018).
14. Lindau, D., Gielen, P., Kroesen, M., Wesseling, P. & Adema, G. J. The immunosuppressive tumour network: myeloid-derived suppressor cells, regulatory T cells and natural killer T cells. *Immunology* **138**, 105–15 (2013).
15. Speiser, D. E., Ho, P.-C. & Verdeil, G. Regulatory circuits of T cell function in cancer. *Nat. Rev. Immunol.* **16**, 599–611 (2016).
16. Petrova, V., Annicchiarico-Petruzzelli, M., Melino, G. & Amelio, I. The hypoxic tumour microenvironment. *Oncogenesis* **7**, 10 (2018).
17. Ren, W. *et al.* Amino-acid transporters in T-cell activation and differentiation. *Cell Death Dis.* **8**, e2655 (2017).
18. MacIver, N. J., Michalek, R. D. & Rathmell, J. C. Metabolic regulation of T lymphocytes. *Annu. Rev. Immunol.* **31**, 259–83 (2013).
19. Murray, P. J. Amino acid auxotrophy as a system of immunological control nodes. *Nat. Immunol.* **17**, 132–9 (2016).
20. Wang, W. & Zou, W. Amino acids and their transporters in T cell immunity and cancer therapy. *Mol. Cell* **80**, 384–95 (2020).
21. DeBerardinis, R. J., Lum, J. J., Hatzivassiliou, G. & Thompson, C. B. The biology of cancer: metabolic reprogramming fuels cell growth and proliferation. *Cell Metab.* **7**, 11–20 (2008).
22. Wang, Z. *et al.* Targeting glutaminolysis: new perspectives to understand cancer development and novel strategies for potential target therapies. *Front. Oncol.* **10**, 589508 (2020).
23. Grzywa, T. M. *et al.* Myeloid cell-derived arginase in cancer immune response. *Front. Immunol.* **11**, 938 (2020).

24. Peñarando, J., Aranda, E. & Rodríguez-Ariza, A. Immunomodulatory roles of nitric oxide in cancer: tumor microenvironment says “NO” to antitumor immune response. *Transl. Res.* **210**, 99–108 (2019).
25. Opitz, C. A. *et al.* The therapeutic potential of targeting tryptophan catabolism in cancer. *Br. J. Cancer* **122**, 30–44 (2020).
26. Sadik, A. *et al.* IL411 is a metabolic immune checkpoint that activates the AHR and promotes tumor progression. *Cell* **182**, 1252–70.e34 (2020).
27. Castilho, B. A. *et al.* Keeping the eIF2 alpha kinase Gcn2 in check. *Biochim. Biophys. Acta* **1843**, 1948–68 (2014).
28. Szwed, A., Kim, E. & Jacinto, E. Regulation and metabolic functions of mTORC1 and mTORC2. *Physiol. Rev.* **101**, 1371–426 (2021).
29. McGaha, T. L. *et al.* Amino acid catabolism: a pivotal regulator of innate and adaptive immunity. *Immunol. Rev.* **249**, 135–57 (2012).
30. Murray, I. A., Patterson, A. D. & Perdew, G. H. Aryl hydrocarbon receptor ligands in cancer: friend and foe. *Nat. Rev. Cancer* **14**, 801–14 (2014).
31. Gutiérrez-Vázquez, C. & Quintana, F. J. Regulation of the immune response by the aryl hydrocarbon receptor. *Immunity* **48**, 19–33 (2018).
32. Smith, R. J. Glutamine metabolism and its physiologic importance. *JPEN J. Parenter. Enter. Nutr.* **14**, 40S–4S (1990).
33. Lacey, J. M. & Wilmore, D. W. Is glutamine a conditionally essential amino acid? *Nutr. Rev.* **48**, 297–309 (1990).
34. Yoo, H. C., Yu, Y. C., Sung, Y. & Han, J. M. Glutamine reliance in cell metabolism. *Exp. Mol. Med.* **52**, 1496–516 (2020).
35. Vander Heiden, M. G., Cantley, L. C. & Thompson, C. B. Understanding the Warburg effect: the metabolic requirements of cell proliferation. *Science* **324**, 1029–33 (2009).
36. Warburg, O. On the origin of cancer cells. *Science* **123**, 309–14 (1956).
37. Aledo, J. C., Gómez-Fabre, P. M., Olalla, L. & Márquez, J. Identification of two human glutaminase loci and tissue-specific expression of the two related genes. *Mamm. Genome* **11**, 1107–10 (2000).
38. GTEx Consortium. The Genotype-Tissue Expression (GTEx) pilot analysis: multitissue gene regulation in humans. *Science* **348**, 648–60 (2015).
39. Wise, D. R. *et al.* Myc regulates a transcriptional program that stimulates mitochondrial glutaminolysis and leads to glutamine addiction. *Proc. Natl. Acad. Sci. U. S. A.* **105**, 18782–7 (2008).
40. Gao, P. *et al.* c-Myc suppression of miR-23a/b enhances mitochondrial glutaminase expression and glutamine metabolism. *Nature* **458**, 762–5 (2009).
41. Hu, W. *et al.* Glutaminase 2, a novel p53 target gene regulating energy metabolism and antioxidant function. *Proc. Natl. Acad. Sci. U. S. A.* **107**, 7455–60 (2010).
42. Suzuki, S. *et al.* Phosphate-activated glutaminase (GLS2), a p53-inducible regulator of glutamine metabolism and reactive oxygen species. *Proc. Natl. Acad. Sci. U. S. A.* **107**, 7461–6 (2010).
43. Liu, J. *et al.* Glutaminase 2 negatively regulates the PI3K/AKT signaling and shows tumor suppression activity in human hepatocellular carcinoma. *Oncotarget* **5**, 2635–47 (2014).
44. Saha, S. K. *et al.* Multiomics analysis reveals that GLS and GLS2 differentially modulate the clinical outcomes of cancer. *J. Clin. Med.* **8**, 1–28 (2019).
45. Suzuki, S. *et al.* GLS2 is a tumor suppressor and a regulator of ferroptosis in hepatocellular carcinoma. *Cancer Res.* **82**, 3209–22 (2022).
46. Zhang, C. *et al.* Glutaminase 2 is a novel negative regulator of small GTPase Rac1 and mediates p53 function in suppressing metastasis. *Elife* **5**, e10727 (2016).
47. Xiao, D. *et al.* Myc promotes glutaminolysis in human neuroblastoma through direct activation of glutaminase 2. *Oncotarget* **6**, 40655–66 (2015).

48. Lukey, M. J. *et al.* Liver-type glutaminase GLS2 is a druggable metabolic node in luminal-subtype breast cancer. *Cell Rep.* **29**, 76–88.e7 (2019).
49. Dias, M. M. *et al.* GLS2 is protumorigenic in breast cancers. *Oncogene* **39**, 690–702 (2020).
50. Dion, H. W., Fusari, S. A., Jakubowski, Z. L., Zora, J. G. & Bartz, Q. R. 6-Diazo-5-oxo-L-norleucine, a new tumor-inhibitory substance. II. Isolation and characterization. *J. Am. Chem. Soc.* **78**, 3075–7 (1956).
51. Pinkus, L. M. Glutamine binding sites. *Methods Enzymol.* **46**, 414–27 (1977).
52. Leone, R. D. *et al.* Glutamine blockade induces divergent metabolic programs to overcome tumor immune evasion. *Science* **366**, 1013–21 (2019).
53. Yokoyama, Y., Estok, T. M. & Wild, R. Sirpi-glenastat (DRP-104) induces antitumor efficacy through direct, broad antagonism of glutamine metabolism and stimulation of the innate and adaptive immune systems. *Mol. Cancer Ther.* **21**, 1561–72 (2022).
54. Robinson, M. M. *et al.* Novel mechanism of inhibition of rat kidney-type glutaminase by bis-2-(5-phenylacetamido-1,2,4-thiazol-2-yl)ethyl sulfide (BPTES). *Biochem. J.* **406**, 407–14 (2007).
55. Gross, M. I. *et al.* Antitumor activity of the glutaminase inhibitor CB-839 in triple-negative breast cancer. *Mol. Cancer Ther.* **13**, 890–901 (2014).
56. Soth, M. J. *et al.* Discovery of IPN60090, a clinical stage selective glutaminase-1 (GLS-1) inhibitor with excellent pharmacokinetic and physicochemical properties. *J. Med. Chem.* **63**, 12957–77 (2020).
57. Schulte, M. L. *et al.* Pharmacological blockade of ASCT2-dependent glutamine transport leads to antitumor efficacy in preclinical models. *Nat. Med.* **24**, 194–202 (2018).
58. Lemberg, K. M., Vornov, J. J., Rais, R. & Slusher, B. S. We're not 'DON' yet: optimal dosing and prodrug delivery of 6-diazo-5-oxo-L-norleucine. *Mol. Cancer Ther.* **17**, 1824–32 (2018).
59. Carr, E. L. *et al.* Glutamine uptake and metabolism are coordinately regulated by ERK/MAPK during T lymphocyte activation. *J. Immunol.* **185**, 1037–44 (2010).
60. Wang, R. *et al.* The transcription factor Myc controls metabolic reprogramming upon T lymphocyte activation. *Immunity* **35**, 871–82 (2011).
61. Sinclair, L. V. *et al.* Control of amino-acid transport by antigen receptors coordinates the metabolic reprogramming essential for T cell differentiation. *Nat. Immunol.* **14**, 500–8 (2013).
62. Nakaya, M. *et al.* Inflammatory T cell responses rely on amino acid transporter ASCT2 facilitation of glutamine uptake and mTORC1 kinase activation. *Immunity* **40**, 692–705 (2014).
63. Nicklin, P. *et al.* Bidirectional transport of amino acids regulates mTOR and autophagy. *Cell* **136**, 521–34 (2009).
64. Edwards, D. N. *et al.* Selective glutamine metabolism inhibition in tumor cells improves antitumor T lymphocyte activity in triple-negative breast cancer. *J. Clin. Invest.* **131**, 1–16 (2021).
65. Johnson, M. O. *et al.* Distinct regulation of Th17 and Th1 cell differentiation by glutaminase-dependent metabolism. *Cell* **175**, 1780–95.e19 (2018).
66. Klysz, D. *et al.* Glutamine-dependent α -ketoglutarate production regulates the balance between T helper 1 cell and regulatory T cell generation. *Sci. Signal.* **8**, ra97 (2015).
67. Metzler, B., Gfeller, P. & Guinet, E. Restricting glutamine or glutamine-dependent purine and pyrimidine syntheses promotes human T cells with high FOXP3 expression and regulatory properties. *J. Immunol.* **196**, 3618–30 (2016).
68. Lian, G. *et al.* Glutathione de novo synthesis but not recycling process coordinates with glutamine catabolism to control redox homeostasis and directs murine T cell differentiation. *Elife* **7**, 1–28 (2018).

69. Loftus, R. M. *et al.* Amino acid-dependent cMyc expression is essential for NK cell metabolic and functional responses in mice. *Nat. Commun.* **9**, 2341 (2018).
70. Wang, J.-B. *et al.* Targeting mitochondrial glutaminase activity inhibits oncogenic transformation. *Cancer Cell* **18**, 207–19 (2010).
71. Xiang, Y. *et al.* Targeted inhibition of tumor-specific glutaminase diminishes cell-autonomous tumorigenesis. *J. Clin. Invest.* **125**, 2293–306 (2015).
72. Varghese, S. *et al.* The glutaminase inhibitor CB-839 (telaglenastat) enhances the antimelanoma activity of T-cell-mediated immunotherapies. *Mol. Cancer Ther.* **20**, 500–11 (2021).
73. Liu, P.-S. *et al.* α -ketoglutarate orchestrates macrophage activation through metabolic and epigenetic reprogramming. *Nat. Immunol.* **18**, 985–94 (2017).
74. Wu, W.-C. *et al.* Immunosuppressive immature myeloid cell generation is controlled by glutamine metabolism in human cancer. *Cancer Immunol. Res.* **7**, 1605–18 (2019).
75. Udumula, M. P. *et al.* Ovarian cancer modulates the immunosuppressive function of CD11b⁺Gr1⁺ myeloid cells via glutamine metabolism. *Mol. Metab.* **53**, 101272 (2021).
76. Biancur, D. E. *et al.* Compensatory metabolic networks in pancreatic cancers upon perturbation of glutamine metabolism. *Nat. Commun.* **8**, 15965 (2017).
77. Lemberg, K. M., Gori, S. S., Tsukamoto, T., Rais, R. & Slusher, B. S. Clinical development of metabolic inhibitors for oncology. *J. Clin. Invest.* **132**, e148550 (2022).
78. Halama, A. *et al.* Accelerated lipid catabolism and autophagy are cancer survival mechanisms under inhibited glutaminolysis. *Cancer Lett.* **430**, 133–47 (2018).
79. Méndez-Lucas, A. *et al.* Identifying strategies to target the metabolic flexibility of tumours. *Nat. Metab.* **2**, 335–50 (2020).
80. Oh, M.-H. *et al.* Targeting glutamine metabolism enhances tumor-specific immunity by modulating suppressive myeloid cells. *J. Clin. Invest.* **130**, 3865–84 (2020).
81. Byun, J.-K. *et al.* Inhibition of glutamine utilization synergizes with immune checkpoint inhibitor to promote antitumor immunity. *Mol. Cell* **80**, 592–606.e8 (2020).
82. Ma, G. *et al.* Glutamine deprivation induces PD-L1 expression via activation of EGFR/ERK/c-Jun signaling in renal cancer. *Mol. Cancer Res.* **18**, 324–39 (2020).
83. Gross, M. *et al.* Glutaminase inhibition with CB-839 enhances anti-tumor activity of PD-1 and PD-L1 antibodies by overcoming a metabolic checkpoint blocking T cell activation. *Cancer Res.* **76**, 2329 (2016).
84. Li, Q. *et al.* Inhibitor of glutamine metabolism V9302 promotes ROS-induced autophagic degradation of B7H3 to enhance antitumor immunity. *J. Biol. Chem.* **298**, 101753 (2022).
85. Meric-Bernstam, F. *et al.* A phase 1/2 study of CB-839, a first-in-class glutaminase inhibitor, combined with nivolumab in patients with advanced melanoma (MEL), renal cell carcinoma (RCC), or non-small cell lung cancer (NSCLC). *Soc. Immunother. Cancer Annu. Meet.* **5**, O16 (2017).
86. Wu, G., Meininger, C. J., Knabe, D. A., Bazer, F. W. & Rhoads, J. M. Arginine nutrition in development, health and disease. *Curr. Opin. Clin. Nutr. Metab. Care* **3**, 59–66 (2000).
87. Morris, S. M. Arginine metabolism: boundaries of our knowledge. *J. Nutr.* **137**, 1602S–9S (2007).
88. Jenkinson, C. P., Grody, W. W. & Cederbaum, S. D. Comparative properties of arginases. *Comp. Biochem. Physiol. B. Biochem. Mol. Biol.* **114**, 107–32 (1996).
89. Munder, M. Arginase: an emerging key player in the mammalian immune system. *Br. J. Pharmacol.* **158**, 638–51 (2009).
90. Morris, S. M. Recent advances in arginine metabolism: roles and regulation of the arginases. *Br. J. Pharmacol.* **157**, 922–30 (2009).
91. Steggerda, S. M. *et al.* Inhibition of arginase by CB-1158 blocks myeloid cell-mediated immune suppression in the tumor micro-environment. *J. Immunother. Cancer* **5**, 101 (2017).

92. Lennartz, M. *et al.* Large-scale tissue microarray evaluation corroborates high specificity of high-level arginase-1 immunostaining for hepatocellular carcinoma. *Diagnostics (Basel)* **11**, 2351 (2021).
93. Bronte, V. *et al.* Boosting antitumor responses of T lymphocytes infiltrating human prostate cancers. *J. Exp. Med.* **201**, 1257–68 (2005).
94. Rotondo, R. *et al.* Arginase 2 is expressed by human lung cancer, but it neither induces immune suppression, nor affects disease progression. *Int. J. Cancer* **123**, 1108–16 (2008).
95. Bron, L. *et al.* Prognostic value of arginase-II expression and regulatory T-cell infiltration in head and neck squamous cell carcinoma. *Int. J. Cancer* **132**, E85–93 (2013).
96. Mussai, F. *et al.* Acute myeloid leukemia creates an arginase-dependent immunosuppressive microenvironment. *Blood* **122**, 749–58 (2013).
97. Corraliza, I. M., Soler, G., Eichmann, K. & Modolell, M. Arginase induction by suppressors of nitric oxide synthesis (IL-4, IL-10 and PGE2) in murine bone-marrow-derived macrophages. *Biochem. Biophys. Res. Commun.* **206**, 667–73 (1995).
98. Munder, M. *et al.* Th1/Th2-regulated expression of arginase isoforms in murine macrophages and dendritic cells. *J. Immunol.* **163**, 3771–7 (1999).
99. Munder, M. *et al.* Arginase I is constitutively expressed in human granulocytes and participates in fungicidal activity. *Blood* **105**, 2549–56 (2005).
100. Rodriguez, P. C. *et al.* Arginase I-producing myeloid-derived suppressor cells in renal cell carcinoma are a subpopulation of activated granulocytes. *Cancer Res.* **69**, 1553–60 (2009).
101. Rodriguez, P. C. *et al.* Arginase I production in the tumor microenvironment by mature myeloid cells inhibits T-cell receptor expression and antigen-specific T-cell responses. *Cancer Res.* **64**, 5839–49 (2004).
102. Jacobsen, L. C., Theilgaard-Mönch, K., Christensen, E. I. & Borregaard, N. Arginase 1 is expressed in myelocytes/metamyelocytes and localized in gelatinase granules of human neutrophils. *Blood* **109**, 3084–7 (2007).
103. Rotondo, R. *et al.* Exocytosis of azurophil and arginase 1-containing granules by activated polymorphonuclear neutrophils is required to inhibit T lymphocyte proliferation. *J. Leukoc. Biol.* **89**, 721–7 (2011).
104. Wang, Y. *et al.* Exosomes released by granulocytic myeloid-derived suppressor cells attenuate DSS-induced colitis in mice. *Oncotarget* **7**, 15356–68 (2016).
105. Czystowska-Kuzmicz, M. *et al.* Small extracellular vesicles containing arginase-1 suppress T-cell responses and promote tumor growth in ovarian carcinoma. *Nat. Commun.* **10**, 3000 (2019).
106. Zea, A. H. *et al.* Arginase-producing myeloid suppressor cells in renal cell carcinoma patients: a mechanism of tumor evasion. *Cancer Res.* **65**, 3044–8 (2005).
107. Liu, C.-Y. *et al.* Population alterations of L-arginase- and inducible nitric oxide synthase-expressed CD11b⁺/CD14⁻/CD15⁻/CD33⁺ myeloid-derived suppressor cells and CD8⁺ T lymphocytes in patients with advanced-stage non-small cell lung cancer. *J. Cancer Res. Clin. Oncol.* **136**, 35–45 (2010).
108. Vasquez-Dunddel, D. *et al.* STAT3 regulates arginase-I in myeloid-derived suppressor cells from cancer patients. *J. Clin. Invest.* **123**, 1580–9 (2013).
109. Zhang, J. *et al.* CD13^{hi} neutrophil-like myeloid-derived suppressor cells exert immune suppression through Arginase 1 expression in pancreatic ductal adenocarcinoma. *Oncotarget* **6**, e1258504 (2017).
110. Sippel, T. R. *et al.* Neutrophil degranulation and immunosuppression in patients with GBM: restoration of cellular immune function by targeting arginase I. *Clin. Cancer Res.* **17**, 6992–7002 (2011).

111. Rotondo, R. *et al.* IL-8 induces exocytosis of arginase 1 by neutrophil polymorphonuclears in non-small cell lung cancer. *Int. J. Cancer* **125**, 887–93 (2009).
112. Sullivan, M. R. *et al.* Quantification of microenvironmental metabolites in murine cancers reveals determinants of tumor nutrient availability. *Elife* **8**, 1–27 (2019).
113. Singh, R., Pervin, S., Karimi, A., Cederbaum, S. & Chaudhuri, G. Arginase activity in human breast cancer cell lines: *N*^ω-hydroxy-L-arginine selectively inhibits cell proliferation and induces apoptosis in MDA-MB-468 cells. *Cancer Res.* **60**, 3305–12 (2000).
114. Chang, C. I., Liao, J. C. & Kuo, L. Macrophage arginase promotes tumor cell growth and suppresses nitric oxide-mediated tumor cytotoxicity. *Cancer Res.* **61**, 1100–6 (2001).
115. Geiger, R. *et al.* L-Arginine modulates T cell metabolism and enhances survival and anti-tumor activity. *Cell* **167**, 829–42.e13 (2016).
116. Werner, A. *et al.* Induced arginine transport via cationic amino acid transporter-1 is necessary for human T-cell proliferation. *Eur. J. Immunol.* **46**, 92–103 (2016).
117. Bansal, V. *et al.* Citrulline can preserve proliferation and prevent the loss of CD3 ζ chain under conditions of low arginine. *JPEN. J. Parenter. Enteral Nutr.* **28**, 423–30 (2004).
118. Werner, A. *et al.* Reconstitution of T cell proliferation under arginine limitation: activated human T cells take up citrulline via L-type amino acid transporter 1 and use it to regenerate arginine after induction of argininosuccinate synthase expression. *Front. Immunol.* **8**, 864 (2017).
119. Zea, A. H. *et al.* L-Arginine modulates CD3 ζ expression and T cell function in activated human T lymphocytes. *Cell. Immunol.* **232**, 21–31 (2004).
120. Munder, M. *et al.* Suppression of T-cell functions by human granulocyte arginase. *Blood* **108**, 1627–34 (2006).
121. Taheri, F. *et al.* L-Arginine regulates the expression of the T-cell receptor ζ chain (CD3 ζ) in Jurkat cells. *Clin. Cancer Res.* **7**, 958s–65s (2001).
122. Rodriguez, P. C., Quiceno, D. G. & Ochoa, A. C. L-arginine availability regulates T-lymphocyte cell-cycle progression. *Blood* **109**, 1568–73 (2007).
123. Rodriguez, P. C. *et al.* L-arginine deprivation regulates cyclin D3 mRNA stability in human T cells by controlling HuR expression. *J. Immunol.* **185**, 5198–204 (2010).
124. Cobbold, S. P. *et al.* Infectious tolerance via the consumption of essential amino acids and mTOR signaling. *Proc. Natl. Acad. Sci. U. S. A.* **106**, 12055–60 (2009).
125. Wang, S. *et al.* Lysosomal amino acid transporter SLC38A9 signals arginine sufficiency to mTORC1. *Science* **347**, 188–94 (2015).
126. Feldmeyer, N. *et al.* Arginine deficiency leads to impaired cofilin dephosphorylation in activated human T lymphocytes. *Int. Immunol.* **24**, 303–13 (2012).
127. Munder, M. *et al.* Cytotoxicity of tumor antigen specific human T cells is unimpaired by arginine depletion. *PLoS One* **8**, e63521 (2013).
128. Sosnowska, A. *et al.* Inhibition of arginase modulates T-cell response in the tumor microenvironment of lung carcinoma. *Oncoimmunology* **10**, 1956143 (2021).
129. Serafini, P., Mgebroff, S., Noonan, K. & Borrello, I. Myeloid-derived suppressor cells promote cross-tolerance in B-cell lymphoma by expanding regulatory T cells. *Cancer Res.* **68**, 5439–49 (2008).
130. Chang, J. *et al.* Retinoic acid promotes the development of Arg1-expressing dendritic cells for the regulation of T-cell differentiation. *Eur. J. Immunol.* **43**, 967–78 (2013).
131. Van de Velde, L.-A. *et al.* Neuroblastoma formation requires unconventional CD4 T cells and arginase-1-dependent myeloid cells. *Cancer Res.* **81**, 5047–59 (2021).
132. Wu, H. *et al.* Arginase-1-dependent promotion of TH17 differentiation and disease progression by MDSCs in systemic lupus erythematosus. *Sci. Transl. Med.* **8**, 331ra40 (2016).

133. Xiao, L., Eneroth, P. H. & Qureshi, G. A. Nitric oxide synthase pathway may mediate human natural killer cell cytotoxicity. *Scand. J. Immunol.* **42**, 505–11 (1995).
134. Oberlies, J. *et al.* Regulation of NK cell function by human granulocyte arginase. *J. Immunol.* **182**, 5259–67 (2009).
135. Lamas, B. *et al.* Altered functions of natural killer cells in response to L-Arginine availability. *Cell. Immunol.* **280**, 182–90 (2012).
136. Fletcher, M. *et al.* L-Arginine depletion blunts antitumor T-cell responses by inducing myeloid-derived suppressor cells. *Cancer Res.* **75**, 275–83 (2015).
137. Choi, B.-S. *et al.* Differential impact of L-arginine deprivation on the activation and effector functions of T cells and macrophages. *J. Leukoc. Biol.* **85**, 268–77 (2009).
138. Vockley, J. G. *et al.* Cloning and characterization of the human type II arginase gene. *Genomics* **38**, 118–23 (1996).
139. Baggio, R. *et al.* Inhibition of Mn²⁺-arginase by borate leads to the design of a transition state analogue inhibitor, 2(S)-amino-6-borohexanoic acid. *J. Am. Chem. Soc.* **119**, 8107–8 (1997).
140. Custot, J. *et al.* The new α -amino acid N^ω-hydroxy-nor-L-arginine: a high-affinity inhibitor of arginase well adapted to bind to its manganese cluster. *J. Am. Chem. Soc.* **119**, 4086–7 (1997).
141. Golebiowski, A. *et al.* Synthesis of quaternary α -amino acid-based arginase inhibitors via the Ugi reaction. *Bioorg. Med. Chem. Lett.* **23**, 4837–41 (2013).
142. Havlinova, Z., Babicova, A., Hroch, M. & Chladek, J. Comparative pharmacokinetics of N^ω-hydroxy-nor-L-arginine, an arginase inhibitor, after single-dose intravenous, intraperitoneal and intratracheal administration to brown Norway rats. *Xenobiotica* **43**, 886–94 (2013).
143. Borek, B. *et al.* Arginase 1/2 inhibitor OATD-02: from discovery to first-in-man setup in cancer immunotherapy. *Mol. Cancer Ther.* **22**, 807–17 (2023).
144. Shi, O., Morris, S. M., Zoghbi, H., Porter, C. W. & O'Brien, W. E. Generation of a mouse model for arginase II deficiency by targeted disruption of the arginase II gene. *Mol. Cell. Biol.* **21**, 811–3 (2001).
145. Martí i Líndez, A.-A. *et al.* Mitochondrial arginase-2 is a cell-autonomous regulator of CD8⁺ T cell function and antitumor efficacy. *JCI Insight* **4**, e132975 (2019).
146. Lowe, M. M. *et al.* Regulatory T cells use arginase 2 to enhance their metabolic fitness in tissues. *JCI Insight* **4**, e129756 (2019).
147. Grzybowski, M. M. *et al.* OATD-02 validates the benefits of pharmacological inhibition of arginase 1 and 2 in cancer. *Cancers (Basel)* **14**, 1–17 (2022).
148. Austin, M. *et al.* Structural and functional characterization of C0021158, a high-affinity monoclonal antibody that inhibits Arginase 2 function via a novel non-competitive mechanism of action. *MABs* **12**, 1801230 (2020).
149. Palte, R. L. *et al.* Cryo-EM structures of inhibitory antibodies complexed with arginase 1 provide insight into mechanism of action. *Commun. Biol.* **4**, 927 (2021).
150. Weis-Banke, S. E. *et al.* The metabolic enzyme arginase-2 is a potential target for novel immune modulatory vaccines. *Oncoimmunology* **9**, 1771142 (2020).
151. Jørgensen, M. A. *et al.* Arginase 1-based immune modulatory vaccines induce anticancer immunity and synergize with anti-PD-1 checkpoint blockade. *Cancer Immunol. Res.* **9**, 1316–26 (2021).
152. Colegio, O. R. *et al.* Functional polarization of tumour-associated macrophages by tumour-derived lactic acid. *Nature* **513**, 559–63 (2014).
153. Miret, J. J. *et al.* Suppression of myeloid cell arginase activity leads to therapeutic response in a NSCLC mouse model by activating anti-tumor immunity. *J. Immunother. Cancer* **7**, 32 (2019).
154. Pilanc, P. *et al.* A novel oral arginase 1/2 inhibitor enhances the antitumor effect of PD-1 inhibition in murine experimental gliomas by altering the immunosuppressive environment. *Front. Oncol.* **11**, 703465 (2021).

155. Naing, A. *et al.* Phase I study of the arginase inhibitor INCB001158 (1158) alone and in combination with pembrolizumab (PEM) in patients (Pts) with advanced/metastatic (adv/met) solid tumours. *Ann. Oncol.* **30**, v160 (2019).
156. Förstermann, U. *et al.* Nitric oxide synthase isozymes. Characterization, purification, molecular cloning, and functions. *Hypertension* **23**, 1121–31 (1994).
157. Alderton, W. K., Cooper, C. E. & Knowles, R. G. Nitric oxide synthases: structure, function and inhibition. *Biochem. J.* **357**, 593–615 (2001).
158. Pautz, A. *et al.* Regulation of the expression of inducible nitric oxide synthase. *Nitric Oxide* **23**, 75–93 (2010).
159. Forrester, K. *et al.* Nitric oxide-induced p53 accumulation and regulation of inducible nitric oxide synthase expression by wild-type p53. *Proc. Natl. Acad. Sci. U. S. A.* **93**, 2442–7 (1996).
160. Matthews, J. R., Botting, C. H., Panico, M., Morris, H. R. & Hay, R. T. Inhibition of NF- κ B DNA binding by nitric oxide. *Nucleic Acids Res.* **24**, 2236–42 (1996).
161. Lee, J., Ryu, H., Ferrante, R. J., Morris, S. M. & Ratan, R. R. Translational control of inducible nitric oxide synthase expression by arginine can explain the arginine paradox. *Proc. Natl. Acad. Sci. U. S. A.* **100**, 4843–8 (2003).
162. Guzik, T. J., Korbout, R. & Adamek-Guzik, T. Nitric oxide and superoxide in inflammation and immune regulation. *J. Physiol. Pharmacol.* **54**, 469–87 (2003).
163. Radi, R. Nitric oxide, oxidants, and protein tyrosine nitration. *Proc. Natl. Acad. Sci. U. S. A.* **101**, 4003–8 (2004).
164. Pacher, P., Beckman, J. S. & Liaudet, L. Nitric oxide and peroxynitrite in health and disease. *Physiol. Rev.* **87**, 315–424 (2007).
165. Smith, B. C. & Marletta, M. A. Mechanisms of S-nitrosothiol formation and selectivity in nitric oxide signaling. *Curr. Opin. Chem. Biol.* **16**, 498–506 (2012).
166. Sawa, T. & Ohshima, H. Nitritative DNA damage in inflammation and its possible role in carcinogenesis. *Nitric Oxide* **14**, 91–100 (2006).
167. Baker, P. R. S., Schopfer, F. J., O'Donnell, V. B. & Freeman, B. A. Convergence of nitric oxide and lipid signaling: anti-inflammatory nitro-fatty acids. *Free Radic. Biol. Med.* **46**, 989–1003 (2009).
168. Bogdan, C. Nitric oxide synthase in innate and adaptive immunity: an update. *Trends Immunol.* **36**, 161–78 (2015).
169. Denninger, J. W. & Marletta, M. A. Guanylate cyclase and the * NO/cGMP signaling pathway. *Biochim. Biophys. Acta* **1411**, 334–50 (1999).
170. Fukumura, D., Kashiwagi, S. & Jain, R. K. The role of nitric oxide in tumour progression. *Nat. Rev. Cancer* **6**, 521–34 (2006).
171. Choudhari, S. K., Chaudhary, M., Bagde, S., Gadball, A. R. & Joshi, V. Nitric oxide and cancer: a review. *World J. Surg. Oncol.* **11**, 118 (2013).
172. Chang, C., Diers, A. R. & Hogg, N. Cancer cell metabolism and the modulating effects of nitric oxide. *Free Radic. Biol. Med.* **79**, 324–36 (2015).
173. Niedbala, W. *et al.* Nitric oxide preferentially induces type 1 T cell differentiation by selectively up-regulating IL-12 receptor β 2 expression via cGMP. *Proc. Natl. Acad. Sci. U. S. A.* **99**, 16186–91 (2002).
174. Obermajer, N. *et al.* Induction and stability of human Th17 cells require endogenous NOS2 and cGMP-dependent NO signaling. *J. Exp. Med.* **210**, 1433–45 (2013).
175. Lee, S.-W., Choi, H., Eun, S.-Y., Fukuyama, S. & Croft, M. Nitric oxide modulates TGF- β -directive signals to suppress Foxp3 $^{+}$ regulatory T cell differentiation and potentiate Th1 development. *J. Immunol.* **186**, 6972–80 (2011).
176. Liu, L. & Stamler, J. S. NO: an inhibitor of cell death. *Cell Death Differ.* **6**, 937–42 (1999).

177. Bingisser, R. M., Tilbrook, P. A., Holt, P. G. & Kees, U. R. Macrophage-derived nitric oxide regulates T cell activation via reversible disruption of the Jak3/STAT5 signaling pathway. *J. Immunol.* **160**, 5729–34 (1998).
178. Duhé, R. J. *et al.* Nitric oxide and thiol redox regulation of Janus kinase activity. *Proc. Natl. Acad. Sci. U. S. A.* **95**, 126–31 (1998).
179. Brito, C. *et al.* Peroxynitrite inhibits T lymphocyte activation and proliferation by promoting impairment of tyrosine phosphorylation and peroxynitrite-driven apoptotic death. *J. Immunol.* **162**, 3356–66 (1999).
180. Mazzoni, A. *et al.* Myeloid suppressor lines inhibit T cell responses by an NO-dependent mechanism. *J. Immunol.* **168**, 689–95 (2002).
181. Mundy-Bosse, B. L. *et al.* Myeloid-derived suppressor cell inhibition of the IFN response in tumor-bearing mice. *Cancer Res.* **71**, 5101–10 (2011).
182. Feng, S. *et al.* Myeloid-derived suppressor cells inhibit T cell activation through nitrating LCK in mouse cancers. *Proc. Natl. Acad. Sci. U. S. A.* **115**, 10094–9 (2018).
183. Saio, M., Radoja, S., Marino, M. & Frey, A. B. Tumor-infiltrating macrophages induce apoptosis in activated CD8⁺ T cells by a mechanism requiring cell contact and mediated by both the cell-associated form of TNF and nitric oxide. *J. Immunol.* **167**, 5583–93 (2001).
184. Cartwright, A. N. R. *et al.* Immunosuppressive myeloid cells induce nitric oxide-dependent DNA damage and p53 pathway activation in CD8⁺ T cells. *Cancer Immunol. Res.* **9**, 470–85 (2021).
185. Huang, F. P. *et al.* Nitric oxide regulates Th1 cell development through the inhibition of IL-12 synthesis by macrophages. *Eur. J. Immunol.* **28**, 4062–70 (1998).
186. Niedbala, W., Wei, X. Q., Piedrafita, D., Xu, D. & Liew, F. Y. Effects of nitric oxide on the induction and differentiation of Th1 cells. *Eur. J. Immunol.* **29**, 2498–505 (1999).
187. Niedbala, W. *et al.* Regulation of type 17 helper T-cell function by nitric oxide during inflammation. *Proc. Natl. Acad. Sci. U. S. A.* **108**, 9220–5 (2011).
188. Yang, J. *et al.* T cell–derived inducible nitric oxide synthase switches off Th17 cell differentiation. *J. Exp. Med.* **210**, 1447–62 (2013).
189. Niedbala, W. *et al.* Nitric oxide induces CD4⁺CD25⁺ Foxp3⁺ regulatory T cells from CD4⁺CD25⁺ T cells via p53, IL-2, and OX40. *Proc. Natl. Acad. Sci. U. S. A.* **104**, 15478–83 (2007).
190. Stiff, A. *et al.* Nitric oxide production by myeloid-derived suppressor cells plays a role in impairing Fc receptor-mediated natural killer cell function. *Clin. Cancer Res.* **24**, 1891–904 (2018).
191. Everts, B. *et al.* Commitment to glycolysis sustains survival of NO-producing inflammatory dendritic cells. *Blood* **120**, 1422–31 (2012).
192. Van den Bossche, J. *et al.* Mitochondrial dysfunction prevents repolarization of inflammatory macrophages. *Cell Rep.* **17**, 684–96 (2016).
193. Kashfi, K., Kannikal, J. & Nath, N. Macrophage reprogramming and cancer therapeutics: role of iNOS-derived NO. *Cells* **10**, 1–22 (2021).
194. Sektioglu, I. M. *et al.* Macrophage-derived nitric oxide initiates T-cell diapedesis and tumor rejection. *Oncoimmunology* **5**, e1204506 (2016).
195. Buckanovich, R. J. *et al.* Endothelin B receptor mediates the endothelial barrier to T cell homing to tumors and disables immune therapy. *Nat. Med.* **14**, 28–36 (2008).
196. Gehad, A. E. *et al.* Nitric oxide-producing myeloid-derived suppressor cells inhibit vascular E-selectin expression in human squamous cell carcinomas. *J. Invest. Dermatol.* **132**, 2642–51 (2012).
197. Molon, B. *et al.* Chemokine nitration prevents intratumoral infiltration of antigen-specific T cells. *J. Exp. Med.* **208**, 1949–62 (2011).

198. Jayaraman, P. *et al.* Tumor-expressed inducible nitric oxide synthase controls induction of functional myeloid-derived suppressor cells through modulation of vascular endothelial growth factor release. *J. Immunol.* **188**, 5365–76 (2012).
199. Birnboim, H. C., Lemay, A.-M., Lam, D. K. Y., Goldstein, R. & Webb, J. R. Cutting edge: MHC class II-restricted peptides containing the inflammation-associated marker 3-nitrotyrosine evade central tolerance and elicit a robust cell-mediated immune response. *J. Immunol.* **171**, 528–32 (2003).
200. Hardy, L. L., Wick, D. A. & Webb, J. R. Conversion of tyrosine to the inflammation-associated analog 3'-nitrotyrosine at either TCR- or MHC-contact positions can profoundly affect recognition of the MHC class I-restricted epitope of lymphocytic choriomeningitis virus glycoprotein 33 by CD8 T cells. *J. Immunol.* **180**, 5956–62 (2008).
201. Nagaraj, S. *et al.* Altered recognition of antigen is a mechanism of CD8⁺ T cell tolerance in cancer. *Nat. Med.* **13**, 828–35 (2007).
202. Nagaraj, S., Schrum, A. G., Cho, H.-I., Celis, E. & Gabrilovich, D. I. Mechanism of T cell tolerance induced by myeloid-derived suppressor cells. *J. Immunol.* **184**, 3106–16 (2010).
203. Corzo, C. A. *et al.* HIF-1 α regulates function and differentiation of myeloid-derived suppressor cells in the tumor microenvironment. *J. Exp. Med.* **207**, 2439–53 (2010).
204. Lu, T. *et al.* Tumor-infiltrating myeloid cells induce tumor cell resistance to cytotoxic T cells in mice. *J. Clin. Invest.* **121**, 4015–29 (2011).
205. Harari, O. & Liao, J. K. Inhibition of MHC II gene transcription by nitric oxide and antioxidants. *Curr. Pharm. Des.* **10**, 893–8 (2004).
206. Huang, Z., Fu, J. & Zhang, Y. Nitric oxide donor-based cancer therapy: advances and prospects. *J. Med. Chem.* **60**, 7617–35 (2017).
207. Granados-Principal, S. *et al.* Inhibition of iNOS as a novel effective targeted therapy against triple-negative breast cancer. *Breast Cancer Res.* **17**, 25 (2015).
208. Dao, V. T.-V. *et al.* Nitric oxide synthase inhibitors into the clinic at last. *Handb. Exp. Pharmacol.* **264**, 169–204 (2021).
209. Thomsen, L. L. *et al.* Selective inhibition of inducible nitric oxide synthase inhibits tumor growth in vivo: studies with 1400W, a novel inhibitor. *Cancer Res.* **57**, 3300–4 (1997).
210. Dufait, I. *et al.* *Ex vivo* generation of myeloid-derived suppressor cells that model the tumor immunosuppressive environment in colorectal cancer. *Oncotarget* **6**, 12369–82 (2015).
211. Pershing, N. L. K., Yang, C.-F. J., Xu, M. & Counter, C. M. Treatment with the nitric oxide synthase inhibitor L-NAME provides a survival advantage in a mouse model of *Kras* mutation-positive, non-small cell lung cancer. *Oncotarget* **7**, 42385–92 (2016).
212. Jayaraman, P. *et al.* iNOS expression in CD4⁺ T cells limits Treg induction by repressing TGF β 1: combined iNOS inhibition and Treg depletion unmask endogenous antitumor immunity. *Clin. Cancer Res.* **20**, 6439–51 (2014).
213. Chung, A. W. *et al.* A phase 1/2 clinical trial of the nitric oxide synthase inhibitor L-NMMA and taxane for treating chemoresistant triple-negative breast cancer. *Sci. Transl. Med.* **13**, eabj5070 (2021).
214. Palego, L., Betti, L., Rossi, A. & Giannaccini, G. Tryptophan biochemistry: structural, nutritional, metabolic, and medical aspects in humans. *J. Amino Acids* **2016**, 8952520 (2016).
215. Platten, M., Nollen, E. A. A., Röhrig, U. F., Fallarino, F. & Opitz, C. A. Tryptophan metabolism as a common therapeutic target in cancer, neurodegeneration and beyond. *Nat. Rev. Drug Discov.* **18**, 379–401 (2019).
216. Fiore, A. & Murray, P. J. Tryptophan and indole metabolism in immune regulation. *Curr. Opin. Immunol.* **70**, 7–14 (2021).

217. Yoshida, R., Imanishi, J., Oku, T., Kishida, T. & Hayaishi, O. Induction of pulmonary indoleamine 2,3-dioxygenase by interferon. *Proc. Natl. Acad. Sci. U. S. A.* **78**, 129–32 (1981).
218. Théate, I. *et al.* Extensive profiling of the expression of the indoleamine 2,3-dioxygenase 1 protein in normal and tumoral human tissues. *Cancer Immunol. Res.* **3**, 161–72 (2015).
219. Pfefferkorn, E. R. Interferon γ blocks the growth of *Toxoplasma gondii* in human fibroblasts by inducing the host cells to degrade tryptophan. *Proc. Natl. Acad. Sci. U. S. A.* **81**, 908–12 (1984).
220. Ball, H. J. *et al.* Characterization of an indoleamine 2,3-dioxygenase-like protein found in humans and mice. *Gene* **396**, 203–13 (2007).
221. Metz, R. *et al.* Novel tryptophan catabolic enzyme IDO2 is the preferred biochemical target of the antitumor indoleamine 2,3-dioxygenase inhibitory compound D-1-methyl-tryptophan. *Cancer Res.* **67**, 7082–7 (2007).
222. Prendergast, G. C., Metz, R., Muller, A. J., Merlo, L. M. F. & Mandik-Nayak, L. IDO2 in immunomodulation and autoimmune disease. *Front. Immunol.* **5**, 585 (2014).
223. Mondanelli, G. *et al.* Current challenges for IDO2 as target in cancer immunotherapy. *Front. Immunol.* **12**, 679953 (2021).
224. Pantouris, G., Serys, M., Yuasa, H. J., Ball, H. J. & Mowat, C. G. Human indoleamine 2,3-dioxygenase-2 has substrate specificity and inhibition characteristics distinct from those of indoleamine 2,3-dioxygenase-1. *Amino Acids* **46**, 2155–63 (2014).
225. Metz, R. *et al.* IDO2 is critical for IDO1-mediated T-cell regulation and exerts a non-redundant function in inflammation. *Int. Immunol.* **26**, 357–67 (2014).
226. Schutz, G. & Feigelson, P. Purification and properties of rat liver tryptophan oxygenase. *J. Biol. Chem.* **247**, 5327–32 (1972).
227. Kanai, M. *et al.* Tryptophan 2,3-dioxygenase is a key modulator of physiological neurogenesis and anxiety-related behavior in mice. *Mol. Brain* **2**, 8 (2009).
228. Uyttenhove, C. *et al.* Evidence for a tumoral immune resistance mechanism based on tryptophan degradation by indoleamine 2,3-dioxygenase. *Nat. Med.* **9**, 1269–74 (2003).
229. Muller, A. J., DuHadaway, J. B., Donover, P. S., Sutanto-Ward, E. & Prendergast, G. C. Inhibition of indoleamine 2,3-dioxygenase, an immunoregulatory target of the cancer suppression gene Bin1, potentiates cancer chemotherapy. *Nat. Med.* **11**, 312–9 (2005).
230. Balachandran, V. P. *et al.* Imatinib potentiates antitumor T cell responses in gastrointestinal stromal tumor through the inhibition of IDO. *Nat. Med.* **17**, 1094–100 (2011).
231. Hennequart, M. *et al.* Constitutive IDO1 expression in human tumors is driven by cyclooxygenase-2 and mediates intrinsic immune resistance. *Cancer Immunol. Res.* **5**, 695–709 (2017).
232. Litzenburger, U. M. *et al.* Constitutive IDO expression in human cancer is sustained by an autocrine signaling loop involving IL-6, STAT3 and the AHR. *Oncotarget* **5**, 1038–51 (2014).
233. Munn, D. H. *et al.* Potential regulatory function of human dendritic cells expressing indoleamine 2,3-dioxygenase. *Science* **297**, 1867–70 (2002).
234. Meisel, R. *et al.* Human bone marrow stromal cells inhibit allogeneic T-cell responses by indoleamine 2,3-dioxygenase-mediated tryptophan degradation. *Blood* **103**, 4619–21 (2004).
235. Riesenberger, R. *et al.* Expression of indoleamine 2,3-dioxygenase in tumor endothelial cells correlates with long-term survival of patients with renal cell carcinoma. *Clin. Cancer Res.* **13**, 6993–7002 (2007).
236. Li, T. *et al.* Hepatocellular carcinoma-associated fibroblasts trigger NK cell dysfunction via PGE2 and IDO. *Cancer Lett.* **318**, 154–61 (2012).
237. Zhao, Q. *et al.* Activated CD69⁺ T cells foster immune privilege by regulating IDO expression in tumor-associated macrophages. *J. Immunol.* **188**, 1117–24 (2012).

238. Yu, J. *et al.* Myeloid-derived suppressor cells suppress antitumor immune responses through IDO expression and correlate with lymph node metastasis in patients with breast cancer. *J. Immunol.* **190**, 3783–97 (2013).
239. Brandacher, G. *et al.* Prognostic value of indoleamine 2,3-dioxygenase expression in colorectal cancer: effect on tumor-infiltrating T cells. *Clin. Cancer Res.* **12**, 1144–51 (2006).
240. Curti, A. *et al.* Modulation of tryptophan catabolism by human leukemic cells results in the conversion of CD25⁺ into CD25⁺ T regulatory cells. *Blood* **109**, 2871–7 (2007).
241. Ino, K. *et al.* Inverse correlation between tumoral indoleamine 2,3-dioxygenase expression and tumor-infiltrating lymphocytes in endometrial cancer: its association with disease progression and survival. *Clin. Cancer Res.* **14**, 2310–7 (2008).
242. Brody, J. R. *et al.* Expression of indoleamine 2,3-dioxygenase in metastatic malignant melanoma recruits regulatory T cells to avoid immune detection and affects survival. *Cell Cycle* **8**, 1930–4 (2009).
243. Inaba, T. *et al.* Role of the immunosuppressive enzyme indoleamine 2,3-dioxygenase in the progression of ovarian carcinoma. *Gynecol. Oncol.* **115**, 185–92 (2009).
244. Holmgaard, R. B. *et al.* Tumor-expressed IDO recruits and activates MDSCs in a Treg-dependent manner. *Cell Rep.* **13**, 412–24 (2015).
245. Godin-Ethier, J., Hanafi, L.-A., Piccirillo, C. A. & Lapointe, R. Indoleamine 2,3-dioxygenase expression in human cancers: clinical and immunologic perspectives. *Clin. Cancer Res.* **17**, 6985–91 (2011).
246. Wells, G., Kennedy, P. T. & Dahal, L. N. Investigating the role of indoleamine 2,3-dioxygenase in acute myeloid leukemia: a systematic review. *Front. Immunol.* **12**, 651687 (2021).
247. Opitz, C. A. *et al.* An endogenous tumour-promoting ligand of the human aryl hydrocarbon receptor. *Nature* **478**, 197–203 (2011).
248. Pilotte, L. *et al.* Reversal of tumoral immune resistance by inhibition of tryptophan 2,3-dioxygenase. *Proc. Natl. Acad. Sci. U. S. A.* **109**, 2497–502 (2012).
249. Novikov, O. *et al.* An aryl hydrocarbon receptor-mediated amplification loop that enforces cell migration in ER⁺/PR⁺/Her2⁻ human breast cancer cells. *Mol. Pharmacol.* **90**, 674–88 (2016).
250. Ochs, K. *et al.* Tryptophan-2,3-dioxygenase is regulated by prostaglandin E2 in malignant glioma via a positive signaling loop involving prostaglandin E receptor-4. *J. Neurochem.* **136**, 1142–54 (2016).
251. Ott, M. *et al.* Suppression of TDO-mediated tryptophan catabolism in glioblastoma cells by a steroid-responsive FKBP52-dependent pathway. *Glia* **63**, 78–90 (2015).
252. Kudo, T. *et al.* Constitutive expression of the immunosuppressive tryptophan dioxygenase TDO2 in glioblastoma is driven by the transcription factor C/EBP β . *Front. Immunol.* **11**, 657 (2020).
253. Hoffmann, D. *et al.* Tryptophan 2,3-dioxygenase expression identified in human hepatocellular carcinoma cells and in intratumoral pericytes of most cancers. *Cancer Immunol. Res.* **8**, 19–31 (2020).
254. Rohatgi, N., Ghoshdastider, U., Baruah, P., Kulshrestha, T. & Skanderup, A. J. A pan-cancer metabolic atlas of the tumor microenvironment. *Cell Rep.* **39**, 110800 (2022).
255. Hsu, Y.-L. *et al.* Lung cancer-derived galectin-1 contributes to cancer associated fibroblast-mediated cancer progression and immune suppression through TDO2/kynurenine axis. *Oncotarget* **7**, 27584–98 (2016).
256. Pham, Q. T. *et al.* TDO2 overexpression is associated with cancer stem cells and poor prognosis in esophageal squamous cell carcinoma. *Oncology* **95**, 297–308 (2018).
257. Greene, L. I. *et al.* A role for tryptophan-2,3-dioxygenase in CD8 T-cell suppression and evidence of tryptophan catabolism in breast cancer patient plasma. *Mol. Cancer Res.* **17**, 131–39 (2019).

258. Wardhani, L. O. *et al.* Expression of the IDO1/TDO2-AhR pathway in tumor cells or the tumor microenvironment is associated with Merkel cell polyomavirus status and prognosis in Merkel cell carcinoma. *Hum. Pathol.* **84**, 52–61 (2019).
259. Liu, Q. *et al.* Comprehensive analysis of the expression and prognosis for TDO2 in breast cancer. *Mol. Ther. Oncolytics* **17**, 153–68 (2020).
260. Löb, S. *et al.* IDO1 and IDO2 are expressed in human tumors: levo- but not dextro-1-methyl tryptophan inhibits tryptophan catabolism. *Cancer Immunol. Immunother.* **58**, 153–7 (2009).
261. Lob, S. *et al.* Levo- but not dextro-1-methyl tryptophan abrogates the IDO activity of human dendritic cells. *Blood* **111**, 2152–4 (2008).
262. Trabanelli, S. *et al.* The SOCS3-independent expression of IDO2 supports the homeostatic generation of T regulatory cells by human dendritic cells. *J. Immunol.* **192**, 1231–40 (2014).
263. Munn, D. H. *et al.* GCN2 kinase in T cells mediates proliferative arrest and anergy induction in response to indoleamine 2,3-dioxygenase. *Immunity* **22**, 633–42 (2005).
264. Metz, R. *et al.* IDO inhibits a tryptophan sufficiency signal that stimulates mTOR: a novel IDO effector pathway targeted by D-1-methyl-tryptophan. *Oncimmunology* **1**, 1460–8 (2012).
265. DiNatale, B. C. *et al.* Kynurenic acid is a potent endogenous aryl hydrocarbon receptor ligand that synergistically induces interleukin-6 in the presence of inflammatory signaling. *Toxicol. Sci.* **115**, 89–97 (2010).
266. Mezrich, J. D. *et al.* An interaction between kynurenine and the aryl hydrocarbon receptor can generate regulatory T cells. *J. Immunol.* **185**, 3190–8 (2010).
267. Seok, S.-H. *et al.* Trace derivatives of kynurenine potentially activate the aryl hydrocarbon receptor (AHR). *J. Biol. Chem.* **293**, 1994–2005 (2018).
268. Munn, D. H. *et al.* Inhibition of T cell proliferation by macrophage tryptophan catabolism. *J. Exp. Med.* **189**, 1363–72 (1999).
269. Hwu, P. *et al.* Indoleamine 2,3-dioxygenase production by human dendritic cells results in the inhibition of T cell proliferation. *J. Immunol.* **164**, 3596–9 (2000).
270. Munn, D. H., Sharma, M. D. & Mellor, A. L. Ligation of B7-1/B7-2 by human CD4⁺ T cells triggers indoleamine 2,3-dioxygenase activity in dendritic cells. *J. Immunol.* **172**, 4100–10 (2004).
271. Fallarino, F. *et al.* The combined effects of tryptophan starvation and tryptophan catabolites down-regulate T cell receptor ζ -chain and induce a regulatory phenotype in naive T cells. *J. Immunol.* **176**, 6752–61 (2006).
272. Fallarino, F. *et al.* T cell apoptosis by tryptophan catabolism. *Cell Death Differ.* **9**, 1069–77 (2002).
273. Frumento, G. *et al.* Tryptophan-derived catabolites are responsible for inhibition of T and natural killer cell proliferation induced by indoleamine 2,3-dioxygenase. *J. Exp. Med.* **196**, 459–68 (2002).
274. Terness, P. *et al.* Inhibition of allogeneic T cell proliferation by indoleamine 2,3-dioxygenase-expressing dendritic cells: mediation of suppression by tryptophan metabolites. *J. Exp. Med.* **196**, 447–57 (2002).
275. Siska, P. J. *et al.* Kynurenine induces T cell fat catabolism and has limited suppressive effects in vivo. *EBioMedicine* **74**, 103734 (2021).
276. Liu, Y. *et al.* Tumor-repopulating cells induce PD-1 expression in CD8⁺ T cells by transferring kynurenine and AHR activation. *Cancer Cell* **33**, 480–94.e7 (2018).
277. Campesato, L. F. *et al.* Blockade of the AHR restricts a Treg-macrophage suppressive axis induced by L-Kynurenine. *Nat. Commun.* **11**, 4011 (2020).
278. Amobi-McCloud, A. *et al.* IDO1 expression in ovarian cancer induces PD-1 in T cells via aryl hydrocarbon receptor activation. *Front. Immunol.* **12**, 678999 (2021).

279. Liu, X. *et al.* Selective inhibition of IDO1 effectively regulates mediators of antitumor immunity. *Blood* **115**, 3520–30 (2010).
280. Sharma, M. D. *et al.* Plasmacytoid dendritic cells from mouse tumor-draining lymph nodes directly activate mature Tregs via indoleamine 2,3-dioxygenase. *J. Clin. Invest.* **117**, 2570–82 (2007).
281. Baban, B. *et al.* IDO activates regulatory T cells and blocks their conversion into Th17-like T cells. *J. Immunol.* **183**, 2475–83 (2009).
282. Sharma, M. D. *et al.* Indoleamine 2,3-dioxygenase controls conversion of Foxp3⁺ Tregs to TH17-like cells in tumor-draining lymph nodes. *Blood* **113**, 6102–11 (2009).
283. Della Chiesa, M. *et al.* The tryptophan catabolite L-kynurenine inhibits the surface expression of Nkp46- and NKG2D-activating receptors and regulates NK-cell function. *Blood* **108**, 4118–25 (2006).
284. Fang, X. *et al.* IDO1 can impair NK cells function against non-small cell lung cancer by downregulation of NKG2D ligand via ADAM10. *Pharmacol. Res.* **177**, 106132 (2022).
285. Spaggiari, G. M. *et al.* Mesenchymal stem cells inhibit natural killer-cell proliferation, cytotoxicity, and cytokine production: role of indoleamine 2,3-dioxygenase and prostaglandin E2. *Blood* **111**, 1327–33 (2008).
286. Brenk, M. *et al.* Tryptophan deprivation induces inhibitory receptors ILT3 and ILT4 on dendritic cells favoring the induction of human CD4⁺CD25⁺ Foxp3⁺ T regulatory cells. *J. Immunol.* **183**, 145–54 (2009).
287. Ravishankar, B. *et al.* The amino acid sensor GCN2 inhibits inflammatory responses to apoptotic cells promoting tolerance and suppressing systemic autoimmunity. *Proc. Natl. Acad. Sci. U. S. A.* **112**, 10774–9 (2015).
288. Takenaka, M. C. *et al.* Control of tumor-associated macrophages and T cells in glioblastoma via AHR and CD39. *Nat. Neurosci.* **22**, 729–40 (2019).
289. Smith, C. *et al.* IDO is a nodal pathogenic driver of lung cancer and metastasis development. *Cancer Discov.* **2**, 722–35 (2012).
290. Timosenko, E. *et al.* Nutritional stress induced by tryptophan-degrading enzymes results in ATF4-dependent reprogramming of the amino acid transporter profile in tumor cells. *Cancer Res.* **76**, 6193–204 (2016).
291. Adam, I. *et al.* Upregulation of tryptophanyl-tRNA synthetase adapts human cancer cells to nutritional stress caused by tryptophan degradation. *Oncoimmunology* **7**, e1486353 (2018).
292. Bartok, O. *et al.* Anti-tumour immunity induces aberrant peptide presentation in melanoma. *Nature* **590**, 332–7 (2021).
293. Pataskar, A. *et al.* Tryptophan depletion results in tryptophan-to-phenylalanine substituents. *Nature* **603**, 721–7 (2022).
294. Bishnupuri, K. S. *et al.* IDO1 and kynurenine pathway metabolites activate PI3K-Akt signaling in the neoplastic colon epithelium to promote cancer cell proliferation and inhibit apoptosis. *Cancer Res.* **79**, 1138–50 (2019).
295. Venkateswaran, N. *et al.* MYC promotes tryptophan uptake and metabolism by the kynurenine pathway in colon cancer. *Genes Dev.* **33**, 1236–51 (2019).
296. Chen, J.-Y. *et al.* Cancer/stroma interplay via cyclooxygenase-2 and indoleamine 2,3-dioxygenase promotes breast cancer progression. *Breast Cancer Res.* **16**, 410 (2014).
297. Mondal, A. *et al.* IDO1 is an integral mediator of inflammatory neovascularization. *EBioMedicine* **14**, 74–82 (2016).
298. Vigneron, N., van Baren, N. & Van den Eynde, B. J. Expression profile of the human IDO1 protein, a cancer drug target involved in tumoral immune resistance. *Oncoimmunology* **4**, e1003012 (2015).
299. Schramme, F. *et al.* Inhibition of tryptophan-dioxygenase activity increases the antitumor efficacy of immune checkpoint inhibitors. *Cancer Immunol. Res.* **8**, 32–45 (2020).
300. Schafer, C. C. *et al.* Indoleamine 2,3-dioxygenase regulates anti-tumor immunity in lung cancer by metabolic reprogramming of immune cells in the tumor microenvironment. *Oncotarget* **7**, 75407–24 (2016).

301. Wainwright, D. A. *et al.* IDO expression in brain tumors increases the recruitment of regulatory T cells and negatively impacts survival. *Clin. Cancer Res.* **18**, 6110–21 (2012).
302. Holmgaard, R. B., Zamarin, D., Munn, D. H., Wolchok, J. D. & Allison, J. P. Indoleamine 2,3-dioxygenase is a critical resistance mechanism in antitumor T cell immunotherapy targeting CTLA-4. *J. Exp. Med.* **210**, 1389–402 (2013).
303. Takamatsu, M. *et al.* Inhibition of indoleamine 2,3-dioxygenase 1 expression alters immune response in colon tumor micro-environment in mice. *Cancer Sci.* **106**, 1008–15 (2015).
304. Banerjee, T. *et al.* A key in vivo antitumor mechanism of action of natural product-based brassinins is inhibition of indoleamine 2,3-dioxygenase. *Oncogene* **27**, 2851–7 (2008).
305. Fu, R. *et al.* LW106, a novel indoleamine 2,3-dioxygenase 1 inhibitor, suppresses tumour progression by limiting stroma-immune crosstalk and cancer stem cell enrichment in tumour micro-environment. *Br. J. Pharmacol.* **175**, 3034–49 (2018).
306. Zheng, X. *et al.* Reinstalling antitumor immunity by inhibiting tumor-derived immunosuppressive molecule IDO through RNA interference. *J. Immunol.* **177**, 5639–46 (2006).
307. Koblish, H. K. *et al.* Hydroxyamidine inhibitors of indoleamine-2,3-dioxygenase potently suppress systemic tryptophan catabolism and the growth of IDO-expressing tumors. *Mol. Cancer Ther.* **9**, 489–98 (2010).
308. Cheong, J. E., Ekkati, A. & Sun, L. A patent review of IDO1 inhibitors for cancer. *Expert Opin. Ther. Pat.* **28**, 317–30 (2018).
309. Tang, K., Wu, Y.-H., Song, Y. & Yu, B. Indoleamine 2,3-dioxygenase 1 (IDO1) inhibitors in clinical trials for cancer immunotherapy. *J. Hematol. Oncol.* **14**, 68 (2021).
310. Gomes, B. *et al.* Characterization of the selective indoleamine 2,3-dioxygenase-1 (IDO1) catalytic inhibitor EOS200271/PF-06840003 supports IDO1 as a critical resistance mechanism to PD-(L)1 blockade therapy. *Mol. Cancer Ther.* **17**, 2530–42 (2018).
311. Spranger, S. *et al.* Mechanism of tumor rejection with doublets of CTLA-4, PD-1/PD-L1, or IDO blockade involves restored IL-2 production and proliferation of CD8⁺ T cells directly within the tumor microenvironment. *J. Immunother. Cancer* **2**, 3 (2014).
312. Wainwright, D. A. *et al.* Durable therapeutic efficacy utilizing combinatorial blockade against IDO, CTLA-4, and PD-L1 in mice with brain tumors. *Clin. Cancer Res.* **20**, 5290–301 (2014).
313. Brown, Z. J. *et al.* Indoleamine 2,3-dioxygenase provides adaptive resistance to immune checkpoint inhibitors in hepatocellular carcinoma. *Cancer Immunol. Immunother.* **67**, 1305–15 (2018).
314. Toulmonde, M. *et al.* Use of PD-1 targeting, macrophage infiltration, and IDO pathway activation in sarcomas: a phase 2 clinical trial. *JAMA Oncol.* **4**, 93–7 (2018).
315. Li, H. *et al.* Metabolomic adaptations and correlates of survival to immune checkpoint blockade. *Nat. Commun.* **10**, 4346 (2019).
316. Kozlova, A. & Frédéric, R. Current state on tryptophan 2,3-dioxygenase inhibitors: a patent review. *Expert Opin. Ther. Pat.* **29**, 11–23 (2019).
317. Du, L. *et al.* Both IDO1 and TDO contribute to the malignancy of gliomas via the Kyn-AhR-AQP4 signaling pathway. *Signal Transduct. Target. Ther.* **5**, 10 (2020).
318. Naing, A. *et al.* Preclinical investigations and a first-in-human phase I trial of M4112, the first dual inhibitor of indoleamine 2,3-dioxygenase 1 and tryptophan 2,3-dioxygenase 2, in patients with advanced solid tumors. *J. Immunother. Cancer* **8**, e000870 (2020).
319. Hamid, O. *et al.* Epcadostat plus pembrolizumab in patients with advanced melanoma: phase 1 and 2 efficacy and safety results from ECHO-202/KEYNOTE-037. *Ann. Oncol.* **28**(Suppl 5), 428–48 (2017).

320. Daud, A. *et al.* Epacadostat plus nivolumab for advanced melanoma: updated phase 2 results of the ECHO-204 study. *J. Clin. Oncol.* **36**(Suppl), 9511 (2018).
321. Long, G. V. *et al.* Epacadostat plus pembrolizumab versus placebo plus pembrolizumab in patients with unresectable or metastatic melanoma (ECHO-301/KEYNOTE-252): a phase 3, randomised, double-blind study. *Lancet. Oncol.* **20**, 1083–97 (2019).
322. Sonpavde, G. *et al.* ENERGIZE: a Phase III study of neoadjuvant chemotherapy alone or with nivolumab with/without linodostat mesylate for muscle-invasive bladder cancer. *Future Oncol.* **16**, 4359–68 (2020).
323. Muller, A. J., Manfredi, M. G., Zakharia, Y. & Prendergast, G. C. Inhibiting IDO pathways to treat cancer: lessons from the ECHO-301 trial and beyond. *Semin. Immunopathol.* **41**, 41–8 (2019).
324. Van den Eynde, B. J., van Baren, N. & Baurain, J. F. Is there a clinical future for IDO1 inhibitors after the failure of epacadostat in melanoma? *Annu. Rev. Cancer Biol.* **4**, 241–56 (2020).
325. Beatty, G. L. *et al.* First-in-human phase I study of the oral inhibitor of indoleamine 2,3-dioxygenase-1 epacadostat (INCB-024360) in patients with advanced solid malignancies. *Clin. Cancer Res.* **23**, 3269–76 (2017).
326. Pallotta, M. T. *et al.* Indoleamine 2,3-dioxygenase is a signaling protein in long-term tolerance by dendritic cells. *Nat. Immunol.* **12**, 870–8 (2011).
327. Mondanelli, G. *et al.* A relay pathway between arginine and tryptophan metabolism confers immunosuppressive properties on dendritic cells. *Immunity* **46**, 233–44 (2017).
328. Zhai, L. *et al.* Tumor cell IDO enhances immune suppression and decreases survival independent of tryptophan metabolism in glioblastoma. *Clin. Cancer Res.* **27**, 6514–28 (2021).
329. Moyer, B. J. *et al.* Indoleamine 2,3-dioxygenase 1 (IDO1) inhibitors activate the aryl hydrocarbon receptor. *Toxicol. Appl. Pharmacol.* **323**, 74–80 (2017).
330. Odunsi, K. *et al.* Metabolic adaptation of ovarian tumors in patients treated with an IDO1 inhibitor constrains antitumor immune responses. *Sci. Transl. Med.* **14**, eabg8402 (2022).
331. Jackson, J. J. *et al.* Potent GCN2 inhibitor capable of reversing MDSC-driven T cell suppression demonstrates in vivo efficacy as a single agent and in combination with anti-angiogenesis therapy. *J. Med. Chem.* **65**, 12895–924 (2022).
332. Triplett, T. A. *et al.* Reversal of indoleamine 2,3-dioxygenase-mediated cancer immune suppression by systemic kynurenine depletion with a therapeutic enzyme. *Nat. Biotechnol.* **36**, 758–64 (2018).
333. Kjeldsen, J. W. *et al.* A phase 1/2 trial of an immune-modulatory vaccine against IDO/PD-L1 in combination with nivolumab in metastatic melanoma. *Nat. Med.* **27**, 2212–23 (2021).
334. Chu, C. C. & Paul, W. E. Fig1, an interleukin 4-induced mouse B cell gene isolated by cDNA representational difference analysis. *Proc. Natl. Acad. Sci. U. S. A.* **94**, 2507–12 (1997).
335. Chavan, S. S. *et al.* Characterization of the human homolog of the IL-4 induced gene-1 (Fig1). *Biochim. Biophys. Acta* **1576**, 70–80 (2002).
336. Mason, J. M. *et al.* IL-4-induced gene-1 is a leukocyte L-amino acid oxidase with an unusual acidic pH preference and lysosomal localization. *J. Immunol.* **173**, 4561–7 (2004).
337. Boulland, M.-L. *et al.* Human IL4I1 is a secreted L-phenylalanine oxidase expressed by mature dendritic cells that inhibits T-lymphocyte proliferation. *Blood* **110**, 220–7 (2007).
338. Zeitler, L. *et al.* Anti-ferroptotic mechanism of IL4i1-mediated amino acid metabolism. *Elife* **10**, 1–22 (2021).
339. Wiemann, S., Kolb-Kokocinski, A. & Poustka, A. Alternative pre-mRNA processing regulates cell-type specific expression of the IL4I1 and NUP62 genes. *BMC Biol.* **3**, 16 (2005).

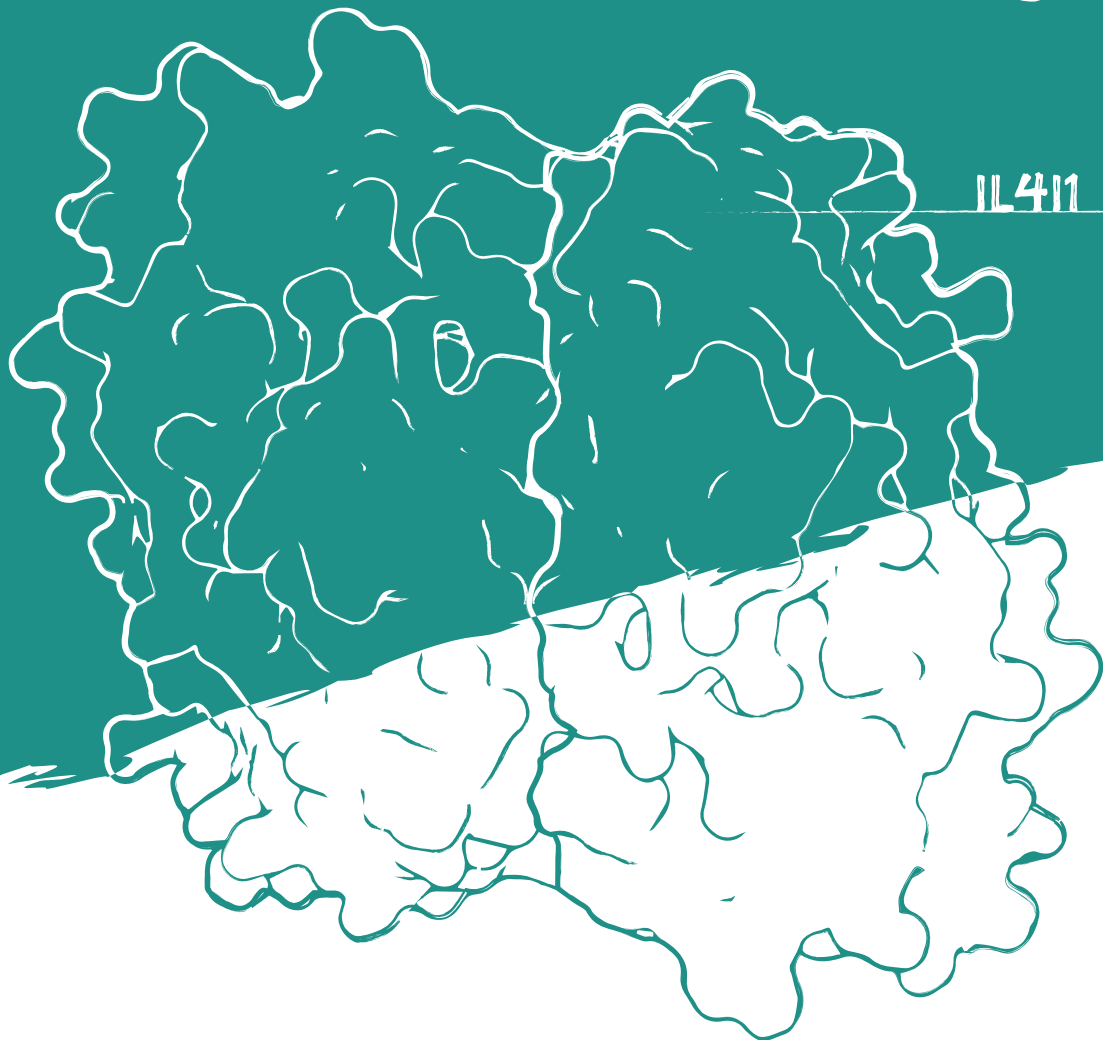
340. Copie-Bergman, C. *et al.* Interleukin 4-induced gene 1 is activated in primary mediastinal large B-cell lymphoma. *Blood* **101**, 2756–61 (2003).
341. Carbonnelle-Puscian, A. *et al.* The novel immunosuppressive enzyme IL4I1 is expressed by neoplastic cells of several B-cell lymphomas and by tumor-associated macrophages. *Leukemia* **23**, 952–60 (2009).
342. Marquet, J. *et al.* Dichotomy between factors inducing the immunosuppressive enzyme IL-4-induced gene 1 (IL4I1) in B lymphocytes and mononuclear phagocytes. *Eur. J. Immunol.* **40**, 2557–68 (2010).
343. Scarlata, C.-M., Celse, C., Pignon, P., Ayyoub, M. & Valmori, D. Differential expression of the immunosuppressive enzyme IL4I1 in human induced Aiolos⁺, but not natural Helios⁺, FOXP3⁺ Treg cells. *Eur. J. Immunol.* **45**, 474–9 (2015).
344. Santarlasci, V. *et al.* Rarity of human T helper 17 cells is due to retinoic acid orphan receptor-dependent mechanisms that limit their expansion. *Immunity* **36**, 201–14 (2012).
345. Maggi, L. *et al.* Distinctive features of classic and nonclassic (Th17 derived) human Th1 cells. *Eur. J. Immunol.* **42**, 3180–8 (2012).
346. Gallina, G. *et al.* Tumors induce a subset of inflammatory monocytes with immunosuppressive activity on CD8⁺ T cells. *J. Clin. Invest.* **116**, 2777–90 (2006).
347. Schlecker, E. *et al.* Tumor-infiltrating monocytic myeloid-derived suppressor cells mediate CCR5-dependent recruitment of regulatory T cells favoring tumor growth. *J. Immunol.* **189**, 5602–11 (2012).
348. Mulder, K. *et al.* Cross-tissue single-cell landscape of human monocytes and macrophages in health and disease. *Immunity* **54**, 1883–900.e5 (2021).
349. Finak, G. *et al.* Stromal gene expression predicts clinical outcome in breast cancer. *Nat. Med.* **14**, 518–27 (2008).
350. Ramspott, J. P. *et al.* Emerging role of IL-4-induced gene 1 as a prognostic biomarker affecting the local T-cell response in human cutaneous melanoma. *J. Invest. Dermatol.* **138**, 2625–34 (2018).
351. Liu, M. *et al.* A cluster of metabolism-related genes predict prognosis and progression of clear cell renal cell carcinoma. *Sci. Rep.* **10**, 12949 (2020).
352. Xu, T. *et al.* Integrated analysis reveals the participation of IL4I1, ITGB7, and FUT7 in reshaping the TNBC immune microenvironment by targeting glycolysis. *Ann. Med.* **53**, 916–28 (2021).
353. Zhao, H. *et al.* Single-cell analysis revealed that IL4I1 promoted ovarian cancer progression. *J. Transl. Med.* **19**, 454 (2021).
354. Choueiry, F. *et al.* Integration of metabolomics and gene expression profiling elucidates IL4I1 as modulator of ibrutinib resistance in ABC-diffuse large B cell lymphoma. *Cancers (Basel)* **13**, 1–22 (2021).
355. Bod, L. *et al.* IL-4-induced gene 1: a negative immune checkpoint controlling B cell differentiation and activation. *J. Immunol.* **200**, 1027–38 (2018).
356. Kono, K. *et al.* Hydrogen peroxide secreted by tumor-derived macrophages down-modulates signal-transducing zeta molecules and inhibits tumor-specific T cell-and natural killer cell-mediated cytotoxicity. *Eur. J. Immunol.* **26**, 1308–13 (1996).
357. Schmielau, J. & Finn, O. J. Activated granulocytes and granulocyte-derived hydrogen peroxide are the underlying mechanism of suppression of T-cell function in advanced cancer patients. *Cancer Res.* **61**, 4756–60 (2001).
358. Malmberg, K. J. *et al.* Inhibition of activated/memory (CD45RO⁺) T cells by oxidative stress associated with block of NF- κ B activation. *J. Immunol.* **167**, 2595–601 (2001).
359. Takahashi, A. *et al.* Preferential cell death of CD8⁺ effector memory (CCR7⁻CD45RA⁻) T cells by hydrogen peroxide-induced oxidative stress. *J. Immunol.* **174**, 6080–7 (2005).

360. Mougiakakos, D., Johansson, C. C. & Kiessling, R. Naturally occurring regulatory T cells show reduced sensitivity toward oxidative stress-induced cell death. *Blood* **113**, 3542–5 (2009).
361. Cousin, C. *et al.* The immunosuppressive enzyme IL411 promotes FoxP3⁺ regulatory T lymphocyte differentiation. *Eur. J. Immunol.* **45**, 1772–82 (2015).
362. Castellano, F., Prevost-Blondel, A., Cohen, J. L. & Molinier-Frenkel, V. What role for AHR activation in IL411-mediated immunosuppression? *Oncoimmunology* **10**, 1924500 (2021).
363. Puiffe, M.-L. *et al.* IL411 accelerates the expansion of effector CD8⁺ T cells at the expense of memory precursors by increasing the threshold of T-cell activation. *Front. Immunol.* **11**, 600012 (2020).
364. Yue, Y. *et al.* IL411 is a novel regulator of M2 macrophage polarization that can inhibit T cell activation via L-tryptophan and arginine depletion and IL-10 production. *PLoS One* **10**, e0142979 (2015).
365. Zhang, X. *et al.* Endogenous indole pyruvate pathway for tryptophan metabolism mediated by IL411. *J. Agric. Food Chem.* **68**, 10678–84 (2020).
366. Heath-Pagliuso, S. *et al.* Activation of the Ah receptor by tryptophan and tryptophan metabolites. *Biochemistry* **37**, 11508–15 (1998).
367. Zelante, T. *et al.* Tryptophan catabolites from microbiota engage aryl hydrocarbon receptor and balance mucosal reactivity via interleukin-22. *Immunity* **39**, 372–85 (2013).
368. Vyhřádalová, B. *et al.* Gut microbial catabolites of tryptophan are ligands and agonists of the aryl hydrocarbon receptor: a detailed characterization. *Int. J. Mol. Sci.* **21**, 1–17 (2020).
369. Aubatin, A. *et al.* IL4-induced gene 1 is secreted at the immune synapse and modulates TCR activation independently of its enzymatic activity. *Eur. J. Immunol.* **48**, 106–19 (2018).
370. Rao, D. *et al.* Pan-cancer analysis combined with experimental validation revealed IL411 as an immunological and prognostic biomarker. *Int. Immunopharmacol.* **111**, 109091 (2022).
371. Lasoudris, F. *et al.* IL411: an inhibitor of the CD8⁺ antitumor T-cell response in vivo. *Eur. J. Immunol.* **41**, 1629–38 (2011).
372. Bod, L. *et al.* IL4-induced gene 1 promotes tumor growth by shaping the immune microenvironment in melanoma. *Oncoimmunology* **6**, e1278331 (2017).
373. Presset, M. *et al.* Identification of inhibitors of the immunosuppressive enzyme IL411. *Bioorg. Chem.* **94**, 103463 (2020).
374. Cash, B. D. *et al.* Il4i1 inhibitors and methods of use. WO/2021/226003 (2021).
375. Giambasu, G. M. *et al.* Il4i1 inhibitors and methods of use. Patent WO/2022/227015 (2022).
376. MacKinnon, A. L. *et al.* Interleukin 4 (IL4)-induced gene 1 inhibitors and methods of use thereof. Patent WO/2022/086892 (2022).
377. MacKinnon, A. *et al.* Anti-tumor activity of CB-668, a potent, selective and orally bioavailable small-molecule inhibitor of the immuno-suppressive enzyme interleukin 4 (IL-4)-induced gene 1 (IL411). *J. Immunother. Cancer* **8(Suppl 3)**, A705 (2020).

IDO1



IL411



Chapter 3

Amino acid-metabolizing enzymes in advanced high-grade serous ovarian cancer patients: value of ascites as biomarker source and role for IL4I1 and IDO1

Yvonne Grobben¹, Judith E. den Ouden², Cristina Aguado³, Anne M. van Altena², Aletta D. Kraneveld⁴ and Guido J. R. Zaman¹

¹ Oncolines B.V., Oss, The Netherlands

² Department of Obstetrics and Gynaecology, Radboud university medical centre, Nijmegen, The Netherlands

³ Laboratory of Oncology, Pangaea Oncology, Dexeus University Hospital, Barcelona, Spain

⁴ Division of Pharmacology, Utrecht Institute for Pharmaceutical Sciences, Faculty of Science, Utrecht University, Utrecht, The Netherlands

Cancers (2023) 15:893

Abstract

The molecular mechanisms contributing to immune suppression in ovarian cancer are not well understood, hampering the successful application of immunotherapy. Amino acid-metabolizing enzymes are known to contribute to the immune-hostile environment of various tumors through depletion of amino acids and production of immunosuppressive metabolites. We aimed to collectively evaluate the activity of these enzymes in high-grade serous ovarian cancer patients by performing targeted metabolomics on plasma and ascites samples. Whereas no indication was found for enhanced L-arginine or L-glutamine metabolism by immunosuppressive enzymes in ovarian cancer patients, metabolism of L-tryptophan by indoleamine 2,3-dioxygenase 1 (IDO1) was significantly elevated compared to healthy controls. Moreover, high levels of L-phenylalanine- and L-tyrosine-derived metabolites associated with interleukin 4 induced 1 (IL4I1) activity were found in ovarian cancer ascites samples. While L-tryptophan is a major substrate of both IDO1 and IL4I1, only its enhanced conversion into L-kynurenine by IDO1 could be detected, despite the observed activity of IL4I1 on its other substrates. In ascites of ovarian cancer patients, metabolite levels were higher compared to those in plasma, demonstrating the value of utilizing this fluid for biomarker identification. Finally, elevated metabolism of L-phenylalanine and L-tyrosine by IL4I1 correlated with disease stage, pointing towards a potential role for IL4I1 in ovarian cancer progression.

Introduction

Ovarian cancer is the fifth most lethal malignancy in women in the United States, and is the deadliest among cancers of the female reproductive system.¹ Patients with epithelial ovarian cancer, accounting for about 90% of all cases, are often diagnosed at advanced-stage disease due to the presentation of merely vague and nonspecific symptoms.² At these stages, the prognosis for patients is poor, culminating in a five-year survival rate below 50% for all stages combined.^{2,3}

For over the last two decades, the standard first-line treatment for advanced-stage epithelial ovarian cancer patients has been debulking surgery combined with platinum- and taxane-based combination chemotherapy. In more recent years, clinical trials focused on optimization of surgical and chemotherapy regimens, and Food and Drug Administration (FDA) approval of poly(ADP-ribose) polymerase (PARP) inhibitors and the antiangiogenic drug bevacizumab as frontline maintenance therapies have advanced patient treatment.⁴ Nonetheless, the prognosis for ovarian cancer patients remains grim, particularly due to the high rate of disease recurrence as a result of drug resistance.⁵

For several malignancies, the emergence of immune checkpoint inhibitors aimed at reactivating the anticancer immune response has prompted reshaping of treatment strategies.^{6,7} Unlike classic cytotoxic chemotherapies, which act directly on tumor cells by inducing cell killing, immune checkpoint inhibitors disrupt inhibitory signaling between tumor and immune cells. However, despite their prominent success in different cancer types, clinical trials evaluating immune checkpoint inhibitors have demonstrated limited efficacy in ovarian cancer patients.⁸ A low tumor mutational burden, associated with the production of fewer immunogenic neoantigens, and a highly immunosuppressive tumor microenvironment (TME) may underlie these clinical observations.⁹

Several amino acid-metabolizing enzymes have been implicated in the attenuation of antitumor immune responses (Figure 1), either through depletion of amino acids from the TME or the production of immunosuppressive metabolites. Expression of glutaminase 1 (GLS1) is frequently elevated in malignant cells as a result of their metabolic reprogramming,¹⁰ while arginase 1 (ARG1) is secreted from myeloid cells in patients with various cancer types.¹¹ GLS1 and ARG1 can deprive the TME of L-glutamine (Gln) and L-arginine (Arg), respectively, thereby restraining effector T-cell proliferation and functionality.^{10,11} Alternatively, aberrant metabolism of Arg by tumor or myeloid cell-expressed inducible nitric oxide synthase (iNOS) can yield high concentrations of the small molecule nitric oxide (NO), which has various immunosuppressive properties.¹²

Indoleamine 2,3-dioxygenase 1 (IDO1), expressed by both tumor and immune cells, is the most extensively studied amino acid-metabolizing enzyme relevant to cancer immunology. IDO1 exerts its immunosuppressive effects through local depletion of L-tryptophan (Trp) as well as generation of Trp metabolites that act as agonists of the aryl hydrocarbon receptor (AhR).¹³ The AhR plays a central role in inducing tolerogenic immune responses.¹⁴ Moreover, although considerably less studied, the frequently tumor or stromal cell-overexpressed tryptophan 2,3-dioxygenase (TDO) appears to act through similar mechanisms.^{15,16} Most recently, interleukin 4 induced 1 (IL4I1), secreted by professional antigen-presenting cells in various cancer types,¹⁷ was indicated as yet another enzyme capable of producing AhR agonists through metabolism of Trp.¹⁸ However, its immunosuppressive effects may also arise from the generation of hydrogen peroxide (H₂O₂) through metabolism of its other major substrates, L-phenylalanine (Phe) and L-tyrosine (Tyr).¹⁹

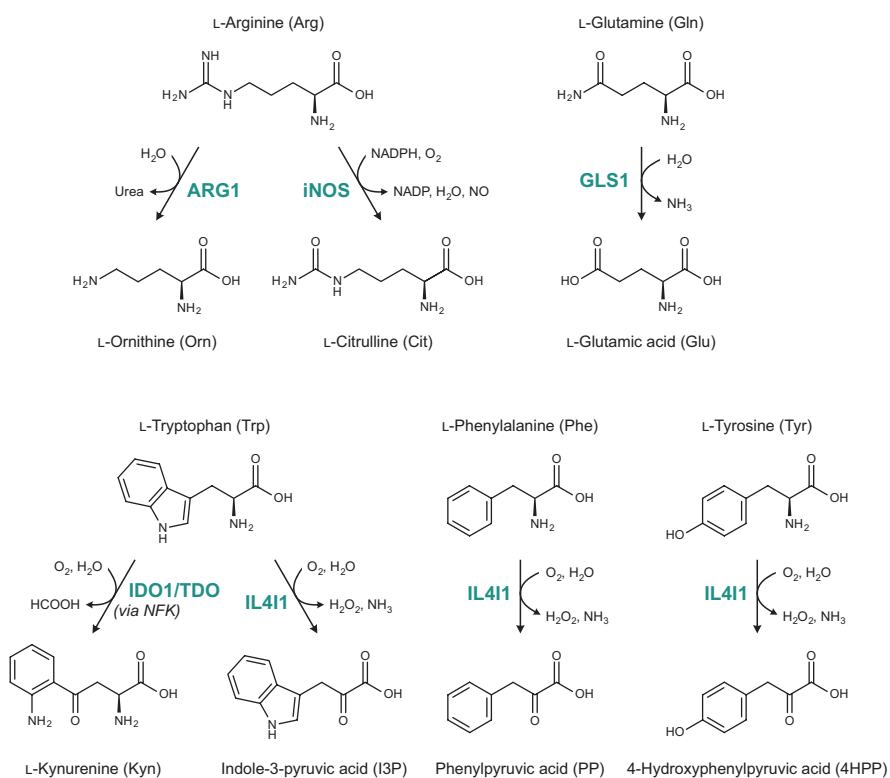


Figure 1. Overview of enzymatic reactions catalyzed by amino-acid metabolizing enzymes with known immunosuppressive properties in cancer. ARG1, arginase 1; GLS1, glutaminase 1; IDO1, indoleamine 2,3-dioxygenase 1; IL4I1, interleukin 4 induced 1; iNOS, inducible nitric oxide synthase; NFK, *N*-formyl-L-kynurenine; TDO, tryptophan 2,3-dioxygenase.

The enzymes described above have each been investigated as a potential drug target for cancer immunotherapy, mostly in combination with immune checkpoint blockade, but can also represent potential biomarkers for disease prognosis.^{10–13,18} Through use of immunohistochemical methods, enhanced expression of amino acid-metabolizing enzymes has been demonstrated in tumor tissue biopsies of various cancer types.^{16,17,20,21} In addition, enzymatic activity has been evaluated in plasma or serum specimens by direct measurement of secreted enzyme activity (in case of ARG1) or indirectly through analysis of amino acid and metabolite abundance.^{21–23} For ovarian cancer patients, the frequent presence of ascites (*i.e.*, fluid build-up in the peritoneal cavity) presents another source of potential biomarkers for diagnostic, prognostic or predictive purposes. Ascites can be obtained through a substantially less invasive procedure compared to tumor biopsy and may provide a stronger indication of tumor-related enzyme activity compared to plasma or serum due to its proximity to the tumor site. A similar opportunity is presented in other types of cancer by the presence of pleural effusion, cerebrospinal fluid or urine as alternative liquid biopsy sources.

In the current study, we aimed to collectively evaluate the presence and role of the different immunosuppressive amino acid-metabolizing enzymes in high-grade serous ovarian cancer, the most common epithelial ovarian cancer subtype.² To this end, the abundance of relevant amino acids and metabolites as indirect markers for enzymatic activity were determined in liquid biopsies by targeted metabolomics using liquid chromatography–tandem mass spectrometry (LC-MS/MS). Moreover, by comparison of plasma and ascites specimens of ovarian cancer patients, we sought to determine the potential benefit of using ascites as a source of biomarkers related to these enzymes. Finally, we aimed to determine whether our findings could be extended beyond high-grade serous ovarian cancer by analysis of pleural effusion samples from non-small cell lung cancer patients.

Results

Patient characteristics

Thirty-four patients diagnosed with advanced-stage (*i.e.*, International Federation of Gynecology and Obstetrics [FIGO] stage IIb–IV) high-grade serous ovarian cancer were included in the study (Table 1). The median age of the patients at the time of diagnosis was 62.5 years (interquartile range, IQR: 58–68 years). Two patients (5.9%) presented with stage II disease, 24 (70.6%) with stage III disease and eight (23.5%) with stage IV disease. Blood and ascites were collected at diagnosis from 24 and 32 patients, respectively, with 22 overlapping patients. Twenty-six patients (76.5%) completed treatment consisting of

surgery and chemotherapy, and were followed-up for periods of 10 to 35 months. Clinicopathological characteristics and details on the treatment of these patients are listed in Supplementary Table 1.

A control group was formed by healthy female blood donors with a closely matched age range (median: 60.5 years; IQR: 55–65) to minimize age-related differences in amino acid metabolism between the groups. Ascites from patients with benign disease could not be collected in sufficient quantities during the study to constitute a direct control group for the malignant ascites samples.

Stability of amino acids and metabolites in blood samples

Blood samples collected from ovarian cancer patients were processed into plasma the day after collection. Before processing, samples were stored at room temperature (RT) to allow for concurrent peripheral blood mononuclear cell (PBMC) collection (material not included in the present study). In contrast, blood from healthy donors and ascites from ovarian cancer patients were kept at 2–8 °C prior to processing.

Table 1. Clinicopathological characteristics of high-grade serous ovarian cancer patients and subgroups thereof.

	Subgroups based on collected samples*			
	All patients (n = 34)	Patients with plasma collected (n = 24)	Patients with ascites collected (n = 32)	Patients with both plasma and ascites collected (n = 22) †
<i>Age (years)</i>				
Median (IQR)	62.5 (58–68)	62.5 (56–69)	63 (59–69)	63 (58–70)
<i>BMI (kg/m²)</i>				
Median (IQR)	24 (22–27)	24 (22–27)	25 (22–28)	24 (22–27)
<i>FIGO stage</i>				
II	2 (5.9%)	1 (4.2%)	2 (6.3%)	1 (4.5%)
III	24 (70.6%)	16 (66.7%)	22 (68.8%)	14 (63.6%)
IV	8 (23.5%)	7 (29.2%)	8 (25.0%)	7 (31.8%)
<i>Primary treatment completed</i>				
Yes	26 (76.5%)	20 (83.3%)	24 (75.0%)	18 (81.8%)
No	8 (23.5%)	4 (16.7%)	8 (25.0%)	4 (18.2%)

BMI, body mass index; FIGO, International Federation of Gynecology and Obstetrics; IQR, interquartile range. Percentages may not total to 100% due to rounding. * Samples from remaining patients were missing for logistic reasons. † Also referred to as "overlapping patients".

To evaluate whether the plasma samples collected from the ovarian cancer patients could reliably be compared to the healthy donor plasma and patient ascites samples, the stability of amino acid and metabolite levels in whole blood samples stored at RT prior to plasma separation were evaluated by LC-MS/MS analysis. While the levels of most amino acids and metabolites remained stable over time, those of Arg, L-ornithine (Orn), L-glutamic acid (Glu), phenylpyruvic acid (PP) and 4-hydroxyphenylpyruvic acid (4HPP) were impacted by extended incubation at RT (Figure 2), a finding that was incorporated in the analysis of the patient samples as described below.

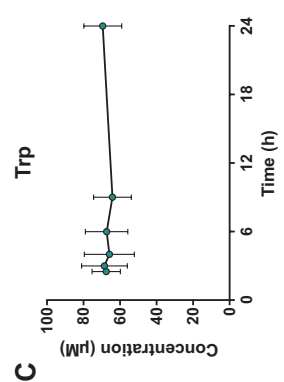
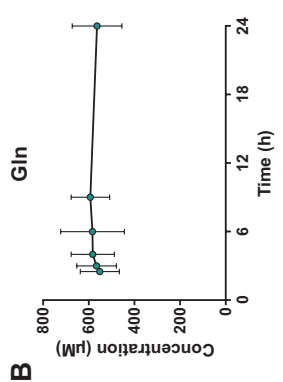
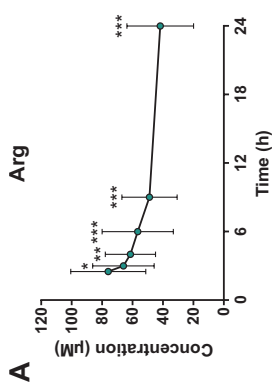
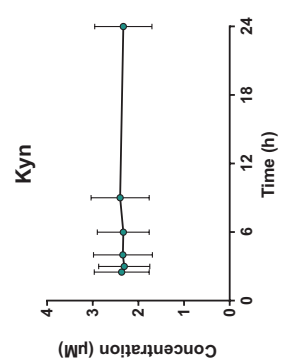
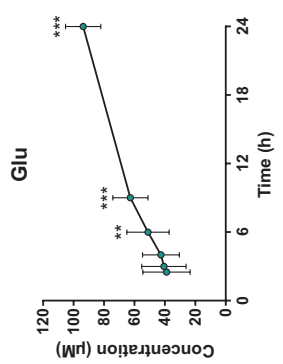
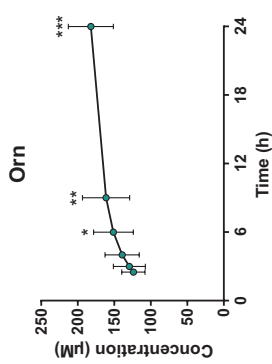
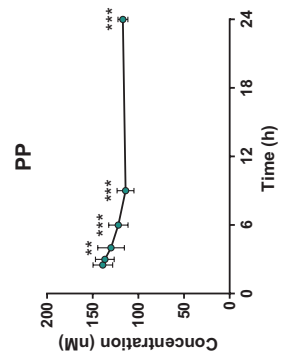
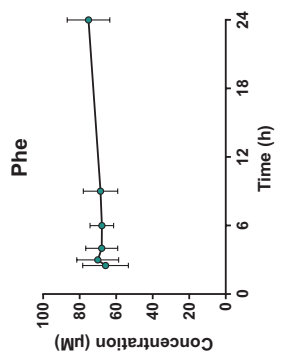
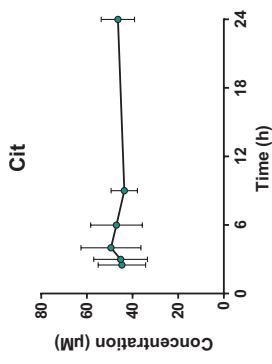
No indication for enhanced ARG1, iNOS or GLS1 activity in ovarian cancer patients

Evaluation of Arg and its metabolites Orn and L-citrulline (Cit) in whole blood kept at RT indicated a significant decrease in Arg and increase in Orn levels over time, whereas Cit levels remained stable (Figure 2A). Moreover, while Gln levels were unaffected by extended RT incubation, levels of its first metabolite Glu were significantly increased (Figure 2B). Comparison of Arg, Orn and Glu levels between healthy donors and ovarian cancer patients could therefore only be performed with their respective plasma and ascites samples, but not with plasma samples of the ovarian cancer patients (Figure 3). Although the composition of malignant ascites bears a certain degree of resemblance to that of plasma, these fluids are not identical²⁴ and direct comparison of plasma from healthy donors with ascites from ovarian cancer patients should therefore be considered with caution. Nonetheless, we believe that this comparison may still provide an initial indication of whether aberrant amino acid metabolism occurs in ovarian cancer patients.

Significantly higher Arg and lower Orn levels were found in the ascites of ovarian cancer patients compared to healthy donor plasma (Figure 3A). Moreover, Cit levels in both plasma and ascites of the patients were significantly lower than those in plasma of healthy donors (Figure 3A). Notably, these differences are opposite to those expected in the case of elevated ARG1 and/or iNOS activity in ovarian cancer. Furthermore, no significant difference in Gln or Glu levels was found between the patient samples and healthy donor plasma (Figure 3B). Overall, these observations do not provide an indication for enhanced ARG1, iNOS or GLS1 enzyme activity in high-grade serous ovarian cancer patients.

Elevated Trp metabolism is dominated by IDO1/TDO—rather than IL4I1—activity

Contrary to the poor stability of Arg, Orn and Glu levels in blood kept at RT (Figures 2A and 2B), Trp and its IDO1/TDO-catalyzed metabolite L-kynurenine (Kyn) showed remarkably stable levels over time (Figure 2C). Therefore, all three sample groups could be compared to evaluate IDO1/TDO-mediated Trp metabolism (Figure 4).



A

B

C

E

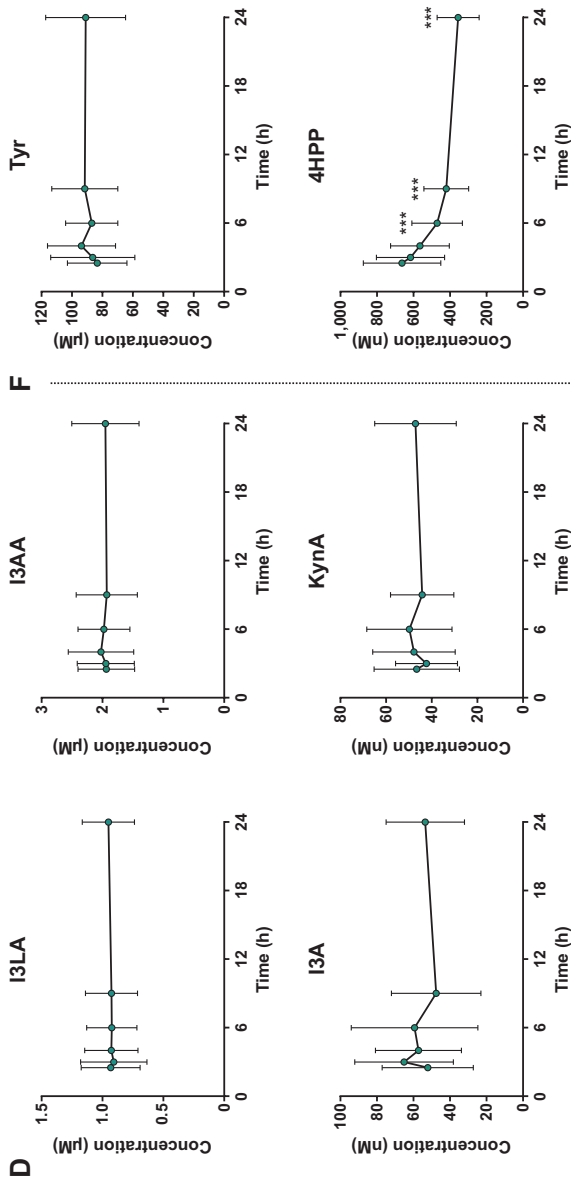


Figure 2. Stability of amino acid and metabolite levels in healthy donor blood stored at room temperature prior to plasma separation. Amino acids and metabolites related to metabolism of (A) Arg, (B) Gln, (C-D) Trp, (E) Phe and (F) Tyr. Amino acid and metabolite levels were determined by LC-MS/MS analysis and are expressed as mean \pm SD of six individual donors. I3LA, I3AA, I3A and KynA are downstream metabolites of the unstable indole-3-pyruvic acid (I3P). One-way repeated measures ANOVA showed an overall effect of time on Arg, Orn, Glu, PP and 4HPP levels (all $p < 0.001$). Significant results of Dunnett's multiple comparisons test with the first timepoint as reference group are indicated in the graphs. * $p \leq 0.05$; ** $p \leq 0.001$; *** $p \leq 0.001$. 4HPP, 4-hydroxyphenylpyruvic acid; Arg, L-arginine; Cit, L-citrulline; Gln, L-glutamine; Glu, L-glutamic acid; I3A, indole-3-aldehyde; I3AA, indole-3-acetic acid; I3LA, indole-3-lactic acid; Kyn, L-kynurenine; KynA, kynurenic acid; Orn, L-ornithine; Phe, L-phenylalanine; PP, phenylpyruvic acid; Trp, L-tryptophan; Tyr, L-tyrosine.

In the plasma of ovarian cancer patients, Trp levels were 2.2-fold decreased (based on geometric means) compared to those of healthy donors, although Kyn levels were not elevated accordingly (Figure 4A). Conversely, Kyn levels in the ovarian cancer ascites samples were on average 2.3- to 2.4-fold higher compared to those in the plasma samples, whereas Trp levels were still significantly lower than those in healthy donor plasma, but 1.4-fold higher compared to those in plasma of the patients (Figure 4A). Overall, significantly increased Kyn/Trp ratios were found in plasma of ovarian cancer patients compared to plasma of healthy donors (Figure 4B), and Kyn/Trp ratios in ovarian cancer ascites were even higher based on analysis of the paired samples (Figure 4C). Moreover, despite the distinct patterns of Trp and Kyn levels in the plasma and ascites samples of ovarian cancer patients (Figure 4A), a clear correlation was present between

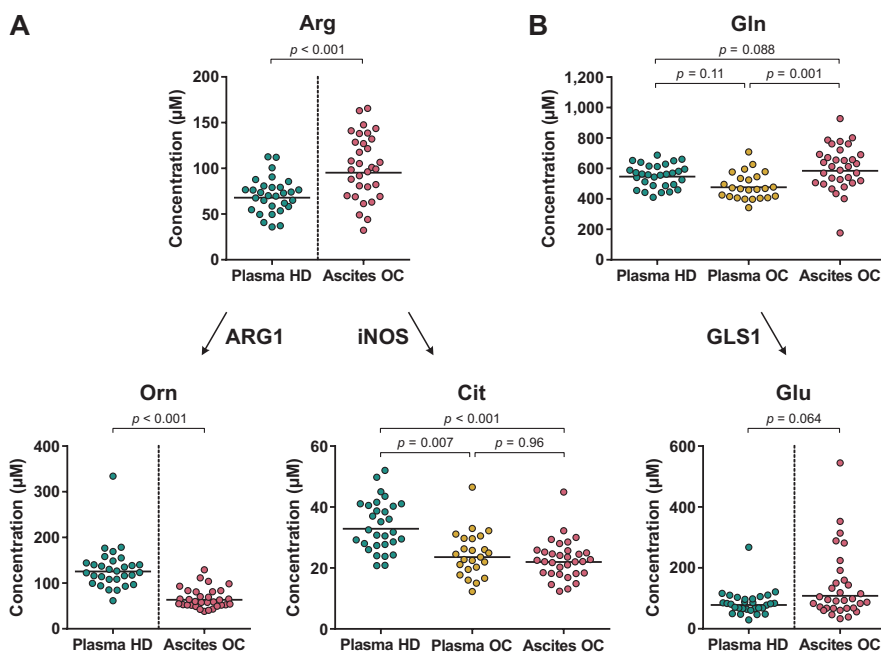


Figure 3. Arg and Gln metabolism in high-grade serous ovarian cancer patients and healthy donors. Amino acid and metabolite levels corresponding to (A) Arg and (B) Gln metabolism in plasma of healthy donors (HD) ($n = 30$) and plasma and ascites of ovarian cancer patients (OC) ($n = 24$ and 32 , respectively, with $n = 22$ overlapping patients). The enzyme names indicate the enzymatic activities that are indirectly studied. Horizontal lines indicate geometric means. Repeated unpaired, two-tailed Kruskal–Wallis tests yielded significant results for comparison of Cit ($p < 0.001$) and Gln levels ($p = 0.005$) between the groups. Results of Dunn’s *post hoc* tests and unpaired, two-tailed Mann–Whitney U tests are indicated in the graphs. Arg, L-arginine; ARG1, arginase 1; Cit, L-citrulline; Gln, L-glutamine; GLS1, glutaminase 1; Glu, L-glutamic acid; iNOS, inducible nitric oxide synthase; Orn, L-ornithine.

the Kyn/Trp ratios (Figure 4D). No significant correlations between Trp levels, Kyn levels or Kyn/Trp ratios and age, BMI, disease stage or progression-free survival (Supplementary Figures 1–3) were found, except for a significant correlation between plasma Trp and BMI (Supplementary Figure 1).

An alternative pathway of Trp metabolism, catalyzed by IL4I1, results in the formation of indole-3-pyruvic acid (I3P) (Figure 1). Inconveniently, we were not able to detect this metabolite by LC-MS/MS analysis, although this finding is in accordance with the

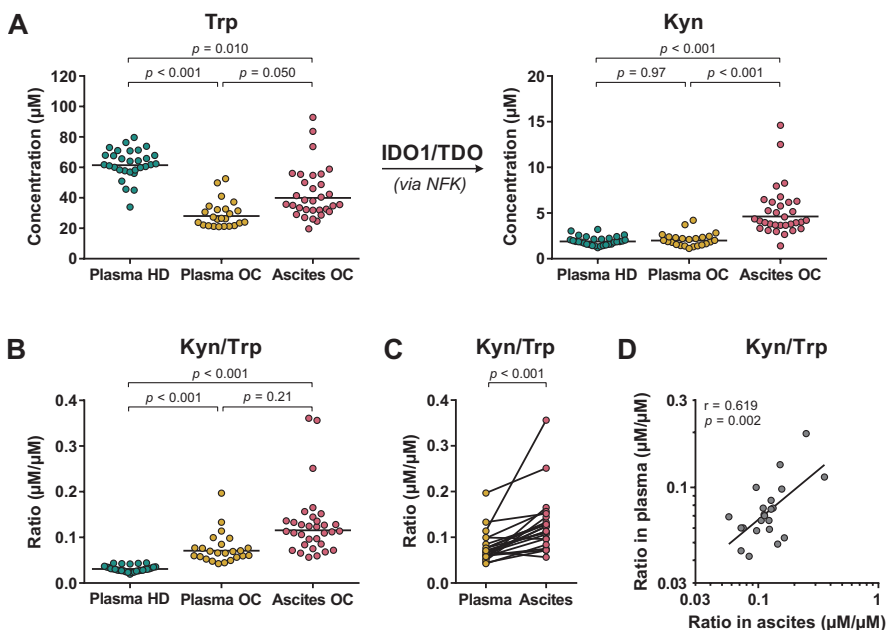


Figure 4. Trp metabolism towards Kyn formation in high-grade serous ovarian cancer patients and healthy donors. **(A)** Trp and Kyn levels and **(B)** Kyn/Trp ratios as indirect measures of IDO1/TDO enzymatic activity in plasma of healthy donors (HD) ($n = 30$) and plasma and ascites of ovarian cancer patients (OC) ($n = 24$ and 32 , respectively, with $n = 22$ overlapping patients). Horizontal lines indicate geometric means. Repeated unpaired, two-tailed Kruskal–Wallis tests yielded significant results for comparison of Trp levels, Kyn levels and Kyn/Trp ratios between the groups ($p < 0.001$ for all). Results of Dunn’s *post hoc* test are indicated in the graphs. **(C)** Comparison and **(D)** correlation of Kyn/Trp ratios in paired plasma and ascites samples of ovarian cancer patients ($n = 22$). Results of a paired, two-tailed Student’s *t*-test and Pearson’s correlation analysis, both performed with log-transformed concentrations, are indicated in the graphs. IDO1, indoleamine 2,3-dioxygenase 1; Kyn, L-kynurenine; NFK, *N*-formyl-L-kynurenine; r , Pearson’s correlation coefficient; TDO, tryptophan 2,3-dioxygenase; Trp, L-tryptophan.

previously reported instability of I3P.^{18,25,26} As an alternative approach to evaluate IL4I1-mediated Trp metabolism, further downstream metabolites of Trp were considered as surrogate markers for I3P formation. Sadik and coworkers reported increased levels of indole-3-lactic acid (I3LA), indole-3-acetic acid (I3AA), indole-3-aldehyde (I3A) and kynurenic acid (KynA) in IL4I1-overexpressing cells compared to control cells.¹⁸ All four of these downstream metabolites remained stable in blood stored at RT prior to plasma separation (Figure 2D) and were therefore evaluated in the healthy donor and ovarian cancer patient samples (Figure 5).

No significant differences in I3LA and KynA levels were found among the three sample groups (Figure 5). Moreover, while significant differences in I3AA and I3A levels were apparent, the levels of these metabolites were lower, rather than higher, in the ovarian cancer patient samples compared to healthy donor plasma (Figure 5). These results argue against an elevated metabolism of Trp by IL4I1 in high-grade serous ovarian cancer patients, and point towards IDO1/TDO as the dominant source of enhanced Trp metabolism.

Enhanced IL4I1-mediated Phe and Tyr metabolism correlates with disease stage

Although Trp metabolism by IL4I1 does not appear enhanced in high-grade serous ovarian cancer patients, this does not exclude an elevated metabolism of other substrates by IL4I1. Two other major substrates of IL4I1 are Phe and Tyr,^{19,27,28} which are converted into PP and 4HPP, respectively (Figure 1). In contrast to I3P, both of these metabolites could be detected by LC-MS/MS analysis, although their levels could not reliably be determined in the ovarian cancer plasma samples due to their instability in blood upon extended incubation at RT (Figures 2E and 2F).

PP and 4HPP levels in ovarian cancer ascites samples were 3.1- and 2.3-fold higher, respectively, compared to those in healthy donor plasma (based on geometric means), whereas Phe levels were only modestly higher and Tyr levels did not significantly differ between these groups (Figures 6A and 6B). Moreover, individual patients showed even up to 50- (PP) or 30-fold (4HPP) higher levels than the geometric mean of the healthy donor plasma samples (Figures 6A and 6B). These findings provide an indication that Phe and Tyr metabolism by IL4I1 may be enhanced in the ovarian cancer patients.

Although the levels of PP and 4HPP in the ovarian cancer plasma samples were affected by the sample processing conditions, a rough estimate of the originally present levels can still be made. Based on the estimated reductions in PP and 4HPP levels of 36% and 62%, respectively, after 24 h of incubation at RT (Supplementary Figure 4), it can be deduced that the true levels in the ovarian cancer plasma samples would likely have been considerably

lower than those found in the ascites samples (Figures 6A and 6B). Moreover, the PP and 4HPP levels in these plasma samples do not appear to be elevated compared to those in healthy donor plasma (Figures 6A and 6B), thus resembling the pattern observed for levels of the Trp-derived metabolite Kyn (Figure 4A).

PP and 4HPP levels in the ascites samples were strongly correlated to each other (Figure 6C), suggesting that they are generated by the same enzyme (*i.e.*, IL4I1), rather

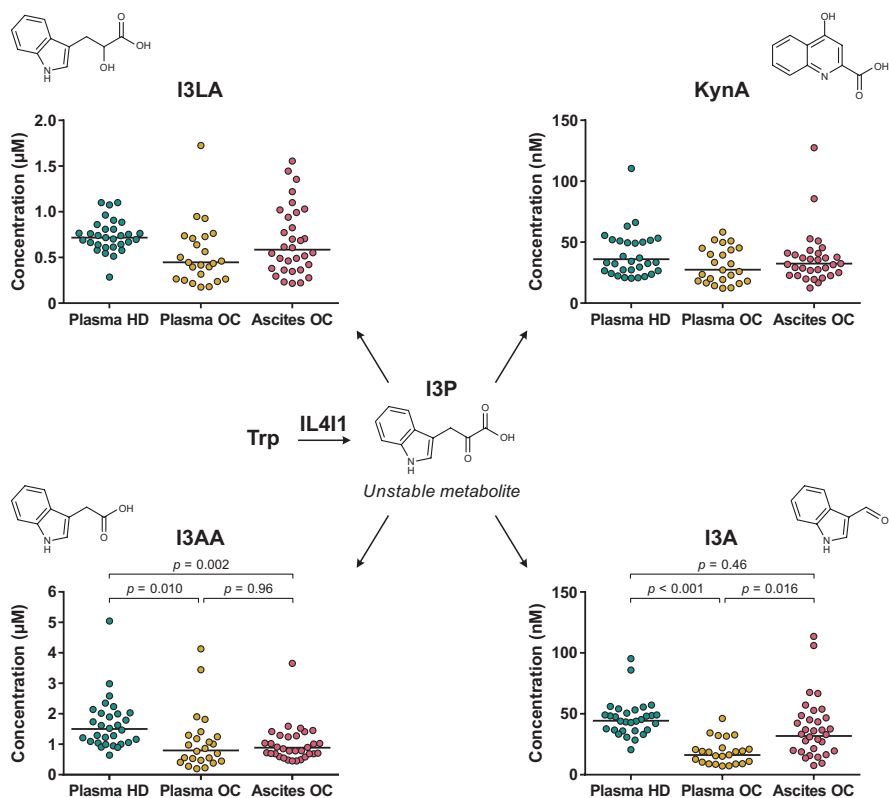
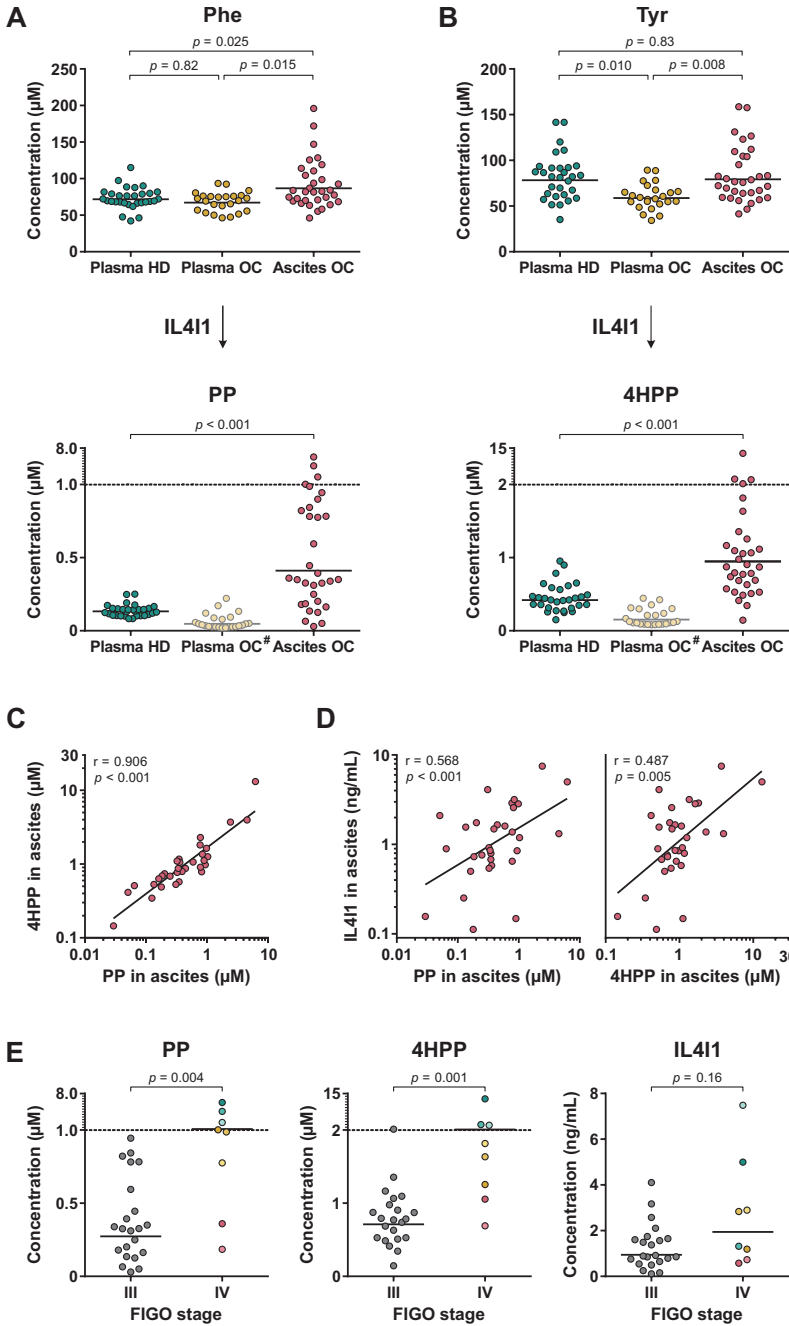


Figure 5. Trp metabolism towards I3P formation in high-grade serous ovarian cancer patients and healthy donors. Levels of Trp downstream metabolites are shown as surrogate measures of Trp-metabolizing IL4I1 activity in plasma of healthy donors (HD) ($n = 30$) and plasma and ascites of ovarian cancer patients (OC) ($n = 24$ and 32 , respectively, with $n = 22$ overlapping patients). Horizontal lines indicate geometric means. Repeated unpaired, two-tailed Kruskal–Wallis tests yielded significant results for comparison of I3AA ($p = 0.002$) and I3A ($p < 0.001$)—but not I3LA and KynA—levels between the groups. Results of Dunn's *post hoc* tests are indicated in the graphs where applicable. I3A, indole-3-aldehyde; I3AA, indole-3-acetic acid; I3LA, indole-3-lactic acid; I3P, indole-3-pyruvic acid; IL4I1, interleukin 4 induced 1; KynA, kynurenic acid; Trp, L-tryptophan.



(Legend on next page)

than a combination of other enzymes capable of producing these metabolites. Since IL411 is a secreted enzyme, in contrast to IDO1 and TDO, its abundance could also directly be evaluated in the plasma and ascites samples. IL411 levels were detectable in an enzyme-linked immunosorbent assay (ELISA) in all ascites samples, and its expression was significantly correlated to both PP and 4HPP levels (Figure 6D). In contrast, the enzyme could not be detected in the majority of the plasma samples (*i.e.*, within the detection range of the ELISA) (Supplementary Table 2 and 3), which is in accordance with the lower PP and 4HPP levels measured in plasma compared to ascites samples (Figures 6A and 6B).

Next, we tested if the PP and 4HPP levels in ovarian cancer ascites samples correlated with clinical parameters of the patients. No significant correlations were found with age, BMI or progression-free survival (Supplementary Figures 5 and 6). However, both PP and 4HPP levels were significantly increased in patients with stage IV compared to stage III disease (Figure 6E). Moreover, while the difference in IL411 levels among the two disease stages was not found to be statistically significant, most stage IV patients with elevated PP and 4HPP levels also showed elevated IL411 levels (Figure 6E). These results indicate a potential role for IL411 in the progression of high-grade serous ovarian cancer through metabolism of Phe and Tyr, despite the apparent absence of elevated Trp metabolism by IL411.

(Figure on previous page)

Figure 6. Phe and Tyr metabolism in high-grade serous ovarian cancer patients and healthy donors. Amino acid and metabolite levels corresponding to (A) Phe and (B) Tyr metabolism as indirect measures of IL411 enzymatic activity in plasma of healthy donors (HD) ($n = 30$) and plasma and ascites of ovarian cancer patients (OC) ($n = 24$ and 32 , respectively, with $n = 22$ overlapping patients). Levels of Phe, Tyr, PP and 4HPP were determined by LC-MS/MS analysis. Horizontal lines indicate geometric means. Repeated unpaired, two-tailed Kruskal–Wallis tests yielded significant results for comparison of Phe ($p = 0.025$) and Tyr levels ($p = 0.011$) between the groups. Results of Dunn's *post hoc* tests are indicated in the graphs. For comparison of PP and 4HPP levels between the two groups, results of the Mann–Whitney U test are indicated in the graphs. (C,D) Correlation between PP, 4HPP and IL411 levels in ascites of ovarian cancer patients ($n = 32$). Results of Pearson's correlation analyses are indicated in the graphs. Levels of IL411 were determined by ELISA. (E) PP, 4HPP and IL411 levels in ascites of patients with stage III ($n = 22$) and stage IV disease ($n = 8$). Samples of patients with stage IV disease are colored individually to allow for comparison between the graphs. Results of unpaired, two-tailed Mann–Whitney U tests are indicated in the graphs. #, levels of PP and 4HPP in plasma of healthy donors are influenced by sample processing conditions and should therefore not directly be compared to those of the other sample groups; 4HPP, 4-hydroxyphenylpyruvic acid; FIGO, International Federation of Gynecology and Obstetrics; IL411, interleukin 4 induced 1; Phe, L-phenylalanine; PP, phenylpyruvic acid; r, Pearson's correlation rank coefficient; Tyr, L-tyrosine.

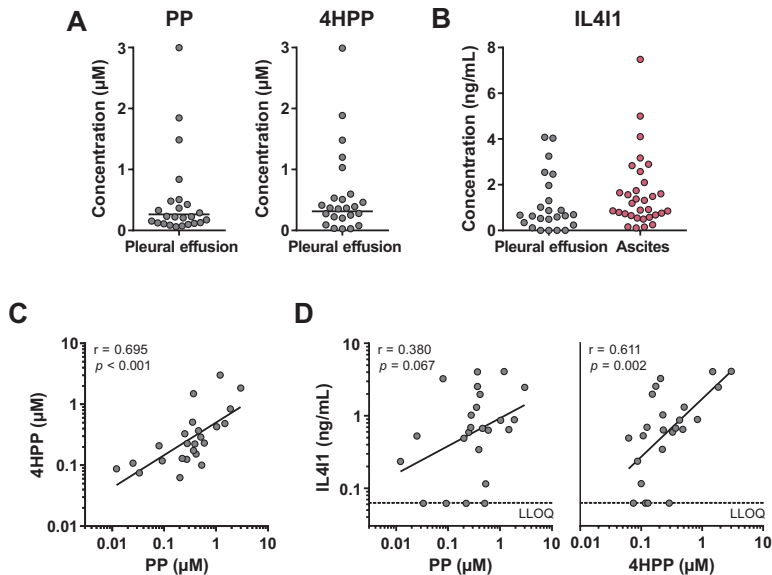


Figure 7. PP, 4HPP and IL4I1 levels in pleural effusion samples of patients with stage IV non-small cell lung cancer. **(A)** PP and 4HPP levels in pleural effusion samples ($n = 24$). Horizontal lines indicate geometric means. **(B)** IL4I1 levels in pleural effusion of non-small cell lung cancer patients ($n = 24$) and ascites of high-grade serous ovarian cancer patients ($n = 32$). IL4I1 levels in four pleural effusion samples were below the lower limit of quantification (LLOQ). Geometric means are therefore not displayed. **(C,D)** Correlation between PP, 4HPP and IL4I1 levels in pleural effusion samples. Dashed lines indicate the LLOQ. Samples with an IL4I1 level below the LLOQ are shown at the LLOQ value. Results of Pearson's correlation analyses are indicated in the graphs. 4HPP, 4-hydroxyphenylpyruvic acid; IL4I1, interleukin 4 induced 1; PP, phenylpyruvic acid; r , Pearson's correlation rank coefficient.

Enhanced Phe and Tyr metabolism by IL4I1 in pleural effusions of lung cancer patients

To evaluate whether elevated metabolism of Phe and Tyr by IL4I1 is limited to ovarian cancer ascites, we analyzed pleural effusions from non-small cell lung cancer patients (Figure 7), which accumulate by similar mechanisms as ascites.²⁹

Pleural effusions were collected from 24 patients with advanced-stage (*i.e.*, American Joint Committee on Cancer [AJCC] stage IV) non-small cell lung cancer. Similar to the ovarian cancer blood samples, pleural effusion samples were stored at RT prior to processing to allow for concurrent collection of tumor cells (material not included in the present study). Overall, lower PP and 4HPP levels were detected in the pleural effusion (Figure 7A) compared to the ascites samples (Figures 6A and 6B), despite the relatively similar IL4I1 levels (Figure 7B). As discussed for blood samples on page 65, this is likely a direct

consequence of the sample storage conditions. However, a subgroup of pleural effusion samples showed considerably higher PP and 4HPP levels (Figure 7A), indicating elevated metabolism in these patients. Similar to the ascites samples, PP and 4HPP levels in the pleural effusion samples were strongly correlated with each other (Figure 7C), while 4HPP levels also significantly correlated with the levels of IL4I1 (Figure 7D). These results demonstrate that elevated metabolism of Phe and Tyr by IL4I1 is not limited to ovarian cancer ascites, although the frequency among patients may differ depending on the type of cancer.

Discussion

Despite recent advances in the treatment of ovarian cancer patients,⁴ the potential clinical benefit of immunotherapy remains untapped due to the incomplete understanding of molecular mechanisms underlying immune suppression in ovarian cancer, including amino acid metabolism. We sought to investigate the role of amino acid-metabolizing enzymes in high-grade serous ovarian cancer by interrogating the abundance of relevant amino acids and metabolites in patient-derived liquid biopsies, including ascites as a promising source for biomarker identification. Our findings demonstrate enhanced amino acid metabolism by IDO1/TDO and IL4I1 in high-grade serous ovarian cancer patients, with markedly elevated metabolite levels in patient ascites samples compared to patient and healthy donor plasma. Notably, the prevailing metabolic profile of ovarian cancer patients was characterized by an apparent lack of elevated IL4I1 activity on Trp, the common substrate of IDO1, TDO and IL4I1. Nonetheless, elevated metabolism of Phe and Tyr by IL4I1 strongly correlated with disease stage, suggesting a potential role for IL4I1 in ovarian cancer progression.

For many years, IDO1 was viewed as one of the most promising targets for battling cancer through reactivation of the anticancer immune response. For this reason, IDO1 expression and activity has been evaluated in countless human cancer types,²⁰ including ovarian cancer.³⁰⁻³⁵ In contrast, a potential role for TDO in tumor immune escape is significantly less studied, particularly in cancers of the ovary.^{36,37} In close agreement with previous findings,³³⁻³⁵ we report a two-fold increase in the Kyn/Trp ratio in ovarian cancer plasma compared to plasma of healthy donors, attributable to significantly decreased Trp levels. Moreover, we demonstrate for the first time that the Kyn/Trp ratio is even higher in the ascites of ovarian cancer patients, owing to concurrently lower Trp and higher Kyn levels. Despite unaltered plasma Kyn levels in ovarian cancer patients, the clear correlation between Kyn/Trp ratios in the plasma and ascites samples suggests that IDO1 and/or TDO activity is responsible for the metabolic changes in both fluids. Although these two enzymatic activities cannot be discriminated based on metabolomic analysis, the stronger mRNA expression of IDO1 compared to that of TDO in serous ovarian cancer tissues,¹⁸

and its considerably higher affinity and turnover rate for Trp,³⁸ strongly point towards IDO1 as the major contributor. In the remainder of this article, we will hence specifically refer to IDO1 when discussing the elevated metabolism of Trp found in the high-grade serous ovarian cancer patients.

Unfortunately, inhibition of IDO1 as an anticancer strategy failed in a phase III clinical trial,³⁹ significantly dampening the interest in IDO1 as a therapeutic target. The cause of these unsatisfactory results has been extensively debated in the literature, with possible explanations including suboptimal drug dosage, a lack of patient selection or stratification on the basis of IDO1 expression, and a compensatory role for TDO in the absence of IDO1 activity.^{40,41} Recently, Sadik and coworkers proposed that IL4I1 expression may also underlie the resistance of patients against IDO1 inhibition, with activation of the AhR presented as their common mechanism of immune response blockade and promotion of tumor cell malignancy.¹⁸ IL4I1 shows enhanced expression in a wide variety of tumor types,^{17,18} and its Trp-metabolizing activity yields various downstream metabolites which are associated with AhR agonism, including I3LA, I3AA, I3A and KynA.^{18,42–44} At baseline disease, we found that the activity of IDO1 was increased in ovarian cancer patients compared to healthy controls, whereas elevated activity of IL4I1 was also found in ovarian cancer ascites samples. However, only IDO1 appeared to metabolize their common substrate, since levels of Trp downstream metabolites attributable to IL4I1 activity were not increased. Although it cannot be excluded that this observation may be related to the further metabolism of the Trp downstream metabolites, it also may reasonably be explained by an inability of IL4I1 to compete with IDO1 for their common substrate, as IL4I1 has a considerably lower affinity for Trp.^{38,45} In contrast, IL4I1 may not experience significant competition from Phe- and Tyr-metabolizing enzymes, allowing efficient IL4I1-mediated conversion of these substrates. Upon inhibition of IDO1 in cancer patients, the amount of Trp available as a substrate for IL4I1 would likely be replenished. Since active IL4I1 is sufficiently expressed in ovarian cancer patients to modulate ascitic PP and 4HPP levels, this would likely allow the enhanced production of Trp-derived AhR agonists by IL4I1. In turn, this can result in maintenance of the immunosuppressive environment initiated by IDO1. The elevated activity of both IDO1 and IL4I1 found in ovarian cancer patients therefore supports the hypothesis of IL4I1 as a potential resistance mechanism against IDO1 inhibition.

Based on the elevated levels of PP and 4HPP found in the ascites of patients with stage IV compared to stage III disease, our data additionally indicate a correlation between IL4I1 activity and ovarian cancer progression. Similarly, IL4I1 mRNA expression is higher in patients with metastatic melanoma compared to those with primary melanoma.¹⁹ *In vitro*, IL4I1 has been shown to promote the proliferation, migration and invasion of various tumor cell types,^{18,46} including ovarian cancer cells.⁴⁷ IL4I1 therefore presents a potential

therapeutic target for ovarian cancer, while its expression, activity or metabolite levels may also serve as a biomarker for disease progression. Notably, metabolite levels associated with IDO1 and IL4I1 activity were elevated in ovarian cancer ascites compared to plasma samples. This indicates that ascites can be a valuable alternative to plasma for biomarker detection, which is in line with other studies investigating different types of biomarkers in this fluid.^{48,49} The elevated metabolite levels in ascites may arise from the proximity of this fluid to the tumor as well as the presence of tumor and immune cells, likely expressing IDO1 and/or IL4I1, in the ascites itself. Alternatively, the further metabolism of these metabolites, or their transport towards tissues capable of this, may be less efficient in ascites compared to plasma. Metabolomic profiling of epithelial ovarian tumor biopsies has additionally demonstrated elevated levels of the same metabolites (*i.e.*, Kyn, PP and 4HPP) when compared to normal ovary biopsies.⁵⁰ This indicates that ascites can also present a feasible, minimally invasive alternative to tumor biopsies for metabolomic analysis.

In addition to IDO1 and IL4I1, enhanced ARG1 expression has previously been reported in the context of human ovarian cancer.^{21,51,52} In contrast, while iNOS and GLS1 overexpression has been demonstrated in various human cancer types,^{10,53} reports in ovarian cancer are sparse.^{54,55} This is in line with the present findings that do not indicate elevated metabolism by iNOS or GLS1 in ovarian cancer patients. Moreover, in contrast to the reported ARG1 expression in ovarian cancer, indications for increased ARG1 activity were not found either. Instead, our findings of decreased Orn and Cit levels in the ovarian cancer patients correlate with other studies showing decreased levels of these metabolites in patient plasma or serum samples.^{56,57} Together with the elevated Arg levels, these changes may signify enhanced Arg synthesis rather than metabolism, since Arg is (in)directly synthesized from Orn and Cit. Argininosuccinate synthase (ASS) and lyase (ASL) are responsible for Arg synthesis, and accordingly, increased ASS mRNA and protein expression has been found in epithelial ovarian tumors,^{58,59} while ASL overexpression has been reported in other cancer types.^{60,61}

The current study provides indications for a role of IL4I1 in high-grade serous ovarian cancer, although these findings should be validated in a larger patient cohort. A larger study could also identify correlations with patient outcome, which may have been missed in this study due to the limited number of patients that could be evaluated for (progression-free) survival and the relatively short follow-up time. Inclusion of patients with other types of ovarian cancer would additionally indicate the applicability of our findings to other ovarian cancer subtypes. Moreover, inclusion of patients with benign disease would further support the malignant nature of the elevated IL4I1 metabolism, while a direct comparison between metabolite levels in ascites and tumor biopsies from the same patients could substantiate the use of ascites over biopsies for biomarker

evaluation. Finally, a lesson to be learned from this study is the importance of considering the stability of amino acid and metabolite levels in blood and other liquid biopsies during sample work-up and interpretation of results. When it is desired to use both plasma and PBMCs for experiments, blood is to be kept at RT prior to processing due to detrimental effects of refrigeration on PBMC recovery and viability.⁶² Similarly, ascites and pleural effusion may require storage at RT for efficient isolation of viable tumor cells. However, extended storage at RT can be problematic for accurate metabolomics, as demonstrated here, in accordance with and in addition to previous reports.^{63,64} These results underline the importance of efficient work-up of liquid biopsy samples and consideration of the potential effects of any delays or sub-optimal storage temperatures.

Conclusions

Our data suggest a role for both IDO1 and IL4I1 in high-grade serous ovarian cancer and indicate that IL4I1 may be involved in progression of the disease through metabolism of Phe and Tyr. The levels of metabolites produced by these enzymes were highest in ascites samples, revealing this fluid as a useful liquid biopsy source for biomarker detection. Further exploration of the implications of enhanced IL4I1 activity is warranted to pave the way for successful immunotherapeutic treatment of ovarian cancer patients.

Materials and methods

Chemicals and reagents

All analytes and isotope-labelled internal standards for LC-MS/MS analysis were obtained from commercial vendors as listed in Supplementary Table 4. UPLC-grade acetonitrile and methanol were purchased from VWR.

Patient and healthy control samples

Blood and ascites were collected from patients with a primary diagnosis of advanced-stage (*i.e.*, FIGO stage IIb–IV) high-grade serous ovarian cancer at Radboud university medical center in Nijmegen, Canisius Wilhelmina Hospital in Nijmegen, Catharina Hospital in Eindhoven and Rijnstate Hospital in Arnhem (The Netherlands). Eligible patients were above eighteen years of age, presented with sufficient ascites for collection, had no previous or concurrent malignant disease, and were chemotherapy naïve. Patients who did not complete primary treatment were excluded from survival analysis. Pleural effusions were collected from patients with a primary diagnosis of advanced-stage (*i.e.*, AJCC stage IV) non-small cell lung cancer at Dexeus University Hospital and Teknon

Medical Center in Barcelona (Spain). Collection of the samples and the research described was conducted with approval of the medical ethical committees of the corresponding hospitals and informed written consent from each subject.

Blood from patients with high-grade serous ovarian cancer was collected in BD Vacutainer Lithium Heparin tubes (BD, cat. no. 367526) and was stored at RT prior to processing. The day after collection, the blood was centrifuged for 10 min at 1,500 rpm and the resultant plasma was stored at -80°C or below. Ascites collected from the patients was stored at $2-8^{\circ}\text{C}$ until processing. The day after collection, the ascites was filtered through a $100\ \mu\text{m}$ cell strainer and centrifuged for 10–15 min at 1,500 rpm. The supernatant was stored at -80°C . Pleural effusion from patients with non-small cell lung cancer was centrifuged for 10 min at 2,300 rpm and the supernatant was stored at -20°C .

Lithium heparin plasma samples from healthy donors were obtained from TCS Biosciences (Buckingham, UK). Blood from these donors was stored at $2-8^{\circ}\text{C}$ prior to processing within 24 h of collection. The age distribution of the healthy donors was matched as closely as possible to those of the ovarian cancer patients, but no exact match could be obtained due to the limited availability of donors with ages above 60 years.

Healthy donor blood samples for evaluation of the stability of amino acid and metabolite levels in whole blood were obtained from Sanquin (Nijmegen, The Netherlands) in BD Vacutainer Lithium Heparin tubes. Blood was aliquoted upon arrival from the provider. At different time points, plasma was separated and stored as described above.

Standard and sample preparation for LC-MS/MS analysis

All analytes and internal standards were dissolved at 10 or 50 mM concentration in MilliQ water (MQ), with one or two equivalents of HCl or NaOH if required for solubility, or 100% DMSO and stored at -80°C . For each LC-MS/MS experiment, eight calibration standards, four quality control samples and an internal standard mixture were prepared by dilution in MQ.

For hydrophilic interaction liquid chromatography (HILIC)-MS/MS analysis, $5\ \mu\text{L}$ plasma, ascites, pleural effusion or 5% BSA in PBS was diluted with $50\ \mu\text{L}$ standard solution, quality control solution or MQ in a 2 mL 96-well Masterblock® plate (Greiner Bio-One, cat. no. 780270). All samples were spiked with $45\ \mu\text{L}$ internal standard mixture and agitated at 1,500 rpm for 1 min. Extraction was performed with $400\ \mu\text{L}$ acetonitrile and agitation at 1,400 rpm for 1 min. The samples were centrifuged for 30 min at 4,000 rpm at 4°C and $300\ \mu\text{L}$ supernatant was transferred to a 2 mL TrueTaper® 96-well collection plate (Screening Devices, cat. no. 968820) using a Hamilton Microlab STARlet liquid handler (Hamilton).

For reversed-phase liquid chromatography (RPLC)-MS/MS analyses, a surrogate matrix was prepared by incubating pooled healthy donor plasma with 60 mg activated charcoal per mL plasma for two hours, followed by centrifugation at 14,000 rpm for 10 min, according to the previous literature.⁶⁵ In a 2 mL 96-well Masterblock® plate, 30 µL plasma, ascites, pleural effusion or surrogate matrix was diluted with 10 µL standard solution, quality control solution or MQ. All samples were spiked with 10 µL internal standard mixture and agitated at 1,650 rpm for 1 min. Extraction was performed with 325 µL acetonitrile and agitation at 1,200 rpm for 1 min. The samples were centrifuged for 60 min at 4,000 rpm at 4 °C and 300 µL supernatant was transferred to a 1 mL TrueTaper® 96-well plate (Screening Devices, cat. no. 968810). The samples were evaporated for 42 min under a 50 °C nitrogen stream at 7 psi pressure using an Ultravap (Porvair Sciences) with straight needle head and were subsequently dissolved in 60 µL 0.1% acetic acid in MQ. The samples were centrifuged for 60 min at 4,000 rpm at 4 °C to precipitate undissolved components and 50 µL supernatant was transferred to a 2 mL TrueTaper® 96-well collection plate. Plates were covered with a pre-slit silicone mat (Screening Devices, cat. no. 964085) and kept in the autosampler at 10 °C until analysis.

Validation of the surrogate matrices (*i.e.*, 5% BSA in PBS for HILIC-MS/MS and charcoal-stripped plasma for RPLC-MS/MS) was performed by evaluation of the absence of endogenous metabolite levels in these matrices and the standard curve parallelism between the surrogate matrices and all sample matrices (*i.e.*, plasma, ascites and pleural effusion) using the method of standard addition.⁶⁶

Liquid chromatography

Analyte separation was performed on an ACQUITY UPLC System (Waters Corporation). Arginine, ornithine, citrulline, glutamine, glutamic acid, phenylalanine, tyrosine, tryptophan and their respective internal standards were separated by HILIC on an ACQUITY UPLC BEH amide column (130 Å; 1.7 µM; 2.1 mm × 100 mm; Waters, cat. no. 186004801) with 10 mM NH₄HCO₂ in MQ at pH 3.0 as mobile phase A and 0.1% formic acid in acetonitrile as mobile phase B. Elution was performed after injection of 2 µL sample at a flow rate of 0.4 mL/min and a column temperature of 35 °C using the following gradient: 0–0.5 min, 80% B; 0.5–5 min, 80–79% B; 5–7 min, 79–60% B; 7–8 min, 60–50% B; 8–9 min, 50% B; 9–10 min, 50–80% B; followed by 10 min at 80% B for column re-equilibration.

The remaining analytes and their internal standards were separated by RPLC on an ACQUITY UPLC HSS T3 column (100 Å; 1.8 µM; 2.1 mm × 50 mm; Waters, cat. no. 186003538) at a flow rate of 0.6 mL/min and a column temperature of 25 °C with three different gradients. Kynurenine, kynurenic acid, indole-3-lactic acid, indole-3-acetic acid and their respective internal standards were separated after 5 µL injection using 0.1%

formic acid in MQ as mobile phase A and 0.1% formic acid in acetonitrile as mobile phase B with the following gradient: 0–0.5 min, 1–18% B; 0.5–2.5 min, 18–31% B; 2.5–2.6 min, 31–100% B; 2.6–3.5 min, 100% B; 3.5–3.6 min, 100–1% B; 3.6–4 min, 1% B (method RPLC-1). Indole-3-aldehyde and its internal standard were separated after 5 μ L injection using the same mobile phases with the following gradient: 0–0.25 min, 1–20% B; 0.25–2 min, 20–32% B; 2–2.1 min, 32–100% B; 2.1–3 min, 100% B; 3–3.1 min, 100–1% B; 3.1–3.5 min, 1% B (method RPLC-2). Phenylpyruvic acid, 4-hydroxyphenylpyruvic acid and their respective internal standards were separated after 10 μ L injection using 0.1% acetic acid in MQ as mobile phase A and methanol as mobile phase B with the following gradient: 0–0.5 min, 1–18% B; 0.5–3.5 min, 18–25% B; 3.5–3.6 min, 25–100% B; 3.6–4.5 min, 100% B; 4.5–4.6 min, 100–1% B; 4.6–5 min, 1% B (method RPLC-3). Representative chromatograms for analyte separation are shown in Supplementary Figure 7.

Mass spectrometry

The separated analytes and internal standards were detected using an API 5000 MS/MS (AB Sciex) in multiple reaction monitoring (MRM) mode. Ionization was performed using electrospray ionization–MS/MS in negative mode for indole-3-aldehyde, phenylpyruvic acid, 4-hydroxyphenylpyruvic acid and their internal standards, and in positive mode for the remaining analytes and internal standards. The MRM transitions corresponding to the molecular ions $[M+H]^+$ and $[M-H]^-$ used for analyte and internal standard detection, along with their retention times, are summarized in Supplementary Table 5.

Calibrators were measured in duplicate and quality control samples in triplicate. Samples were measured in duplicate in a randomized order. All plasma and ascites samples were measured within a single experiment to minimize experimental variation. All pleural effusion samples were measured within a separate experiment. Individual amino acid and metabolite concentrations are listed in Supplementary Tables 2, 3 and 6.

ELISA

IL411 levels were determined using the Human IL-411 DuoSet ELISA (R&D Systems, cat. no. DY5684-05) with the DuoSet ELISA Ancillary Reagent Kit 3 (R&D Systems, cat. no. DY009) as described in the manufacturer's protocol. All samples were measured in duplicate. Individual IL411 concentrations are listed in Supplementary Tables 2, 3 and 6.

Statistical analyses

Geometric means are presented in the graphs as a measure of central tendency since the amino acid, metabolite and IL411 levels follow a more lognormal rather than normal distribution.

The stability of amino acid and metabolite levels in blood stored at RT was evaluated using a one-way repeated measures ANOVA followed by Dunnett's multiple comparisons test with the first timepoint as reference group. Significance of ANOVA p -values of the 15 performed tests was determined using the Benjamini–Hochberg procedure (FDR = 0.05). Unadjusted p -values are reported.

Differences between two sample groups (*i.e.*, plasma of healthy donors *versus* ascites of ovarian cancer patients; or FIGO stage III *versus* stage IV disease) were analyzed using an unpaired, two-tailed Mann–Whitney U test. Paired differences between two sample groups (*i.e.*, plasma *versus* ascites of ovarian cancer patients) were analyzed using a paired, two-tailed Student's t -test using log-transformed concentrations. All significant differences were confirmed upon application of the Benjamini–Hochberg procedure (FDR = 0.05). Unadjusted p -values are reported.

Differences between three sample groups (*i.e.*, plasma of healthy donors and plasma and ascites of ovarian cancer patients) were analyzed using a two-tailed, unpaired Kruskal–Wallis test followed by Dunn's *post hoc* test. Since the data contain partially overlapping samples (*i.e.*, $n = 22$ paired observations and, respectively, $n = 2$ and 10 unpaired observations for the ovarian cancer plasma and ascites groups), unpaired testing was performed after randomly assigning 15 of the 22 paired observations to the ovarian cancer plasma group, and the remaining 7 paired observations to the ovarian cancer ascites group, resulting in two groups of equal size ($n = 17$). Reported Kruskal–Wallis and *post hoc* p -values represent the 95th percentile of p -values obtained from repeated ($k = 10,000$) testing of datasets with randomly assigned observations.

Correlations between continuous variables were evaluated using Pearson's correlation analysis using log-transformed concentrations. Values below the lower limit of quantification (LLOQ) were included at the LLOQ value in correlation analyses. Analysis of progression-free survival data was performed using the log-rank test with continuous variables split at the median and using univariate Cox regression analysis. Progression-free survival was defined as the duration of time between treatment completion and clinical disease progression. Correlation with overall survival was not evaluated, since 81% of the patients were still alive at the last follow-up.

A p -value ≤ 0.05 was considered to be statistically significant. All statistical analyses were performed in SPPS (version 27.0) or R (version 4.1.2).

References

1. Siegel, R. L., Miller, K. D., Fuchs, H. E. & Jemal, A. Cancer statistics, 2022. *CA. Cancer J. Clin.* **72**, 7–33 (2022).
2. Torre, L. A. *et al.* Ovarian cancer statistics, 2018. *CA. Cancer J. Clin.* **68**, 284–96 (2018).
3. American Cancer Society. *Cancer Facts & Figures 2022*. (American Cancer Society, 2022).
4. Kurnit, K. C., Fleming, G. F. & Lengyel, E. Updates and new options in advanced epithelial ovarian cancer treatment. *Obstet. Gynecol.* **137**, 108–21 (2021).
5. McMullen, M., Karakasis, K., Madariaga, A. & Oza, A. M. Overcoming platinum and PARP-inhibitor resistance in ovarian cancer. *Cancers (Basel)* **12**, 1607 (2020).
6. Robert, C. A decade of immune-checkpoint inhibitors in cancer therapy. *Nat. Commun.* **11**, 3801 (2020).
7. Bagchi, S., Yuan, R. & Engleman, E. G. Immune checkpoint inhibitors for the treatment of cancer: clinical impact and mechanisms of response and resistance. *Annu. Rev. Pathol.* **16**, 223–49 (2021).
8. Gaillard, S. L., Secord, A. A. & Monk, B. The role of immune checkpoint inhibition in the treatment of ovarian cancer. *Gynecol. Oncol. Res. Pract.* **3**, 11 (2016).
9. Rodriguez, G. M., Galpin, K. J. C., McCloskey, C. W. & Vanderhyden, B. C. The tumor microenvironment of epithelial ovarian cancer and its influence on response to immunotherapy. *Cancers (Basel)* **10**, 242 (2018).
10. Wang, Z. *et al.* Targeting glutaminolysis: new perspectives to understand cancer development and novel strategies for potential target therapies. *Front. Oncol.* **10**, 589508 (2020).
11. Grzywa, T. M. *et al.* Myeloid cell-derived arginase in cancer immune response. *Front. Immunol.* **11**, 938 (2020).
12. Peñarando, J., Aranda, E. & Rodríguez-Ariza, A. Immunomodulatory roles of nitric oxide in cancer: tumor microenvironment says “NO” to antitumor immune response. *Transl. Res.* **210**, 99–108 (2019).
13. Opitz, C. A. *et al.* The therapeutic potential of targeting tryptophan catabolism in cancer. *Br. J. Cancer* **122**, 30–44 (2020).
14. Gutiérrez-Vázquez, C. & Quintana, F. J. Regulation of the immune response by the aryl hydrocarbon receptor. *Immunity* **48**, 19–33 (2018).
15. Opitz, C. A. *et al.* An endogenous tumour-promoting ligand of the human aryl hydrocarbon receptor. *Nature* **478**, 197–203 (2011).
16. Hoffmann, D. *et al.* Tryptophan 2,3-dioxygenase expression identified in human hepatocellular carcinoma cells and in intratumoral pericytes of most cancers. *Cancer Immunol. Res.* **8**, 19–31 (2020).
17. Carbonnelle-Puscian, A. *et al.* The novel immunosuppressive enzyme IL4I1 is expressed by neoplastic cells of several B-cell lymphomas and by tumor-associated macrophages. *Leukemia* **23**, 952–60 (2009).
18. Sadik, A. *et al.* IL4I1 is a metabolic immune checkpoint that activates the AHR and promotes tumor progression. *Cell* **182**, 1252–70.e34 (2020).
19. Boulland, M.-L. *et al.* Human IL4I1 is a secreted L-phenylalanine oxidase expressed by mature dendritic cells that inhibits T-lymphocyte proliferation. *Blood* **110**, 220–7 (2007).
20. Uyttenhove, C. *et al.* Evidence for a tumoral immune resistance mechanism based on tryptophan degradation by indoleamine 2,3-dioxygenase. *Nat. Med.* **9**, 1269–74 (2003).
21. Steggerda, S. M. *et al.* Inhibition of arginase by CB-1158 blocks myeloid cell-mediated immune suppression in the tumor microenvironment. *J. Immunother. Cancer* **5**, 101 (2017).

22. Polat, M. F., Taysi, S., Polat, S., Böyük, A. & Bakan, E. Elevated serum arginase activity levels in patients with breast cancer. *Surg. Today* **33**, 655–61 (2003).
23. Badawy, A. A. B. & Guillemin, G. The plasma [kynurenine]/[tryptophan] ratio and indoleamine 2,3-dioxygenase: time for appraisal. *Int. J. Tryptophan Res.* **12**, 1–10 (2019).
24. Rickard, B. P. *et al.* Malignant ascites in ovarian cancer: cellular, acellular, and biophysical determinants of molecular characteristics and therapy response. *Cancers (Basel)* **13**, 4318 (2021).
25. Sardar, P. & Kempken, F. Characterization of indole-3-pyruvic acid pathway-mediated biosynthesis of auxin in *Neurospora crassa*. *PLoS One* **13**, e0192293 (2018).
26. Bittinger, M. A., Nguyen, L. P. & Bradfield, C. A. Aspartate aminotransferase generates proagonists of the aryl hydrocarbon receptor. *Mol. Pharmacol.* **64**, 550–6 (2003).
27. Mason, J. M. *et al.* IL-4-induced gene-1 is a leukocyte L-amino acid oxidase with an unusual acidic pH preference and lysosomal localization. *J. Immunol.* **173**, 4561–7 (2004).
28. Zeitler, L. *et al.* Anti-ferroptotic mechanism of IL4i1-mediated amino acid metabolism. *Elife* **10**, 1–22 (2021).
29. Psallidas, I., Kalomenidis, I., Porcel, J. M., Robinson, B. W. & Stathopoulos, G. T. Malignant pleural effusion: from bench to bedside. *Eur. Respir. Rev.* **25**, 189–98 (2016).
30. Okamoto, A. *et al.* Indoleamine 2,3-dioxygenase serves as a marker of poor prognosis in gene expression profiles of serous ovarian cancer cells. *Clin. Cancer Res.* **11**, 6030–9 (2005).
31. Takao, M. *et al.* Increased synthesis of indoleamine-2,3-dioxygenase protein is positively associated with impaired survival in patients with serous-type, but not with other types of, ovarian cancer. *Oncol. Rep.* **17**, 1333–9 (2007).
32. Inaba, T. *et al.* Role of the immunosuppressive enzyme indoleamine 2,3-dioxygenase in the progression of ovarian carcinoma. *Gynecol. Oncol.* **115**, 185–92 (2009).
33. de Jong, R. A. *et al.* Serum tryptophan and kynurenine concentrations as parameters for indoleamine 2,3-dioxygenase activity in patients with endometrial, ovarian, and vulvar cancer. *Int. J. Gynecol. Cancer* **21**, 1320–7 (2011).
34. Sperner-Unterweger, B. *et al.* Enhanced tryptophan degradation in patients with ovarian carcinoma correlates with several serum soluble immune activation markers. *Immunobiology* **216**, 296–301 (2011).
35. Gostner, J. M. *et al.* Immunobiochemical pathways of neopterin formation and tryptophan breakdown via indoleamine 2,3-dioxygenase correlate with circulating tumor cells in ovarian cancer patients—A study of the OVCAD consortium. *Gynecol. Oncol.* **149**, 371–80 (2018).
36. Smith, L. P., Bitler, B. G., Richer, J. K. & Christenson, J. L. Tryptophan catabolism in epithelial ovarian carcinoma. *Trends Cancer Res.* **14**, 1–9 (2019).
37. Grobбен, Y. *et al.* Targeting indoleamine 2,3-dioxygenase in cancer models using the novel small molecule inhibitor NTRC 3883-0. *Front. Immunol.* **11**, 609490 (2020).
38. Seegers, N. *et al.* High-throughput fluorescence-based screening assays for tryptophan-catabolizing enzymes. *J. Biomol. Screen.* **19**, 1266–74 (2014).
39. Long, G. V. *et al.* Epacadostat plus pembrolizumab versus placebo plus pembrolizumab in patients with unresectable or metastatic melanoma (ECHO-301/KEYNOTE-252): a phase 3, randomised, double-blind study. *Lancet. Oncol.* **20**, 1083–97 (2019).
40. Van den Eynde, B. J., van Baren, N. & Baurain, J.-F. Is there a clinical future for IDO1 inhibitors after the failure of epacadostat in melanoma? *Annu. Rev. Cancer Biol.* **4**, 241–56 (2020).

41. Muller, A. J., Manfredi, M. G., Zakharia, Y. & Prendergast, G. C. Inhibiting IDO pathways to treat cancer: lessons from the ECHO-301 trial and beyond. *Semin. Immunopathol.* **41**, 41–8 (2019).
42. Heath-Pagliuso, S. *et al.* Activation of the Ah receptor by tryptophan and tryptophan metabolites. *Biochemistry* **37**, 11508–15 (1998).
43. DiNatale, B. C. *et al.* Kynurenic acid is a potent endogenous aryl hydrocarbon receptor ligand that synergistically induces interleukin-6 in the presence of inflammatory signaling. *Toxicol. Sci.* **115**, 89–97 (2010).
44. Ehrlich, A. M. *et al.* Indole-3-lactic acid associated with *Bifidobacterium*-dominated microbiota significantly decreases inflammation in intestinal epithelial cells. *BMC Microbiol.* **20**, 357 (2020).
45. Castellano, F., Prevost-Blondel, A., Cohen, J. L. & Molinier-Frenkel, V. What role for AHR activation in IL411-mediated immunosuppression? *Oncoimmunology* **10**, 1924500 (2021).
46. Rao, D. *et al.* Pan-cancer analysis combined with experimental validation revealed IL411 as an immunological and prognostic biomarker. *Int. Immunopharmacol.* **111**, 109091 (2022).
47. Zhao, H. *et al.* Single-cell analysis revealed that IL411 promoted ovarian cancer progression. *J. Transl. Med.* **19**, 454 (2021).
48. Villatoro, S. *et al.* Prospective detection of mutations in cerebrospinal fluid, pleural effusion, and ascites of advanced cancer patients to guide treatment decisions. *Mol. Oncol.* **13**, 2633–45 (2019).
49. Kuk, C. *et al.* Mining the ovarian cancer ascites proteome for potential ovarian cancer biomarkers. *Mol. Cell. Proteomics* **8**, 661–9 (2009).
50. Fong, M. Y., McDunn, J. & Kakar, S. S. Identification of metabolites in the normal ovary and their transformation in primary and metastatic ovarian cancer. *PLoS One* **6**, e19963 (2011).
51. Bak, S. P., Alonso, A., Turk, M. J. & Berwin, B. Murine ovarian cancer vascular leukocytes require arginase-1 activity for T cell suppression. *Mol. Immunol.* **46**, 258–68 (2008).
52. Czystowska-Kuzmicz, M. *et al.* Small extracellular vesicles containing arginase-1 suppress T-cell responses and promote tumor growth in ovarian carcinoma. *Nat. Commun.* **10**, 3000 (2019).
53. Fukumura, D., Kashiwagi, S. & Jain, R. K. The role of nitric oxide in tumour progression. *Nat. Rev. Cancer* **6**, 521–34 (2006).
54. Nomelini, R. S., de Abreu Ribeiro, L. C., Tavares-Murta, B. M., Adad, S. J. & Murta, E. F. C. Production of nitric oxide and expression of inducible nitric oxide synthase in ovarian cystic tumors. *Mediators Inflamm.* **2008**, 186584 (2008).
55. Shen, Y.-A. *et al.* Inhibition of the MYC-regulated glutaminase metabolic axis is an effective synthetic lethal approach for treating chemoresistant ovarian cancers. *Cancer Res.* **80**, 4514–26 (2020).
56. Plewa, S. *et al.* Usefulness of amino acid profiling in ovarian cancer screening with special emphasis on their role in cancerogenesis. *Int. J. Mol. Sci.* **18**, 2727 (2017).
57. D'Amora, P. *et al.* Platinum resistance in gynecologic malignancies: response, disease free and overall survival are predicted by biochemical signature: a metabolomic analysis. *Gynecol. Oncol.* **163**, 162–70 (2021).
58. Szlosarek, P. W. *et al.* Aberrant regulation of argininosuccinate synthetase by TNF- α in human epithelial ovarian cancer. *Int. J. Cancer* **121**, 6–11 (2007).
59. Cheon, D.-J. *et al.* Differential expression of argininosuccinate synthetase in serous and non-serous ovarian carcinomas. *J. Pathol. Clin. Res.* **1**, 41–53 (2015).
60. Huang, H.-L. *et al.* Argininosuccinate lyase is a potential therapeutic target in breast cancer. *Oncol. Rep.* **34**, 3131–9 (2015).
61. Gong, R. *et al.* Down-regulation of argininosuccinate lyase induces hepatoma cell apoptosis through activating Bax signaling pathway. *Genes Dis.* **6**, 296–303 (2019).

62. Jerram, A. *et al.* Effects of storage time and temperature on highly multiparametric flow analysis of peripheral blood samples; implications for clinical trial samples. *Biosci. Rep.* **41**, BSR20203827 (2021).
63. Davis, J. S. *et al.* Ex-vivo changes in amino acid concentrations from blood stored at room temperature or on ice: implications for arginine and taurine measurements. *BMC Clin. Pathol.* **9**, 10 (2009).
64. Stevens, V. L., Hoover, E., Wang, Y. & Zanetti, K. A. Pre-analytical factors that affect metabolite stability in human urine, plasma, and serum: a review. *Metabolites* **9**, 156 (2019).
65. Huang, Y. *et al.* A simple LC-MS/MS method for determination of kynurenine and tryptophan concentrations in human plasma from HIV-infected patients. *Bioanalysis* **5**, 1397–407 (2013).
66. Jones, B. R., Schultz, G. A., Eckstein, J. A. & Ackermann, B. L. Surrogate matrix and surrogate analyte approaches for definitive quantitation of endogenous biomolecules. *Bioanalysis* **4**, 2343–56 (2012).

Supplementary data

Supplementary Table 1. Clinicopathological characteristics and details on the treatment of included high-grade serous ovarian cancer patients who completed primary treatment and subgroups thereof.

	Subgroups based on collected samples *			
	All patients with completed treatment (n = 26)	Patients with plasma collected (n = 20)	Patients with ascites collected (n = 24)	Patients with both plasma and ascites collected (n = 18) [†]
<i>Age (years)</i>				
Median (IQR)	60.5 (57–67)	60 (54–64)	61.5 (58–67)	61 (57–65)
<i>BMI (kg/m²)</i>				
Median (IQR)	26 (22–28)	24 (22–27)	26 (22–29)	24 (22–27)
<i>FIGO stage</i>				
II	2 (7.7%)	1 (5.0%)	2 (8.3%)	1 (5.6%)
III	17 (65.4%)	13 (65.0%)	15 (62.5%)	11 (61.1%)
IV	7 (26.9%)	6 (30.0%)	7 (29.2%)	6 (33.3%)
<i>Surgery</i>				
PDS	11 (42.3%)	10 (50.0%)	10 (41.7%)	9 (50.0%)
IDS	11 (42.3%)	7 (35.0%)	10 (41.7%)	6 (33.3%)
IDS/HIPEC	4 (15.4%)	3 (15.0%)	4 (16.7%)	3 (16.7%)
<i>Outcome surgery</i>				
Optimal	8 (30.8%)	7 (35.0%)	8 (33.3%)	7 (38.9%)
Complete	18 (69.2%)	13 (65.0%)	16 (66.7%)	11 (61.1%)
<i>Chemotherapy</i>				
Carboplatin + paclitaxel	24 (92.3%)	19 (95.0%)	22 (91.7%)	17 (94.4%)
Other regimen	2 (7.7%)	1 (5.0%)	2 (8.3%)	1 (5.6%)
<i>Platinum sensitive[‡]</i>				
Yes	22 (84.6%)	16 (80.0%)	20 (83.3%)	14 (77.8%)
No	4 (15.4%)	4 (20.0%)	4 (16.7%)	4 (22.2%)

BMI, body mass index; FIGO, International Federation of Gynecology and Obstetrics; IDS, interval debulking surgery; IDS/HIPEC, interval debulking surgery in combination with hyperthermic intraperitoneal chemotherapy; IQR, interquartile range; PDS, primary debulking surgery. Percentages may not total to 100% due to rounding.

* Samples from remaining patients were missing for logistic reasons. † Also referred to as "overlapping patients".

‡ Platinum sensitivity is defined as a progression-free survival greater than six months.

Supplementary Table 2. Amino acid, metabolite and IL4I1 concentrations in high-grade serous ovarian cancer patient samples.

Patient	Arg (μM)		Orn (μM)		Cit (μM)		Gln (μM)	
	Plasma	Ascites	Plasma	Ascites	Plasma	Ascites	Plasma	Ascites
1	66.8		189		29.7		578	
2	29.2		106		25.8		469	
3	32.0	81.0	67.9	52.5	26.1	25.9	535	693
4	22.3	79.8	207	43.3	46.5	22.5	576	640
5	35.9	138	120	129	33.0	44.9	463	786
6	28.2	141	135	104	22.5	28.0	406	613
7	14.2	148	147	51.8	29.7	25.7	478	928
8	19.7	63.2	166	51.5	23.6	18.4	407	507
9	65.2	82.2	103	38.0	30.6	20.3	708	497
10	21.9	49.1	127	98.5	20.3	24.2	425	466
11	9.70	44.1	120	65.1	22.0	14.6	545	177
12	26.9	32.3	152	112	24.5	21.0	473	401
13	17.9	69.0	141	52.9	17.7	18.5	342	434
14	19.4	96.3	160	54.2	26.3	13.1	524	569
15	39.6	69.3	129	83.7	24.9	25.2	405	504
16	9.02	70.1	109	48.8	16.7	16.9	397	479
17	35.5	88.1	151	42.5	22.8	18.2	596	589
18	26.8	91.9	197	59.0	32.2	18.2	467	537
19	47.4	163	106	57.9	16.0	24.5	458	778
20	22.9	122	175	54.9	31.1	28.5	399	519
21	22.4	61.5	133	52.2	15.0	12.4	626	631
22	39.2	105	162	69.0	19.5	17.9	415	528
23	16.4	98.4	129	93.2	12.3	22.1	496	655
24	27.9	101	136	59.9	21.1	21.8	418	540
25		107		83.5		22.1		801
26		108		49.6		23.6		671
27		129		65.3		24.7		721
28		144		40.6		22.0		762
29		127		64.3		25.0		652
30		166		81.1		30.0		691
31		99.3		57.8		22.8		612
32		118		70.4		32.2		658
33		132		80.9		14.9		761
34		139		63.3		29.4		570

Supplementary Table 2. *Continued.*

Patient	Glu (μM)		Trp (μM)		Kyn (μM)		I3LA (nM)	
	Plasma	Ascites	Plasma	Ascites	Plasma	Ascites	Plasma	Ascites
1	207		41.1		2.32		503	
2	132		32.7		1.56		395	
3	168	38.7	21.7	32.5	1.84	4.15	216	608
4	208	83.4	37.3	32.3	2.22	4.01	738	552
5	85.8	60.6	29.6	58.8	1.32	4.21	267	1,100
6	200	91.3	26.0	54.7	1.80	3.10	928	490
7	107	67.9	23.5	83.7	1.42	6.29	446	1,445
8	232	33.1	27.4	31.9	1.44	5.27	397	546
9	103	55.9	26.3	28.7	2.02	3.81	176	233
10	195	224	21.4	24.6	4.21	6.18	436	463
11	187	353	31.5	19.6	1.88	1.41	709	295
12	305	545	30.7	27.0	2.02	3.33	765	518
13	197	71.6	21.3	33.4	1.64	3.67	264	381
14	199	68.2	32.3	29.0	2.12	3.08	417	217
15	301	192	49.9	35.6	2.46	5.15	950	1,555
16	202	282	24.1	37.9	1.39	3.69	461	705
17	290	67.1	22.1	31.0	2.20	2.98	250	223
18	213	46.1	34.6	35.7	2.64	4.58	1,725	1,220
19	127	115	52.6	73.7	3.72	8.27	639	941
20	155	83.2	23.9	41.4	2.35	6.48	729	1,020
21	186	60.4	21.3	26.0	2.83	3.95	238	278
22	208	93.4	21.7	38.5	1.51	4.36	182	365
23	140	314	26.6	31.8	1.13	2.67	318	423
24	208	160	21.0	35.1	2.39	12.5	564	1,030
25		144		92.9		7.96		1,355
26		95.6		34.7		3.96		686
27		133		50.1		6.78		772
28		119		55.4		3.30		700
29		87.1		46.0		5.04		363
30		289		40.5		14.6		993
31		99.0		55.7		3.79		825
32		105		42.4		5.77		615
33		67.2		56.0		3.67		492
34		150		48.8		6.19		348

Supplementary Table 2. *Continued.*

Patient	I3AA (nM)		I3A (nM)		KynA (nM)		Phe (μM)	
	Plasma	Ascites	Plasma	Ascites	Plasma	Ascites	Plasma	Ascites
1	1,180		34.3		43.7		77.0	
2	449		19.2		12.2		55.8	
3	552	492	15.6	36.1	18.2	19.8	46.4	74.6
4	1,900	582	19.4	19.6	40.1	22.5	76.0	68.4
5	4,130	3,655	10.4	36.9	12.6	39.5	83.7	147
6	1,295	1,415	31.7	45.0	45.1	29.0	72.8	114
7	1,006	786	8.96	106	18.1	40.9	53.3	172
8	278	482	22.0	27.8	23.0	31.8	80.5	77.6
9	697	905	7.37	7.52	25.9	16.7	74.7	69.4
10	475	592	12.7	27.1	58.4	43.4	57.0	66.2
11	1,815	1,009	18.6	14.4	49.8	22.8	65.5	46.2
12	863	721	20.9	15.7	33.4	29.2	76.2	82.6
13	229	454	8.51	18.9	16.5	20.6	69.8	63.4
14	1,072	687	20.7	16.5	23.5	25.0	64.7	84.4
15	1,410	899	32.7	52.8	14.3	26.8	93.5	72.8
16	559	781	10.9	36.7	39.4	35.5	50.1	70.2
17	978	705	9.01	9.41	16.1	12.5	47.4	55.3
18	3,445	1,590	46.2	114	52.0	45.5	75.4	74.8
19	1,245	1,450	32.2	43.5	27.5	52.8	69.4	119
20	382	781	15.2	67.6	45.4	36.1	62.9	84.0
21	410	688	7.13	13.7	19.3	19.5	73.3	70.9
22	532	1,410	8.77	29.0	32.4	27.5	92.5	105
23	772	698	16.3	21.5	20.0	37.7	75.5	64.2
24	199	452	18.9	57.2	51.0	85.7	51.7	58.2
25		855		46.7		41.0		196
26		1,240		31.0		37.1		87.1
27		1,290		37.5		37.0		98.6
28		690		42.3		ND		126
29		1,275		33.3		31.5		93.9
30		1,023		66.7		128		129
31		1,035		48.6		32.4		81.9
32		550		32.9		28.7		81.5
33		1,525		53.9		22.6		111
34		1,026		20.0		51.1		92.7

Amino acid and metabolite concentrations were determined by LC-MS/MS analysis. IL4I1 concentrations were determined by ELISA. Concentrations indicated in grey *italics* are deleteriously influenced by sample processing conditions. 4HPP, 4-hydroxyphenylpyruvic acid; Arg, L-arginine; Cit, L-citrulline; Gln, L-glutamine; Glu, L-glutamic acid;

Supplementary Table 2. *Continued.*

Patient	PP (nM)		Tyr (μ M)		4HPP (nM)		IL4I1 (pg/mL)	
	Plasma	Ascites	Plasma	Ascites	Plasma	Ascites	Plasma	Ascites
1	133		78.1		445		< 62.5	
2	25.0		52.3		81.6		150	
3	50.6	350	34.3	67.1	303	1,165	< 62.5	792
4	26.9	202	89.3	71.5	168	738	498	1,745
5	92.8	360	64.6	127	298	1,055	< 62.5	579
6	78.8	776	65.9	131	240	1,815	< 62.5	2,896
7	26.2	2,435	54.8	158	110	3,695	1,812	7,487
8	88.0	446	60.5	59.1	212	873	< 62.5	1,652
9	35.3	180	67.6	72.2	212	488	< 62.5	112
10	30.0	249	40.4	46.7	90.6	686	< 62.5	759
11	26.0	29.5	58.0	41.4	90.4	146	< 62.5	156
12	56.8	135	61.4	63.9	128	529	< 62.5	1,560
13	26.8	349	57.2	56.9	85.9	573	< 62.5	678
14	47.3	185	59.4	79.9	110	692	< 62.5	730
15	222	1,035	77.7	58.5	355	1,255	< 62.5	1,189
16	47.6	393	39.0	52.9	114	794	< 62.5	1,489
17	19.1	126	48.8	55.9	84.4	345	< 62.5	251
18	171	6,255	88.7	76.5	424	13,100	1,364	4,995
19	120	987	65.1	110	313	1,635	< 62.5	2,836
20	38.3	821	46.9	69.5	89.0	784	< 62.5	2,578
21	27.3	163	55.1	59.4	94.9	631	< 62.5	499
22	33.6	782	72.6	83.3	127	905	< 62.5	647
23	41.5	50.9	55.2	66.0	92.8	413	< 62.5	2,100
24	20.8	843	54.8	64.6	107	1,355	< 62.5	3,172
25		944		159		978		848
26		325		82.3		1,095		919
27		595		105		1,065		1,601
28		900		112		1,115		148
29		311		82.6		528		4,103
30		4,560		104		3,945		1,315
31		327		78.8		771		540
32		340		75.8		871		855
33		783		123		2,285		1,378
34		64.8		95.2		509		892

I3A, indole-3-aldehyde; I3AA, indole-3-acetic acid; I3LA, indole-3-lactic acid; IL4I1, interleukin 4 induced 1; Kyn, L-kynurenine; KynA, kynurenic acid; ND, not determined; Orn, L-ornithine; Phe, L-phenylalanine; PP, phenylpyruvic acid; Trp, L-tryptophan; Tyr, L-tyrosine.

Supplementary Table 3. Amino acid, metabolite and IL411 concentrations in healthy donor plasma samples.

Healthy donor	Arg (μM)	Orn (μM)	Cit (μM)	Gln (μM)	Glu (μM)	Trp (μM)	Kyn (μM)	I3LA (nM)
1	69.6	93.1	20.8	487	47.8	60.1	1.62	887
2	85.5	130	49.8	513	103	50.9	1.58	703
3	76.5	114	30.6	543	85.4	45.7	1.56	762
4	40.7	139	27.4	443	64.3	61.8	1.21	614
5	113	85.3	24.1	613	87.8	76.4	2.14	862
6	80.7	127	43.5	596	85.8	61.7	1.42	644
7	101	155	20.9	411	268	64.4	1.83	545
8	65.2	177	37.1	640	83.0	68.0	2.40	665
9	79.0	109	29.6	455	121	67.9	1.82	755
10	64.9	84.4	41.1	562	49.6	56.0	1.36	764
11	67.7	94.3	24.3	687	29.2	33.9	1.45	286
12	36.0	135	38.7	526	66.5	61.0	1.70	691
13	37.3	118	23.9	495	81.0	57.8	1.44	669
14	54.8	144	30.8	541	77.9	45.0	1.88	581
15	58.2	179	41.1	651	96.9	60.6	1.90	964
16	112	140	31.8	573	48.4	71.0	2.14	639
17	49.6	99.5	35.2	581	110	57.0	1.87	810
18	49.5	96.9	28.1	442	111	73.1	2.61	718
19	73.0	169	40.3	616	68.1	62.4	1.95	809
20	61.9	61.5	28.6	459	66.2	58.2	1.59	740
21	79.3	108	40.5	556	106	71.3	1.87	908
22	90.7	123	27.7	564	83.6	58.3	2.57	1,100
23	58.8	137	36.0	660	70.9	59.9	2.08	697
24	73.6	116	26.1	446	68.2	65.7	2.42	740
25	74.2	123	38.4	629	116	64.0	1.51	514
26	53.5	149	41.6	653	82.3	65.9	1.98	1,075
27	87.7	334	52.0	558	68.2	73.9	3.21	577
28	70.2	116	32.5	588	46.9	67.7	2.04	1,100
29	76.3	140	45.0	487	98.0	70.9	3.05	766
30	76.7	158	29.2	570	60.9	79.7	2.24	610

Amino acid and metabolite concentrations were determined by LC-MS/MS analysis. IL411 concentrations were determined by ELISA. 4HPP, 4-hydroxyphenylpyruvic acid; Arg, L-arginine; Cit, L-citrulline; Gln, L-glutamine; Glu, L-glutamic acid; I3A, indole-3-aldehyde; I3AA, indole-3-acetic acid; I3LA, indole-3-lactic acid; IL411, interleukin 4 induced 1; Kyn, L-kynurenine; KynA, kynurenic acid; Orn, L-ornithine; Phe, L-phenylalanine; PP, phenylpyruvic acid; Trp, L-tryptophan; Tyr, L-tyrosine.

Supplementary Table 3. *Continued.*

Healthy donor	I3AA (nM)	I3A (nM)	KynA (nM)	Phe (μM)	PP (nM)	Tyr (μM)	4HPP (nM)	IL411 (pg/mL)
1	1,625	50.6	51.6	76.6	249	60.4	349	< 62.5
2	2,235	36.0	38.4	66.3	101	58.7	274	< 62.5
3	1,090	28.4	53.4	76.3	111	57.3	250	< 62.5
4	1,040	45.4	23.7	68.0	121	67.4	262	1,514
5	1,615	95.3	52.0	81.8	192	120	953	< 62.5
6	1,005	37.7	24.3	68.3	103	63.5	310	697
7	949	36.7	33.5	87.9	128	91.4	152	< 62.5
8	1,995	44.0	50.0	64.6	104	91.6	360	< 62.5
9	909	47.6	32.3	79.9	154	81.2	361	< 62.5
10	1,055	42.1	20.8	46.5	116	51.4	358	< 62.5
11	2,585	20.6	20.5	42.2	101	35.3	422	< 62.5
12	1,465	35.9	29.5	66.8	134	83.6	491	< 62.5
13	1,790	48.3	22.4	67.0	125	55.6	269	< 62.5
14	2,985	30.9	21.0	47.6	82.6	51.3	258	< 62.5
15	1,210	43.4	111	69.7	82.5	93.9	395	126
16	2,030	49.0	26.6	76.4	150	93.4	645	< 62.5
17	5,045	53.2	27.3	72.1	167	69.8	423	< 62.5
18	1,735	56.0	21.8	90.2	251	109	654	< 62.5
19	1,225	48.6	63.2	88.7	146	82.1	443	< 62.5
20	896	44.0	33.2	69.0	102	77.5	465	497
21	2,015	86.0	32.6	72.1	144	92.1	787	< 62.5
22	644	33.1	49.6	68.8	131	87.4	454	< 62.5
23	1,895	55.5	27.3	81.8	147	86.8	446	< 62.5
24	1,280	49.0	26.5	78.8	177	86.6	589	< 62.5
25	993	42.9	34.3	69.6	104	62.4	314	< 62.5
26	2,140	33.3	55.5	68.0	106	82.2	413	< 62.5
27	1,290	36.9	49.2	115	147	142	564	< 62.5
28	1,520	57.2	66.2	62.0	144	71.0	470	< 62.5
29	1,160	54.1	51.1	79.1	174	111	899	< 62.5
30	2,350	48.1	37.0	97.3	154	142	617	< 62.5

Supplementary Table 4. List of analytes and isotope-labelled internal standards used for LC-MS/MS analysis.

Analyte	Catalog number	Supplier
L-Arginine-HCl	105000250	Acros Organics
L-Ornithine-HCl	12.956.55	Janssen
L-Citrulline	C7629	Sigma-Aldrich
L-Glutamine	49419	Sigma-Aldrich
L-Glutamic acid	49449	Sigma-Aldrich
L-Phenylalanine	78019	Sigma-Aldrich
L-Tryptophan	T0254	Sigma-Aldrich
L-Tyrosine	T899975	Toronto Research Chemicals
L-Kynurenine	BIB6088	Apollo Scientific
Kynurenic acid	K660500	Toronto Research Chemicals
DL-Indole-3-lactic acid	I627100	Toronto Research Chemicals
Indole-3-acetic acid	I577344	Toronto Research Chemicals
Indole-3-aldehyde	129445	Sigma-Aldrich
4-Hydroxyphenylpyruvic acid	114286	Sigma-Aldrich
Phenylpyruvic acid	286958	Sigma-Aldrich

Supplementary Table 5. Retention times and MRM transitions used for analyte and internal standard detection by LC-MS/MS.

Analyte	Separation method	Ionization mode	RT (min)
L-Arginine	HILIC	Positive	7.2
L-Ornithine	HILIC	Positive	7.4
L-Citrulline	HILIC	Positive	4.9
L-Glutamine	HILIC	Positive	4.2
L-Glutamic acid	HILIC	Positive	3.6
L-Phenylalanine	HILIC	Positive	1.6
L-Tryptophan	HILIC	Positive	1.6
L-Tyrosine	HILIC	Positive	2.2
L-Kynurenine	RPLC-1	Positive	0.8
Kynurenic acid	RPLC-1	Positive	1.0
DL-Indole-3-lactic acid	RPLC-1	Positive	1.7
Indole-3-acetic acid	RPLC-1	Positive	2.2
Indole-3-aldehyde	RPLC-2	Negative	1.6
4-Hydroxyphenylpyruvic acid	RPLC-3	Negative	1.3
Phenylpyruvic acid	RPLC-3	Negative	2.5

HILIC, hydrophilic interaction liquid chromatography; MRM, multiple reaction monitoring; m/z, mass-to-charge ratio; RPLC, reversed-phase liquid chromatography; RT, retention time.

Supplementary Table 4. *Continued.*

Internal standard	Catalog number	Supplier
L-Arginine-d7-HCl	A769501	Toronto Research Chemicals
L-Ornithine-d6-HCl	O695553	Toronto Research Chemicals
L-Citrulline-d7	C535703	Toronto Research Chemicals
L-Glutamine-d5	G597005	Toronto Research Chemicals
L-Glutamic acid-d5	G596963	Toronto Research Chemicals
L-Phenylalanine-d7	P319416	Toronto Research Chemicals
L-Tryptophan-d5	T947212	Toronto Research Chemicals
L-Tyrosine-d2	H899977	Toronto Research Chemicals
L-Kynurenine-d4	K-008005	TLC Pharmaceutical Standards
Kynurenic acid-d5	K660502	Toronto Research Chemicals
D,L-Indole-3-lactic acid-d5	I627102	Toronto Research Chemicals
Indole-3-acetic acid-d5	I577344	Toronto Research Chemicals
Indole-3-aldehyde- ¹³ C ₈	I614993	Toronto Research Chemicals
4-Hydroxyphenylpyruvic acid- ¹³ C ₉	7491	Sigma-Aldrich
Phenylpyruvic acid- ¹³ C ₉	CLM-10604	Cambridge Isotope Laboratories

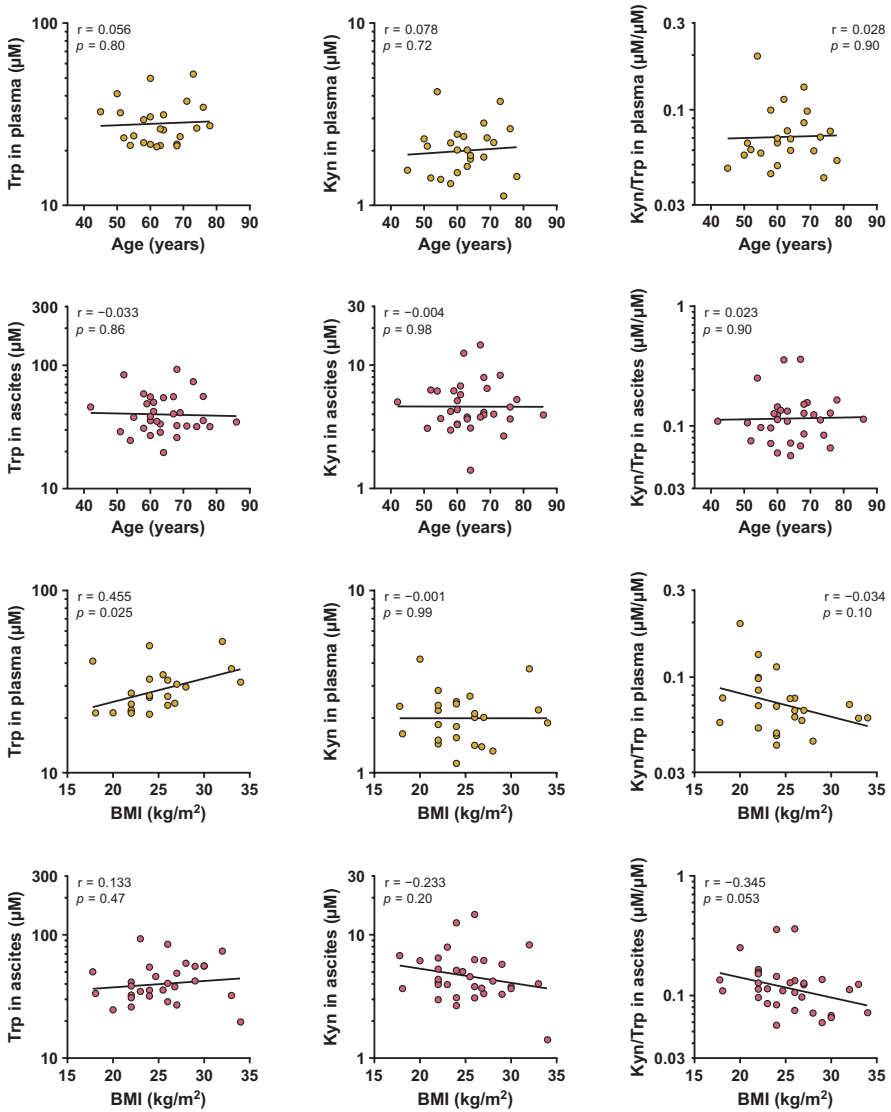
Supplementary Table 5. *Continued.*

MRM-transition (m/z)	Internal standard	MRM-transition (m/z)
175.2 → 70.1	L-Arginine-d7	182.2 → 77.1
133.1 → 70.2	L-Ornithine-d6	139.0 → 76.2
176.1 → 70.0	L-Citrulline-d7	183.2 → 77.2
147.2 → 83.9	L-Glutamine-d5	152.1 → 89.1
148.1 → 84.1	L-Glutamic acid-d5	153.1 → 87.9
166.2 → 102.9	L-Phenylalanine-d7	172.9 → 108.1
205.0 → 118.2	L-Tryptophan-d5	209.9 → 122.1
182.1 → 91.0	L-Tyrosine-d2	184.0 → 92.0
208.8 → 94.1	L-Kynurenine-d4	213.1 → 97.9
190.0 → 162.1	Kynurenic acid-d5	194.9 → 167.1
206.0 → 118.2	D,L-Indole-3-lactic acid-d5	211.1 → 122.0
176.1 → 103.1	Indole-3-acetic acid-d5	181.2 → 107.0
144.0 → 114.9	Indole-3-aldehyde- ¹³ C ₈	152.0 → 123.1
178.9 → 107.0	4-Hydroxyphenylpyruvic acid- ¹³ C ₉	188.0 → 114.1
162.9 → 91.0	Phenylpyruvic acid- ¹³ C ₉	172.0 → 98.0

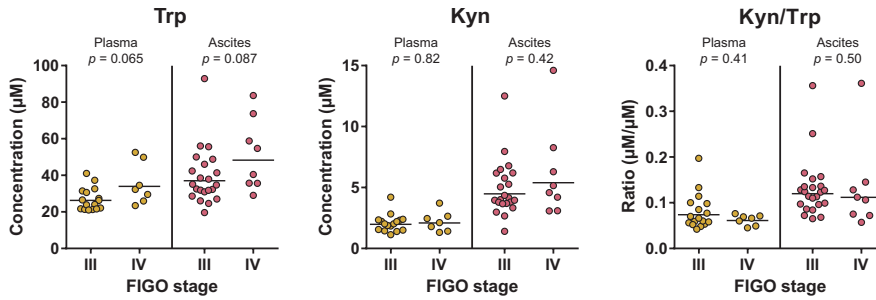
Supplementary Table 6. IL4I1 metabolite and enzyme concentrations in pleural effusion samples from non-small cell lung cancer patients.

Patient	PP (nM)	4HPP (nM)	IL4I1 (pg/mL)
1	1,200	3,005	4,070
2	367	174	2,539
3	368	1,490	4,035
4	12.1	87.5	234
5	279	228	1,018
6	33.5	74.7	62.0
7	1,030	428	868
8	91.9	118	62.0
9	354	508	1,307
10	80.0	208	3,254
11	391	223	341
12	273	125	691
13	25.2	108	525
14	460	368	672
15	251	329	589
16	1,480	482	643
17	223	130	62.0
18	531	100	115
19	202	62.5	489
20	509	290	62.0
21	413	153	1,968
22	2,990	1,850	2,459
23	595	231	630
24	1,885	840	883

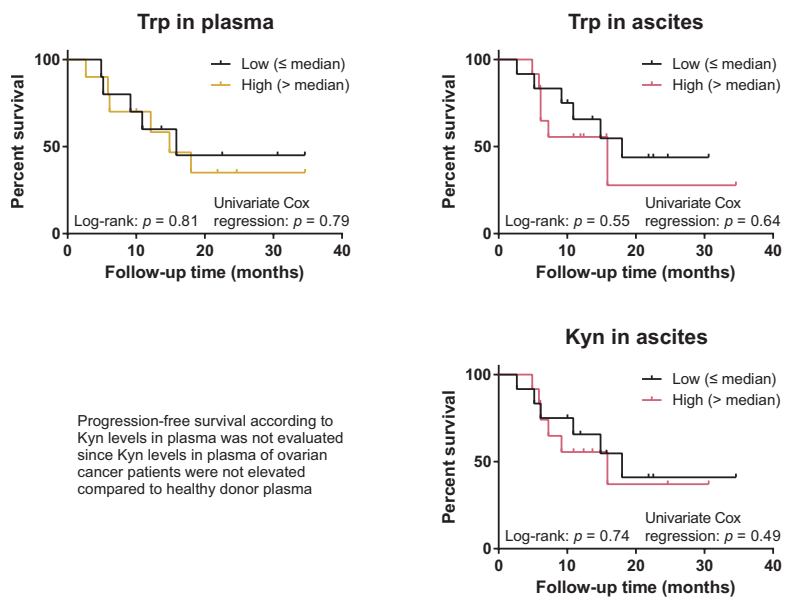
PP and 4HPP concentrations were determined by LC-MS/MS analysis. IL4I1 concentrations were determined by ELISA. 4HPP, 4-hydroxyphenylpyruvic acid; IL4I1, interleukin 4 induced 1; PP, phenylpyruvic acid.



Supplementary Figure 1. Correlation between Trp levels, Kyn levels or Kyn/Trp ratios in plasma ($n = 24$) or ascites ($n = 32$) and age or BMI of high-grade serous ovarian cancer patients. Results of Pearson's correlation analyses are indicated in the graphs. BMI, body mass index; Kyn, L-kynurenine; r, Pearson's correlation coefficient; Trp, L-tryptophan.

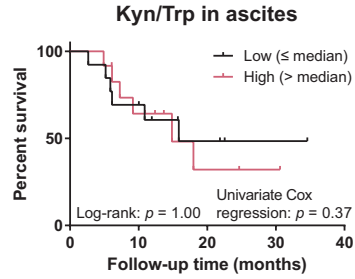
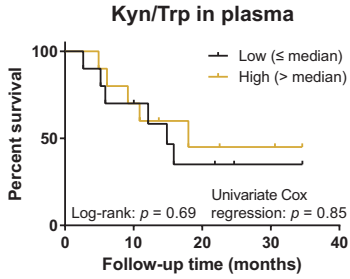


Supplementary Figure 2. Comparison of Trp levels, Kyn levels and Kyn/Trp ratios in high-grade serous ovarian cancer patients with stage III ($n = 16$ for plasma; $n = 22$ for ascites) and stage IV disease ($n = 7$ for plasma; $n = 8$ for ascites). Horizontal lines indicate geometric means. Results of unpaired, two-tailed Mann–Whitney U tests are indicated in the graphs. Since only two patients with stage II disease were included in the study, these patients were excluded from this analysis. FIGO, International Federation of Gynecology and Obstetrics; Kyn, L-kynurenine; Trp, L-tryptophan.

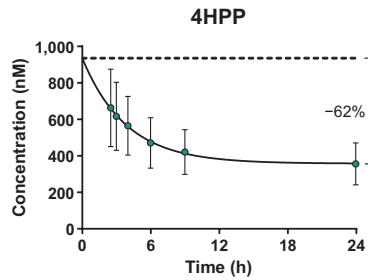
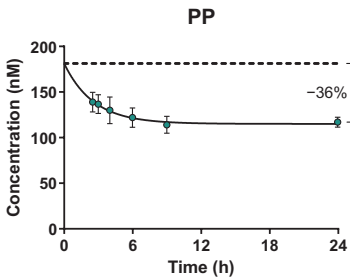


Supplementary Figure 3. Kaplan–Meier progression-free survival curves according to Trp levels, Kyn levels and Kyn/Trp ratios in plasma or ascites of high-grade serous ovarian cancer patients who completed treatment ($n = 20$ for plasma; $n = 24$ for ascites). Results of log-rank and univariate Cox regression analyses are indicated in the graphs. Multivariate regression analysis was not performed due to small sample sizes. Kyn, L-kynurenine; Trp, L-tryptophan.

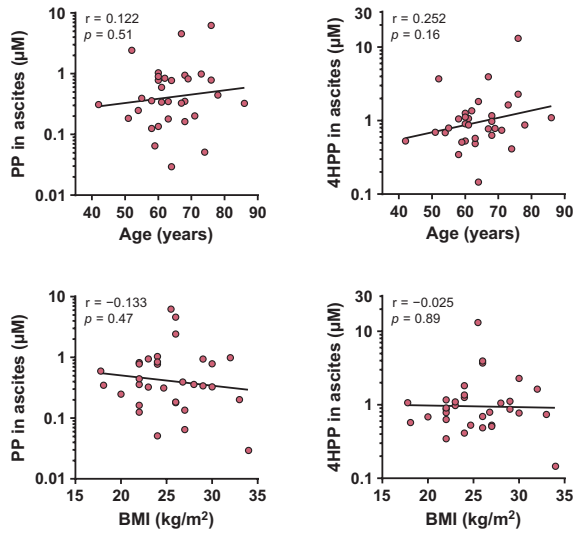
(Figure continued on next page)



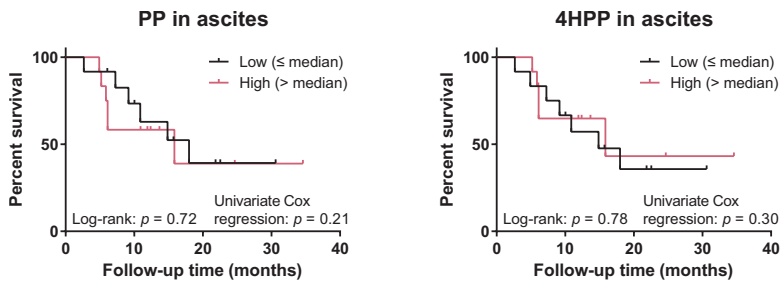
Supplementary Figure 3. *Continued.*



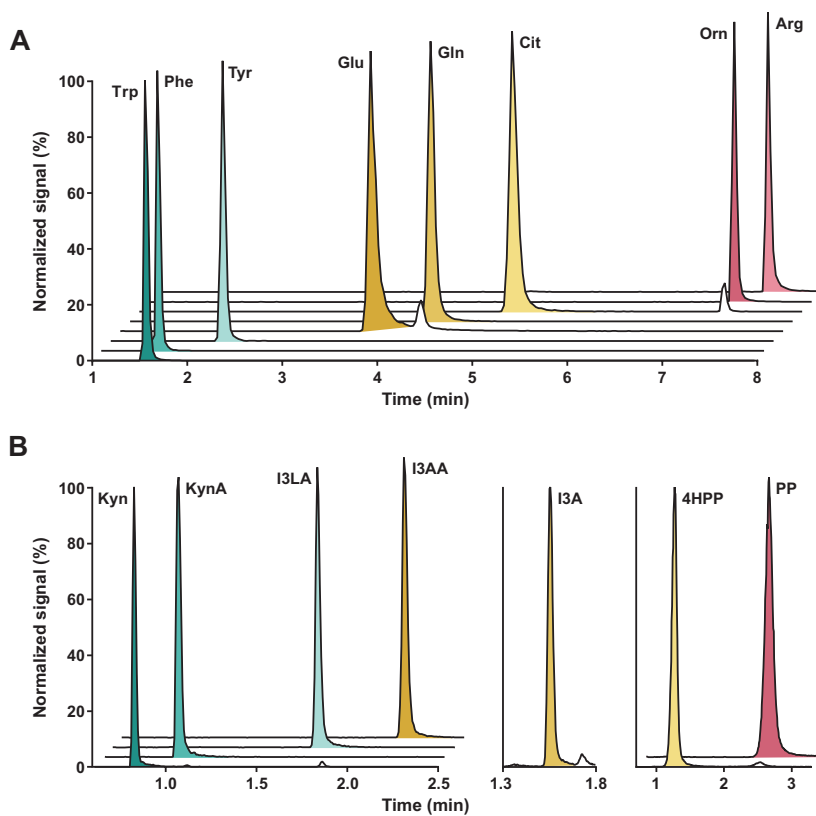
Supplementary Figure 4. Estimation of the reduction in PP and 4HPP levels in healthy donor blood stored at room temperature prior to plasma separation. Data have been fitted with an exponential one-phase decay curve to estimate the reduction in PP and 4HPP levels between the time of blood collection ($t = 0$ h) and the approximated time at which the ovarian cancer patient plasma samples were processed ($t = 24$ h). 4HPP, 4-hydroxyphenylpyruvic acid; PP, phenylpyruvic acid.



Supplementary Figure 5. Correlation between PP or 4HPP levels in ascites and age or BMI of high-grade serous ovarian cancer patients ($n = 32$). Results of Pearson's correlation analyses are indicated in the graphs. BMI, body mass index; 4HPP, 4-hydroxyphenylpyruvic acid; PP, phenylpyruvic acid; r , Pearson's correlation coefficient.



Supplementary Figure 6. Kaplan–Meier progression-free survival curves according to PP and 4HPP levels in ascites of high-grade serous ovarian cancer patients who completed treatment ($n = 24$). Results of log-rank and univariate Cox regression analyses are indicated in the graphs. Multivariate regression analysis was not performed due to small sample sizes. 4HPP, 4-hydroxyphenylpyruvic acid; PP, phenylpyruvic acid.



Supplementary Figure 7. Representative chromatograms for analyte separation in surrogate matrices by **(A)** hydrophilic interaction liquid chromatography (HILIC)- and **(B)** reversed-phase liquid chromatography (RPLC)-tandem mass spectrometry (MS/MS). 4HPP, 4-hydroxyphenylpyruvic acid; Arg, L-arginine; Cit, L-citrulline; Gln, L-glutamine; Glu, L-glutamic acid; I3A, indole-3-aldehyde; I3AA, indole-3-acetic acid; I3LA, indole-3-lactic acid; Kyn, L-kynurenine; KynA, kynurenic acid; Orn, L-ornithine; Phe, L-phenylalanine; PP, phenylpyruvic acid; Trp, L-tryptophan; Tyr, L-tyrosine.

ARG1



Chapter 4

Structural insights into human arginase 1
pH dependence and its inhibition by the
small molecule inhibitor CB-1158

Yvonne Grobбен, Joost C. M. Uitdehaag, Nicole Willemsen-Seegers, Werner W. A. Tabak, Jos de Man, Rogier C. Buijsman and Guido J. R. Zaman

Netherlands Translational Research Center B.V., Oss, The Netherlands

Journal of Structural Biology: X (2020) 4:100014

Abstract

Arginase 1 (ARG1) is a manganese-dependent metalloenzyme that catalyzes the hydrolysis of L-arginine into L-ornithine and urea. ARG1 is abundantly expressed by tumor-infiltrating myeloid cells that promote tumor immunosuppression, which is relieved by inhibition of ARG1. We have characterized the potencies of the ARG1 reference inhibitors (2S)-2-amino-6-boronohexanoic acid (ABH) and *N*^w-hydroxy-nor-L-arginine (nor-NOHA), and studied their pH-dependence and binding kinetics. To gain a better understanding of the structural changes underlying the high pH optimum of ARG1 and its pH-dependent inhibition, we determined the crystal structure of the human ARG1/ABH complex at pH 7.0 and 9.0. These structures revealed that at increased pH, the manganese cluster assumes a more symmetrical coordination structure, which presumably contributes to its increase in catalytic activity. Furthermore, we show that binding of ABH involves the presence of a sodium ion close to the manganese cluster. We also studied the investigational new drug CB-1158 (INCB001158). This inhibitor has a low-nanomolar potency at pH 7.4 and increases the thermal stability of ARG1 more than ABH and nor-NOHA. Moreover, CB-1158 displays slow association and dissociation kinetics at both pH 9.5 and 7.4, as indicated by surface plasmon resonance. The potent character of CB-1158 is presumably due to its increased rigidity compared to ABH as well as the formation of an additional hydrogen-bond network as observed by resolution of the ARG1/CB-1158 crystal structure.

Introduction

The ability of tumors to modify their microenvironment and thereby evade the immune system of the host is increasingly recognized as an important determinant of cancer progression and patient prognosis.^{1,2} The development of immune checkpoint therapies is an effective strategy to enhance anti-tumor immune responses of T cells, for example using antibodies against cytotoxic T-lymphocyte-associated protein 4 (CTLA-4)³ or programmed cell death 1 (PD-1).⁴ However, the clinical response of these therapies is often limited by various resistance mechanisms,⁵ such as immunosuppression induced by the tumor myeloid compartment. One of the most prominent mechanisms contributing to this immunosuppression is the expression of arginase 1 (ARG1) in the tumor microenvironment.^{6,7}

ARG1 (L-arginine amidinohydrolase, EC 3.5.3.1) is a manganese-dependent enzyme responsible for the catalytic hydrolysis of L-arginine into L-ornithine and urea. In the tumor microenvironment, enhanced expression of ARG1 by myeloid cells causes the local depletion of the semi-essential amino acid L-arginine. This results in anergy of effector T cells by inhibition of CD3 ζ chain expression,⁸ and induces the suppression of effector T-cell and natural killer cell proliferation.^{9,10} Reduced levels of intracellular L-arginine can also directly impact the survival of activated T cells.¹¹ Elevated levels of ARG1 have been detected in tumors of patients with various types of cancer, with the highest levels in lung, gastrointestinal and bladder cancers.⁹ Furthermore, elevated plasma ARG1 and reduced L-arginine levels are correlated with suppressed T-cell function and proliferation in patients with different histologies.^{12,13} Pharmacological inhibition of ARG1 has been shown to increase tumor immune cell infiltration and reduce tumor growth in syngeneic mouse models.^{8,9,13–15} ARG1 is therefore an attractive target for the development of new drugs for cancer immunotherapy.

Aside from immuno-oncology, ARG1 has been a drug target for several decades for a variety of diseases and disorders, including pulmonary and vascular disease, and erectile dysfunction.¹⁶ Some broadly studied ARG1 inhibitors in this context are the boronic acid derivative (2S)-2-amino-6-boronohexanoic acid (ABH)¹⁷ and the L-arginine analogue *N*^ω-hydroxy-nor-L-arginine (nor-NOHA) (Figure 1).¹⁸ The clinical application of both types of inhibitors is however limited by poor pharmacokinetic properties.^{19,20} In addition, the boronic acid functionality of ABH may display cross-reactivity towards other proteins, causing potential toxicity.²¹ Recently, efforts aiming at the improvement of ABH for cancer immunotherapy have resulted in the development of the ARG1 inhibitor CB-1158 (INCB001158) by Calithera Biosciences, Inc. (South San Francisco, CA).^{9,19,22,23} CB-1158 is an orally bioavailable inhibitor, which reportedly inhibits human ARG1 in a biochemical

assay with a half-maximal inhibitory concentration (IC_{50}) of 86 nM.⁹ CB-1158 is currently evaluated for the treatment of advanced and metastatic solid tumors as a single agent, and in combination with chemotherapy, immune checkpoint therapy, and the IDO1 inhibitor epacadostat (see for example www.clinicaltrials.gov under NCT02903914, NCT-03314935 and NCT03361228).

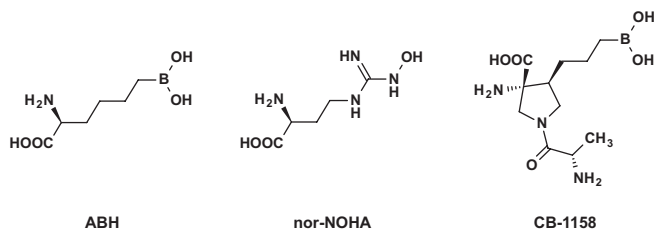


Figure 1. Chemical structures of the ARG1 inhibitors characterized in this study.

Biochemical inhibition of human ARG1 (and the isozyme ARG2) is reported in multiple studies, as summarized for ABH, nor-NOHA and CB-1158 in Table 1. Remarkably, there is significant discrepancy between the reported (low-)nanomolar binding affinities (K_D) and the low-micromolar IC_{50} values of ABH and nor-NOHA (Table 1). Moreover, inhibition of ARG2 by ABH is reported to be pH-dependent, having an inhibition constant (K_i) of 0.25 μ M

Table 1. Potencies and binding affinities of the ARG1 and ARG2 reference inhibitors ABH, nor-NOHA and CB-1158 in the literature.

Inhibitor	Human ARG1	Human ARG2	Method	Reference(s)
ABH	$K_D = 5$ nM		ITC at pH 8.5	26
	$K_D = 18$ nM		SPR at pH 8.5	27
	$IC_{50} = 1.45\text{--}1.55$ μ M	$IC_{50} = 1.92\text{--}2.55$ μ M	Enzyme assay at pH 7.4	19, 22, 23, 25 ^a
		$K_i = 0.25$ μ M	Enzyme assay at pH 7.5	24
nor-NOHA	$K_D \approx 50$ nM		ITC at pH 8.5	28
	$K_D = 517$ nM		SPR at pH 8.5	28
		$K_i = 51$ nM	Enzyme assay at pH 7.5	24
	$IC_{50} = 1.36$ μ M	$IC_{50} = 1.26$ μ M	Enzyme assay at pH 7.4	25
CB-1158	$IC_{50} = 86$ nM	$IC_{50} = 296$ nM	Enzyme assay at pH 7.4	9

^a Refs. 22, 23 and 25 are inconclusive about whether the *R*-isomer or racemic ABH is used, despite reporting identical or highly similar IC_{50} values. The use of racemic ABH can be assumed based on comparison to Ref. 19. IC_{50} , half-maximal inhibitory concentration; ITC, isothermal titration calorimetry; K_D , binding affinity; K_i , inhibition constant; SPR, surface plasmon resonance.

at pH 7.5 and a K_i of 8.5 nM at pH 9.5.²⁴ However, it is unclear if the same holds for ARG1. It is worth noting that inhibitory potencies reported in the literature for human ARG1 (and ARG2) are generally determined at physiological pH 7.4,^{9,22,23,25} whereas binding affinities were measured at pH 8.5.^{26–28} However, the pH optimum of human ARG1 lies between pH 9.0 and 10.0.^{29–32}

In this work, we characterized the biochemical potency of the reference inhibitors ABH and nor-NOHA, and the clinical compound CB-1158, side-by-side. Differences in pH-dependent inhibition profiles were further studied in a thermal stability assay and by surface plasmon resonance (SPR). A crystal structure of ARG1 in complex with ABH at pH 7.0 and 9.0 shows the determinants of the alkaline pH optimum of ARG1. Finally, we demonstrate the high potency of the clinical compound CB-1158 (Figure 1),⁹ display its slow association and dissociation kinetics and reveal a crystal structure of CB-1158 bound in the ARG1 active site.

Results

Enzyme kinetics and thermal stability of ARG1

To enable characterization of the inhibitors in biochemical assays, human ARG1 was expressed in *Escherichia coli* with an N-terminal hexa-histidine tag and purified by affinity chromatography to > 95% purity (Supplementary Figure 1). Enzyme kinetics of the ARG1 preparation were characterized by determining the apparent Michaelis–Menten parameters both at physiological pH 7.4 and at the pH optimum of 9.5 using a colorimetric urea assay.^{33,34} At pH 7.4, a Michaelis constant (K_M) of 2.3 mM and a catalytic rate constant (k_{cat}) of 57 s^{-1} for the substrate L-arginine were measured, while at pH 9.5, K_M was 4.9 mM and k_{cat} was $4.6 \times 10^2 \text{ s}^{-1}$. These values correspond well with K_M values of 1.9, 2.3 and 1.5 mM and k_{cat} values of 3.0×10^2 and $1.9 \times 10^2 \text{ s}^{-1}$ reported in the literature,^{35–37} despite differences in the pH value and temperature used during determination. The 8-fold increase in k_{cat} and 4-fold increase of the specificity constant k_{cat}/K_M at pH 9.5 compared to pH 7.4 demonstrate the pH dependence of the ARG1 enzyme kinetics and underline the remarkable decrease in catalytic activity at physiological, but non-optimal pH.

We reasoned that the higher enzymatic activity of ARG1 at pH 9.5 compared to pH 7.4 could be related to an altered stability of the enzyme at pH 9.5. To investigate this further, we developed a thermal shift assay and determined the melting temperature (T_m) of unliganded ARG1 at both pH conditions relevant for ARG1 activity, i.e., pH 9.5 and 7.4. The melting temperature at pH 7.4 was 72.9 °C, whereas at pH 9.5 it was 77.4 °C (Figure 2 and Table 2; Buffer control). This difference is significant as is apparent from the low standard

Table 2. Effect of inhibitors on ARG1 thermal stability, and inhibition constants in the ARG1 colorimetric urea assay at pH 9.5 and 7.4.

Inhibitor	Thermal shift assay			Inhibition assay		
	T_m (°C)	SD T_m	ΔT_m (°C)	IC ₅₀ (nM) (95% CI) ^a	K_i (nM) (95% CI) ^a	K_i (nM) (95% CI) ^a
Buffer control	77.4	0.13	–	–	–	–
pH 9.5						
ABH	80.9	0.09	3.5	22 (19–26)	–	11 (9.4–13)
nor-NOHA	82.1	0.10	4.7	109 (91–130)	–	54 (45–64)
CB-1158	83.0	0.11	5.6	132 (109–159)	–	65 (54–79)
Buffer control	72.9	0.13	–	–	–	–
pH 7.4						
ABH	77.4	0.10	4.5	184 (171–198)	–	88 (82–95)
nor-NOHA	77.7	0.04	4.8	59 (50–70)	–	28 (24–34)
CB-1158	81.0	0.23	8.1	8.6 (8.4–8.9)	–	4.1 (4.0–4.3)

^a Average IC₅₀ and K_i values and 95% confidence intervals (95% CI) were determined using respectively the $-^{10}\log IC_{50}$ (i.e., pIC₅₀) and $-^{10}\log K_i$ (i.e., pK_i) values of the individual experiments. IC₅₀, half-maximal inhibitory concentration; K_i , inhibition constant; SD, standard deviation; ΔT_m , melting temperature; T_m , melting temperature; ΔT_m , change in melting temperature relative to the buffer control.

Table 3. Kinetic parameters of inhibitor binding to ARG1 determined by SPR at pH 9.5 and 7.4.

Inhibitor	k_a (M ⁻¹ s ⁻¹)	log(k_a)	SD log(k_a)	k_d (s ⁻¹)	log(k_d)	SD log(k_d)	K_D (nM)	τ (s)	n
ABH	5.1×10^3	3.71	0.03	1.4×10^{-4}	-3.86	0.03	27	7,200	3
pH 9.5									
nor-NOHA	3.6×10^4	4.55	0.15	6.2×10^{-3}	-2.21	0.15	173	160	3
CB-1158	1.3×10^3	3.11	0.04	9.2×10^{-5}	-4.04	0.04	72	11,000	3
ABH	1.2×10^4	4.09	0.21	9.9×10^{-3}	-2.00	0.21	797	100	6
pH 7.4									
nor-NOHA	1.2×10^4	4.09	0.21	1.9×10^{-2}	-1.73	0.21	1,497	54	6
CB-1158	4.8×10^3	3.68	–	1.8×10^{-4}	-3.74	–	38	5,500	2

k_a , association rate constant; k_d , dissociation rate constant; K_D , binding affinity; n , number of experimental replicates; SD, standard deviation; τ , target residence time.

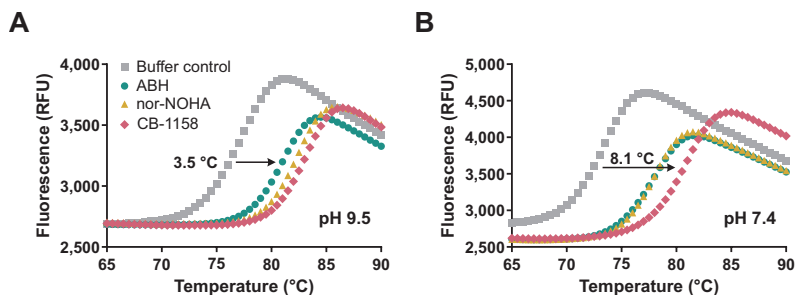


Figure 2. Stabilization of ARG1 from thermal unfolding by inhibitors in a thermal shift assay. (A) Representative melting curves of ARG1 in the presence of ABH, nor-NOHA and CB-1158 at pH 9.5 and (B) at pH 7.4. The arrow in both graphs indicates an example shift of the midpoint of unfolding.

deviations (Table 2). Moreover, these values are similar to the T_m reported for rat ARG1 of 75 °C at pH 7.5,³⁸ and are slightly lower than the T_m of 81.0 °C previously reported for recombinant human ARG1 at pH 7.4,³⁹ thereby confirming the remarkable thermal stability of ARG1.^{38,39} Thus, ARG1 is not only less active at pH 7.4 compared to pH 9.5 (as determined from the apparent Michaelis–Menten parameters), but also has a significantly decreased thermal stability.

Inhibition of ARG1 by ABH and CB-1158 is pH-dependent

To elucidate the role of pH in ARG1 inhibition, we compared inhibitor dose-response curves in the colorimetric urea assay for ARG1 activity at pH 7.4 and 9.5 (Table 2 and Supplementary Figure 2). ABH, nor-NOHA and CB-1158 are all potent ARG1 inhibitors with low- to mid-nanomolar potencies at both pH 9.5 and 7.4. Since the activity assay-based IC_{50} values in literature are generally determined at pH 7.4, and the binding assay-based K_D values at pH 8.5 (Table 1), we can best compare our values at pH 7.4 with the literature data.

For ABH, the activity assay-based K_i value of 88 nM lies in between the reported K_D values of 5 and 18 nM, and IC_{50} values of 1.45–1.55 μ M (Tables 1 and 2).^{19,22,23,25–27} For nor-NOHA, the K_i value is 28 nM at pH 7.4, which is similar to the previously reported K_D of 50 nM based on isothermal titration calorimetry,²⁸ but deviates considerably from the K_D of 517 nM reported in the same publication based on SPR experiments²⁸ and deviates even further from its reported IC_{50} value of 1.36 μ M (Tables 1 and 2).²⁵ CB-1158, with an activity assay-based K_i value of 4.1 nM at pH 7.4, is considerably more potent than previously reported (IC_{50} of 86 nM; Tables 1 and 2).⁹

Comparison of the K_i values at the two pH values demonstrates that the potency of nor-NOHA is only slightly affected by an increase of the pH from 7.4 to 9.5 (Table 2). In

contrast, an increase of the pH from 7.4 to 9.5 results in an 8-fold decrease in the K_i of ABH from 88 to 11 nM, whereas the K_i of CB-1158 contrastingly increases 16-fold from 4.1 to 65 nM (Table 2).

ARG1 is thermally stabilized by inhibitors

Next, we studied the effect of the three inhibitors on the ARG1 melting temperature at both pH values. We found that all three inhibitors clearly increase the T_m of ARG1 (Figure 2 and Table 2). Melting temperature shifts (ΔT_m) varied from 3.5 to 8.1 °C, with the largest shift of 8.1 °C observed for CB-1158 at pH 7.4. Thus, the binding of ARG1 inhibitors can be measured using thermal shift analysis. At both pH values, the rank order of the inhibitor-induced melting temperature shifts is identical. ABH induces the least stabilization of ARG1 followed by nor-NOHA and CB-1158, which increasingly stabilize the enzyme (Table 2). This rank order is identical to the potency rank order in the biochemical activity assay at pH 7.4, while at pH 9.5, the rank order opposes that of the biochemical assay (Table 2). Therefore, inhibitory potency and thermal stabilization are correlated at pH 7.4, but not at pH 9.5.

ABH and CB-1158 display slow association and dissociation kinetics

To further characterize the inhibitors, we determined the kinetic parameters of their association and dissociation by SPR (Figure 3 and Table 3). The association rate constants (k_a) of all three inhibitors at pH 9.5 and 7.4 are substantially below the typical diffusion-controlled limit of $\sim 10^8$ – 10^9 M⁻¹ s⁻¹.⁴⁰ CB-1158 at pH 9.5 shows the slowest formation of the enzyme–inhibitor complex having a k_a of 1.3×10^3 M⁻¹ s⁻¹. The dissociation rate constants (k_d) vary up to 200-fold among the inhibitors and pH conditions (Table 3), with

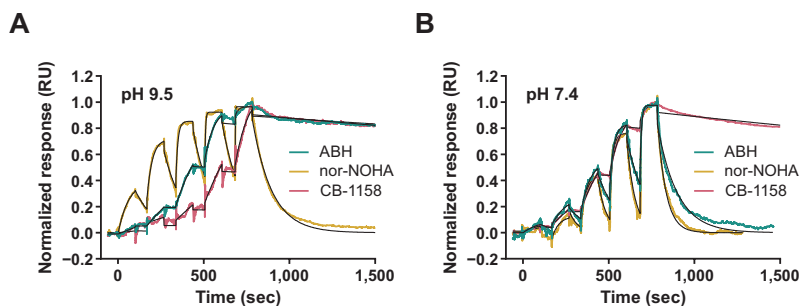


Figure 3. Surface plasmon resonance sensorgrams of ARG1 inhibitors. **(A)** Binding of inhibitors to immobilized ARG1 at pH 9.5 and **(B)** at pH 7.4 measured using single-cycle kinetics. The data used for curve fitting are truncated to the time point when the baseline level is reached. The colored lines show the actual response determined by SPR, while the black lines display the fits obtained using a 1:1 binding model. Individual graphs with absolute responses and a longer time scale (for the inhibitors with long target residence times) can be found in Supplementary Figure 3.

CB-1158 at pH 9.5 also having the slowest dissociation kinetics with a k_d of $9.2 \times 10^{-5} \text{ s}^{-1}$ and a target residence time (τ) of 3 h (*i.e.*, 11,000 s). Moreover, two other conditions show particularly slow kinetics. At pH 9.5, ABH has a k_a of $5.1 \times 10^3 \text{ M}^{-1} \text{ s}^{-1}$, and its dissociation kinetics (k_d of $1.4 \times 10^{-4} \text{ s}^{-1}$) are only slightly faster than those of CB-1158 at the same pH. Additionally, CB-1158 at pH 7.4 has k_a and k_d values of respectively $4.8 \times 10^3 \text{ M}^{-1} \text{ s}^{-1}$ and $1.8 \times 10^{-4} \text{ s}^{-1}$ (Table 3). Nor-NOHA has the fastest association and dissociation kinetics at both pH values.

We compared our data to the previously reported SPR-based K_D values of ABH and nor-NOHA determined at pH 8.5 (Table 1).^{27,28} For ABH, the K_D of 27 nM at pH 9.5 is similar to the reported K_D of 18 nM,²⁷ while the K_D of 797 nM at pH 7.4 deviates considerably from this value (Tables 1 and 3). For nor-NOHA, the previously reported K_D value of 517 nM lies neatly between our K_D values of 173 nM and 1,497 nM at pH 9.5 and 7.4, respectively (Tables 1 and 3).²⁸

Structure of the ARG1/ABH complex shows an active site-bound sodium ion

To investigate the structural basis of the pH-dependent changes in both ARG1 enzyme kinetics and inhibitor potencies, we set up crystallization experiments with the same ARG1 enzyme, containing the intact hexa-histidine tag and linker, as used in the biochemical assays (Supplementary Figure 1A). After initial screening, we discovered crystallization conditions at a low pH of 4.0 resulting in crystals belonging to space group P6₃, a space group not previously reported for human ARG1 according to the Protein Data Bank (PDB). These crystals were formed in the absence of the problematic hemihedral twinning growth defect reported for all human ARG1 crystal structures in the literature. However, when we increased the pH of the formed crystals and soaked them with inhibitors, the hemihedral twinning problem returned and the crystals shifted to the apparent space group P3. Upon solving the crystal structures, we noticed that this is presumably due to changes in the crystal contacts between intact ARG1 homotrimers.

We soaked the crystals with the inhibitor ABH, since this is the most extensively studied ARG1 inhibitor in the literature. Despite the twinning problem, we obtained high-quality data of the crystal structure of the ARG1/ABH complex (Table 4). Although a previous structure of this complex at pH 6.5 existed in the PDB with a resolution of 1.29 Å (hereafter referred to by its PDB ID: 2AEB),²⁶ we wanted to look specifically at the effect of the pH on the ARG1 crystal structure and ABH binding. Therefore, we prepared and measured two crystals under identical conditions, with the only exception being the pH used during soaking with ABH. Both crystal structures have a high resolution of respectively 1.50 and 1.66 Å at pH 7.0 and 9.0 (Table 4).

Table 4. Data collection and refinement statistics.

<i>Structure details</i>			
PDB ID	6Q92	6Q9P	6QAF
Ligand	ABH	ABH	CB-1158
pH	7.0	9.0	9.0
<i>Data collection^a</i>			
Beamline	ID30A-1 (ESRF)	ID30A-1 (ESRF)	ID30A-1 (ESRF)
Wavelength (Å)	0.966	0.966	0.966
Space group	P 3	P 3	P 3
<i>Unit cell parameters</i>			
<i>a, b, c</i> (Å)	90.4, 90.4, 69.3	90.0, 90.0, 69.1	90.1, 90.1, 69.1
<i>α, β, γ</i> (°)	90, 90, 120	90, 90, 120	90, 90, 120
Resolution limits (Å) ^b	39.14–1.50 (1.53–1.50)	44.99–1.66 (1.69–1.66)	51.74–1.61 (1.64–1.61)
Total reflections	238,075 (9,936)	174,685 (8,764)	160,083 (8,063)
Unique reflections	99,464 (4,790)	73,201 (3,621)	79,090 (3,888)
Mean <i>I</i> / <i>σ</i> (<i>I</i>)	6.9 (1.8)	6.0 (1.2)	6.9 (1.1)
Completeness (%)	98.2 (96.4)	98.9 (97.5)	96.9 (96.0)
<i>R</i> _{merge}	0.097 (0.608)	0.098 (0.736)	0.058 (0.658)
<i>R</i> _{pim}	0.074 (0.508)	0.077 (0.587)	0.049 (0.561)
CC _{1/2} ^c	0.987 (0.293)	0.971 (0.385)	0.996 (0.368)
Wilson B-factor (Å ²)	12.2	21.6	20.7
<i>Refinement^d</i>			
<i>R</i> _{work} / <i>R</i> _{free} (%)	13.5/14.7	14.8/17.8	14.7/17.7
No. of test reflections	4,377 (4.3%)	3,816 (5.2%)	4,210 (5.2%)
No. of atoms	5,486	5,184	5,254
Average B-factor (Å ²)	17	25	25
<i>Ramachandran plot (%)</i>			
Favored	96.7	96.9	96.8
Allowed	3.0	2.6	2.8
Outliers	0.3	0.5	0.3
RMSD bond lengths (Å)	0.007	0.011	0.009
RMSD bond angles (°)	1.306	1.524	1.357

^a Data reduction statistics were calculated using the program Aimless (version 0.7.1) in the CCP4i2 package.⁴²

^b Values in parentheses are for the highest resolution shell. Data in this resolution shell were used to calculate the statistics in parentheses in the lines below. ^c Correlation coefficient between equivalent reflections. A value of > 0.3 in the last resolution shell was used to determine the resolution cut-off. ^d Data refinement statistics are reported as determined by the Protein Data Bank validation pipeline, or the program Refmac5 (version 5.8.0218) in the CCP4i2 package.⁴²

In our crystal structure of the ARG1/ABH complex at pH 7.0 (PDB ID: 6Q92), ARG1 exists as a homotrimer with ABH bound as a tetrahedral boronate anion to the manganese cluster in the active site (Figure 4A). This form of ABH, which mimics the tetrahedral intermediate in the hydrolysis mechanism of ARG1,⁴¹ was also observed in previous structures of ARG1 in complex with ABH, for example 2AEB.²⁶

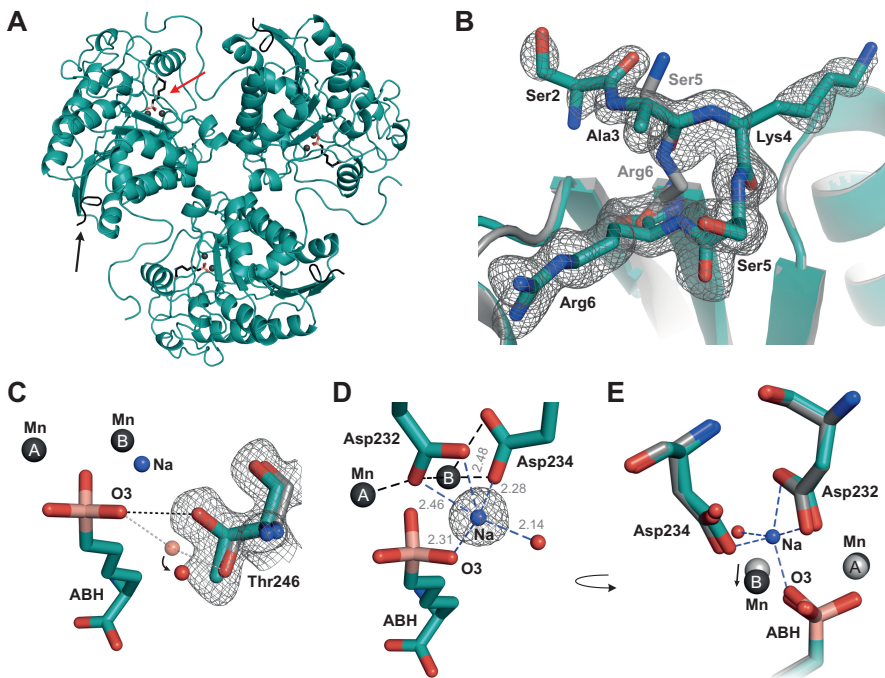


Figure 4. Overlay of the crystal structure of the ARG1/ABH complex at pH 7.0 (PDB ID: 6Q92; teal) and the previously reported ARG1/ABH crystal structure (PDB ID: 2AEB; grey).²⁶ (A) Overview of structure 6Q92 showing the trimeric quaternary structure of ARG1. The red arrow indicates the location of the active site into which ABH is bound. The black arrow indicates the N-terminal residues Ser2 to Arg6. (B) The N-terminal residues Ser2 to Arg6 of the human ARG1/ABH complex at pH 7.0. Electron density around the N-terminal residues is displayed as an $2F_{\text{obs}} - F_{\text{calc}}$ omit map contoured at 1.0σ (standard deviation of electron density). The previously reported human ARG1/ABH crystal structure 2AEB is displayed in grey for only the backbone atoms. (C) Active site structure focusing on the alternate conformation of Thr246 compared to the structure 2AEB (grey with water molecule displayed in light red). Electron density is displayed as in panel B. (D) Observed electron density for a sodium ion in the active site and its coordination interactions. Electron density is displayed as in panel B. (E) Different orientation of the Asp232 and Asp234 residues, and the different position of the manganese ions between our structure (dark grey) and 2AEB (light grey).

During initial refinement of the ARG1/ABH crystal structure at pH 7.0, we noticed the presence of substantial difference density in the $F_{\text{obs}} - F_{\text{calc}}$ map around the N-terminal residues Ser5 and Arg6. This indicated that these residues were present in a different conformation compared to the structure 2AEB. In addition, the electron density revealed the conformation of the N-terminal residues Ser2, Ala3 and Lys4 (Figure 4B). We expect that the presence of the purification tag has reduced the flexibility of the N-terminus and allowed visualization of these N-terminal residues of ARG1 for the first time. Comparison of the active site of our crystal structure and 2AEB further reveals that in our complex the hydroxyl group of residue Thr246 is pointed towards the O3 hydroxyl group of ABH and can interact directly with this group through a hydrogen bond (Figure 4C). In the structure 2AEB, the Thr246 hydroxyl group is pointed away from the O3-hydroxyl of ABH and binds it only via a water-mediated hydrogen bond. Since Thr246 forms a direct hydrogen bond to ABH in our structure, this is accompanied by a displacement of the water molecule (Figure 4C).

During refinement of the ARG1/ABH crystal structure at pH 7.0, we also observed a strong difference density in the $F_{\text{obs}} - F_{\text{calc}}$ map, consistent with the presence of water, or an ion with a low molecular mass, close to the manganese cluster (Figure 4D). The distances between the center of this electron density and most surrounding atoms were too short for hydrogen-bond interactions but consistent with metal-ion solvation (Figure 4D). The negative charge of the surrounding Asp232 and Asp234 residues as well as the boronate anion of ABH (Figure 4D) indicated that the ion carried a positive charge. Since the distances to most surrounding atoms were close to the ideal Na–O distance of 2.41 Å (Figure 4D),⁴³ we suspected the presence of a sodium ion. The ion valence determined using the CheckMyMetal web server⁴³ is consistent with the monovalency of sodium, as is the five-coordinate geometry⁴³ observed for the ion (Figure 4D). Sodium was also the only metal present in a significant concentration in the crystallization solution. While the monovalent sodium ion is not generally surrounded by more than one negatively charged carboxyl side chain,⁴³ as we observed for the ion, this can be explained by the additional coordination of these side chains (*i.e.*, Asp232 and Asp234) to the manganese ions (Figure 4D). Thus, we conclude that the binding of ABH to ARG1 introduces the binding of an additional sodium ion in the active site.

A consequence of the presence of a sodium ion close to the manganese cluster is that the $\text{Mn}_{\text{B}}^{2+}$ -ion is displaced with respect to the $\text{Mn}_{\text{A}}^{2+}$ -ion and the protein, when compared to structure 2AEB (Figure 4E). This is accompanied by an increase in the $\text{Mn}_{\text{A}}^{2+}$ – $\text{Mn}_{\text{B}}^{2+}$ distance from 3.33 Å to 3.43 Å. Moreover, the Asp232 and Asp234 side chains have shifted considerably with respect to the manganese cluster (Figure 4E). These observations might be explained by both the manganese ions and the sodium ion aiming to achieve ideal coordination geometry. Since the manganese cluster and the sodium ion share the

Asp232 and Asp234 residues as coordinating ligands, a displacement of the Mn_B^{2+} -ion as well as a different orientation of the Asp232 and Asp234 residues are needed to achieve the most optimal coordination geometry for all metal ions.

Notably, we only observe the presence of the sodium ion in ARG1 crystal structures with boron-containing ligands, including our complexes with ABH at pH 7.0 and 9.0 and our complex with CB-1158 (see below), but not with other types of ligands or the unliganded enzyme. This suggests that these boron-containing ligands bind in a sodium-dependent manner. Interestingly, the sodium ion is not observed in previous ARG1/ABH structures, either from human or rat ARG1 (PDB ID: 2AEB and 1D3V), although this might be explained by the fact that there was no sodium included in the crystallization conditions used to prepare these crystals.^{26,41} Unfortunately, the original diffraction data were not deposited for these structures, precluding a check if this sodium ion was missed from the electron density in these structures.

pH-dependent structural changes in the ARG1/ABH complex

Comparison of the ARG1/ABH complexes at pH 7.0 and 9.0 (PDB IDs: 6Q92 and 6Q9P) yielded a root-mean-square deviation (RMSD) of all main chain atoms of 0.31 Å for superposition of the 313 residues of monomer A and 0.33 Å for the 309 residues of monomer B. This degree of deviation is primarily caused by a change in the surface loop consisting of residues Glu42 to Asp46 (Figure 5A), which can adopt different conformations (Figure 5B). This loop appears to be relatively flexible with high average B-factors of 28 Å² at pH 7.0 and 48 Å² at pH 9.0, compared to the lower overall B-factors of the protein of 17 Å² and 25 Å², respectively (Table 4). Omission of these residues from the RMSD calculation results in values of 0.13 Å and 0.17 Å for, respectively, superposition of monomers A and B, indicating that there are no other major conformational changes occurring upon increase of the pH.

Comparison of the active site residues in the manganese coordination structure shows that residues Asp232 and Asp234 undergo the most notable pH-dependent changes (Figures 6A–C). At pH 7.0, the Asp232-Oδ2 atom is strongly coordinated to Mn_A^{2+} , but has a distance to Mn_B^{2+} that is too long to be considered inner-sphere metal coordination (Figure 6B). Upon increase of the pH from 7.0 to 9.0, the Asp232-Oδ2 atom shifts away from Mn_A^{2+} and towards Mn_B^{2+} , and thereby forms an inner-sphere metal coordination interaction with Mn_B^{2+} and bridges the manganese ions more symmetrically (Figures 6A–C). The side chain of the nearby Asp234 also moves upon increase of the pH, resulting in a stronger coordination of the Asp234-Oδ1 atom to Mn_B^{2+} , while coordination of the Asp234-Oδ2 atom to Mn_B^{2+} is slightly weakened (Figures 6A–C). These results indicate that the manganese coordination structure of ARG1 is more symmetrical and forms stronger bonds at pH 9.0 compared to pH 7.0.

Although ABH binds in similar fashion in both structures, a clear change in its binding mode is observed upon increase of the pH from 7.0 to 9.0. The boronate anion of ABH is rotated with respect to the manganese ions upon increase of the pH. As a result, the coordination distance of the ABH-O2 atom to Mn_A^{2+} has lengthened, while the distance between the ABH-O3 atom and Mn_A^{2+} has become shorter at pH 9.0 compared to pH 7.0 (Figures 6A, 6B and 6D). Moreover, the ABH-O1 atom adopts a more symmetrical coordination to the manganese cluster at pH 9.0 by shortening of its distance to Mn_A^{2+} and lengthening its distance to Mn_B^{2+} (Figure 6B). In the remaining part of the ABH structure, the hydrogen bond interactions of the α -amino group remain practically unchanged, while the hydrogen-bond interactions of the α -carboxylate group are more sensitive to a change of the pH (Figure 6E). Thus, the pH-dependent difference in the binding mode of ABH is focused mostly around the boronate anion adopting a more symmetrical and therefore more ideal coordination structure to the manganese cluster (Figures 6A, 6B and 6D).

Binding mode of CB-1158 in the ARG1 active site

To study the structural basis of the high potency, slow association kinetics and long target residence time of CB-1158, we determined the crystal structure of human ARG1 with CB-1158 at pH 9.0 at a resolution of 1.61 Å (Table 4; PDB ID: 6QAF). The crystal structure shows that the inhibitor binds in the ARG1 active site as a tetrahedral boronate anion coordinated to the manganese cluster (Figure 7A). Superposition with our crystal structure of the ARG1/ABH complex at pH 9.0 (PDB ID: 6Q9P) shows that the two inhibitors align

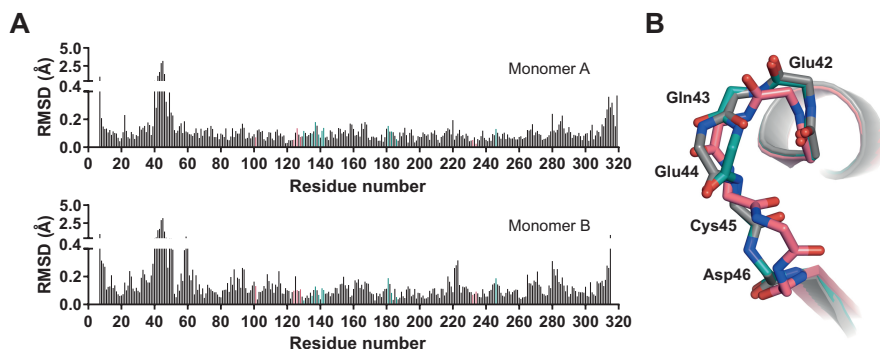


Figure 5. Comparison of the overall structure of the ARG1/ABH complexes at pH 7.0 and 9.0. **(A)** Root-mean-square deviation (RMSD) between the main chain atoms (Ca, C, O and N) of the pH 7.0 complex (PDB ID: 6Q92) and the pH 9.0 complex (PDB ID: 6Q9P) calculated per residue. Pink bars indicate manganese-coordinating residues, while teal bars indicate active site residues interacting with ABH. **(B)** Superposition of the backbone atoms of the Glu42 to Asp46 surface loop in the two structures (pH 7.0 in teal and pH 9.0 in pink) and the previously reported ARG1/ABH crystal structure (PDB ID: 2AEB; grey).

nearly perfectly in the active site (RMSD of 0.17 Å for the 13 matching atoms; Figure 7B). Binding of CB-1158 does not cause any significant conformational changes in the ARG1 active site when compared to the binding of ABH (Figure 7B), and the structure also shows the presence of the active site-bound sodium ion. Moreover, the three direct and four water-mediated hydrogen bonds made by the α -carboxylate and α -amino substituents of ABH (Figure 6E) are likewise maintained for CB-1158 (Figure 7C).

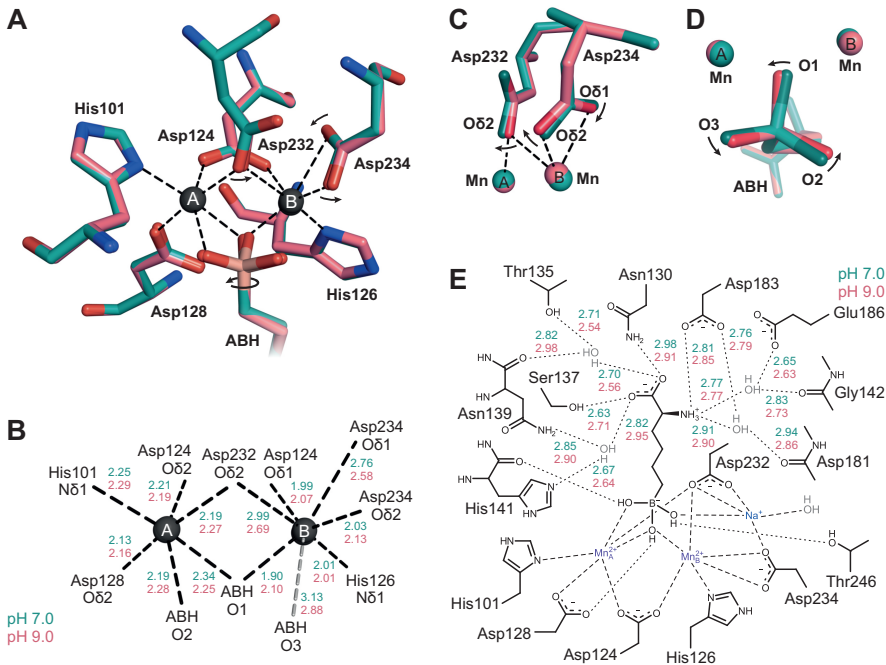


Figure 6. Structural differences between the active sites of the ARG1/ABH complexes at pH 7.0 (teal) and 9.0 (pink). **(A)** Active site detail of the superposition of structures at pH 7.0 (PDB ID: 6Q92) and pH 9.0 (PDB ID: 6Q9P). The black dashed lines indicate the coordination interactions of the complex at pH 9.0. The arrows indicate the direction of the most prominent changes in the manganese coordination structure going from pH 7.0 to 9.0. **(B)** Manganese coordination distances corresponding to the interactions displayed in panel A. Ideal Mn–O distances are 1.91 and 2.19 Å, while ideal Mn–N distances are 1.99 and 2.29 Å.⁴³ The grey dashed line displays an interaction that is not an inner-sphere coordination interaction and is not shown in panel A. **(C)** Detail of the Asp232 and Asp234 residues coordinating to the manganese cluster. The arrows indicate the direction of the structural changes going from pH 7.0 to 9.0. **(D)** Detail of the ABH boronate anion bound near the manganese cluster, displayed as in panel C. **(E)** Schematic representation of ABH bound in the ARG1 active site. Dashed lines indicate coordination interactions with the metal ions, while dotted lines indicate hydrogen-bond interactions made by ABH.

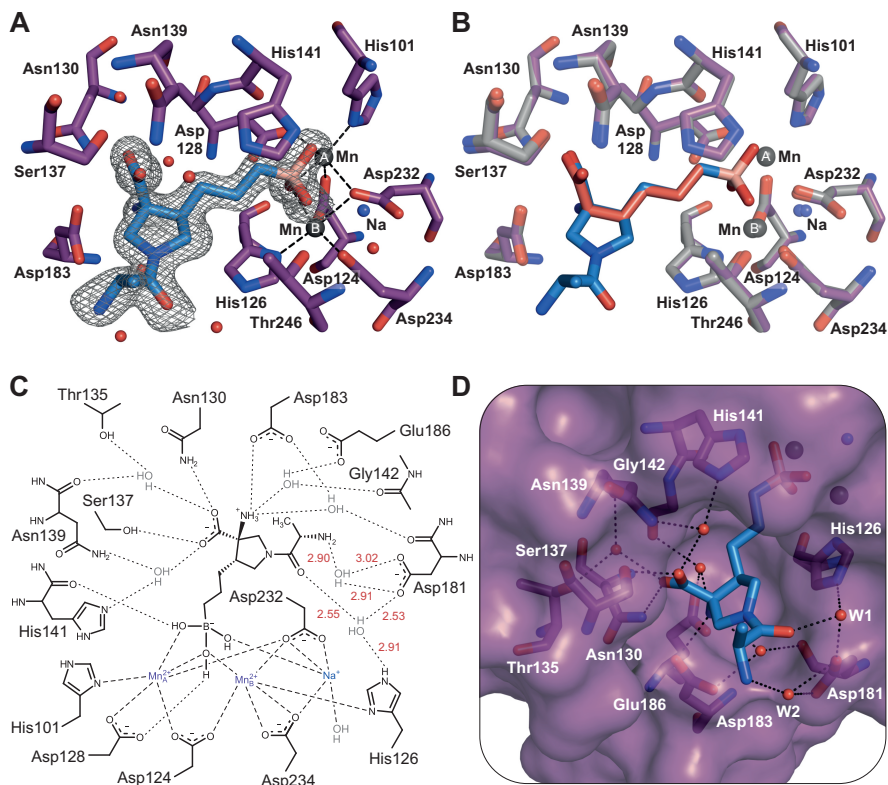


Figure 7. Binding mode of CB-1158 in the human ARG1 active site (PDB ID: 6QAF). **(A)** The ARG1 active site containing the inhibitor CB-1158. The electron density surrounding the inhibitor in monomer A is displayed as a $2F_{\text{obs}} - F_{\text{calc}}$ omit map contoured at 1.0σ . The dashed lines indicate coordination interactions of the inhibitor and active site residues with the manganese cluster. Water molecules are displayed as red spheres. **(B)** Superposition of the crystal structures of the ARG1/CB-1158 complex (PDB ID: 6QAF; purple and blue) and the ARG1/ABH complex at pH 9.0 (PDB ID: 6Q9P; grey and red). **(C)** Schematic representation of CB-1158 bound in the ARG1 active site of monomer A. Dashed lines indicate coordination interactions with the metal ions, while dotted lines indicate hydrogen-bond interactions made by CB-1158. The α -amino group of CB-1158 is displayed in its protonated form, although this group may only be partially protonated at pH 9.0 based on its estimated pK_a of 9.0. Hydrogen-bond distances of the 2-aminopropanoyl functionality are displayed in red. Thr246 and its hydrogen-bond interaction with CB-1158 are excluded from this figure for reasons of clarity. **(D)** Orientation of CB-1158 in the active site pocket in monomer A. Water molecules (W) are shown as red spheres. Important hydrogen-bond networks are displayed as dotted lines.

The additional 2-aminopropanoyl-functionalised pyrrolidine ring of CB-1158 protrudes from the active site pocket towards the bulk solvent (Figure 7D), which is in contrast with the tight embedding of the entire structure of ABH in the ARG1 active site. The methyl group of the 2-aminopropanoyl functionality of CB-1158 is pointed towards the same side of the pyrrolidine ring as the α -carboxylate on the opposite side of the ring (Figures 7A and 7D). In monomer A of our structure, we observe two important water molecules (W1 and W2 in Figure 7D) in close proximity to this 2-aminopropanoyl functionality. In monomer B of the asymmetric unit, we did not observe clear electron density for the outermost water molecule (W2), which is why we focus on monomer A to describe the full binding potential of CB-1158. In this monomer, the presence of the two water molecules allows for two indirect hydrogen-bond interactions to be made with the enzyme, which are not seen in the ABH complex. The water molecule W1 is involved in an indirect hydrogen bond between the oxygen atom of the amide functionality, and both the surface-exposed Asp181 residue and the active site-lining His126 residue (Figures 7C and 7D), while W2 interacts solely with the side chain of Asp181. The opportunity to form new hydrogen-bond interactions is likely to contribute to the favorable potency and binding kinetics of CB-1158 compared to ABH (Tables 2 and 3).

Discussion

The role of ARG1 in tumor immune suppression and its potential as a drug target for cancer immunotherapy has culminated in the clinical development of CB-1158.⁹ Given the importance of ARG1 inhibitors, we studied the characteristics of ABH, nor-NOHA and CB-1158 side-by-side in different biochemical and biophysical assays, including SPR and protein crystallography.

The biochemical activity assay shows that the most potent inhibition of ARG1 occurs by CB-1158 at pH 7.4 ($IC_{50} = 4.1$ nM; Table 2), which is respectively 21- and 6.8-fold more potent than ABH and nor-NOHA at this pH (Table 2). Moreover, nor-NOHA has a potency which is intermediate to the potencies of ABH and CB-1158 at both pH values, which indicates that the boronic acid warhead is not a requisite for strong ARG1 inhibition (Figure 1). Comparison of the inhibitor potencies at pH 7.4 and 9.5 demonstrates that the pH is an important determinant for the potency of ABH and CB-1158, while nor-NOHA remains mostly unaffected by the pH. Interestingly, ABH and CB-1158 have opposing pH-dependent inhibition profiles, with ABH being less potent at pH 7.4 compared to pH 9.5, while CB-1158 becomes more potent (Table 2). The 8-fold decrease in potency of ABH is in line with a previous study showing that the potency of ABH for human ARG2 is almost 30 times lower at pH 7.5 compared to pH 9.5 (Table 1).²⁴

In the thermal shift assay, CB-1158 is the strongest stabilizer of ARG1 at both pH values ($\Delta T_m = 5.6$ and 8.1 °C at respectively pH 7.4 and 9.5; Table 2). At pH 7.4, the melting temperature shift induced by CB-1158 ($\Delta T_m = 8.1$ °C) is even more than 3 °C stronger than the shifts induced by ABH and nor-NOHA ($\Delta T_m = 4.5$ and 4.8 °C, respectively; Table 2). For both nor-NOHA and CB-1158, there is a correlation between the activity assay-based inhibitory potencies and the shifts in thermal stability. When comparing both pH values, nor-NOHA has roughly equal potency in the activity assay as well as an equal effect in the thermal shift assay. CB-1158 has a considerably higher potency in the activity assay at pH 7.4 compared to pH 9.5, consistent with its larger shift of thermal stability at pH 7.4 (Table 2).

The inhibitor binding kinetics determined by SPR show that CB-1158 has both the slowest association and the slowest dissociation kinetics among the inhibitors (Table 3). We expect that these slow dissociation kinetics contribute to its favorable inhibitory potency in the activity assay, which is especially observed at pH 7.4 (Table 2), since the equilibrium binding constant is inversely related to the dissociation constant. For ABH, we observe slow association and dissociation kinetics only at pH 9.5, while its kinetics at pH 7.4 are similar to the relatively fast kinetics of nor-NOHA (Table 3). The slower dissociation of ABH at higher pH is consistent with its increased inhibitory potency at pH 9.5 compared to pH 7.4.

The side-by-side comparison of ABH, nor-NOHA and CB-1158 in different biochemical assays shows that CB-1158 has overall the most favorable characteristics at both pH values, thereby supporting its potential as a drug for targeting tumor immune suppression. Nonetheless, it should be noted that nor-NOHA performed most consistently among the two pH values in the different assays. Therefore, despite its poor pharmacokinetic properties,²⁰ nor-NOHA may still prove valuable as a tool compound for studying ARG1 *in vitro*. Moreover, the relatively potent activity of nor-NOHA indicates that potent ARG1 inhibitors without a boronic acid warhead can be developed.

In order to understand the pH-dependent effects of ARG1 inhibition and stabilization, we studied the pH optimum of ARG1. We measured a roughly 8-fold higher catalytic rate constant (k_{cat}) of ARG1 at pH 9.5 compared to pH 7.4, which is consistent with the frequently reported alkaline pH optimum of the enzyme.²⁹⁻³² This pH optimum could simply result from the catalytic mechanism of ARG1 requiring a hydroxide ion to be bound in the active site, which is present in higher concentrations at alkaline pH.³⁸ However, given the general notion that enzymes evolve to function at their physiologically relevant pH, this would suggest that alkaline pH is relevant for the biological function of ARG1. For granulocytic ARG1, it has been proposed that its enzymatic activity is initiated by a rise in the

phagosomal pH up to 8.5–9.5 upon initiation of neutrophil phagocytosis.^{44,45} Nevertheless, in the context of cancer, it is known that the extracellular tumor microenvironment is slightly acidic (pH 6.5–7.1), while the intracellular pH of tumors ranges between 7.2 and 7.5.^{46,47} In tumors, ARG1 may therefore function at alkaline pH during the early phase of phagocytosis,⁴⁴ while it may continue to function at more neutral pH values in the later stages of phagosome maturation and in the extracellular tumor microenvironment. Therefore, alkaline pH values close to the ARG1 optimum as well as more neutral pH values may both be relevant for ARG1 functioning inside a tumor.

To study the structural basis of the alkaline pH optimum, we determined the crystal structures of the ARG1/ABH complex at pH 7.0 and 9.0. We observe a number of small but significant shifts in the manganese coordination structure, which becomes more symmetrical at increased pH (Figures 6A–D). This probably allows for a more optimal positioning of the hydroxide ion required for ARG1 catalytic activity, which is represented in our structures by the O1-atom of ABH (Figure 6D). The more symmetrical coordination of the manganese cluster presumably underlies the increased activity of ARG1 at higher pH (Figures 6A–D).

In order to understand the increased potency of ABH at increased pH, we looked specifically into the binding mode of ABH in the ARG1 active site at pH 7.0 and 9.0 (Figures 6A, 6B and 6D). Since ABH mimics the tetrahedral intermediate in the ARG1 catalytic mechanism, we postulate that it may bind better to a catalytically more competent enzyme, *i.e.*, ARG1 at pH 9.0. This is substantiated by our crystal structures showing that the boronate anion of ABH assumes a more symmetrical coordination to the manganese cluster at increased pH (Figures 6B and 6D). Since there are no considerable changes observed in the orientation or the interactions made by the remainder of the ABH structure (Figure 6E), we expect that this more symmetrical orientation with respect to the manganese cluster is the reason why ABH binds more potently at increased pH.

Interesting is also the observation of the sodium ion in the ARG1 active site of our structures, which has not been previously reported for any ARG1 crystal structure. Since this sodium ion is located in such close proximity to the manganese cluster (Figure 4D), and has a direct influence on the position of the Mn₆²⁺-ion as well as the orientation of the Asp232 and Asp234 side chains (Figure 4E), we expect that this sodium ion could prove important in the mechanism of ARG1 inhibition by boron-containing inhibitors.

The structural basis of the favorable potency of CB-1158 was uncovered by the crystal structure of ARG1 in complex with this inhibitor (Figure 7). This structure indicates that the binding mode of CB-1158 is consistent with the binding mode of ABH that we observe

in our structures. Moreover, an additional hydrogen-bond network involving two water molecules and the residues Asp181 and His126 (Figure 7) is expected to contribute to its potent inhibition character (Table 2). Water-mediated hydrogen-bond interactions with Asp181 have previously been reported for α,α -disubstituted ABH analogues, and this correlated with a more favorable potency of these analogues compared to ABH.²² The crystal structure of CB-1158 is the first to also show a water-mediated hydrogen-bond interaction with the more buried His126 residue. This crystal structure therefore indicates that binding towards these active site residues is beneficial for inhibitor affinity. Moreover, CB-1158 is expected to have an increased rigidity compared to ABH due to a decrease in the number of rotatable bonds by introduction of the pyrrolidine ring (Figure 1), which constricts CB-1158 into the correct rotamer for binding into the ARG1 active site (Figure 7). We expect that this rigidity also contributes to the potent inhibition of ARG1 by CB-1158, as measured in the biochemical activity assays (Table 2).

CB-1158 is more potent at pH 7.4 compared to pH 9.5. The amino group of the 2-amino-propanoyl functionality of CB-1158 (Figure 1) has a predicted pK_a value of 8.2, indicating that this group is predominantly protonated at pH 7.4 and unprotonated at pH 9.5. While the amino group is pointed away from the acidic Asp181 residue and forms only a water-mediated hydrogen bond with this residue at pH 9.0 (Figures 7C and 7D), binding of the inhibitor at pH 7.4 may be favored by electrostatic interaction of the protonated amino group with the active site Asp181 residue. Alternatively, another nearby residue such as the acidic Asp183 (Figure 7D) may facilitate the positioning of the inhibitor in the ARG1 active site at pH 7.4. This may explain the observed increase in potency at lower pH. The increase in potency of CB-1158 contrasts with the decrease in potency observed for ABH at pH 7.4 compared to pH 9.5 (Table 2). The crystal structures show that ABH makes less interactions with the ARG1 active site than CB-1158, apart from the boronate anion (Figures 6E and 7C). This could indicate that the coordination symmetry of the boronate anion to the manganese cluster plays the most significant role in inhibitor binding at pH 9.5, whereas at pH 7.4, the interactions made by the remaining structure of the inhibitor are more important for inhibitor potency.

CB-1158 appears to be an ARG1 inhibitor with a long target residence time at both pH 9.5 and 7.4 (Figure 3 and Table 3), which could be very interesting due to anticipated favorable pharmacokinetic properties.⁴⁰ Moreover, formation of the enzyme–inhibitor complex appears to occur with slow association. For ABH at pH 9.5, slow association and dissociation kinetics similar to those of CB-1158 are found. While slow-binding inhibitors of ARG1 have not previously been reported, this is in agreement with a previous study on ARG2 claiming that ABH has a slow-binding character at pH 9.5.²⁴ This is explained by the fact that at pH 9.5 the tetrahedral boronate form of boron-containing inhibitors

is expected to predominate over the trigonal boronic acid form. Slow association of the inhibitor may therefore be caused by a slow conformational change of the active site required to accommodate the tetrahedral boronate species. Additionally, binding of the tetrahedral inhibitor species requires the expulsion of the tightly-bound manganese-coordinated hydroxide ion from the active site, which is replaced by a hydroxyl group of the boronate anion. This displacement is suggested to be a slow event, which could contribute to the slow association kinetics of the inhibitor.²⁴ However, the fact that CB-1158 has slow association and dissociation kinetics at both pH 7.4 and 9.5, while ABH only has comparable slow kinetics at pH 9.5, indicates that another factor contributes to the kinetics of CB-1158. We propose that the slow binding kinetics of CB-1158 are due to, or enhanced by, an active site conformational change. As we do not observe such a change in the crystal structure of the ARG1/CB-1158 complex (Figure 7B), we expect that a conformational change is only a temporary adaptation required for the binding event of the inhibitor, and that the conformation of the enzyme returns to normal once the inhibitor is bound. Such conformational plasticity may only be required for binding of CB-1158 in the active site, but not for ABH or nor-NOHA, because CB-1158 has a larger size and reduced flexibility compared to these inhibitors. This binding mechanism may also explain the long target residence time of CB-1158, since dissociation of the tetrahedral boronate form of the inhibitor from the enzyme active site will require a similar conformational change to take place.

In summary, we show that the alkaline pH optimum of ARG1 is not merely a consequence of the higher abundance of hydroxide ions at increased pH, but that ARG1 also shows changes at a structural level by the catalytic manganese ions adopting a more symmetrical coordination structure at elevated pH. We have uncovered the contrasting pH-dependence of the potencies of ABH and CB-1158. We propose that at increased pH, the coordination symmetry of the boronate anion to the manganese cluster becomes increasingly important for inhibitor potency compared to interactions made by the remainder of the inhibitor. Using SPR, we show that association and dissociation of CB-1158 from the ARG1 active site occurs through slow kinetics. We propose that active site conformational plasticity is involved in inhibitor binding, probably due to its increased rigidity. Finally, comparison of the crystal structures of ARG1 bound to ABH and CB-1158 reveals an additional hydrogen-bond network formed by CB-1158, which, in addition to the increased rigidity of this inhibitor, might underly its favorable potency. The crystal structure of the ARG1/CB-1158 complex will support future structure-based drug design efforts of ARG1 inhibitors.

Materials and methods

Protein expression and purification of ARG1

Full-length human ARG1 containing an N-terminal hexa-histidine tag and thrombin-cleavable linker (Supplementary Figure 1A) was expressed in *Escherichia coli* Rosetta (DE3) competent cells (Novagen, cat. no. 70954-4). Bacteria were cultured in LB medium containing 35 µg/mL chloramphenicol and 100 µg/mL ampicillin in a shaking incubator at 37 °C to OD₆₀₀ of 0.6–0.8. Expression was induced by addition of 0.1 mM isopropyl-β-D-thiogalactopyranoside, followed by incubation at 37 °C for 3–4 h. The cells were harvested by centrifugation and the resulting pellets were stored at –20 °C. For purification, the bacterial pellets were resuspended in purification buffer, consisting of 10 mM HEPES, pH 7.5, 100 mM NaCl, 1 mM TCEP, 1 mM MnCl₂ and cOmplete™ EDTA-free protease inhibitor cocktail (Roche). The cells were lysed using a liquid homogenizer (Avestin). After centrifugation, the supernatant was heated to 60 °C for 20 min and purification was performed by affinity chromatography using Ni-NTA Superflow beads (Qiagen). For use in biochemical assays, thermal shift assays and surface plasmon resonance, the purified protein was desalted on PD-10 columns (GE Healthcare) and supplemented with 20% glycerol (Acros Organics) prior to storage at –80 °C. Purity of the enzyme was estimated by visual inspection of SDS-PAGE gels (Supplementary Figures 1B and 1C). For use in protein crystallography, the purification buffer was exchanged to crystallization buffer (50 mM Bicine, pH 8.5, and 100 µM MnCl₂), followed by concentration of the enzyme to 3.6 mg/mL, as determined using a NanoDrop 2000 Spectrophotometer (Thermo Scientific), and storage at –80 °C.

Inhibitors

ABH was purchased from Sigma-Aldrich (cat. no. SML1466), nor-NOHA from Tocris Bioscience (cat. no. 6370) and CB-1158 ((3*R*,4*S*)-3-amino-1-[(2*S*)-2-aminopropanoyl]-4-(3-boronopropyl)pyrrolidine-3-carboxylic acid) from ChemieTek (cat. no. CT-CB1158).

Colorimetric urea assay

ARG1 activity was monitored by measurement of the rate of urea formation in a classic colorimetric assay.^{33,34} All components of the assay were diluted in reaction buffer 1 (8 mM Na₂HPO₄, 2 mM KH₂PO₄, pH 7.4, 137 mM NaCl, 2.7 mM KCl and 0.05% Tween-20) or reaction buffer 2 (10 mM glycine, pH 9.5, 137 mM NaCl, 2.7 mM KCl and 0.05% Tween-20). Compounds were either dissolved and diluted in DMSO, followed by further dilution in reaction buffer, or dissolved in MilliQ water (MQ) and diluted in reaction buffer to the desired concentrations. In a clear 384-well plate (Greiner, cat. no. 781101), 10 µL diluted compound and 10 µL of 3 nM (pH 9.5) or 15 nM (pH 7.4) ARG1 were combined and incubated for 90 min at room temperature. Then, 10 µL of 15 mM (pH 9.5) or 7.5 mM

(pH 7.4) L-arginine (Acros Organics, cat. no. 105000250) was added to the plate, followed by incubation for 30 min. A 1:1 mixture of reagent A (10 mM *o*-phthaldialdehyde, 0.4% polyoxyethylene (23) lauryl ether (w/v) and 1.8 M sulfuric acid) and reagent B (1.3 mM primaquine diphosphate, 0.4% polyoxyethylene (23) lauryl ether (w/v), 130 mM boric acid and 3.6 M sulfuric acid) was prepared. The enzymatic reaction was stopped by addition of 30 μ L of the reagent A + B mixture. After incubation with the reagent mixture for 60 min (pH 9.5) or 120 min (pH 7.4), the absorbance was measured at 450 nm using the EnVision 2104 Multilabel Plate Reader (PerkinElmer; excitation filter P450). The final concentrations of ARG1 and L-arginine in the assay were respectively 1 nM and 5 mM at pH 9.5, and 5 nM and 2.5 mM at pH 7.4.

The reported values were measured in quadruplicate in four independent experiments. Dose-response curves were fitted with a four-parameter logistic regression using XLFit (IDBS) to determine IC_{50} values. Graphs for the manuscript were prepared using Prism (GraphPad Software). Since the evaluated inhibitors are competitive inhibitors of ARG1, inhibition constants (K_i) were determined using the Cheng–Prusoff equation (Eq. [1]),⁴⁸ in which $[S]$ is the substrate concentration and K_M is the Michaelis constant of the enzyme for its substrate.

$$K_i = \frac{IC_{50}}{1 + ([S] / K_M)} \quad (1)$$

Apparent Michaelis–Menten parameters were determined using the colorimetric urea assay at both pH 7.4 and 9.5 by measurement of initial reaction rates in the presence of varying concentrations of L-arginine.

Thermal shift assay

Purified ARG1 was diluted to 0.2 mg/mL in 50 mM glycine pH 9.5 or 50 mM Na_2HPO_4 pH 7.4. In a 96-well PCR plate (Greiner, cat no. 652260), 10 μ L of the enzyme solution was mixed with 5 μ L of 200 μ M compound dissolved in MQ. Incubation was performed for 45 min at room temperature, followed by the addition of 5 μ L 625 times diluted SYPRO Orange (Life Technologies, cat no. S6650) in MQ. The final concentrations in the assay were 0.1 mg/mL ARG1, 50 μ M inhibitor and 2,500 times diluted SYPRO Orange. The plate was sealed with Microseal B Adhesive Sealer (Bio-Rad, cat. no. MSB1001) and placed in a CFX96 Real-Time Detection System (Bio-Rad). The temperature was increased from 20 to 95 $^{\circ}$ C in increments of 0.5 $^{\circ}$ C during which the SYPRO Orange fluorescence was measured. The resulting datasets were first truncated to contain only the data points that lie between the minimal and maximal fluorescence signals. The remaining data were then fitted to the sigmoidal five-parameter equation (Eq. [2]),⁴⁹ in which F_{min} and F_{max} are respectively the minimum and maximum fluorescent signals of the melting transition, T is

the temperature, a is the hill slope and c is the asymmetric factor. The melting temperature (T_m) was then determined as the point of inflection of the melting curve (Eq. [3]).⁴⁹ The reported values were measured in quadruplicate in four independent experiments.

$$F(T) = F_{\min} + \frac{F_{\max} - F_{\min}}{(1 + e^{(T' - T)/a})^c} \quad (2)$$

$$T_m(\text{inflection}) = T' - a \times \ln\left(\frac{1}{c}\right) \quad (3)$$

Surface plasmon resonance

Binding kinetics of the inhibitors were determined by SPR using a Biacore T200 (GE Healthcare). ARG1 was immobilized on a Ni-NTA sensor chip by Ni-mediated affinity capturing and amine-coupling to a level of 4,000 or 6,000 resonance units (RU) using 60 $\mu\text{g}/\text{mL}$ ARG1 in running buffer 1 (50 mM glycine, pH 9.5, 150 mM KCl and 0.01% Tween-20) or running buffer 2 (50 mM Na_2HPO_4 , pH 7.4, 150 mM KCl and 0.01% Tween-20). The inhibitors were diluted in running buffer from a stock solution in MQ and were injected in an increasing concentration range of 0.1, 0.316, 1, 3.16 and 10 μM . Single cycle kinetics were used for measuring compound binding with a flow rate of 30 $\mu\text{L}/\text{min}$, an association time of 100 s per injection, and a dissociation time of 1,800 s. The compound response was subtracted with both the reference channel response and the blank injection. The Biacore Evaluation software was used to fit the data to the Langmuir 1:1 binding model with χ^2 values ranging between 0.0024 and 0.30 RU^2 for R_{\max} values of 3.2 to 32 RU, indicating minimal deviation between the fit and the experimental data. This was confirmed by determination of the reliability of the curve fits as described previously.⁵⁰ All combinations of the inhibitors and pH conditions were measured in at least two technical replicates to determine the kinetic constants k_a , k_d and K_D . The target residence time (τ) was calculated from the k_d value using the formula $\tau = 1/k_d$.

Protein crystallography and X-ray diffraction data collection

Crystals of human ARG1 were prepared through hanging drop vapor diffusion at 21 °C. Drops containing 1 μL of enzyme solution (3.6 mg/mL human ARG1, 50 mM Bicine, pH 8.5, and 100 μM MnCl_2) and 1 μL of precipitant solution, consisting of 200 mM MIB buffer (sodium malonate, imidazole and boric acid in a 2:3:3 M ratio), pH 4.0, and 22–24% (w/v) PEG 1500, were equilibrated against a reservoir containing 500 μL precipitant solution. Rod-like hexagonal crystals generally appeared within a few days. One day prior to soaking of the crystals with inhibitor, the crystals were washed with soaking solution (200 mM MMT buffer [DL -malic acid, MES and Tris base at 1:2:2 M ratios], pH 7.0 or 9.0, and 22–24% PEG 1500). This was done to remove boric acid from the ARG1 active site, since this component of the MIB buffer can also act as an inhibitor.¹⁷ The crystals were

then gradually soaked with 15 mM of the inhibitor during thirteen days for ABH and four days for CB-1158. Subsequently, the crystals were cryoprotected with soaking solution containing an additional 30% ethylene glycol prior to flash cooling in liquid nitrogen.

X-ray diffraction data were collected at the European Synchrotron Radiation Facility (Grenoble, France) on the ID30A-1 beamline. Diffraction data were integrated using Mosflm, followed by space group analysis and data reduction using Pointless, Aimless and CTruncate in the CCP4i2 program suite.⁴² The crystals all exhibited hemihedral twinning and belonged to the space group P3. The crystal structure of ARG1 with CB-1158 was solved by molecular replacement in Molrep using a previously reported ARG1/ABH structure (PDB ID: 2AEB)²⁶ as a search model, while the crystal structures of the ARG1/ABH complexes at pH 7.0 and 9.0 were solved using the crystal structure of ARG1 with CB-1158 as a search model. The structures were refined using the Refmac5 program with twin refinement in CCP4i2⁴² and by manual fitting in WinCoot.⁵¹ To prevent over-refinement, reflections with the same Miller (hkl) indices were used to calculate the free R-factor for all three structures. The presence of the inhibitor in the ARG1 active site of both monomers was established by calculating initial electron density in absence of the ligand and was further confirmed after refinement by calculating an omit map in CCP4i.⁴² The manganese ions were refined anisotropically. All protein structure images were generated using PyMOL 1.7.4.5.⁵² Data collection and refinement details can be found in Table 4. Superposition and subsequent structural comparison of the ARG1 complexes was performed separately for each monomer (*i.e.*, A and B) to exclude the effect of relative monomer position from the tertiary structure analyses. The valency of the sodium ions was determined using the CheckMyMetal web server.⁴³ Estimation of pK_a values was performed in MarvinSketch. The reported B-factors are a measure of the displacement of atoms from their average position. These B-factors represent both static disorder (*i.e.*, the presence of different conformations in different parts of the crystal) and dynamic disorder (*i.e.*, thermal vibration of the atoms), as well as crystal packing artefacts.⁵³

Accession numbers

The crystal structures of the ARG1/inhibitor complexes have been deposited in the PDB under IDs 6Q92 (ABH at pH 7.0), 6Q9P (ABH at pH 9.0) and 6QAF (CB-1158 at pH 9.0).

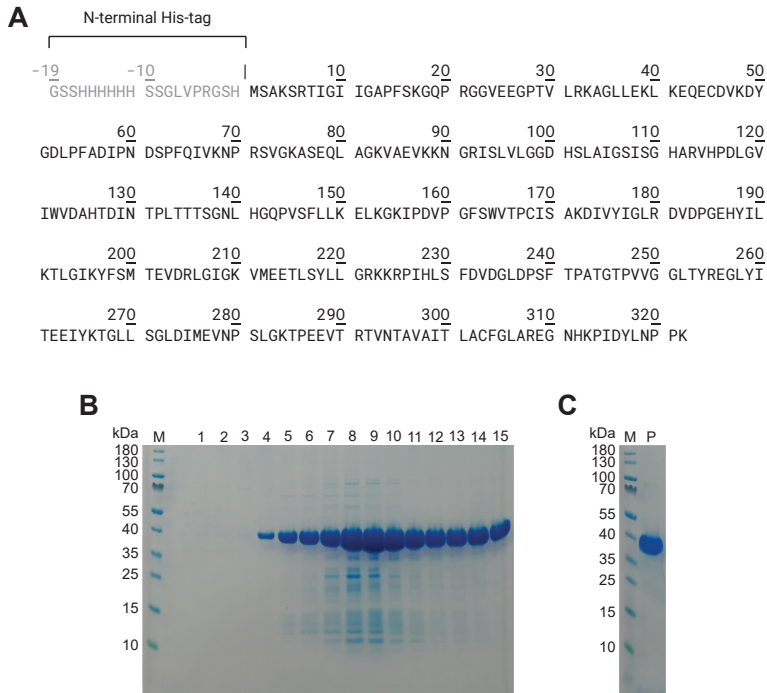
References

1. Gooden, M. J. M., de Bock, G. H., Leffers, N., Daemen, T. & Nijman, H. W. The prognostic influence of tumour-infiltrating lymphocytes in cancer: a systematic review with meta-analysis. *Br. J. Cancer* **105**, 93–103 (2011).
2. Galon, J., Angell, H. K., Bedognetti, D. & Marincola, F. M. The continuum of cancer immunosurveillance: prognostic, predictive, and mechanistic signatures. *Immunity* **39**, 11–26 (2013).
3. Hodi, F. S. *et al.* Improved survival with ipilimumab in patients with metastatic melanoma. *N. Engl. J. Med.* **363**, 711–23 (2010).
4. Robert, C. *et al.* Pembrolizumab versus ipilimumab in advanced melanoma. *N. Engl. J. Med.* **372**, 2521–32 (2015).
5. Jenkins, R. W., Barbie, D. A. & Flaherty, K. T. Mechanisms of resistance to immune checkpoint inhibitors. *Br. J. Cancer* **118**, 9–16 (2018).
6. Gabrilovich, D. I., Ostrand-Rosenberg, S. & Bronte, V. Coordinated regulation of myeloid cells by tumours. *Nat. Rev. Immunol.* **12**, 253–68 (2012).
7. Munder, M. Arginase: an emerging key player in the mammalian immune system. *Br. J. Pharmacol.* **158**, 638–51 (2009).
8. Rodriguez, P. C. *et al.* Arginase I production in the tumor microenvironment by mature myeloid cells inhibits T-cell receptor expression and antigen-specific T-cell responses. *Cancer Res.* **64**, 5839–49 (2004).
9. Steggerda, S. M. *et al.* Inhibition of arginase by CB-1158 blocks myeloid cell-mediated immune suppression in the tumor microenvironment. *J. Immunother. Cancer* **5**, 101 (2017).
10. Oberlies, J. *et al.* Regulation of NK cell function by human granulocyte arginase. *J. Immunol.* **182**, 5259–67 (2009).
11. Geiger, R. *et al.* L-arginine modulates T cell metabolism and enhances survival and anti-tumor activity. *Cell* **167**, 829–42.e13 (2016).
12. Zea, A. H. *et al.* Arginase-producing myeloid suppressor cells in renal cell carcinoma patients: a mechanism of tumor evasion. *Cancer Res.* **65**, 3044–8 (2005).
13. Czystowska-Kuzmicz, M. *et al.* Small extracellular vesicles containing arginase-1 suppress T-cell responses and promote tumor growth in ovarian carcinoma. *Nat. Commun.* **10**, 3000 (2019).
14. Narita, Y. *et al.* The key role of IL-6-arginase cascade for inducing dendritic cell-dependent CD4⁺ T cell dysfunction in tumor-bearing mice. *J. Immunol.* **190**, 812–20 (2013).
15. Miret, J. J. *et al.* Suppression of myeloid cell arginase activity leads to therapeutic response in a NSCLC mouse model by activating anti-tumor immunity. *J. Immunother. Cancer* **7**, 32 (2019).
16. Caldwell, R. W., Rodriguez, P. C., Toque, H. A., Narayanan, S. P. & Caldwell, R. B. Arginase: a multifaceted enzyme important in health and disease. *Physiol. Rev.* **98**, 641–65 (2018).
17. Baggio, R. *et al.* Inhibition of Mn²⁺-arginase by borate leads to the design of a transition state analogue inhibitor, 2(S)-amino-6-borohexanoic acid. *J. Am. Chem. Soc.* **119**, 8107–8 (1997).
18. Custot, J. *et al.* The new α -amino acid N^ω-hydroxy-nor-L-arginine: a high-affinity inhibitor of arginase well adapted to bind to its manganese cluster. *J. Am. Chem. Soc.* **119**, 4086–7 (1997).
19. Golebiowski, A. *et al.* Synthesis of quaternary α -amino acid-based arginase inhibitors via the Ugi reaction. *Bioorg. Med. Chem. Lett.* **23**, 4837–41 (2013).
20. Havlinova, Z., Babicova, A., Hroch, M. & Chladek, J. Comparative pharmacokinetics of N^ω-hydroxy-nor-L-arginine, an arginase inhibitor, after single-dose intravenous, intraperitoneal and intratracheal administration to brown Norway rats. *Xenobiotica* **43**, 886–94 (2013).

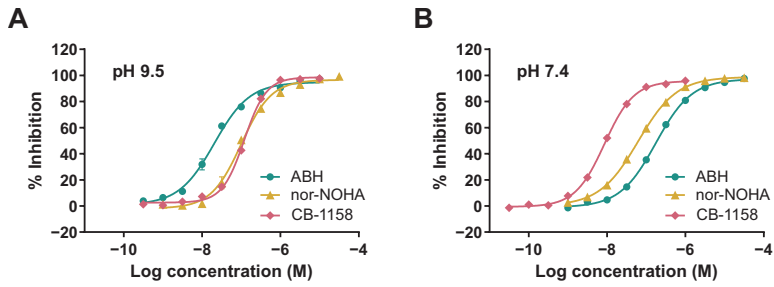
21. Ivanenkov, Y. A. & Chufarova, N. V. Small-molecule arginase inhibitors. *Pharm. Pat. Anal.* **3**, 65–85 (2014).
22. Van Zandt, M. C. *et al.* Discovery of (*R*)-2-amino-6-borono-2-(2-(piperidin-1-yl)ethyl)hexanoic acid and congeners as highly potent inhibitors of human arginases I and II for treatment of myocardial reperfusion injury. *J. Med. Chem.* **56**, 2568–80 (2013).
23. Golebiowski, A. *et al.* 2-Substituted-2-amino-6-borohexanoic acids as arginase inhibitors. *Bioorg. Med. Chem. Lett.* **23**, 2027–30 (2013).
24. Colleluori, D. M. & Ash, D. E. Classical and slow-binding inhibitors of human type II arginase. *Biochemistry* **40**, 9356–62 (2001).
25. Van Zandt, M. C. *et al.* Discovery of *N*-substituted 3-amino-4-(3-boronopropyl)pyrrolidine-3-carboxylic acids as highly potent third-generation inhibitors of human arginase I and II. *J. Med. Chem.* **62**, 8164–77 (2019).
26. Di Costanzo, L. *et al.* Crystal structure of human arginase I at 1.29-Å resolution and exploration of inhibition in the immune response. *Proc. Natl. Acad. Sci. U. S. A.* **102**, 13058–63 (2005).
27. Ilies, M., Di Costanzo, L., Dowling, D. P., Thorn, K. J. & Christianson, D. W. Binding of α,α -disubstituted amino acids to arginase suggests new avenues for inhibitor design. *J. Med. Chem.* **54**, 5432–43 (2011).
28. Di Costanzo, L., Ilies, M., Thorn, K. J. & Christianson, D. W. Inhibition of human arginase I by substrate and product analogues. *Arch. Biochem. Biophys.* **496**, 101–8 (2010).
29. Zakalskiy, A. E. *et al.* Overexpression of (His)₆-tagged human arginase I in *Saccharomyces cerevisiae* and enzyme purification using metal affinity chromatography. *Protein Expr. Purif.* **81**, 63–8 (2012).
30. Jenkinson, C. P., Grody, W. W. & Cederbaum, S. D. Comparative properties of arginases. *Comp. Biochem. Physiol. B. Biochem. Mol. Biol.* **114**, 107–32 (1996).
31. Cabello, J., Basilio, C. & Prajoux, V. Kinetic properties of erythrocyte- and liver arginase. *Biochim. Biophys. Acta* **48**, 148–52 (1961).
32. Berüter, J., Colombo, J. P. & Bachmann, C. Purification and properties of arginase from human liver and erythrocytes. *Biochem. J.* **175**, 449–54 (1978).
33. Jung, D., Biggs, H., Erikson, J. & Ledyard, P. U. New colorimetric reaction for end-point, continuous-flow, and kinetic measurement of urea. *Clin. Chem.* **21**, 1136–40 (1975).
34. Zawada, R. J. X., Kwan, P., Olszewski, K. L., Llinas, M. & Huang, S.-G. Quantitative determination of urea concentrations in cell culture medium. *Biochem. Cell Biol.* **87**, 541–4 (2009).
35. Stone, E. M. *et al.* Replacing Mn²⁺ with Co²⁺ in human Arginase I enhances cytotoxicity toward L-arginine auxotrophic cancer cell lines. *ACS Chem. Biol.* **5**, 333–42 (2010).
36. Alarcón, R. *et al.* Mutational analysis of substrate recognition by human arginase type I – agmatinase activity of the N130D variant. *FEBS J.* **273**, 5625–31 (2006).
37. Tsui, S.-M. *et al.* Pegylated derivatives of recombinant human arginase (rhArg1) for sustained *in vivo* activity in cancer therapy: preparation, characterization and analysis of their pharmacodynamics *in vivo* and *in vitro* and action upon hepatocellular carcinoma cell (HCC). *Cancer Cell Int.* **9**, 9 (2009).
38. Scolnick, L. R., Kanyo, Z. F., Cavalli, R. C., Ash, D. E. & Christianson, D. W. Altering the binuclear manganese cluster of arginase diminishes thermostability and catalytic function. *Biochemistry* **36**, 10558–65 (1997).
39. Romero, P. A. *et al.* SCHEMA-designed variants of human Arginase I and II reveal sequence elements important to stability and catalysis. *ACS Synth. Biol.* **1**, 221–8 (2012).
40. Copeland, R. A., Pompliano, D. L. & Meek, T. D. Drug-target residence time and its implications for lead optimization. *Nat. Rev. Drug Discov.* **5**, 730–9 (2006).
41. Cox, J. D., Kim, N. N., Traish, A. M. & Christianson, D. W. Arginase-boronic acid complex highlights a physiological role in erectile function. *Nat. Struct. Biol.* **6**, 1043–7 (1999).

42. Winn, M. D. *et al.* Overview of the CCP4 suite and current developments. *Acta Crystallogr. D. Biol. Crystallogr.* **67**, 235–42 (2011).
43. Zheng, H. *et al.* CheckMyMetal: a macromolecular metal-binding validation tool. *Acta Crystallogr. D. Struct. Biol.* **73**, 223–33 (2017).
44. Munder, M. *et al.* Arginase I is constitutively expressed in human granulocytes and participates in fungicidal activity. *Blood* **105**, 2549–56 (2005).
45. Levine, A. P., Duchon, M. R., de Villiers, S., Rich, P. R. & Segal, A. W. Alkalinity of neutrophil phagocytic vacuoles is modulated by HVCN1 and has consequences for myeloperoxidase activity. *PLoS One* **10**, e0125906 (2015).
46. Schwartz, L., Seyfried, T., Alfarouk, K. O., Da Veiga Moreira, J. & Fais, S. Out of Warburg effect: an effective cancer treatment targeting the tumor specific metabolism and dysregulated pH. *Semin. Cancer Biol.* **43**, 134–8 (2017).
47. Webb, B. A., Chimenti, M., Jacobson, M. P. & Barber, D. L. Dysregulated pH: a perfect storm for cancer progression. *Nat. Rev. Cancer* **11**, 671–7 (2011).
48. Cheng, Y. & Prusoff, W. H. Relationship between the inhibition constant (K_i) and the concentration of inhibitor which causes 50 per cent inhibition (I_{50}) of an enzymatic reaction. *Biochem. Pharmacol.* **22**, 3099–108 (1973).
49. Schulz, M. N., Landström, J. & Hubbard, R. E. MTSA—a Matlab program to fit thermal shift data. *Anal. Biochem.* **433**, 43–7 (2013).
50. Willemsen-Seegers, N. *et al.* Compound selectivity and target residence time of kinase inhibitors studied with surface plasmon resonance. *J. Mol. Biol.* **429**, 574–86 (2017).
51. Emsley, P., Lohkamp, B., Scott, W. G. & Cowtan, K. Features and development of Coot. *Acta Crystallogr. D. Biol. Crystallogr.* **66**, 486–501 (2010).
52. DeLano, W. L. The Pymol Molecular Graphics System, version 1.5, Schrödinger, LLC, New York. (2012).
53. Rhodes, G. *Crystallography made crystal clear: a guide for users of macromolecular models.* (Academic Press, 1993).

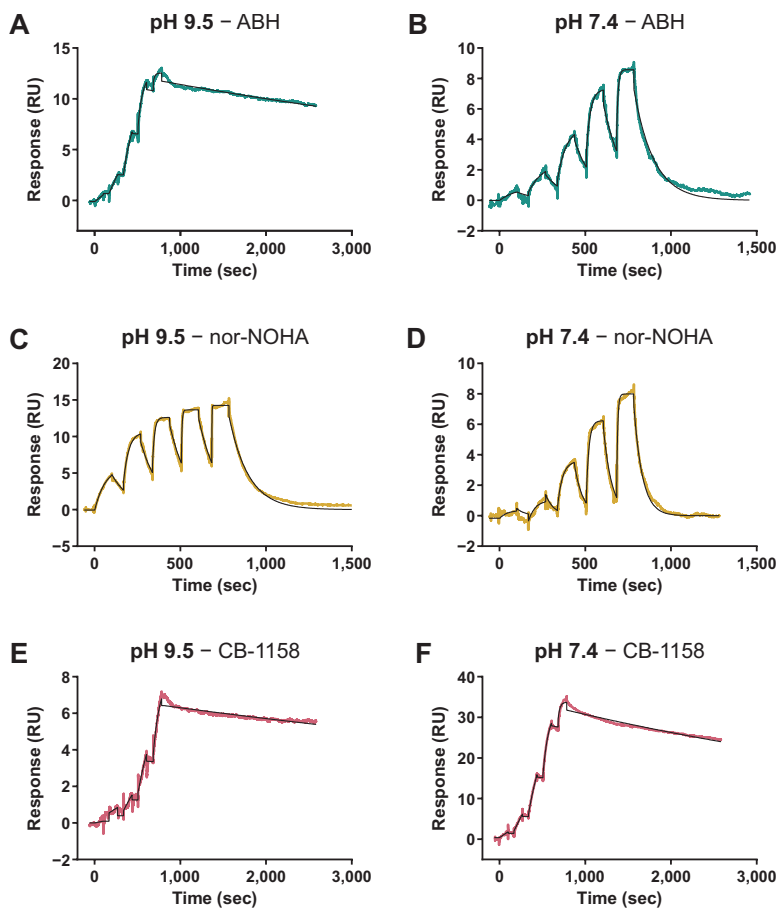
Supplementary data



Supplementary Figure 1. Amino acid sequence and SDS-PAGE analysis of the recombinantly expressed human ARG1 enzyme. **(A)** Amino acid sequence of full-length human ARG1 containing an N-terminal hexa-histidine tag and thrombin-cleavable linker. The N-terminal tag is indicated with negative numbers to allow direct comparison of this sequence with other human ARG1 sequences. **(B)** SDS-PAGE analysis of the fractions obtained during affinity chromatography (indicated by the numbers 1 to 15). Fractions 6 to 15 were combined to obtain the purified enzyme preparation shown in panel C. M, marker; P, purified enzyme preparation.



Supplementary Figure 2. Dose-response curves of inhibitors in the ARG1 colorimetric urea assay. (A) Dose-response curves of ABH, nor-NOHA and CB-1158 at pH 9.5 and (B) at pH 7.4. The data points represent the mean of four technical replicates. Error bars indicate standard deviation. Missing error bars indicate that these errors are smaller than the symbol size.



Supplementary Figure 3. Individual surface plasmon resonance sensorgrams of ARG1 inhibitors at pH 9.5 and 7.4. The displayed graphs present the same data sets as in Figure 3, but with the absolute responses and a longer time scale for the inhibitors with long target residence times. The colored lines show the actual response determined by SPR, while the black lines displays the fit obtained using a 1:1 binding model.

ARG1



Chapter 5

High-throughput fluorescence-based activity assay for arginase 1

Yvonne Grobben¹, Nicole Willemsen-Seegers¹, Joost C. M. Uitdehaag¹, Jos de Man¹, Jan van Groningen², Johan Friesen², Helma van den Hurk², Rogier C. Buijsman¹ and Guido J. R. Zaman¹

¹ Netherlands Translational Research Center B.V., Oss, The Netherlands

² Pivot Park Screening Centre, Oss, The Netherlands

***SLAS Discovery* (2020) 25:1018–1025**

Abstract

Arginase 1, which converts the amino acid L-arginine into L-ornithine and urea, is a promising new drug target for cancer immunotherapy, as it has a role in the regulation of T-cell immunity in the tumor microenvironment. To enable the discovery of small molecule arginase 1 inhibitors by high-throughput screening, we developed a novel homogeneous (mix-and-measure) fluorescence-based activity assay. The assay measures the conversion of L-arginine into L-ornithine by a decrease in fluorescent signal due to quenching of a fluorescent probe, Arginase Gold. This way, inhibition of arginase 1 results in a gain of signal when compared with the uninhibited enzyme. Side-by-side profiling of reference inhibitors in the fluorescence-based assay and a colorimetric urea formation assay revealed similar potencies and the same potency rank order among the two assay formats. The fluorescence-based assay was successfully automated for high-throughput screening of a small molecule library in 384-well format with a good Z'-factor and hit confirmation rate. Finally, we show that the assay can be used to study the binding kinetics of inhibitors.

Introduction

Although immunotherapeutics targeting the immune checkpoints CTLA-4, PD-1 and PD-L1 have contributed substantially to recent progress in cancer treatment, a considerable proportion of patients remains unresponsive.¹ The enzyme arginase 1 (ARG1), converting the amino acid L-arginine into L-ornithine and urea, is a promising new drug target for cancer immunotherapy, based on its role in the regulation of T-cell activity in the tumor microenvironment.^{2,3} ARG1 secreted by myeloid cells in the tumor microenvironment depletes local L-arginine, causing T-cell anergy and the suppression of T-cell and natural killer cell proliferation.^{2,3}

Arginase enzyme activity is commonly determined by measuring the rate of urea formation in a colorimetric assay.^{4,5} A disadvantage of the urea formation assay is that it requires strong acidic solutions (sulfuric acid), which are incompatible with the tubing of automated dispensers commonly used for high-throughput screening (HTS). Here we describe a novel fluorescence-based screening assay for ARG1 and its validation using reference inhibitors and by HTS. The assay is developed to be addition-only, and consists of only two reaction steps: (1) incubation of the enzyme with compound and (2) addition of the Arginase Gold probe and the substrate L-arginine, followed by development of the reaction and measurement of the fluorescence. The fluorescence of the probe is quenched upon conversion of L-arginine into L-ornithine, resulting in a decrease of the fluorescent signal. Inhibition of ARG1 decreases this conversion and therefore causes a gain of the fluorescent signal compared with the uninhibited enzyme.

Results

Fluorescence-based ARG1 activity assay

Initial development of the fluorescence-based activity assay was performed at pH 9.5, which is the pH optimum of human ARG1. The assay was subsequently optimized at both pH 9.5 and physiological pH of 7.4 with regard to the enzyme concentration and reaction time. The L-arginine concentration was chosen at 2.5 mM for both pH values, which roughly equals K_M at pH 7.4 and half of K_M at pH 9.5.⁶ The fluorescent response of the assay was confirmed to be linear up to this concentration at both pH values by measurement of a calibration curve consisting of decreasing L-arginine concentrations combined with increasing L-ornithine concentrations (Figures 1A and 1B). The enzyme concentration and reaction time were optimized for the assay to be within the linear range of substrate conversion while still maintaining a sufficient assay window (Figures 1C and 1D). The ARG1 concentration and reaction time were chosen at 10 nM and 30 min at pH 9.5 and at 20 nM

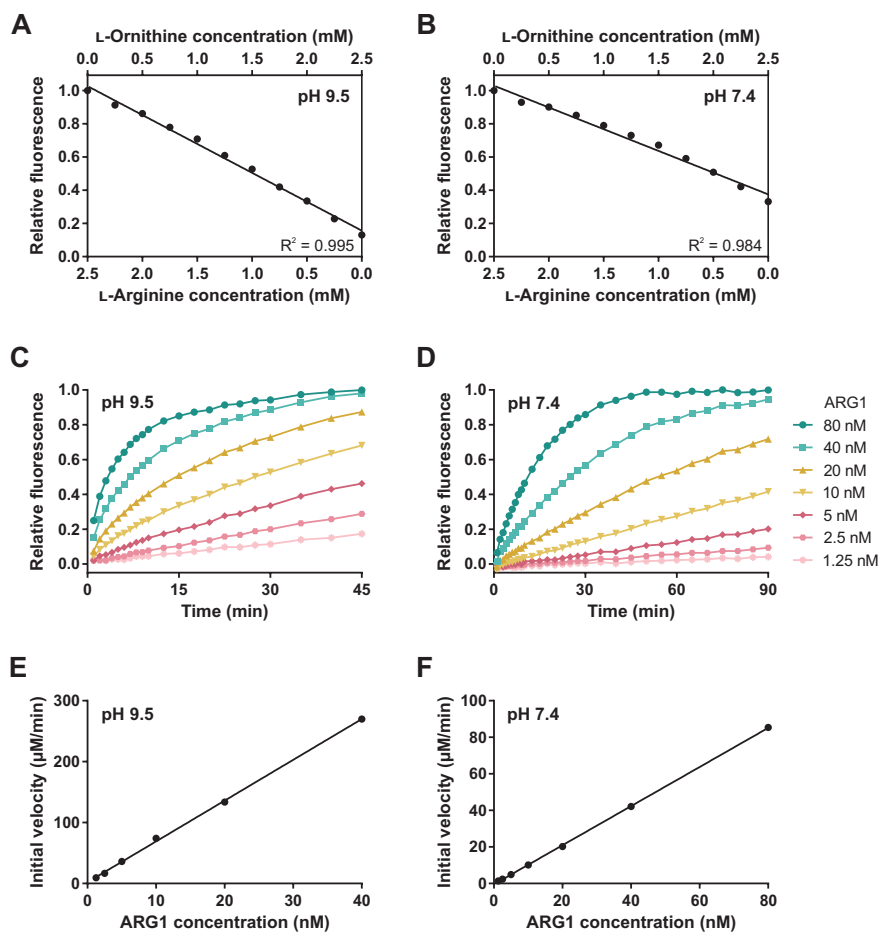


Figure 1. Development and optimization of the fluorescence-based ARG1 activity assay. **(A)** Combined L-arginine and L-ornithine calibration curve at pH 9.5 and **(B)** pH 7.4 demonstrating that the fluorescent signal is linearly proportional to the L-arginine and L-ornithine concentrations within the measuring range of the assay. The concentrations present in the calibration curve correspond to the concentrations that can occur in the assay when performed with a starting concentration of 2.5 mM L-arginine, which is converted by ARG1 into L-ornithine. **(C)** Time course of ARG1 activity at different enzyme concentrations after addition of 2.5 mM L-arginine and the fluorescent probe at pH 9.5 and **(D)** at pH 7.4 measured in real time. The fluorescence signal in panels A and B is subtracted with the background signal measured in the absence of ARG1. **(E)** Correlation between the reaction velocity and enzyme concentration at pH 9.5 and **(F)** at pH 7.4. The reaction velocity of 80 nM ARG1 at pH 9.5 was too fast to be determined accurately.

and 60 min at pH 7.4, respectively. The higher enzyme concentration and longer reaction time required at pH 7.4 compared with pH 9.5 can be attributed to the lower catalytic activity of ARG1 at the lower pH (Figures 1E and 1F). Finally, the preincubation time was set at 90 min to allow for slow-binding inhibitors to reach binding equilibrium. Nonetheless, both the preincubation time and reaction time can be varied. By variation of the reaction time, the assay can also be performed as a kinetic assay instead of an endpoint assay.

Pharmacology and HTS

The pharmacology of the assay was validated by testing three reference inhibitors and comparing their potencies with those determined in a colorimetric urea detection assay. The chemical structures of the three compounds are shown in Figure 2. (2*S*)-2-Amino-6-boronohexanoic acid (ABH)⁷ and *N*^ω-hydroxy-nor-L-arginine (nor-NOHA)⁸ are two different synthetic chemical derivatives of L-arginine and are widely used reference inhibitors of ARG1. Compound 3 is a mixture of the ARG1 inhibitor CB-1158 (INCB001158), which is currently in clinical trials,³ and one of its diastereomers. Figure 3 shows representative dose-response curves of the three compounds in the assay performed at pH 9.5 and at pH 7.4. The inhibition constants (K_i) are compared with those determined in the colorimetric urea assay (Table 1). All K_i values showed maximally a 2.5-fold difference between the two assay formats (Table 1). Moreover, the inhibitors maintained the same potency rank order in both assays. These results confirm the correct assay pharmacology of the fluorescence-based assay.

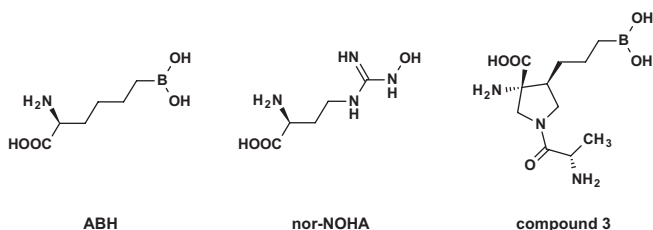


Figure 2. Chemical structures of the ARG1 inhibitors used in this study. The structure shown for compound 3 is that of the active diastereomer CB-1158.^{3,6}

To investigate the applicability of the assay in HTS, a 93,000-compound diversity library was screened for inhibitors of ARG1 on a fully automated robotic system at the Pivot Park Screening Centre. The compounds were screened in 384-well assay plates at a concentration of 2 μ M with a final DMSO concentration of 0.1%. The average Z' -factor of the screen was 0.59 with a signal-to-background ratio (S/B) of 1.64 (Figure 4). A consistent K_i of 87 nM (95% confidence interval: 64–119 nM) was measured for the reference inhibitor ABH throughout the screening campaign, which was highly similar to

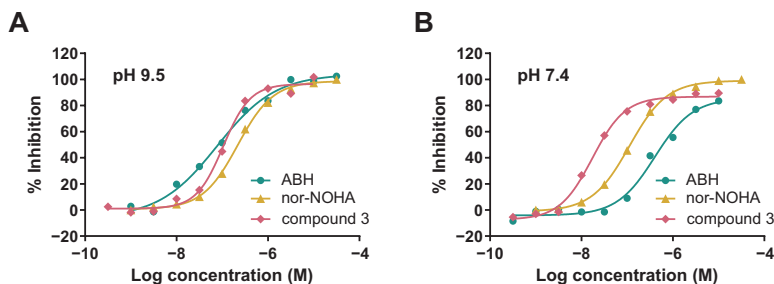


Figure 3. Representative dose-response curves of inhibitors in the ARG1 fluorescence-based activity assay. **(A)** Dose-response curves of (2S)-2-amino-6-borohexanoic acid (ABH), *N*^ω-hydroxy-nor-L-arginine (nor-NOHA) and compound 3 at pH 9.5 and **(B)** at pH 7.4. The data points represent the mean of two technical replicates. See Table 1 for the corresponding K_i values.

the K_i value of 72 nM measured on the bench (Table 1). Although this demonstrates that the screen was sensitive, we were able to identify only 62 compounds with an effect $\geq 50\%$ at 2 μM . We therefore selected compounds showing a signal at least three standard deviations above the negative control mean of the respective plate (*i.e.*, $Z\text{-score} \geq 3$), which corresponds to a roughly 20% to 25% effect, resulting in the identification of 621 hits (0.7% hit rate). These compounds were retested at a single test concentration of 2 μM in an assay with an average Z' -factor of 0.76 and S/B of 1.8. Of the 621 hits, 48% could be confirmed. The 297 confirmed hits were supplemented with 49 compounds structurally related to the hits (by *in silico* criteria) from the same library. The resulting 346 compounds were tested in dose-response curves in the fluorescence-based assay. To examine the compounds for interfering properties, such as autofluorescence or the ability to interact with the fluorescent probe, the same assay was also performed in the absence of enzyme. Furthermore, all 346 compounds were analyzed in the colorimetric urea assay as an

Table 1. Inhibition constants (K_i) of inhibitors in the ARG1 fluorescence-based and colorimetric urea formation assays at pH 9.5 and pH 7.4.

Inhibitor	pH 9.5		pH 7.4	
	K_i (nM) (95% CI) in ARG1 assay	K_i (nM) (95% CI) in urea assay	K_i (nM) (95% CI) in ARG1 assay	K_i (nM) (95% CI) in urea assay
ABH	72 (48–107)	30 (24–38)	265 (216–327)	156 (132–185)
nor-NOHA	123 (108–141)	80 (70–92)	57 (48–67)	50 (46–54)
compound 3	55 (41–72)	31 (23–42)	9.5 (8.5–10.5)	4.9 (4.2–5.8)

The corresponding IC_{50} values are listed in Supplementary Table 1. All values were determined in either three or four independent experiments. K_i values of individual experiments were averaged using their respective $^{-10}\log K_i$ (*i.e.*, pK_i) values. CI, confidence interval.

orthogonal assay. Of the 346 compounds, 224 compounds were deselected based on displaying either autofluorescence or interaction with the fluorescent probe, or both. Based on the analysis of all obtained dose-response curves and medicinal chemistry expertise, 13 compounds were ordered from a commercial vendor and retested at concentrations up to 1 and 10 mM, respectively, in the fluorescence-based and colorimetric urea formation assays. Because only minimal activity could be measured for these hits, they were not further pursued for medicinal chemistry optimization. Despite this result, we conclude that, based on the favorable Z'-factor and the consistent K_i value of ABH in the screen, the Arginase Gold assay is robust and suitable for HTS.

Real-time kinetics

The fluorescence-based assay format has no final step in which the signal needs to be developed. Instead, the fluorescent signal can be continuously monitored. However, in some cases, it might be desirable to stop the assay after a set amount of time. For this, we studied various reaction stop protocols, such as acidic pH and reducing conditions. It appeared that addition of tris(2-carboxyethyl)phosphine (TCEP) to a final concentration of 1 mM was suitable to stop all ARG1 activity without sacrificing the Z'-factor of the assay. The continuous readout also generates the possibility of following the reaction in real time, thereby allowing the kinetics of inhibitor binding to be studied. The assay was therefore also developed to allow monitoring of the reaction progress of L-arginine conversion by ARG1 in real time. To determine whether the reaction time in the presence of L-arginine has an effect on the measured K_i values, the inhibition of ARG1 was monitored as a function of the reaction time (Figure 5).

The potencies of nor-NOHA and compound 3 decreased only slightly over time at pH 9.5 and pH 7.4 (Figure 5). The same was true for ABH at pH 7.4 (Figure 5). In contrast, for ABH at pH 9.5, a more considerable decrease in potency as a function of reaction time was found, which may be explained by a decreased stability of the compound at increased pH. Nonetheless, considering the stable profile of nor-NOHA and compound 3 at both pH values as well as ABH at pH 7.4, these results indicate that the assay reagents do not deteriorate during the times used for the assay and that therefore the assay is suitable for performing kinetic inhibition experiments.

Discussion

Despite the renewed interest in ARG1 as a therapeutic drug target, the number of different chemotypes described in scientific publications and patents remains rather low. Early inhibitors are analogues of the substrate L-arginine, such as the boronic acid derivative

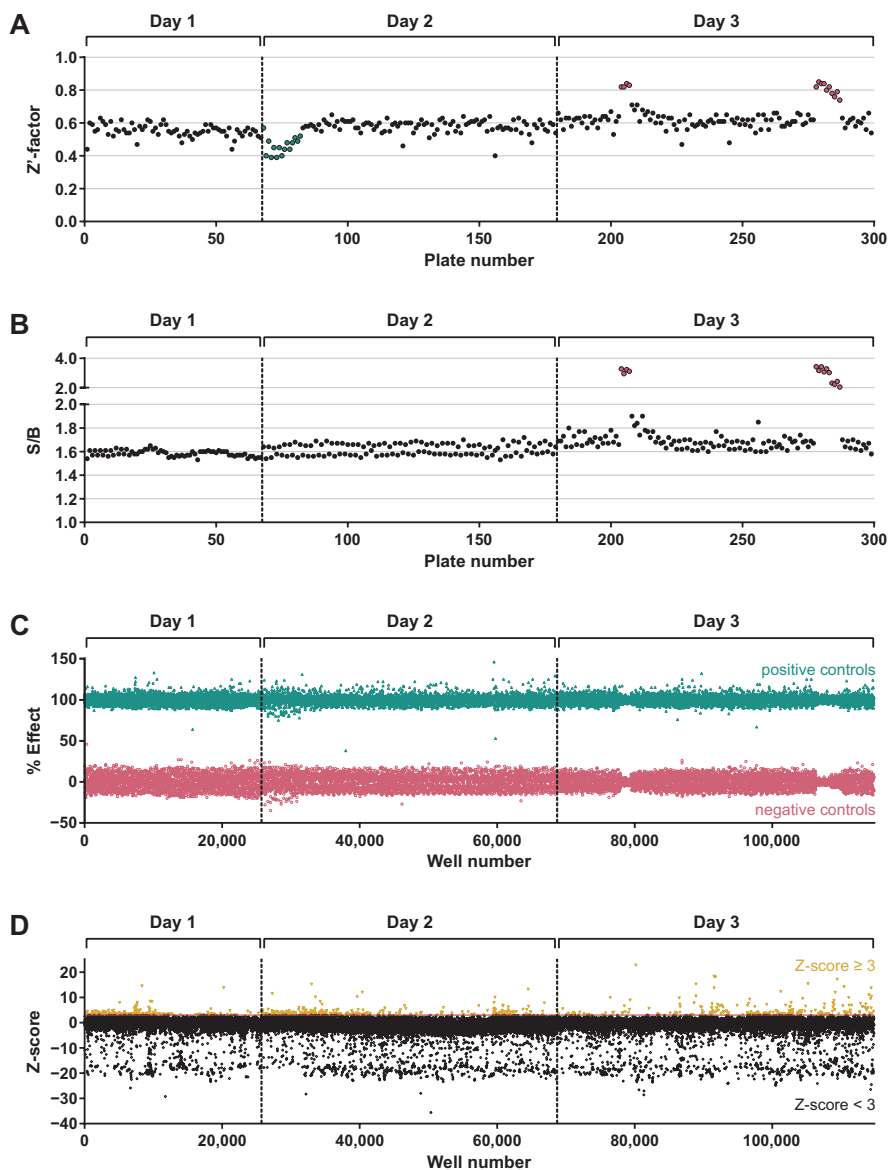


Figure 4. Performance of the fluorescence-based ARG1 activity assay in high-throughput screening. (A) Z'-factor and (B) signal-to-background (S/B) ratio per assay plate. (C) Scatter plot of the percentage effect of the positive control samples (teal triangles) and negative control samples (pink circles) measured throughout the screen. (D) Scatter plot of the compound Z-score measured at 2 μM concentration throughout the screen. Compounds above the Z-score threshold of 3 (indicated by the red line) are identified as hits (yellow triangles). The reagent solutions and enzyme dilution were prepared fresh
(Legend continued on next page)

ABH.⁷ Macromolecular co-crystal structures of ARG1 and inhibitors have enabled the development of more potent inhibitors, such as CB-1158,³ which is currently investigated in phase I/II clinical trials. The primary focus on rational design and structure-based medicinal chemistry approaches may in part be related to the lack of suitable assays for HTS. Previously reported assays are generally poorly compatible with robotic screening because of the requirement of multiple reaction steps,⁹ harsh assay conditions,^{4,5} the use of radioactive substrate,¹⁰ or the use of low-turnover substrates other than L-arginine.¹¹

For arginase 2, an automated mass spectrometry method has been described, referred to as RapidFire mass spectrometry (RapidFire-MS), which was used to screen a library of several thousands of small molecule fragments.¹² Mass spectrometry is a label-free method, and therefore, technology interferences are rare. However, disadvantages of RapidFire-MS in comparison with probe-based screening methods include the requirement of specifically trained operators, the high price of equipment, and the cost of integration. Furthermore, the assay throughput is much lower. Cycle times reported for RapidFire-MS start at 5 to 10 s per sample, which equals about 1 h per 384-well plate,¹³ whereas the RapidFire arginase 2 screen was performed with a cycle time of > 18 s per sample.¹² In contrast, the Envision multimode reader used in our studies measures 384 samples in one 384-well plate within 1 min.

The fluorescence-based activity assay for ARG1 is shown to be robust and suitable for HTS, as evidenced by the consistent K_i value of ABH measured throughout the screening campaign and the favorable Z' -factor. This assay will therefore be of value for the identification of novel ARG1 inhibitor scaffolds. Because enzyme inhibition results in a gain of fluorescence signal in the assay, the chance of false-positive signals by fluorescent dye interference is expected to be low. Furthermore, the assay allows deselection of autofluorescent compounds and compounds interacting with the fluorescent probe by performance of the assay in the absence of enzyme. Moreover, the availability of a stop solution (*i.e.*, TCEP) provides additional flexibility when performing an assay on the bench or applying it for HTS. However, the effect of the stop solution on the interference of compounds with the assay readout still needs to be determined. Finally, an important aspect of our assay is that it can be used to monitor the binding kinetics of inhibitors in real time.

(Legend continued from previous page)

at the start of each screening day. On the second screening day, the first 15 assay plates (numbered 69 to 82; indicated by teal dots in panel A) experienced a start-up effect resulting in lower Z' -factors for these plates. On the third screening day, two robotic errors occurred which caused plate numbers 205 to 208 and 279 to 285 (indicated by pink dots in panels A and B) to have a prolonged reaction time (outside of the optimal linear range), resulting in higher Z' -factor and S/B values for these plates.

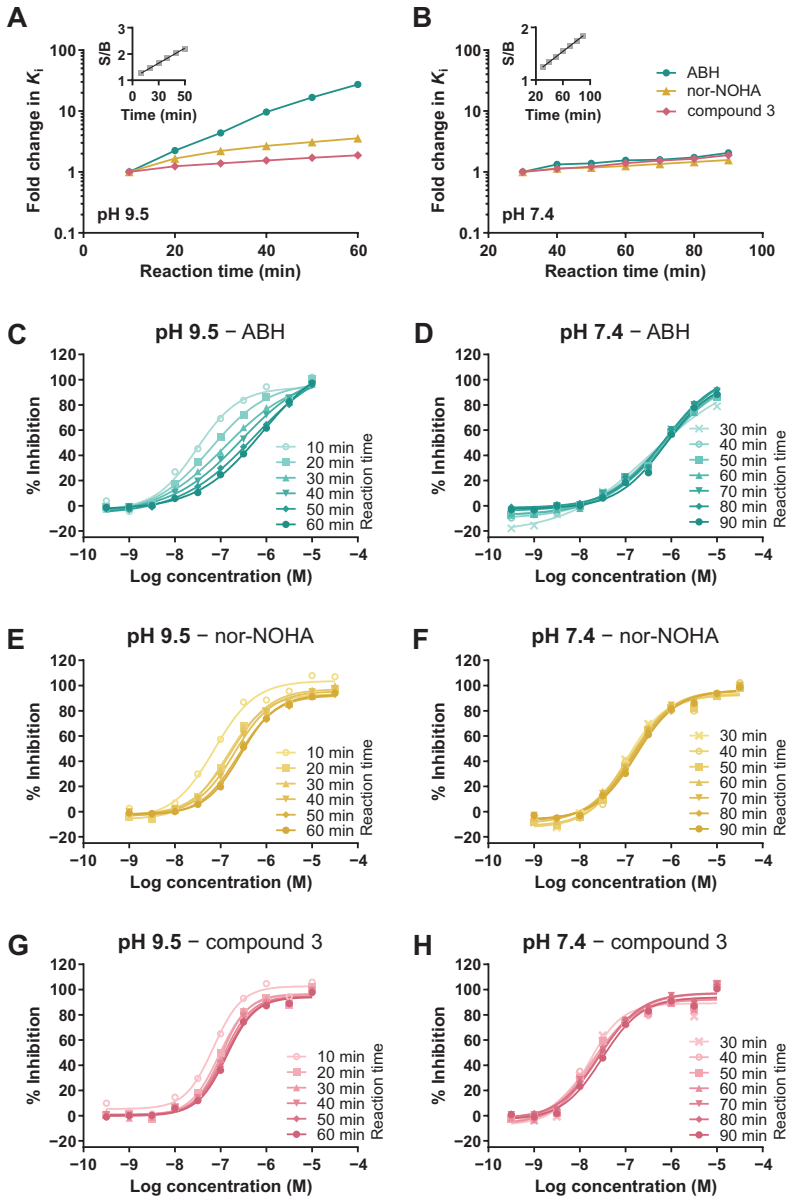


Figure 5. Inhibition constants and dose-response curves in the ARG1 fluorescence-based activity assay with increasing reaction times at pH 9.5 and 7.4. (A) Effect of increasing reaction time on inhibition constants (K_i) at pH 9.5. The reaction time indicates the incubation time after addition of L-arginine to ARG1 and the inhibitor, during which L-arginine can be enzymatically hydrolyzed prior to readout of the assay. For each inhibitor, the K_i values were scaled to the K_i value of the first time point.

(Legend continued on next page)

Materials and methods

Inhibitors and compound library

ABH⁷ was prepared according to patent WO/2016/037298.¹⁴ Nor-NOHA⁸ was purchased from Tocris Bioscience (cat. no. 6370). Compound 3 was synthesized according to procedures described for structure 10 from patent WO/2017/075363.¹⁵ The compound library screened at the Pivot Park Screening Centre (Oss, The Netherlands; www.ppscreeningcentre.com) consisted of a diverse set of 87,000 lead-like compounds from a commercial supplier (Specs, Delft, The Netherlands) supplemented with 6,000 compounds from another supplier (Mera Pharmaceuticals, Kailua-Kona, HI). The incorporation of desired molecular properties as well as their synthetic tractability was ensured by the Pivot Park Screening Centre.

Protein expression

Full-length human ARG1 (L-arginine amidinohydrolase, EC 3.5.3.1) was expressed with an N-terminal hexahistidine tag in *Escherichia coli* and purified by affinity chromatography using Ni-NTA agarose beads (Qiagen) to 95% purity, as determined by polyacrylamide gel electrophoresis. The purified protein was desalted on a PD-10 column (GE Healthcare) and stored at -80 °C in aliquots in buffer containing 20% glycerol. The Michaelis–Menten parameters of the protein were characterized previously.⁶

Fluorescence-based ARG1 assay

All components of the assay were diluted in assay buffer composed of either 5 mM glycine, pH 9.5, and 0.05% Tween-20 or 10 mM NaH₂PO₄, pH 7.4, and 0.01% Tween-20. Compounds were dissolved and diluted in DMSO or in MilliQ water and then further diluted in assay buffer to the desired concentrations. In a black 384-well plate (Corning, cat. no. 3573), 10 µL compound solution and 10 µL of 40 nM (pH 9.5) or 80 nM (pH 7.4) ARG1 were combined and incubated for 90 min at room temperature. Then, 20 µL of fluorescent probe (Arginase Gold; prepared in-house and commercially available at Oncolines B.V.; www.residencetimer.com) combined with 5 mM L-arginine (Acros Organics, cat. no. 105000250) was added to each well, followed by incubation for 30 min (pH 9.5) or 60 min (pH 7.4) at room temperature. To determine the conversion of L-arginine into L-ornithine, the fluorescence signal was read on an EnVision 2104 Multilabel Plate Reader

(Legend continued from previous page)

The data points represent the mean of two independent experiments. **(B)** Effect of increasing reaction time on *K_i* values at pH 7.4. The inserts in panels A and B show the linear response of the assay in time. **(C–H)** Representative dose-response curves with increasing reaction time at pH 9.5 and 7.4. The data points represent the mean of two technical replicates.

(PerkinElmer; excitation filter X320 and emission filter M510W). The final concentration of ARG1 in the assay at pH 9.5 was 10 nM; at pH 7.4, it was 20 nM. The final concentration of L-arginine was 2.5 mM at both pH conditions. All experiments were performed with duplicate measurements. The Z'-factor of the assay was calculated using Eq. (1),¹⁶ with σ and μ as the standard deviation and mean, respectively of the positive control samples (including all reaction components except enzyme; denoted with +) and negative control samples (including all reaction components; denoted with -).

$$Z'\text{-factor} = 1 - \frac{3(\sigma_+ + \sigma_-)}{|\mu_+ - \mu_-|} \quad (1)$$

Dose-response curves were fit in XLFit (IDBS) with a four-parameter logistic regression to determine the IC₅₀ values. IC₅₀ values were then converted to inhibition constants (K_i) using the Cheng–Prusoff equation (Eq. [2]) with [S] as the L-arginine concentration and K_M as the Michaelis constant of ARG1 for L-arginine.

$$K_i = \frac{IC_{50}}{1 + ([S] / K_M)} \quad (2)$$

The average Z'-factor of the assay at pH 9.5 was 0.70 ± 0.05, and the average S/B was 1.67 ± 0.11 when performed on the lab bench. The assay was sensitive to the addition of 0.1% DMSO with a slight drop in assay performance (average Z'-factor of 0.67 ± 0.05 vs. 0.73 ± 0.04 for with and without 0.1% DMSO, respectively), whereas the S/B remained identical for both conditions. At pH 7.4, the average Z'-factor was 0.62 ± 0.08, with an average S/B of 1.52 ± 0.11.

Colorimetric urea formation assay

The colorimetric urea formation assay was performed as previously described,⁶ with the exception of the assay buffers, which were composed of either 5 mM glycine, pH 9.5, and 0.05% Tween-20 or 5 mM NaH₂PO₄, pH 7.4, and 0.05% Tween-20.

High-throughput screening

The diversity compound library was screened using the ARG1 activity assay at pH 9.5 on a HighRes Biosolutions robotic system (Manchester, UK). Compounds were dissolved at 2 mM in DMSO, and 40 nL of the compound solutions was transferred to the assay plates using an Echo Liquid Handler (Labcyte). The compounds were diluted by addition of 10 μL assay buffer (5 mM glycine, pH 9.5, and 0.05% Tween-20) using a Flexdrop dispenser (PerkinElmer). The assay was further executed as described above, with all solutions added using the Flexdrop dispenser. Confirmation of active compounds was performed by plating the compounds using Echo acoustic dispensers and performing the assay manually on the bench. To determine potential interference by autofluorescent

compounds, the background fluorescence signal was read prior to addition of the fluorescent probe. Alternatively, to correct for any interference of the library compounds in the assay, a deselection assay was performed with assay buffer added to all wells of the plates instead of the enzyme solution.

Assay quality was monitored by determining the Z'-factor and S/B for each 384-well plate. The Z-score for ARG1 inhibition in each well was calculated using Eq. (3) with x as the sample value and with σ_{-} and μ_{-} as the mean and standard deviation, respectively, of the negative control samples (including all reaction components).

$$\text{Z-score} = \frac{x - \mu_{-}}{\sigma_{-}} \quad (3)$$

The robustness of the assay was monitored by measuring dose-response curves of the inhibitor ABH throughout the screening campaign. Autofluorescent compounds and compounds interacting with the fluorescent probe were deselected based on the criteria that the increase in either the fluorescent background signal or the fluorescent signal in the absence of enzyme relative to the control samples must be less than 25% of the assay window (*i.e.*, the difference between the minimal and maximal fluorescent signals in the complete assay).

References

1. Jenkins, R. W., Barbie, D. A. & Flaherty, K. T. Mechanisms of resistance to immune checkpoint inhibitors. *Br. J. Cancer* **118**, 9–16 (2018).
2. Gabrilovich, D. I., Ostrand-Rosenberg, S. & Bronte, V. Coordinated regulation of myeloid cells by tumours. *Nat. Rev. Immunol.* **12**, 253–68 (2012).
3. Steggerda, S. M. *et al.* Inhibition of arginase by CB-1158 blocks myeloid cell-mediated immune suppression in the tumor micro-environment. *J. Immunother. Cancer* **5**, 101 (2017).
4. Jung, D., Biggs, H., Erikson, J. & Ledyard, P. U. New colorimetric reaction for end-point, continuous-flow, and kinetic measurement of urea. *Clin. Chem.* **21**, 1136–40 (1975).
5. Zawada, R. J. X., Kwan, P., Olszewski, K. L., Llinas, M. & Huang, S.-G. Quantitative determination of urea concentrations in cell culture medium. *Biochem. Cell Biol.* **87**, 541–4 (2009).
6. Grobden, Y. *et al.* Structural insights into human Arginase-1 pH dependence and its inhibition by the small molecule inhibitor CB-1158. *J. Struct. Biol. X* **4**, 100014 (2020).
7. Baggio, R. *et al.* Inhibition of Mn^{2+} -arginase by borate leads to the design of a transition state analogue inhibitor, 2(S)-amino-6-borohexanoic acid. *J. Am. Chem. Soc.* **119**, 8107–8 (1997).
8. Custot, J. *et al.* The new α -amino acid N^{ω} -hydroxy-nor-L-arginine: a high-affinity inhibitor of arginase well adapted to bind to its manganese cluster. *J. Am. Chem. Soc.* **119**, 4086–7 (1997).
9. Garganta, C. L. & Bond, J. S. Assay and kinetics of arginase. *Anal. Biochem.* **154**, 388–94 (1986).
10. Rüegg, U. T. & Russell, A. S. A rapid and sensitive assay for arginase. *Anal. Biochem.* **102**, 206–12 (1980).
11. Baggio, R., Cox, J. D., Harper, S. L., Speicher, D. W. & Christianson, D. W. A new chromophoric assay for arginase activity. *Anal. Biochem.* **276**, 251–3 (1999).
12. Asano, W., Takahashi, Y., Kawano, M. & Hantani, Y. Identification of an arginase II inhibitor via RapidFire mass spectrometry combined with hydrophilic interaction chromatography. *SLAS Discov.* **24**, 457–65 (2019).
13. Adam, G. C. *et al.* Use of high-throughput mass spectrometry to reduce false positives in protease uHTS screens. *J. Biomol. Screen.* **20**, 212–22 (2015).
14. Preite, M. D. *et al.* Method for the enantioselective synthesis of 2(S)-amino-6-borohexanoic acid (ABH) and purification thereof. Patent WO/2016/037298 (2016).
15. Sjorgen, E. B., Li, J., Van Zandt, M. & Whitehouse, D. Composition and methods for inhibiting arginase activity. Patent WO/2017/075363 (2017).
16. Zhang, J., Chung, T. & Oldenburg, K. A simple statistical parameter for use in evaluation and validation of high throughput screening assays. *J. Biomol. Screen.* **4**, 67–73 (1999).

Supplementary data

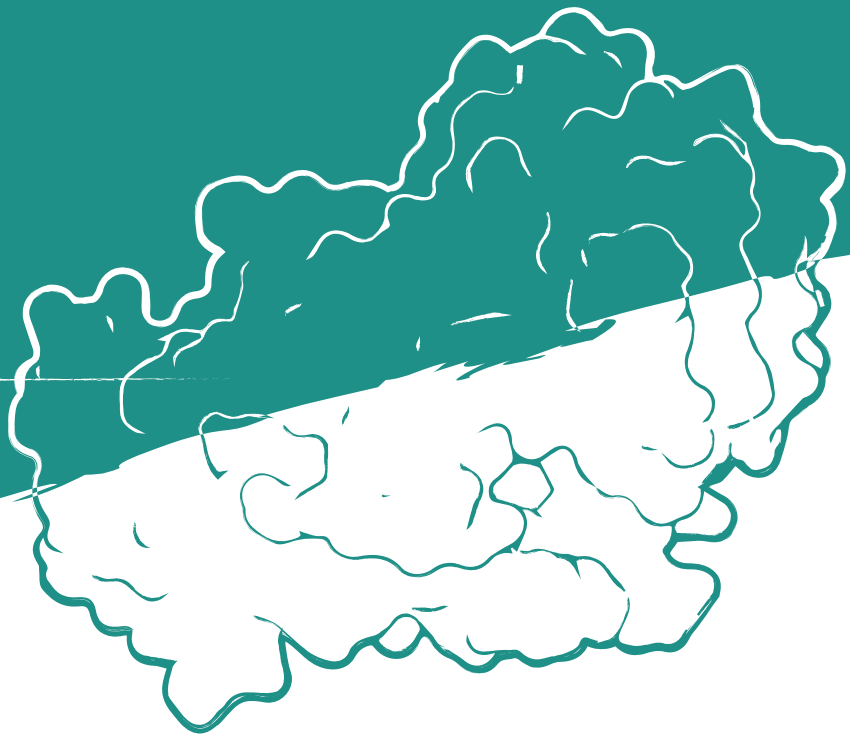
Supplementary Table 1. Half-maximal inhibitory concentration (IC_{50}) of inhibitors in the ARG1 fluorescence-based and colorimetric urea formation assays at pH 9.5 and pH 7.4.

Inhibitor	pH 9.5		pH 7.4	
	IC_{50} (nM) (95% CI) in ARG1 assay	IC_{50} (nM) (95% CI) in urea assay	IC_{50} (nM) (95% CI) in ARG1 assay	IC_{50} (nM) (95% CI) in urea assay
ABH	108 (73–161)	61 (48–77)	554 (450–682)	326 (275–386)
nor-NOHA	186 (163–213)	162 (140–186)	119 (101–140)	104 (96–113)
compound 3	82 (63–109)	63 (47–84)	19.7 (17.8–21.9)	10.3 (8.7–12)

All values were determined in either three or four independent experiments. IC_{50} values of individual experiments were averaged using their respective $-\log IC_{50}$ (i.e., pIC_{50}) values. CI, confidence interval.



IDO1



IDO1

Chapter 6

Targeting indoleamine 2,3-dioxygenase 1 (IDO1) in cancer models using the novel small molecule inhibitor NTRC 3883-O

Yvonne Grobben¹, Jos de Man¹, Antoon M. van Doornmalen¹, Michelle Muller¹, Nicole Willemsen-Seegers¹, Diep Vu-Pham¹, Winfried R. Mulder¹, Martine B. W. Prinsen¹, Joeri de Wit¹, Jan Gerard Sterrenburg¹, Freek van Cauter¹, Judith E. den Ouden², Anne M. van Altena², Leon F. Massuger², Joost C. M. Uitdehaag¹, Rogier C. Buijsman¹ and Guido J. R. Zaman¹

¹ Netherlands Translational Research Center B.V., Oss, The Netherlands

² Department of Obstetrics and Gynaecology, Radboud university medical centre, Nijmegen, The Netherlands

Frontiers in Immunology (2021) 11:609490

Abstract

Indoleamine 2,3-dioxygenase 1 (IDO1) is a key regulator of immune suppression by catalyzing the oxidation of L-tryptophan. IDO1 expression has been related to poor prognosis in several cancers and to resistance to checkpoint immunotherapies. We describe the characterization of a novel small molecule IDO1 inhibitor, NTRC 3883-0, in a panel of biochemical and cell-based assays, and various cancer models. NTRC 3883-0 released the inhibitory effect of IDO1 on CD8-positive T-cell proliferation in co-cultures of IDO1-overexpressing cells with healthy donor lymphocytes, demonstrating its immune modulatory activity. In a syngeneic mouse model using IDO1-overexpressing B16F10 melanoma cells, NTRC 3883-0 effectively counteracted the IDO1-induced modulation of L-tryptophan and L-kynurenine levels, demonstrating its *in vivo* target modulation. Finally, we studied the expression and activity of IDO1 in primary cell cultures established from the malignant ascites of ovarian cancer patients. In these cultures, IDO1 expression was induced upon stimulation with IFN γ , and its activity could be inhibited by NTRC 3883-0. Based on these results, we propose the use of ascites cell-based functional assays for future patient stratification. Our results are discussed in light of the recent discontinuation of clinical trials of more advanced IDO1 inhibitors and the reconsideration of IDO1 as a valid drug target.

Introduction

The essential amino acid L-tryptophan (Trp) is an important regulator of cancer progression due to its regulatory role in immune cell activity.^{1,2} Depletion of Trp in the tumor microenvironment results in T-cell anergy and inhibition of natural killer cell activity.^{1,2} The catabolism of Trp is regulated by two distinct, evolutionarily unrelated enzymes, indoleamine 2,3-dioxygenase 1 (IDO1) (EC 1.13.11.42) and tryptophan 2,3-dioxygenase (TDO) (EC 1.13.11.11). Both enzymes catalyze the oxidation of Trp, resulting in the formation of *N*-formyl-L-kynurenine (NFK), which is rapidly converted into L-kynurenine (Kyn) by the enzyme kynurenine formamidase.

IDO1 and TDO have a distinct tissue distribution and carry out different physiological roles. IDO1 is broadly expressed at low levels in normal tissues,³ but is strongly induced by pro-inflammatory stimuli, such as IFN γ .⁴ In this manner, the expression of IDO1 by various cell types, including immune, endothelial and epithelial cells, provides a control mechanism to dampen the immune response.^{5,6} In contrast, TDO is constitutively expressed at high levels in the liver, where it functions to maintain Trp homeostasis.⁷ Consistent with this role, TDO has a relatively low affinity for Trp ($K_{M,Trp}$ 190 μ M) in comparison to IDO1 ($K_{M,Trp}$ 6 μ M).⁸

In cancer, expression of IDO1 has been observed in both tumor and immune cells. IDO1 expression has been correlated with poor prognosis, increased progression and reduced survival in several cancers.^{9,10} Moreover, it has been related to resistance to anti-PD-1 and anti-PD-L1 immunotherapies.^{10,11} In the past decade, several small molecule IDO1 inhibitors have been developed to enhance the efficacy of immunotherapy.¹² The first-in-class and most advanced IDO1 inhibitor is epacadostat (INCB024360), which is a reversible, substrate-competitive enzyme inhibitor.¹³ More recently, increasingly potent IDO1 inhibitors have been described which act by displacing the heme cofactor of the enzyme, as exemplified by linrodostat (BMS-986205).¹⁴ Phase I clinical studies with epacadostat have demonstrated that IDO1 inhibition is well tolerated in human patients and results in dose-dependent reductions of Kyn levels and Kyn/Trp ratios in plasma.¹⁵ In a phase I combination trial with the anti-PD-1 immunotherapeutic pembrolizumab, objective response was seen in 12 out of 22 melanoma patients treated with epacadostat.¹⁶ However, a large phase III combination trial with pembrolizumab (ECHO-301/KEYNOTE-252) was terminated prematurely, since there was no clinical benefit of the combination over pembrolizumab plus placebo.¹⁷

Here we describe NTRC 3883-0, a potent, selective and orally bioavailable IDO1 inhibitor, which is structurally distinct from existing IDO1 inhibitors.¹² NTRC 3883-0 was profiled side-by-side with epacadostat in biochemical and cell-based assays for human (h) and

mouse (m) IDO1, and the selectivity target TDO. Its immunomodulatory activity was studied *in vitro* in a co-culture assay of an *hIDO1*-overexpressing cell line with lymphocytes. Modulation of IDO1 activity *in vivo* was studied in a syngeneic mouse model of melanoma induced with *mIDO1*-overexpressing B16F10 cells. Finally, we studied the expression of IDO1 and its modulation by NTRC 3883-0 in *ex vivo* primary cell cultures established from the malignant ascites of ovarian cancer patients.

Results

Discovery of a novel class of IDO1 inhibitors

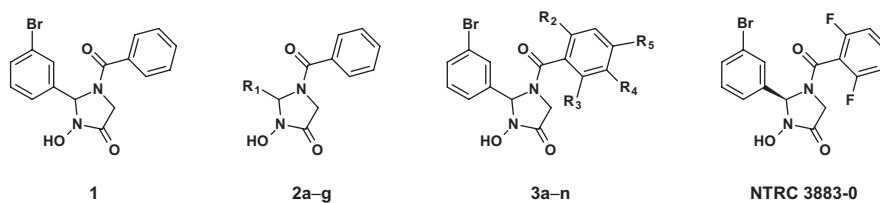
A 3-hydroxyimidazolin-4-one class of IDO1 inhibitors was identified in a biochemical screen of IDO1 performed by the European Lead Factory. The initial hit, compound **1** in Table 1, inhibited IDO1 with a half-maximal inhibitory concentration (IC_{50}) of 1.2 μ M and was inactive on human TDO at the highest tested concentration of 31.6 μ M. Cellular activity was determined by measuring inhibition of Trp-catabolizing activity in the human A375 melanoma cell line, which expresses IDO1 after stimulation with IFN γ . Analogues of compound **1** were synthesized with modifications at five positions (Table 1) and isolated as racemic mixtures except for **3k** and NTRC 3883-0. Optimization was started with the synthesis of analogs **2a–g**, in which the 3-bromophenyl moiety was varied. These analogs showed that this position of the molecule possesses a very tight structure-activity relationship, since deletion (**2a**), substitution (**2b**, **f** and **g**) or an alternative position (**2c** and **d**) of the 3-bromo group resulted in a significant loss of potency. Having established the importance of the 3-bromophenyl pharmacophore, efforts were focused on analogs of the benzoyl moiety (**3a–j** in Table 1). Contrary to the introduction of a fluoro group at the *para* (**3a**) or *meta* (**3b**) position, introduction of an *o*-fluoro (**3c**) group resulted in a potency improvement in both the enzymatic and cellular IDO1 assay (Table 1). Other substituents at the *ortho* position (**3d–f**) were not tolerated, except for the *o*-chloro substitution, which showed a similar potency, albeit at the expense of a higher molecular weight. Addition of a second fluoro group to **3c** resulted in compounds **3h–j**. The strongest increase in potency was observed for compound **3j**. The additional *o*-fluoro group in **3j** presumably helps to orientate the phenyl group in a favorable position perpendicular to the 3-hydroxyimidazolin-4-one core, thereby reducing the entropy loss upon binding to IDO1. After chiral separation of the two enantiomers of **3j**, NTRC 3883-0 was identified as the more active enantiomer (eutomer).

In vitro characterization of NTRC 3883-0

NTRC 3883-0 inhibited human IDO1 with an IC_{50} of 123 nM and was inactive on TDO (Table 2). Trp-catabolizing activity in IFN γ -stimulated A375 cells was inhibited with an

IC₅₀ of 182 nM, whereas the compound had no effect on Trp-catabolizing activity in the human colorectal carcinoma SW48 cell line, which constitutively expresses TDO.⁸ Cellular activity was additionally determined in HEK-293 cells stably overexpressing the full-length human *IDO1* (HEK-hIDO1) or *TDO2* cDNA (the gene encoding the TDO enzyme; HEK-hTDO)

Table 1. Structure-activity relationship of NTRC 3883-0 and analogues.



Compound	Configuration	R ₁	R ₂	R ₃	R ₄	R ₅	IC ₅₀ IDO1 (nM)	IC ₅₀ A375 (nM)
1	<i>R/S</i>	3-Br-Ph	-	-	-	-	1,220	4,520
2a	<i>R/S</i>	Ph	-	-	-	-	> 31,600	> 31,600
2b	<i>R/S</i>	3-Cl-Ph	-	-	-	-	2,380	5,220
2c	<i>R/S</i>	2-Br-Ph	-	-	-	-	> 31,600	> 31,600
2d	<i>R/S</i>	4-Br-Ph	-	-	-	-	> 31,600	> 31,600
2e	<i>R/S</i>	cyclohexyl	-	-	-	-	> 31,600	> 31,600
2f	<i>R/S</i>	3-CN-Ph	-	-	-	-	17,900	> 31,600
2g	<i>R/S</i>	3-CF ₃ -Ph	-	-	-	-	2,460	5,290
3a	<i>R/S</i>	-	H	H	H	F	2,170	11,000
3b	<i>R/S</i>	-	H	H	F	H	910	5,240
3c	<i>R/S</i>	-	F	H	H	H	479	1,150
3d	<i>R/S</i>	-	CH ₃	H	H	H	4,020	21,700
3e	<i>R/S</i>	-	OCH ₃	H	H	H	> 31,600	> 31,600
3f	<i>R/S</i>	-	Cl	H	H	H	784	4,600
3g	<i>R/S</i>	-	Br	H	H	H	1,780	12,500
3h	<i>R/S</i>	-	F	H	F	H	600	2,830
3i	<i>R/S</i>	-	F	H	H	F	582	2,140
3j (NTRC 3748-0)	<i>R/S</i>	-	F	F	H	H	198	589
3k	<i>R</i>	-	F	F	H	H	2,170	4,590
NTRC 3883-0	<i>S</i>	-	F	F	H	H	123	182

NTRC 3883-0 and its analogues were developed by medicinal chemistry optimization from a 3-hydroxyimidazolin-4-one hit compound (**1**) identified by ultra-high throughput screening. Inhibitory potencies (IC₅₀) were determined in a human IDO1 biochemical assay and a cell-based assay with IFN γ -stimulated A375 human melanoma cells. All analogues were inactive in a biochemical assay for TDO (IC₅₀ > 31.6 μ M).

(Figure 1A), since these cells have no detectable endogenous expression of either IDO1 or TDO as determined by quantitative real-time PCR (qPCR) and immunoblot analysis (Figure 1A). NTRC 3883-0 inhibited Trp-catabolizing activity in the HEK-hIDO1 cell line with an IC_{50} of 119 nM and had no effect on Trp-catabolizing activity in the HEK-hTDO cells (Figure 1B and Table 2). The effect on IDO1 activity in normal cells was determined in assays with human whole blood (hWB) from healthy donors after stimulation with IFN γ . In the hWB assay, NTRC 3883-0 inhibited Trp-catabolizing activity with an IC_{50} of 378 nM (Table 2).

The clinical IDO1 inhibitor epacadostat¹³ was profiled in the same assays for reference purposes (Table 2). Our data confirm that epacadostat is a potent IDO1 inhibitor (Figure 1B and Table 2). However, a striking discrepancy in its selectivity over TDO in biochemical and cell-based assays was noted. Epacadostat potently inhibited TDO in the biochemical assay with an IC_{50} of 54 nM, which is in the same range as its potency in the biochemical assay for IDO1 (Figure 1B and Table 2). In contrast, epacadostat showed more than 400 times lower activity on TDO in the HEK-hTDO assay, demonstrating that it is selective cellularly.

In vitro profiling of NTRC 3883-0 against a panel of 44 pharmacologically relevant receptors, ion channels, transporters and enzymes at a concentration of 10 μ M at Eurofins-CEREP (Le Bois L'Évêque, France) revealed no cross-reactivities, further demonstrating

Table 2. *In vitro* characteristics of NTRC 3883-0 and epacadostat.

Assay	NTRC 3883-0	epacadostat
hIDO1	123 (116–130) ($n = 85$)	27 (25–29) ($n = 91$)
hTDO	< 20% inhibition @ 31,600 ($n = 82$)	54 (50–58) ($n = 89$)
HEK-hIDO1	119 ($n = 2$)	7.9 ($n = 2$)
HEK-hTDO	< 20% inhibition @ 31,600 ($n = 2$)	24,100 ($n = 2$)
A375 + IFN γ (hIDO1)	182 (155–214) ($n = 63$)	20 (18–22) ($n = 70$)
SW48 (hTDO)	< 20% inhibition @ 31,600 ($n = 19$)	6,460 (5,650–7,390) ($n = 24$)
hWB + IFN γ (hIDO1)	378 (349–408) ($n = 12$)	54 (48–62) ($n = 12$)
mIDO1	93 ($n = 2$)	39 (30–49) ($n = 4$)
mTDO	< 20% inhibition @ 31,600 ($n = 2$)	225 (102–492) ($n = 3$)
B16F10-mIDO1	18 ($n = 2$)	88 ($n = 2$)
GL-261-mTDO	< 20% inhibition @ 31,600 ($n = 2$)	28% inhibition @ 31,600 ($n = 2$)

Inhibitory potency (IC_{50}) in nM of IDO1 inhibitors NTRC 3883-0 and epacadostat in biochemical and cell-based assays for human (h) and mouse (m) IDO1 or TDO. 95% confidence intervals and number of experimental replicates (n) are given within brackets. hWB, human whole blood.

the selectivity of NTRC 3883-0. NTRC 3883-0 also did not inhibit the activity of the cytochrome P450 (CYP) enzymes CYP2D6 and CYP3A4 at 10 μM . Since CYPs, like IDO1, contain a heme center, these data demonstrate that NTRC 3883-0 interacts selectively with the active site of IDO1.

Modulation of cytotoxic T-cell proliferation

To determine whether NTRC 3883-0 can modulate immune cell activity *in vitro*, co-culture experiments of HEK-hIDO1 cells with peripheral blood mononuclear cells (PBMCs) from healthy donors were performed (Figure 2). Since T-cell anergy is reported to occur only at Trp concentrations of 1 μM and lower,^{6,18} the cells were co-cultured in Trp-free medium supplemented with a low concentration of Trp (*i.e.*, 7.5 μM Trp). Cytotoxic T-cell proliferation was determined by labeling PBMCs with carboxyfluorescein succinimidyl ester (CFSE), a fluorescent dye that dilutes upon proliferation of cells, followed by analysis of CD8-positive T cells by flow cytometry. CD8-positive T cells stopped to proliferate when co-cultured with HEK-hIDO1 cells in medium containing 7.5 μM Trp (Figure 2A). When a high concentration of Trp (200 μM) was added to the co-culture with HEK-hIDO1 cells, the CD8-positive T cells continued to proliferate (Figure 2A). This indicates that the inhibitory effect of IDO1 is

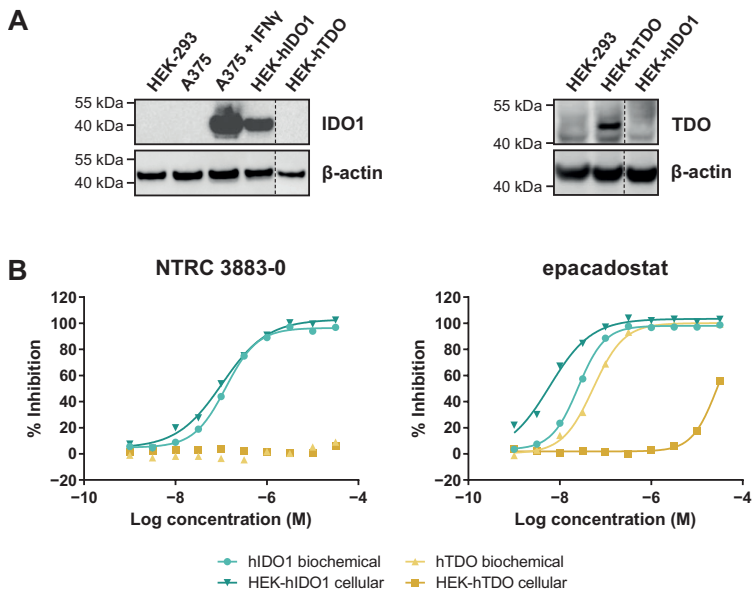


Figure 1. Side-by-side comparison of biochemical and cellular activity of NTRC 3883-0 and epacadostat. **(A)** Immunoblot analysis of the HEK-hIDO1, HEK-hTDO, and IFN γ -stimulated A375 cell lines used for cellular assays. **(B)** Inhibition profile of NTRC 3883-0 and epacadostat in the hIDO1 and hTDO biochemical and HEK-293 cell-based assays.

caused by depletion of Trp and is not due to the production of an immunosuppressive metabolite. Addition of 10 μM NTRC 3883-0 to co-cultures of HEK-hIDO1 and PBMCs at low Trp concentration relieved the inhibitory effect of IDO1 expression on T-cell proliferation (Figure 2B), analogous to the effect of treatment with 1 μM epacadostat (Figure 2C). This demonstrates that NTRC 3883-0 can modulate immune cell function.

***In vivo* target modulation in syngeneic mouse models**

Next, we aimed to assess the *in vivo* activity of NTRC 3883-0 in a syngeneic mouse model. This first required the selection of a suitable IDO1-expressing, implantable cell line. There exist only a small number of mouse cancer cell lines as compared to human cancer cell lines, and only a few have been reported to express IDO1 *in vitro*.^{19,20} In the colon carcinoma CT26 and melanoma B16F10 cell lines, the expression of IDO1 is low¹⁹ or not detectable

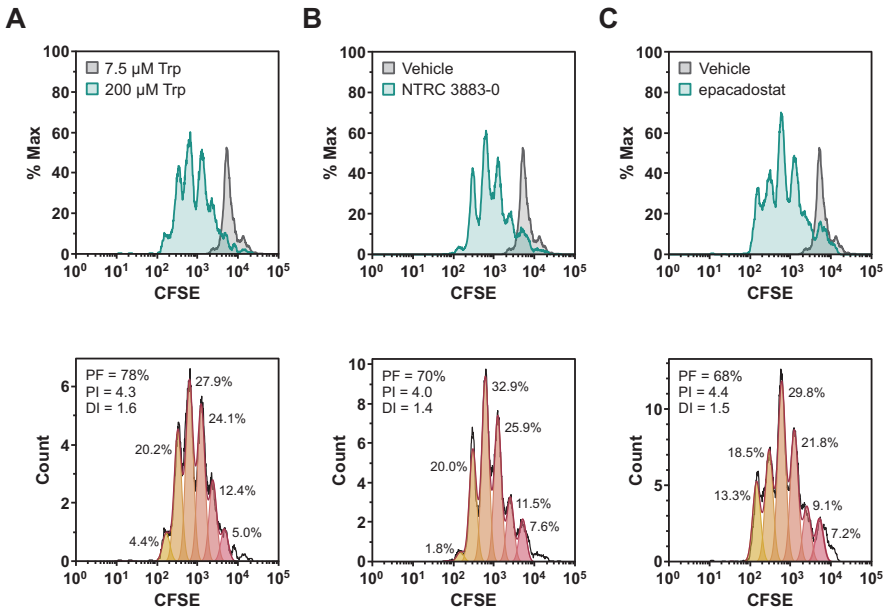


Figure 2. Co-culture assays of HEK-hIDO1 cells with lymphocytes from a healthy donor. Proliferation of CFSE-labeled CD8-positive T cells co-cultured for 5 days with HEK-hIDO1 cells upon addition of (A) 200 μM Trp as a positive control for T-cell proliferation, (B) 10 μM NTRC 3883-0 and (C) 1 μM epacadostat. Each panel shows an overlay with CD8-positive T cells co-cultured for 5 days with HEK-hIDO1 cells upon addition of 7.5 μM Trp and vehicle (top), and the cell proliferation analysis (bottom). PF, precursor frequency (the percentage of cells from the original population that have proliferated); PI, proliferation index (the average number of cell divisions undergone by the proliferating cell population); DI, division index (the average number of cell divisions undergone by the entire cell population). The percentages indicate the percentage of the total amount of cells in each generation.

in cell culture.²¹ However, the expression of *IDO1* in CT26 cells is strongly increased after implantation in syngeneic mice,¹⁹ while implanted B16F10 cells have been found to promote IDO1 expression in dendritic cells.²² This indicates that *IDO1* gene expression can be induced by the tumor microenvironment, which is substantiated by studies with mice deficient for IFN γ or depleted of CD8-positive T cells indicating that upregulation of IDO1 in the tumor microenvironment is regulated by IFN γ released by CD8-positive T cells.²³

We initially selected the CT26 model to assess the *in vivo* efficacy of NTRC 3883-0, since this model has previously been used by others to evaluate several IDO1 inhibitors, including epacadostat.¹⁹ The effect of treatment with NTRC 3748-0 (Table 1), NTRC 3883-0 and epacadostat was evaluated in two CT26 mouse model experiments performed at different contract research organizations (Supplementary Figure 1). While the first study reported inhibition of tumor growth with both NTRC 3748-0 and epacadostat (Supplementary Figure 1A), no inhibition of tumor growth was found in the second study with either NTRC 3883-0 or epacadostat (Supplementary Figure 1B). The tumors from both studies were harvested and analyzed for *mIDO1* gene expression by qPCR and Kyn levels by liquid chromatography–tandem mass spectrometry (LC-MS/MS). In both studies, *mIDO1* gene expression was detected in most, but not all CT26-derived tumors, while the expression levels were low and varied considerably among the mice (Supplementary Figures 1C and 1D). Nonetheless, in both studies a similar, considerable reduction of Kyn levels was found in the tumor (Supplementary Figures 1E and 1F), indicating target modulation regardless of tumor growth inhibition.

With the aim to establish a mouse model with stable *mIDO1* gene expression, we next evaluated the use of an *mIDO1*-overexpressing cell line for the generation of a mouse model. We therefore generated stable sublines of the B16F10 melanoma cell line overexpressing mouse IDO1 (B16F10-mIDO1) (Figure 3). Transfection of full-length *mIDO1* cDNA followed by subcloning resulted in two stable sublines with different mIDO1 mRNA and protein levels (Figures 3A and 3B). The Trp-catabolizing activity of the sublines could be inhibited with NTRC 3883-0 and epacadostat (Table 2), while the selective IDO inhibitor NTRC 3531-0 was inactive (*i.e.*, $IC_{50} > 31.6 \mu\text{M}$). Whereas NTRC 3883-0 and epacadostat inhibited mIDO1 activity in a biochemical assay with similar potency (Table 2), NTRC 3883-0 was five times more potent compared to epacadostat in the cell-based B16F10-mIDO1 assay (Table 2).

To determine the effect of *mIDO1* expression on tumor growth, the parental B16F10 cell line and the two stable *mIDO1*-overexpressing sublines were implanted into female B6D2F1 syngeneic mice. The tumors grew rapidly, but there was no difference in growth rate between tumors derived from the parental cell line and the *mIDO1*-overexpressing

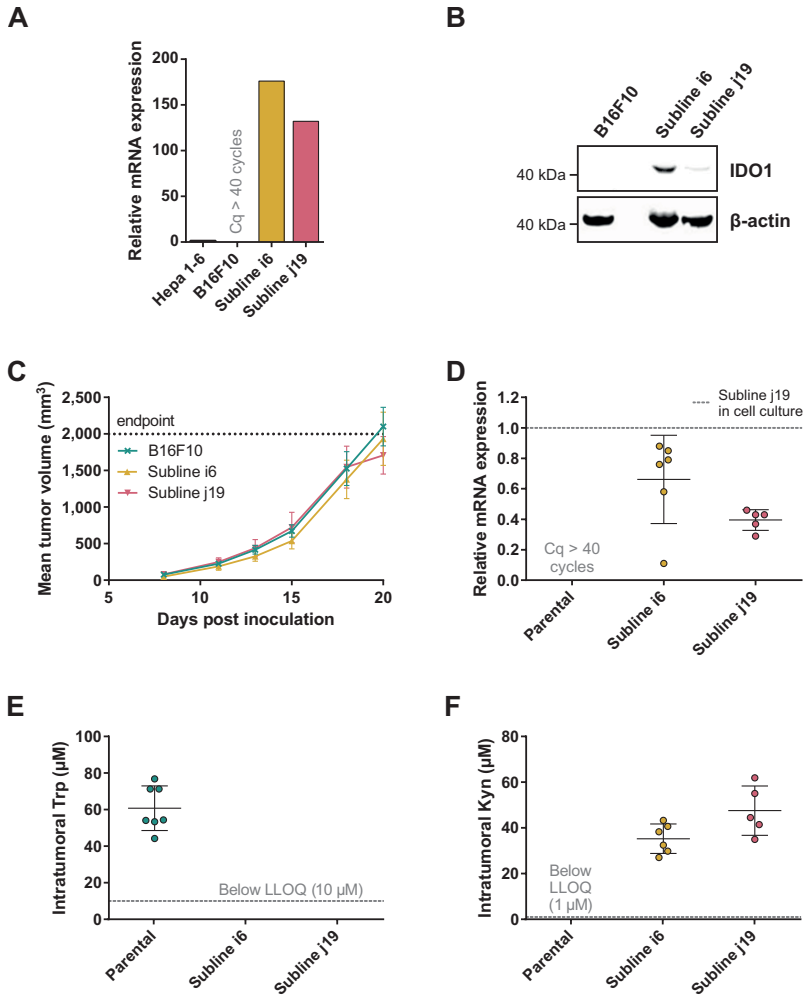


Figure 3. Development of a syngeneic mouse model using a B16F10 melanoma cell line stably overexpressing *mIDO1*. **(A)** Analysis of *mIDO1* mRNA levels by qPCR in the parental B16F10 cell line and two *mIDO1*-transfected stable sublines (i6 and j19). mRNA levels were normalized for the expression of three housekeeping genes (*ACTB*, *GAPDH* and *RPL37*), and scaled based on the hepatoma Hepa 1-6 cell line stimulated with IFN γ (included as a positive control). **(B)** Immunoblot analysis of the parental B16F10 cell line and *mIDO1*-overexpressing sublines. **(C)** Mean tumor volume after implantation of the B16F10-*mIDO1* i6 and j19 sublines in B6D2F1 mice. Results are expressed as mean \pm SEM. **(D)** Analysis of *mIDO1* mRNA levels in the tumor tissues by qPCR. mRNA levels are scaled based on the mRNA level of the B16F10-*mIDO1* subline j19 in cell culture. **(E)** Intratumoral Trp and **(F)** Kyn levels as determined by LC-MS/MS. LLOQ in panels E and F indicates the lower limit of quantification of the experiment. Results in panels D–F are expressed as mean \pm SD.

sublines (Figure 3C). After sacrifice of the mice, the tumors were collected and analyzed for *mIDO1* gene expression by qPCR, while the Trp and Kyn levels were measured by LC-MS/MS. *mIDO1* expression was maintained in all tumors collected from the B16F10-mIDO1 sublines i6 and j19, with the mRNA levels in the tumors deviating on average only 2.0- and 2.5-fold from their respective cell lines in culture (Figures 3A and 3D). *mIDO1* expression resulted in strongly reduced Trp and increased Kyn levels (Figures 3E and 3F), indicating that the model could be suitable for pharmacodynamic studies of IDO1 inhibitors. The subline j19 was chosen for further experiments, as this subline showed the least variation in mRNA levels (Figure 3D) and induced on average the highest increase in Kyn levels in the tumors (Figure 3F).

For evaluation of the *in vivo* effect of NTRC 3883-0 in the B16F10-mIDO1 mouse model, NTRC 3883-0 and epacadostat were both administered twice daily at 100 mg/kg. Dosing of the IDO1 inhibitors was started prior to establishment of the tumor (*i.e.*, prophylactic administration) (Figure 4A), based on previous experience of Charles River Laboratories, where the study was performed. In 22 out of the 32 animals, a tumor developed from the grafted B16F10-mIDO1 cells. Comparison of plasma Trp and Kyn levels among the mice revealed that vehicle-treated, tumor-bearing animals had significantly lower plasma Trp and higher plasma Kyn levels compared to non-tumor bearing animals (Figures 4B and 4C). This indicates that there is a direct effect of *mIDO1* expression in the tumors on systemic Trp and Kyn concentrations. The effect was diminished upon IDO1 inhibitor treatment (Figures 4B and 4C), indicating effective IDO1 inhibition. Treatment with NTRC 3883-0 or epacadostat had no effect on tumor growth in comparison to vehicle-treated animals (Figure 4D), although a delay in tumor growth could be observed when correcting the tumor growth data for the variation in time until tumor establishment (Figure 4E). After sacrifice of the mice, qPCR analysis revealed that the *mIDO1* expression in the tumors was remarkably stable (Figure 4F). Comparison of inhibitor concentrations revealed that NTRC 3883-0 reached on average 1.8 and 2.2 times lower levels in plasma and the tumors, respectively, compared to epacadostat (Figure 4G). IDO1 inhibitor treatment resulted in significantly increased intratumoral Trp levels and reduced Kyn levels (Figures 4H and 4I). Treatment with NTRC 3883-0 resulted in 3.6 times lower levels of Kyn compared to epacadostat, while it was also slightly more efficient in increasing Trp (Figures 4H and 4I). We conclude that NTRC 3883-0 can modulate IDO1 activity *in vivo*, thus showing target engagement.

Modulation of IDO1 activity in primary ovarian cancer cells

We next extended our studies to primary, ascites-derived cells of ovarian cancer patients. In ovarian cancer, IDO1 has been related to disease progression,²⁴ chemotherapy resistance⁹ and impaired survival,^{9,25} based on expression analysis of IDO1 by *in situ* hybridization and immunohistochemistry of tumor specimens.^{9,24,25} Patients with advanced ovarian cancer

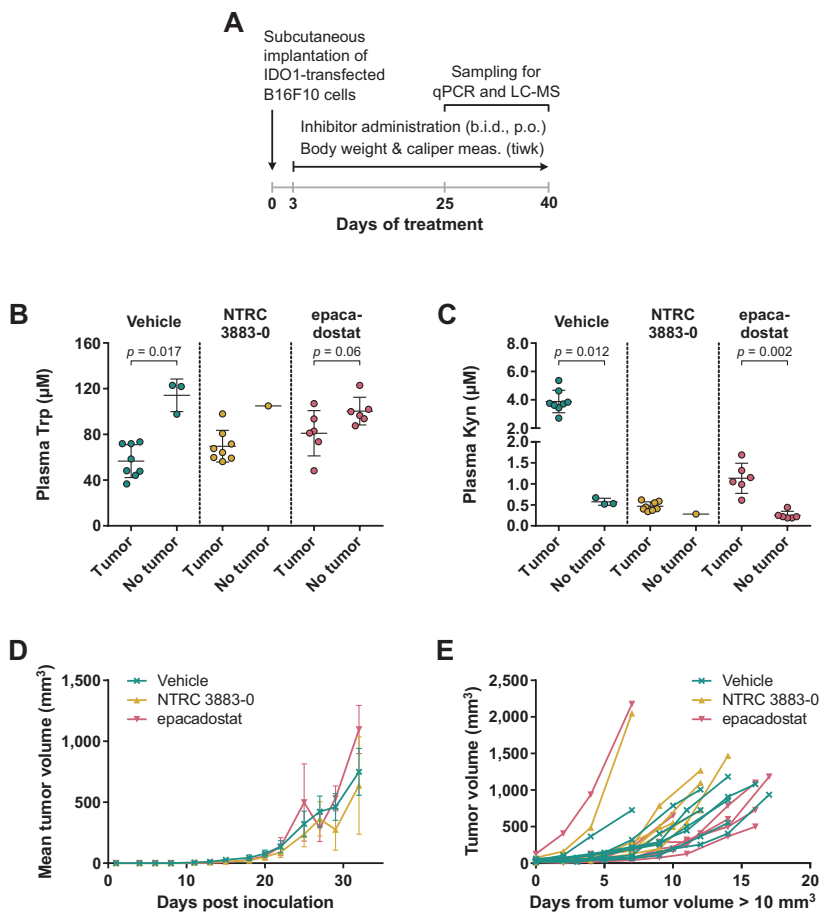


Figure 4. *In vivo* effect of NTRC 3883-0 and epacadostat in the B16F10-mIDO1 mouse model. (A) Experimental schedule of the intervention study with prophylactic administration of IDO1 inhibitors. (B) Analysis of Trp and (C) Kyn levels in plasma by LC-MS/MS. Results of the Mann–Whitney U test are indicated in the panels. Mice treated with NTRC 3883-0 were excluded from the statistical analysis as this group contained only one mouse without a tumor. Trp and Kyn levels are expressed as mean \pm SD. (D) Mean tumor volume and (E) individual tumor volume of mice treated with vehicle, NTRC 3883-0 or epacadostat. The time scale in panel E takes into account the variation in time until tumors were established (defined as a tumor volume $>$ 10 mm³). (F) Analysis of *mIDO1* mRNA levels in the tumor tissues by qPCR. mRNA levels were normalized for the expression of three housekeeping genes (*ACTB*, *GAPDH* and *RPL37*), and scaled based on the mRNA level of the B16F10-mIDO1 subline j19 in cell culture. (G) Analysis of plasma and intratumoral inhibitor levels by LC-MS/MS. (H) Analysis of intratumoral Trp and (I) Kyn levels by LC-MS/MS. Welch’s ANOVA showed an overall effect of IDO1 inhibitor treatment on both Trp and Kyn levels ($p < 0.001$ for both inhibitors). Games–Howell *post hoc* results are indicated in the panels. Results in panels F–I are expressed as mean \pm SD.

(Figure continued on next page)

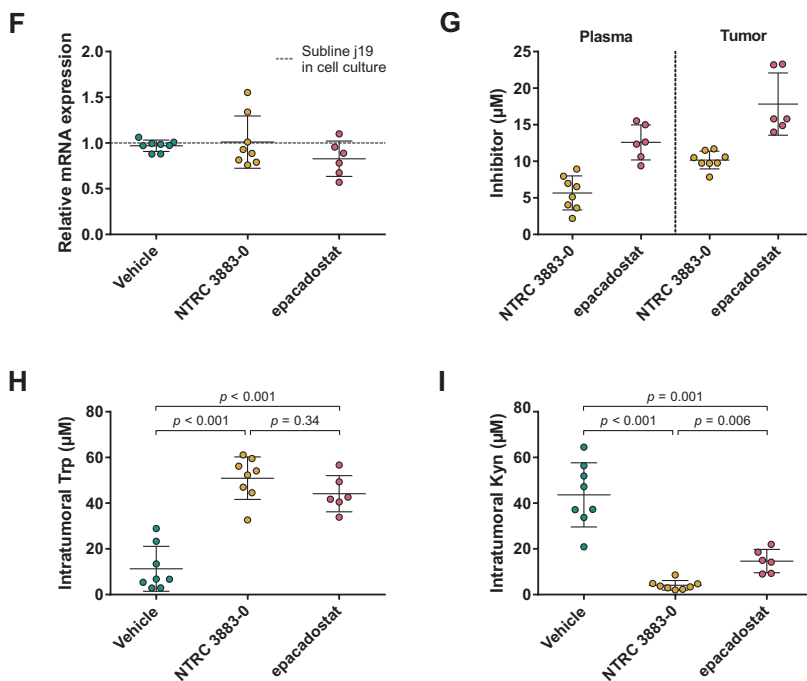


Figure 4. Continued.

often present with high volumes of malignant ascites, which is routinely collected for diagnostic purposes or relieve of symptoms. Ascites is a potential source for biomarkers to monitor disease progression and to determine chemotherapy response *ex vivo*.

Adherent cell samples were isolated from the ascites collected from nineteen ovarian cancer patients with different histologies (Supplementary Table 1). The presence of tumor cells in these samples was confirmed by qPCR analysis of the ovarian cancer marker genes *MUC16* and *HE4* (Supplementary Figure 2), while five of the nineteen cell samples were additionally analyzed for cell surface expression of mucin-16 and epithelial cell adhesion molecule (EpCAM) by flow cytometry (Supplementary Figure 3 and Supplementary Table 2). Basal *IDO1* gene expression could be detected by qPCR in fifteen of the nineteen samples, while basal *TDO2* expression was found in all nineteen samples (Figure 5A).

Five of the nineteen samples were further analyzed for *IDO1* and *TDO2* gene expression, *IDO1* protein levels, and Trp-catabolizing activity both in the presence and absence of IFN γ , a known inducer of *IDO1* gene expression (Figures 5B–D). qPCR analysis revealed that four out of the five samples showed comparable, relatively low basal *IDO1* mRNA levels,

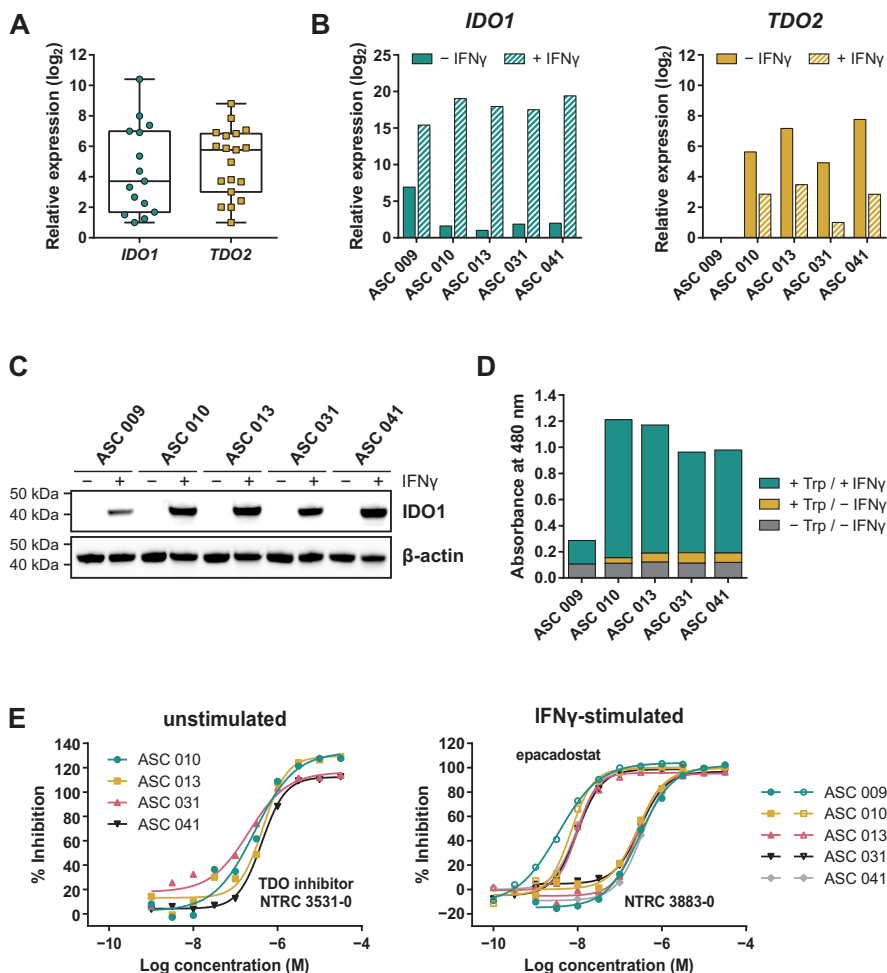


Figure 5. Expression and modulation of IDO1 and TDO in adherent cell samples isolated from the ascites of ovarian cancer patients. **(A)** Tukey boxplot of basal *IDO1* and *TDO2* gene expression as determined by qPCR in adherent cell samples cultured for two to three passages. For *IDO1*, only the fifteen samples with detectable expression are shown. mRNA levels were normalized for the expression of the *ACTB* housekeeping gene, and scaled based on the lowest expressing samples. **(B)** Analysis of *IDO1* and *TDO2* mRNA levels in five adherent cell samples in the absence and presence of IFN_γ. mRNA levels were normalized for the expression of the *ACTB* and *RPS18* housekeeping genes, and scaled based on the lowest expressing samples. **(C)** IDO1 protein levels measured in the same sample subset as in panel B. TDO protein levels of the samples could not be analyzed due to the lack of a suitable antibody. **(D)** Trp-catabolizing activity in the same sample subset as in panel B. The activities are displayed as the absorbance measured using the pDMAB assay, and are based on three replicate experiments for ASC 009, ASC 031 and ASC 041, and two replicate experiments for ASC 010 (Legend continued on next page)

which were highly increased (*i.e.*, on average 120,000-fold) upon stimulation with IFN γ (Figure 5B). In contrast, 40-fold higher basal *IDO1* expression was found in ASC 009, which was increased by 360-fold upon IFN γ stimulation (Figure 5B). Immunoblot analysis of IDO1 revealed a consistent pattern (Figure 5C). Analysis of the *TDO2* mRNA levels showed clear basal *TDO2* expression in four samples, albeit with slightly more variation among the samples compared to *IDO1*, while no *TDO2* expression was detected in ASC 009 either with or without stimulation (Figure 5B). Notably, *TDO2* expression was found to be consistently downregulated 7- to 30-fold upon stimulation with IFN γ (Figure 5B).

Assessment of the Trp-catabolizing activity in the samples showed basal activity in four out of the five samples (Figure 5D; + Trp/- IFN γ). Treatment with the TDO-selective inhibitor NTRC 3531-0 resulted in a concentration-dependent inhibition of this activity with an average IC₅₀ of 300 nM (Figure 5E and Supplementary Table 3). In contrast, NTRC 3883-0 and epacadostat showed no or only minimal inhibition (Supplementary Table 3). This indicates that the Trp-catabolizing activity in the absence of stimulation can be solely attributed to the activity of TDO, and not IDO1, despite the constitutive expression of *IDO1* observed in most samples (Figures 5A and 5B). Stimulation of the ascites cell samples with IFN γ induced a further increase in Trp-catabolizing activity (Figure 5D; + Trp/+ IFN γ), with a consistent pattern as that observed for IDO1 mRNA and protein levels. In the stimulated samples, treatment with either NTRC 3883-0 or epacadostat resulted in potent inhibition of the Trp-catabolizing activity with IC₅₀ values of respectively 261 nM and 8.3 nM (Figure 5E and Supplementary Table 3), which are in close agreement with the potencies found in the A375- and HEK-hIDO1-based assays (Table 2). Moreover, the Trp-catabolizing activity could not be inhibited by the TDO inhibitor NTRC 3531-0 (*i.e.*, IC₅₀ > 31.6 μ M). This demonstrates that the IFN γ -dependent Trp-catabolizing activity of the primary patient-derived cancer cells can be attributed to IDO1 activity, and can be selectively inhibited by NTRC 3883-0.

Discussion

IDO1 is a key regulator of the immune modulatory activity of Trp and is therefore a candidate drug target to increase the efficacy of checkpoint inhibitor therapy. We have described the pharmacological characterization of a novel, selective IDO1 inhibitor, NTRC 3883-0, which was profiled in various biochemical and cell-based assays along-

(Legend continued from previous page)

and ASC 013. (E) Inhibition of the Trp-catabolizing activity in unstimulated samples by the selective TDO inhibitor NTRC 3531-0, and in IFN γ -stimulated samples by NTRC 3883-0 (closed symbols) and epacadostat (open symbols). The corresponding IC₅₀ values are listed in Supplementary Table 3.

side epacadostat. In a co-culture assay with healthy donor lymphocytes, our data confirm that IDO1 expression suppresses cytotoxic T-cell proliferation *in vitro* by decreasing the Trp concentration. Treatment with an IDO1 inhibitor (*i.e.*, NTRC 3883-0 or epacadostat) abolished this inhibitory effect.

In search of a mouse model to additionally profile the *in vivo* efficacy of NTRC 3883-0, we initially chose the frequently used CT26 mouse model, which is described to endogenously express *IDO1* when grafted in mice.¹⁹ However, this model was found to be unreliable based on unreproducible tumor growth inhibition results among our two similar studies. Moreover, strong variation in the intratumoral *IDO1* mRNA levels was found, with some mice having undetectably low expression. To abolish the potential effect of the low and strongly variable *IDO1* expression on the reliability of the efficacy model, we developed a syngeneic mouse model using B16F10 melanoma cells stably overexpressing *mIDO1*. While we have demonstrated strong target modulation in this model upon treatment with NTRC 3883-0, we did not observe an effect of IDO1 expression or IDO1 inhibitor treatment on the tumor growth rate. This is in contrast with the results obtained by Holmgaard and coworkers, who describe the first use of this model, and who describe an increased tumor growth rate after IDO1 overexpression, which is reduced by IDO1 inhibitor treatment.²¹ The reason for this discrepancy is unclear, but may be related to subtle differences in the *mIDO1*-overexpressing or parental cell lines, the mouse strains used or the breeding conditions. Nonetheless, based on the demonstrated target modulation observed for both NTRC 3883-0 and epacadostat, the B16F10-mIDO1 model has proven suitable for application in pharmacodynamic studies of IDO1 inhibitors.

When our studies were still in progress, negative clinical results were reported on several IDO1 inhibitors, including epacadostat,¹⁷ EOS200271/PF-0684003²⁶ and navoximod (NLG-919).²⁷ Several experts have commented on these results, in particular on those obtained in the phase III combination trial of epacadostat with pembrolizumab.^{28–30} Among the potential causes mentioned for the negative results, the dosing strategy was prominently discussed, since the dose of epacadostat may have been too low to obtain sufficient target coverage in the ECHO-301/KEYNOTE-252 clinical trial. The lack of a good patient stratification strategy was additionally criticized, since patients included in this study had not been selected on the basis of IDO1 expression, although tumor *IDO1* gene expression was assessed as part of the study.¹⁷ A third possibility raised is that TDO may compensate for inhibition of IDO1, and it has been suggested that dual IDO1/TDO inhibitors may result in more effective anti-tumor immunity.³¹

Learning from these lessons, NTRC 3883-0 was not pursued for further clinical development. This was decided based on allometric scaling indicating that NTRC 3883-0

is unlikely to reach sufficient target coverage of human IDO1 at acceptable dose levels in cancer patients (Supplementary Figure 4 and Supplementary Table 4). However, because of its favorable inhibitory potency on mouse IDO1, its better selectivity in biochemical assays, and its higher degree of *in vivo* target modulation compared to epacadostat, NTRC 3883-0 may become an important tool compound to study the role of IDO1 in mouse disease models. In addition to cancer models, this may support research on neurodegenerative and infectious diseases, for which a role of IDO1 has also been implicated.^{32,33}

In the phase III clinical trial of epacadostat, *IDO1* gene expression in tumor samples was quantified by *in situ* hybridization.¹⁷ Our studies with primary ovarian cancer cell cultures isolated from ascites indicate that determination of basal *IDO1* gene expression may not be sufficient. We found that only after stimulation with IFN γ , modulation of Trp-catabolizing activity by IDO1 inhibitors could be observed. We propose that functional cell-based assays for IDO1 are included as diagnostic tools to select patients most likely to respond to IDO1 inhibitor therapy. Our research demonstrates for the first time the use of malignant ascites as a source of biomarkers for clinical research on IDO1. The use of cells from ascites has a major advantage over the use of surgical biopsies or organoid cultures.³⁴ The collection of ascites is minimally invasive and assays to determine the activity of compounds can be performed *ex vivo* prior to the start of therapy.

Notably, we could detect *TDO* gene expression in all nineteen primary ovarian cancer cell cultures examined. By making use of a selective inhibitor, we demonstrated basal TDO activity in four cultures. Thus far, only a few cancer cell lines that express TDO constitutively are known, while many cell lines express IDO1 upon stimulation with IFN γ .^{8,35} TDO has been implicated in cancer, but its role is not well understood. Based on its high $K_{M,Trp}$ of 190 μ M, it is unlikely that TDO contributes to the regulation of the low Trp concentrations that induce T-cell anergy, which are around 1 μ M and lower.^{6,18} However, TDO may regulate immune function through the metabolite Kyn, which is a ligand of the aryl hydrocarbon receptor.³⁶ Furthermore, roles of TDO in tumor metastasis³⁷ and angiogenesis³⁸ have been described. Because of the different roles of IDO1 and TDO in cancer, it is unlikely that TDO expression may have compensated for IDO1 inhibition in the ECHO-301/KEYNOTE-252 trial. Therefore, there is no strong rationale for the development of dual IDO1/TDO inhibitors, since the possible beneficial effects of dual inhibition have to be balanced with the risk of interfering with the role of TDO in Trp homeostasis.

While many companies have de-prioritized their IDO1 programs, the development of the selective and potent IDO1 inhibitor linrodostat has continued. Linrodostat has demonstrated safety and good target coverage upon once-daily oral dosing in a phase I/IIa study,³⁹ and is currently investigated in a Phase III combination trial with the anti-PD-1 immuno-

therapeutic nivolumab and chemotherapy for advanced bladder cancer.⁴⁰ Preliminary clinical response data hold promise for IDO1 as a valid drug target for immunotherapy.⁴⁰ A positive outcome will undoubtedly fuel interest in the development of additional IDO1 inhibitors with differentiating properties. The novel IDO1 inhibitor scaffold described here as well as our *in vitro* and *in vivo* pharmacological models may support these R&D activities.

Materials and methods

Inhibitors

The synthesis of NTRC 3883-0 and analogues (Table 1) is described in patent application WO/2017/153459,⁴¹ where NTRC 3748-0 and NTRC 3883-0 are referred to as Example 27 and 142b, respectively. For preparative purification of NTRC 3883-0, a chirally pure acid (*i.e.*, (S)-(+)-2-phenylbutyric acid) was introduced at the hydroxyl amide function of NTRC 3748-0, followed by separation of the two diastereoisomers by straight phase column chromatography. Deprotection of the chiral auxiliary resulted in **3k** and NTRC 3883-0 (Table 1). The absolute configuration of the stereogenic center in NTRC 3883-0 was established by single-crystal X-ray diffraction, which additionally confirmed the orientation of the *o,o*-difluorobenzoyl group (Supplementary Figure 5). Epacadostat was purchased at PharmaBlock (cat. no. PBLJ9203). The selective TDO inhibitor NTRC 3531-0 was synthesized as described in patent application WO/2018/011227 A1.⁴²

IDO1, TDO and CYP biochemical assays

Full-length recombinant human and mouse IDO1 were expressed in *Escherichia coli* with a hexahistidine tag at the N-terminus, and purified by affinity chromatography to > 95% purity, as described.⁸ Human and mouse TDO containing a C-terminal hexahistidine tag were analogously expressed and purified to > 95% purity.⁸ The inhibitory activity of compounds was determined with the NFK GreenScreen assay technology under the conditions as described,⁸ except for the reaction buffer for IDO1, which was replaced by 50 mM NaH₂PO₄, pH 7.0, supplemented with 0.01% Tween-20 and 1% glycerol. Inhibition of the CYP3A4 and CYP2D6 enzymes was determined with the P450-Glo™ Screening System with Luciferin-IPA (Promega, cat. no. V9920 and V9890). For determination of IC₅₀ values, the effect of inhibitors was determined in 10-point duplicate dose-response curves. Graphs were fitted to a four-parameter logistics equation in XLfit (IDBS) from which IC₅₀ values were calculated.

Cancer cell lines

The A375 and SW48 cancer cell lines were purchased from the American Type Culture Collection (ATCC, cat. no. CRL-1619 and CCL-231) and cultured in the ATCC-recommended

media. All experiments with non-recombinant cell lines were carried out within ten passages from the original vials of ATCC who authenticated the cell lines by short tandem repeat analysis.

Recombinant cell lines

The GripTite™ 293 MSR cell line was purchased from ThermoFisher (cat. no. R79507), the B16F10 cell line from ATCC (cat. no. CRL-6475), and the GL-261 cell line from the Deutsche Sammlung von Mikroorganismen und Zellkulturen (DSMZ, cat. no. ACC 802). Each cell line was cultured in the medium recommended by the supplier, with FBS replaced by BCS for the B16F10 and GL-261 cell lines. Sublines of GripTite™ 293 MSR stably overexpressing human *IDO1* (HEK-hIDO1), GripTite™ 293 MSR stably overexpressing human *TDO2* (HEK-hTDO), B16F10 stably overexpressing mouse *IDO1* (B16F10-mIDO1), and GL-261 stably overexpressing mouse *TDO2* (GL-261-mTDO) were generated by transfection of the respective cells with respectively full-length *hIDO1*, *hTDO2*, *mIDO1* or *mTDO2* cDNA cloned in the expression vector pEF6v5 (Thermo Fisher, cat. no. V96120). Cells were transfected with Lipofectamine 3000 (Thermo Fisher) and single cell clones were selected by blasticidin selection and limited dilution in 384-well culture plates. Trp-catabolizing activity was evaluated using NFK Green or 4-(dimethylamino)benzaldehyde (pDMAB).⁴³ To assess the stability of *IDO1* or *TDO2* expression, clones were cultured for 4 weeks in the absence of blasticidin, during which they were tested weekly for Trp-catabolizing activity. Afterwards, the mRNA and protein levels, and the inhibitory potency of reference compounds were determined in the resulting sublines. Cell-based assays with the transfected cell lines were performed in the absence of blasticidin.

Cell-based assays

Inhibition of the Trp-catabolizing activity in A375 cells, HEK-hTDO cells, GL-261-mTDO cells and primary patient samples (all seeded at 8,000 cells/well) was determined after incubation of the cells with compound for 1 h, followed by supplementation of the culture medium with 200 μ M Trp and incubation for 42 h. The A375 cells and primary patient samples were stimulated with 200 ng/mL IFN γ prior to the incubation period. The remaining cell-based assays were performed analogously to the HEK-hTDO and GL-261-mTDO assays, with the following exceptions. For the SW48 cells, incubation with compound and Trp was performed for 18 h. For the HEK-hIDO1 cells, the cells were seeded at 16,000 cells/well, and no additional Trp was added to the culture medium. For the B16F10-mIDO1 cells, no additional Trp was added to the culture medium, and the cells were incubated for 66 h with compound. Inhibition of the Trp-catabolizing activity in heparinized human whole blood was determined after three-fold dilution of the blood in RPMI 1640 supplemented with 1% penicillin/streptomycin (P/S), incubation of the diluted blood with compound for 1 h, addition of 800 μ M Trp and 200 ng/mL IFN γ , and incubation for 66 h.

For the A375, SW48, HEK-hIDO1 and HEK-hTDO cell-based assays, the Trp-to-NFK conversion was measured with NFK Green, as described previously.⁸ For the B16F10-mIDO1 cells, GL-261-mTDO cells and heparinized human whole blood, the Trp-to-NFK conversion was measured with pDMAB.⁴³ Briefly, 5% trichloroacetic acid in Milli-Q water was added to each well, followed by incubation at 55 °C for 1 h, centrifugation for 20 min at 2,900 *g*, transfer of the supernatant to a new plate, and addition of 2% pDMAB (Fisher Chemicals) dissolved in acetic acid to each supernatant. After incubation for 10 min at room temperature, the formation of Kyn was determined by measurement of the absorbance at 480 nm. In parallel with the cell-based NFK Green assays, the cytotoxicity of the compounds was determined in cell viability assays using ATPlite™ 1Step (PerkinElmer).⁸ NTRC 3883-0, epacadostat and NTRC 3531-0 were not cytotoxic to any cell line used in this study.

Gene expression analysis

RNA was isolated from cell cultures and tumors with the RNeasy Mini kit (Qiagen). cDNA was prepared using the QuantiTect Reverse Transcription kit (Qiagen) and qPCR was performed in a Bio-Rad CFX96 cycler using SYBR™ Select Master Mix (Thermo Fisher) following standard protocols.⁴⁴ The sequences of the qPCR primers are provided in Supplementary Table 5.

Immunoblot analysis

The expression of hIDO1, mIDO1 and hTDO in cell cultures was determined by SDS-PAGE and immunoblot analysis. hIDO1 and mIDO1 were detected with anti-IDO1 rabbit monoclonal antibody (Cell Signaling, cat. no. 86630), HRP-conjugated anti-rabbit IgG (Cell Signaling, cat. no. 7074) and enhanced chemiluminescence (ECL) using Clarity™ Western ECL substrate (BioRad, cat. no. 170-5060). hTDO was detected with anti-TDO mouse monoclonal antibody (OriGene, cat. no. TA504879), HRP-conjugated anti-mouse IgG (Cell Signaling, cat. no. 7076S) and ECL. To control for equal loading of the samples on SDS-PAGE gels, the blots were stripped using Restore™ Plus Western Blot Stripping Buffer (ThermoFisher, cat. no. 46430), after which β -actin was detected using anti- β -actin rabbit polyclonal antibody (Cell Signaling, cat. no. 4967), HRP-conjugated anti-rabbit IgG (Cell Signaling) and ECL.

Co-culture assay

HEK-hIDO1 cells were seeded at high density (25,000 cells per well) in clear 96-well culture plates (Greiner, cat. no. 651101) in RPMI 1640 medium without Trp (PAN Biotech, cat. no. P04-17598), supplemented with 10% FBS and 1% P/S. Trp was added to a final concentration of 7.5 μ M, or 200 μ M as a control. NTRC 3883-0 or epacadostat was added to a final concentration of 10 or 1 μ M, respectively. The next day, PBMCs isolated from a buffy coat were labeled with 0.5 μ M CFSE in PBS at 37 °C in the dark for 13 min. The labeling reaction was stopped with complete RPMI 1640 medium, supplemented with

10% FBS and 1% P/S. After washing twice with medium, the PBMCs were stimulated with α CD2/ α CD3/ α CD28-coupled microbeads (Miltenyi, cat. no. 130-091-441) at a bead-to-cell ratio of 1:1, and added to the HEK-293 cells at a density of 100,000 cells per well. After co-culturing for 5 days, the PBMCs were transferred to a V-bottom plate (Greiner, cat. no. 651101), washed twice with ice-cold PBS containing 0.5% bovine serum albumin (BSA) (Sigma-Aldrich, cat. no. A7906-100G) and incubated for 10 min at 4 °C with Fc-receptor blocking reagent (Miltenyi, cat. no. 130-059-901). Without washing the PBMCs, α CD8-PE (Miltenyi, clone REA734, cat. no. 130-110-678) and REA-S isotype control (Miltenyi, cat. no. 130-113-439) were added. After incubation for 10 min at 4 °C, the PBMCs were washed twice with 0.5% BSA in PBS and analyzed on a Guave® easyCyte 5HT Benchtop Flow Cytometer (Merck Millipore) with a blue 488 nm laser. Flow cytometry data were analyzed using Kaluza Analysis (Beckman Coulter Life Sciences, version 2.1). Quantitative analysis of the cell proliferation data was performed using flowFit in RStudio.⁴⁵

***In vivo* pharmacokinetics and pharmacodynamics models**

In vivo pharmacokinetics studies were performed at Charles River Laboratories ('s-Hertogenbosch, The Netherlands). *In vivo* pharmacodynamic and intervention studies were performed at ProQinase (Freiburg, Germany) and Charles River Laboratories (Morrisville, NC). All experimental protocols were approved by, and performed in accordance with the guidelines of the Ethics Committee for Animal Experimentation of the respective organizations.

Pharmacokinetic properties of NTRC 3883-0 were determined in plasma following single oral (p.o.) and intravenous (i.v.) administration to male CD-1 mice ($N = 6$ per treatment group with three mice sampled per time point), Wistar rats ($N = 3$), cynomolgus monkey ($N = 1$) and Beagle dogs ($N = 3$). Formulations were prepared in DMSO, Kolliphor® EL, 5% D-mannitol in Elix water at a volume ratio of 1:1:8 for i.v. administration, and in 0.5% gelatin, 5% D-mannitol in Elix water for p.o. administration. Plasma samples were collected at eight to eleven time points up to 24 h after administration. Pharmacokinetic properties and required dosing in humans were predicted by allometric scaling by Karin Jorga Life Science Consulting (Basel, Switzerland) (Supplementary Figure 4 and Supplementary Table 4).

For the first CT26 mouse model study, performed at ProQinase, 5×10^5 CT26 cells were implanted subcutaneously into female BALB/c mice on day 0. From day 8 onwards, 50 mg/kg of NTRC 3748-0 (Table 1) or 100 mg/kg of epacadostat was administered p.o., respectively twice daily (b.i.d.) and once daily (q.d.), as a suspension in 0.5% gelatin, 5% mannitol in water, with $N = 8$ mice per treatment group. Tumor growth was monitored using caliper measurement two times weekly. The study was terminated at day 22 based on the tumor burden. Tumors and plasma were sampled 2 h post last dose.

For the second study, performed at Charles River Laboratories, 3×10^5 CT26 cells were implanted subcutaneously into female BALB/c mice on day 0. From day 8 onwards, 100 mg/kg of NTRC 3883-0 or epacadostat was administered p.o. b.i.d. as a suspension in 0.5% gelatin, 5% mannitol in water, with $N = 10$ mice per treatment group. Tumor growth was monitored using caliper measurement three times weekly. A tumor volume of $2,000 \text{ mm}^3$ was used as the endpoint of the experiment for the individual animals. Tumors were sampled 2 h post last dose.

For development of the *mIDO1*-overexpressing B16F10 mouse model, performed at Charles River Laboratories, female B6D2F1 mice were implanted subcutaneously with 1×10^6 parental B16F10 cells or B16F10-*mIDO1* cells (subline i6 or j19) on day 0 with $N = 10$ mice per group. A tumor volume of $2,000 \text{ mm}^3$ was used as the endpoint of the experiment for the individual animals. To determine the optimal inoculation cell concentration, mice were implanted with 3×10^5 , 1×10^5 or 3×10^4 parental or *mIDO1*-overexpressing B16F10 cells (subline j19) with $N = 5$ mice per group. The same endpoint of the experiment was used as described above. This yielded on average no differences in growth rate between the parental and *mIDO1*-overexpressing groups, but instead resulted in a strong reduction of the take rate at the lower inoculation concentrations. For the intervention study, 3×10^5 cells of the B16F10-*mIDO1* subline j19 were implanted on day 0, and treatment was started on day 3 with vehicle (DMSO, Kolliphor, 5% mannitol; 10/10/80, v/v/v), 100 mg/kg NTRC 3883-0 or epacadostat administered p.o. b.i.d. with $N = 12$ mice per treatment group. Four animals were excluded from analysis due to non-treatment-related deaths. Tumors and plasma were sampled 2 h post last dose.

Quantification of inhibitor, Trp and Kyn levels

Tissues were homogenized in PBS at a ratio of 1 mg per 10 μL using micro pellet pestles mounted on a Micro-Tube Homogenizer System (Thomas Scientific). After centrifugation, proteins were removed from the homogenized tissue supernatants and plasma samples by precipitation with methanol. The concentrations of inhibitor, Trp and Kyn were determined by LC-MS/MS.

Patient samples

Ascites was collected from patients with a primary diagnosis of advanced epithelial ovarian cancer during paracentesis for diagnostics or symptom relieve, or during primary debulking surgery. Ascites was filtered and cells were collected by centrifugation as described.⁴⁶ To enrich for tumor cells, ascites cell samples were allowed to adhere overnight to tissue culture plastic. The cell samples were then cultured for 2–3 weeks in advanced RPMI medium (ThermoFisher), supplemented with 10% FBS, 1% glutamax and 1% P/S, with two or three times passaging of the cells. qPCR analyses of the *MUC16*, *HE4*, *IDO1* and *TDO2*

genes were performed for all samples as described above. Five samples which could be cultured over multiple passages were analyzed for cell surface expression of mucin-16 and EpCAM by flow cytometry using FITC-conjugated anti-mucin-16 (AssayPro, cat. no. 32189-05141) and APC-conjugated anti-EpCAM (Miltenyi, cat. no. 130-111-117) to assure that the cell cultures consisted of malignant cells. IDO1 mRNA and protein levels in these samples were analyzed as described above after incubation with or without 200 ng/mL IFN γ for 24 h. The collection of ascites and the research described was conducted with approval of the medical ethical committee of the Radboud university medical center and informed written consent from each subject.

Statistical analyses

Differences in plasma Trp and Kyn levels between the B16F10-mIDO1 mouse model groups with and without tumor development during the intervention study were analyzed using the Mann–Whitney U test. Differences in intratumoral Trp and Kyn levels between the intervention groups were analyzed by Welch's ANOVA followed by Games–Howell *post hoc* analysis. Statistical analyses were performed in RStudio.

References

1. Prendergast, G. C., Malachowski, W. J., Mondal, A., Scherle, P. & Muller, A. J. Indoleamine 2,3-dioxygenase and its therapeutic inhibition in cancer. *Int. Rev. Cell Mol. Biol.* **336**, 175–203 (2018).
2. Opitz, C. A. *et al.* The therapeutic potential of targeting tryptophan catabolism in cancer. *Br. J. Cancer* **122**, 30–44 (2020).
3. Théate, I. *et al.* Extensive profiling of the expression of the indoleamine 2,3-dioxygenase 1 protein in normal and tumoral human tissues. *Cancer Immunol. Res.* **3**, 161–72 (2015).
4. Takikawa, O., Kuroiwa, T., Yamazaki, F. & Kido, R. Mechanism of interferon- γ action. Characterization of indoleamine 2,3-dioxygenase in cultured human cells induced by interferon- γ and evaluation of the enzyme-mediated tryptophan degradation in its anti-cellular activity. *J. Biol. Chem.* **263**, 2041–8 (1988).
5. Munn, D. H. *et al.* Prevention of allogeneic fetal rejection by tryptophan catabolism. *Science* **281**, 1191–3 (1998).
6. Munn, D. H. *et al.* Inhibition of T cell proliferation by macrophage tryptophan catabolism. *J. Exp. Med.* **189**, 1363–72 (1999).
7. Schutz, G. & Feigelson, P. Purification and properties of rat liver tryptophan oxygenase. *J. Biol. Chem.* **247**, 5327–32 (1972).
8. Seegers, N. *et al.* High-throughput fluorescence-based screening assays for tryptophan-catabolizing enzymes. *J. Biomol. Screen.* **19**, 1266–74 (2014).
9. Okamoto, A. *et al.* Indoleamine 2,3-dioxygenase serves as a marker of poor prognosis in gene expression profiles of serous ovarian cancer cells. *Clin. Cancer Res.* **11**, 6030–9 (2005).
10. Godin-Ethier, J., Hanafi, L.-A., Piccirillo, C. A. & Lapointe, R. Indoleamine 2,3-dioxygenase expression in human cancers: clinical and immunologic perspectives. *Clin. Cancer Res.* **17**, 6985–91 (2011).
11. Dill, E. A., Dillon, P. M., Bullock, T. N. & Mills, A. M. IDO expression in breast cancer: an assessment of 281 primary and metastatic cases with comparison to PD-L1. *Mod. Pathol.* **31**, 1513–22 (2018).
12. Röhrig, U. F. *et al.* Inhibition mechanisms of indoleamine 2,3-dioxygenase 1 (IDO1). *J. Med. Chem.* **62**, 8784–95 (2019).
13. Yue, E. W. *et al.* INCB24360 (epacadostat), a highly potent and selective indoleamine-2,3-dioxygenase 1 (IDO1) inhibitor for immuno-oncology. *ACS Med. Chem. Lett.* **8**, 486–91 (2017).
14. Nelp, M. T. *et al.* Immune-modulating enzyme indoleamine 2,3-dioxygenase is effectively inhibited by targeting its apoforn. *Proc. Natl. Acad. Sci. U. S. A.* **115**, 3249–54 (2018).
15. Beatty, G. L. *et al.* First-in-human phase I study of the oral inhibitor of indoleamine 2,3-dioxygenase-1 epacadostat (INCB-024360) in patients with advanced solid malignancies. *Clin. Cancer Res.* **23**, 3269–76 (2017).
16. Mitchell, T. C. *et al.* Epacadostat plus pembrolizumab in patients with advanced solid tumors: phase I results from a multicenter, open-label phase I/II trial (ECHO-202/KEYNOTE-037). *J. Clin. Oncol.* **36**, 3223–30 (2018).
17. Long, G. V. *et al.* Epacadostat plus pembrolizumab versus placebo plus pembrolizumab in patients with unresectable or metastatic melanoma (ECHO-301/KEYNOTE-252): a phase 3, randomised, double-blind study. *Lancet. Oncol.* **20**, 1083–97 (2019).
18. Laing, A. G. *et al.* Mesenchymal stem cells inhibit T-cell function through conserved induction of cellular stress. *PLoS One* **14**, e0213170 (2019).
19. Koblisch, H. K. *et al.* Hydroxyamidine inhibitors of indoleamine-2,3-dioxygenase potently suppress systemic tryptophan catabolism and the growth of IDO-expressing tumors. *Mol. Cancer Ther.* **9**, 489–98 (2010).

20. Levina, V., Su, Y. & Gorelik, E. Immunological and nonimmunological effects of indoleamine 2,3-dioxygenase on breast tumor growth and spontaneous metastasis formation. *Clin. Dev. Immunol.* **2012**, 173029 (2012).
21. Holmgaard, R. B. *et al.* Tumor-expressed IDO recruits and activates MDSCs in a Treg-dependent manner. *Cell Rep.* **13**, 412–24 (2015).
22. Munn, D. H. *et al.* Expression of indoleamine 2,3-dioxygenase by plasmacytoid dendritic cells in tumor-draining lymph nodes. *J. Clin. Invest.* **114**, 280–90 (2004).
23. Spranger, S. *et al.* Up-regulation of PD-L1, IDO, and T_{regs} in the melanoma tumor micro-environment is driven by CD8⁺ T cells. *Sci. Transl. Med.* **5**, 200ra116 (2013).
24. Inaba, T. *et al.* Role of the immunosuppressive enzyme indoleamine 2,3-dioxygenase in the progression of ovarian carcinoma. *Gynecol. Oncol.* **115**, 185–92 (2009).
25. Takao, M. *et al.* Increased synthesis of indoleamine-2,3-dioxygenase protein is positively associated with impaired survival in patients with serous-type, but not with other types of, ovarian cancer. *Oncol. Rep.* **17**, 1333–9 (2007).
26. Reardon, D. A. *et al.* A phase 1 study of PF-06840003, an oral indoleamine 2,3-dioxygenase 1 (IDO1) inhibitor in patients with recurrent malignant glioma. *Invest. New Drugs* **38**, 1784–95 (2020).
27. Jung, K. H. *et al.* Phase I study of the indoleamine 2,3-dioxygenase 1 (IDO1) inhibitor navoximod (GDC-0919) administered with PD-L1 inhibitor (atezolizumab) in advanced solid tumors. *Clin. Cancer Res.* **25**, 3220–8 (2019).
28. Muller, A. J., Manfredi, M. G., Zakharia, Y. & Prendergast, G. C. Inhibiting IDO pathways to treat cancer: lessons from the ECHO-301 trial and beyond. *Semin. Immunopathol.* **41**, 41–8 (2019).
29. Van den Eynde, B. J., van Baren, N. & Baurain, J.-F. Is there a clinical future for IDO1 inhibitors after the failure of epacadostat in melanoma? *Annu. Rev. Cancer Biol.* **4**, 241–56 (2020).
30. Sondak, V. K. & Khushalani, N. I. Echoes of a failure: what lessons can we learn? *Lancet. Oncol.* **20**, 1037–9 (2019).
31. Prendergast, G. C., Malachowski, W. P., DuHadaway, J. B. & Muller, A. J. Discovery of IDO1 inhibitors: from bench to bedside. *Cancer Res.* **77**, 6795–811 (2017).
32. Platten, M., Nollen, E. A. A., Röhrig, U. F., Fallarino, F. & Opitz, C. A. Tryptophan metabolism as a common therapeutic target in cancer, neurodegeneration and beyond. *Nat. Rev. Drug Discov.* **18**, 379–401 (2019).
33. Barth, H. & Raghuraman, S. Persistent infectious diseases say – IDO. Role of indoleamine-2,3-dioxygenase in disease pathogenesis and implications for therapy. *Crit. Rev. Microbiol.* **40**, 360–8 (2014).
34. Hill, S. J. *et al.* Prediction of DNA repair inhibitor response in short-term patient-derived ovarian cancer organoids. *Cancer Discov.* **8**, 1404–21 (2018).
35. Pilotte, L. *et al.* Reversal of tumoral immune resistance by inhibition of tryptophan 2,3-dioxygenase. *Proc. Natl. Acad. Sci. U. S. A.* **109**, 2497–502 (2012).
36. Opitz, C. A. *et al.* An endogenous tumour-promoting ligand of the human aryl hydrocarbon receptor. *Nature* **478**, 197–203 (2011).
37. D'Amato, N. C. *et al.* A TDO2-AhR signaling axis facilitates anoikis resistance and metastasis in triple-negative breast cancer. *Cancer Res.* **75**, 4651–64 (2015).
38. Hoffmann, D. *et al.* Tryptophan 2,3-dioxygenase expression identified in human hepatocellular carcinoma cells and in intratumoral pericytes of most cancers. *Cancer Immunol. Res.* **8**, 19–31 (2020).

39. Luke, J. J. *et al.* BMS-986205, an indoleamine 2,3-dioxygenase 1 inhibitor (IDO1i), in combination with nivolumab (nivo): updated safety across all tumor cohorts and efficacy in advanced bladder cancer (advBC). *J. Clin. Oncol.* **37**, 358 (2019).
40. Sonpavde, G. *et al.* ENERGIZE: a Phase III study of neoadjuvant chemotherapy alone or with nivolumab with/without linrodostat mesylate for muscle-invasive bladder cancer. *Future Oncol.* **16**, 4359–68 (2020).
41. de Man, A. P. A. *et al.* Inhibitors of indoleamine 2,3-dioxygenase. Patent WO/2017/153459 (2017).
42. de Man, A. P. A. *et al.* Inhibitors of tryptophan 2,3-dioxygenase. Patent WO/2018/011227 (2018).
43. Matin, A., Streete, I. M., Jamie, I. M., Truscott, R. J. W. & Jamie, J. F. A fluorescence-based assay for indoleamine 2,3-dioxygenase. *Anal. Biochem.* **349**, 96–102 (2006).
44. Libouban, M. A. A. *et al.* Stable aneuploid tumors cells are more sensitive to TTK inhibition than chromosomally unstable cell lines. *Oncotarget* **8**, 38309–25 (2017).
45. Rambaldi, D., Pece, S. & Di Fiore, P. P. flowFit: a Bioconductor package to estimate proliferation in cell-tracking dye studies. *Bioinformatics* **30**, 2060–5 (2014).
46. Wefers, C. *et al.* Isolation of mononuclear cell populations from ovarian carcinoma ascites. *Bio. Protoc.* **7**, e2219 (2017).

Supplementary data

Supplementary Table 1. Tumor histopathology of ovarian cancer patients from whom ascites cell cultures were derived.

Sample	FIGO stage	Histopathology
ASC 005	IIIc	HGSOC
ASC 006	IIIc	mucinous
ASC 009	IIIc	LGSOC
ASC 010	IIIc	HGSOC
ASC 011	IIIc	serous
ASC 012	IV	HGSOC
ASC 013	IIIc	HGSOC
ASC 014	IIIc	HGSOC
ASC 016	IVa	HGSOC
ASC 020	IIIc	HGSOC
ASC 022	IIIc	serous
ASC 024	IVb	HGSOC
ASC 025	IVb	HSCOC
ASC 027	IVa	HGSOC
ASC 031	IIIc	HGSOC
ASC 035	IIIc	serous
ASC 036	IIIc	HGSOC
ASC 041	IVa	HGSOC
ASC 045	IV	HGSOC

The disease stage is based on the International Federation of Gynecology and Obstetrics (FIGO) staging system. Low-grade and high-grade serous ovarian cancer are indicated as LGSOC and HGSOC.

Supplementary Table 2. Quantification of the expression of mucin-16 and EpCAM on ovarian cancer cell samples by flow cytometry.

Sample	Passage	Doubling time (h)	MFI ratio	
			Mucin-16	EpCAM
ASC 009	P+11	70	1.3	71.7
ASC 010	P+5	58	1.2	0.9
ASC 013	P+5	56	2.2	1.2
ASC 031	P+7	75	1.6	2.7
ASC 041	P+7	65	2.1	2.0
SK-OV-3	P+2		2.1	43.8

Expression was quantified by determining the ratio of the median fluorescence intensity (MFI) of the peak corresponding to the surface marker and the peak corresponding to the isotype control antibody. Corresponding flow cytometry peak patterns are shown in Supplementary Figure 3.

Supplementary Table 3. Inhibitory potency (IC_{50}) in nM of IDO1 inhibitors NTRC 3883-0 and epacadostat, and TDO inhibitor NTRC 3531-0 in unstimulated and IFN γ -stimulated adherent cell samples isolated from ascites of ovarian cancer patients.

Sample	n	Unstimulated			IFN γ -stimulated		
		NTRC 3883-0	epacadostat	NTRC 3531-0	NTRC 3883-0	epacadostat	NTRC 3531-0
ASC 009	3	–	–	–	236 (156–352)	3.7 (2.3–5.9)	> 31,600
ASC 010	3	> 31,600	9,640 (6,130–15,200)	282 (268–297)	294 (193–450)	9.3 (4.5–19)	> 31,600
ASC 013	2	> 31,600	9,940	328	237	9.0	> 31,600
ASC 031	3	> 31,600	8,630 (4,200–17,700)	256 (157–416)	271 (237–311)	7.2 (5.3–9.7)	> 31,600
ASC 041	3	> 31,600	4,310 (3,320–5,590)	344 (278–425)	321 (174–589)	7.4 (3.9–14)	> 31,600
Mean		> 31,600	7,730 (5,250–11,400)	300 (263–343)	261 (232–293)	8.3 (5.4–13)	> 31,600

n indicates the number of experimental replicates. 95% confidence intervals are given within brackets.

Supplementary Table 4. Pharmacokinetic parameters of NTRC 3883-0 observed in mouse, rat, monkey and dog, and predicted for humans using allometric scaling.

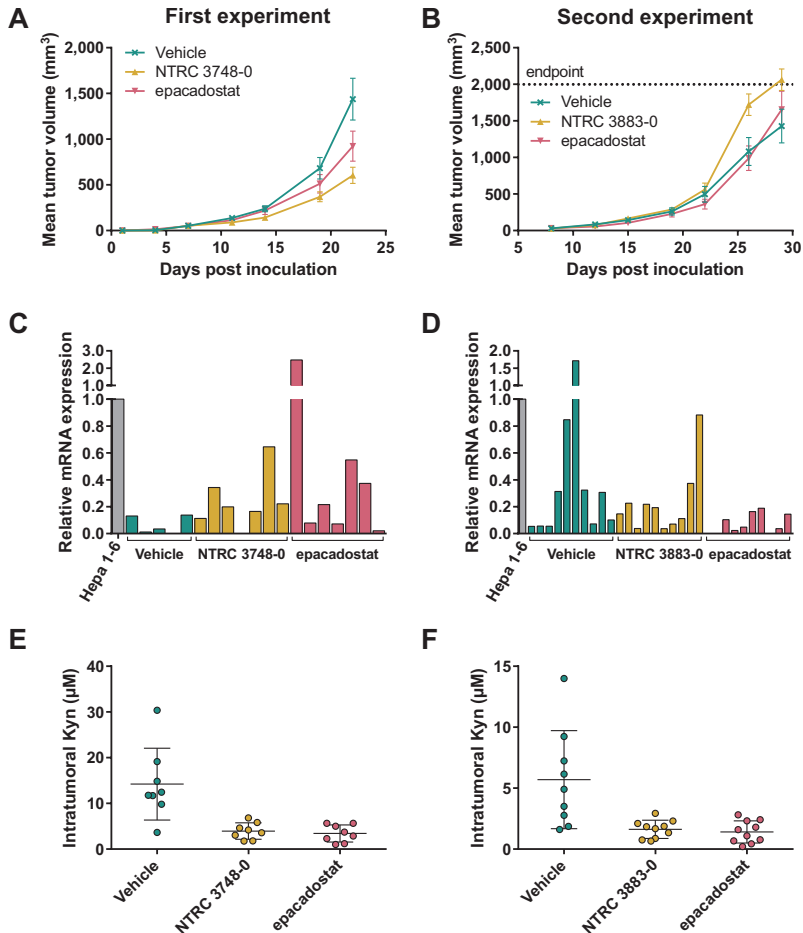
Species	Mouse	Rat	Monkey	Dog	Human (predicted)
Body weight (kg)	0.036	0.29	3.0	10	70
Cl (mL/h/kg)	1,110	1,143	2,222	1,717	
<i>Cl (mL/h)</i>	<i>40</i>	<i>331</i>	<i>6,666</i>	<i>17,170</i>	<i>171,137</i>
V_{ss} (mL/kg)	3,627	1,428	2,246	1,362	
<i>V_{ss} (L)</i>	<i>0.131</i>	<i>0.417</i>	<i>6.738</i>	<i>13.62</i>	<i>79.8</i>
t_{1/2} (h)	5.2	3.3	2.4	2.8	0.47
Bioavailability (F)	ND	91%	49%	32%	
Plasma protein binding (%)	54	85	ND	79	74

Data in bold are measured, while data in italics are calculated or predicted (for humans). The clearance (Cl) and volume of distribution at steady state (V_{ss}) in humans are predicted based on extrapolation of the parameters in the four species as shown in Supplementary Figure 4. No correction was made for plasma protein binding, as this data was not available for monkey. The half-life (t_{1/2}) in humans was predicted as V_{ss}/Cl. Based on the predicted parameters in humans and assuming a 100% bioavailability, a minimum dose of 1,725 mg per day would be required to reach a target concentration of 1 μM (IC₉₀ in dog whole blood assay) on average during the dosing interval. However, considering the high expected clearance in humans, it is likely that the inhibitor undergoes considerable first-pass metabolism and therefore even higher doses would be required to reach the target level. ND, not determined.

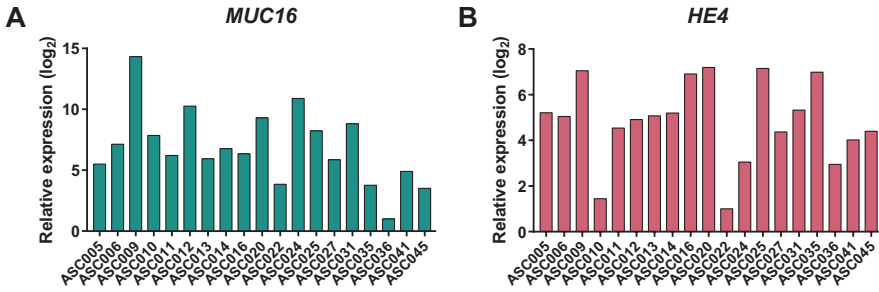
Supplementary Table 5. DNA sequences of oligonucleotide primers used for quantitative real-time PCR analysis of *IDO1*, *TDO2* and ovarian cancer gene markers in cell lines, patient samples and tumors.

Gene	Species	Direction	Sequence
<i>IDO1</i> ^a	human	forward	GGCTTTGCTCTGCCAAATCC
	human	reverse	TTCTCAACTCTTTCTCGAAGCTC
<i>IDO1</i> ^b	human	forward	TTGCTAAAGGCGCTGTTGGA
	human	reverse	GTCTGATAGCTGGGGTTGC
<i>TDO2</i>	human	forward	CTTAGTAAAGGTGAAAGACGG
	human	reverse	GTCCATAAGAGAAGTCAGCA
<i>MUC16</i>	human	forward	CACAGACAACGTCATGCAGC
	human	reverse	TGGGAGTTGTAGGAGGCTCA
<i>HE4</i>	human	forward	CAAGAGTGCGTCTCGGACAG
	human	reverse	TTAATGTTACCTGGGGGCA
<i>ACTB</i>	human	forward	CAAGAGATGGCCACGGCTGCTTCCA
	human	reverse	GCATGGAGTTGAAGGTAGTTTCG
<i>RPS18</i>	human	forward	GACAACAAGCTCCGTGAAGA
	human	reverse	AGAAGTGACGCAGCCCTCTA
<i>IDO1</i>	mouse	forward	GGCTTTGCTCTACCACATCCAC
	mouse	reverse	TAGCCACAAGGACCCAGGG
<i>ACTB</i>	mouse	forward	GGCTGTATTCCCCTCCATCG
	mouse	reverse	CCAGTTGGTAACAATGCCATGT
<i>GAPDH</i>	mouse	forward	ACGGATTTGGTCGTATTGGG
	mouse	reverse	CGCTCCTGGAAGATGGTGAT
<i>RPL37</i>	mouse	forward	TCTGTGGCAAGACCAAGATG
	mouse	reverse	GACAGCAGGGCTTCTACTGG

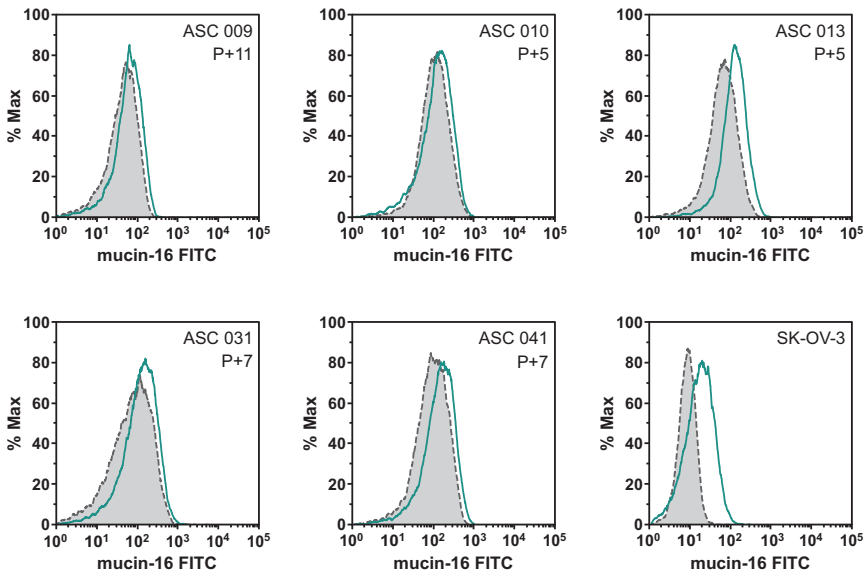
^a Primer set used in Figure 5A; ^b Primer set used in Figure 5B.



Supplementary Figure 1. *In vivo* effect of NTRC 3748-0 (a racemic mixture of NTRC 3883-0 and its enantiomer), NTRC 3883-0 and epacadostat in two CT26 mouse model experiments. **(A)** Mean tumor volume of mice treated with vehicle, 50 mg/kg NTRC 3748-0 (b.i.d.) or 100 mg/kg epacadostat (q.d.) during the first study. **(B)** Mean tumor volume of mice treated with vehicle, 100 mg/kg NTRC 3883-0 (b.i.d.) or 100 mg/kg epacadostat (b.i.d.) during the second study. Results in panels A and B are expressed as mean \pm SEM. **(C)** Analysis of *mIDO1* mRNA levels in the tumor tissues collected from the first study by qPCR. mRNA levels were normalized for the expression of two housekeeping genes (*ACTB* and *RPL37*), and scaled based on the hepatoma Hepa 1-6 cell line stimulated with IFN γ (included as a positive control). Five samples were excluded from the analysis due to poor cDNA quality. Missing bars represent mRNA levels below the detection limit (*i.e.*, Cq > 40 cycles). **(D)** Analysis of *mIDO1* mRNA levels in the tumor tissues collected from the second study, presented as for panel C. In both studies, the mRNA levels were low based on the average Cq values of 36 cycles for the first study (panel C) and 35 cycles for the second study (panel D). **(E)** Analysis of intratumoral Kyn levels by LC-MS/MS for the first study and **(F)** the second study. Results in panels E and F are expressed as mean \pm SD.

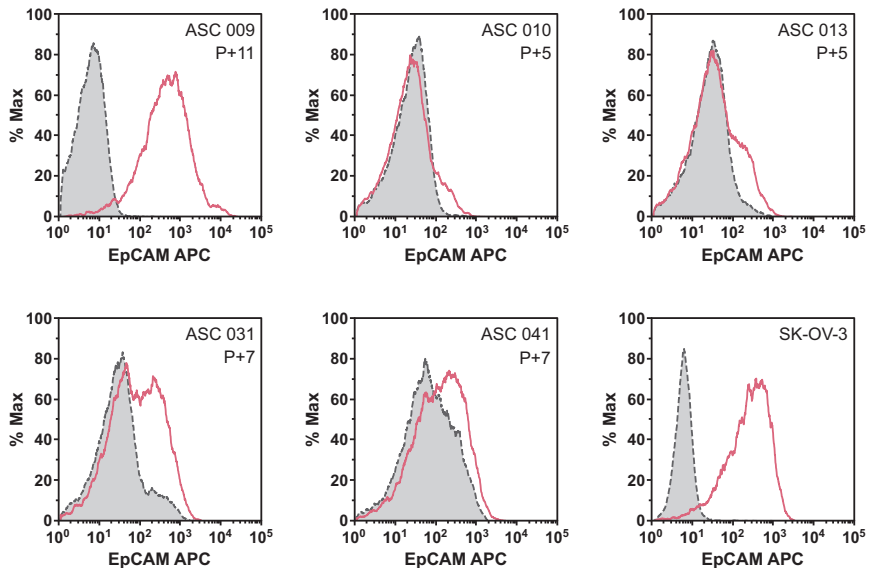


Supplementary Figure 2. Expression analysis by qPCR of the ovarian cancer marker genes (A) *MUC16* and (B) *HE4* in cell cultures isolated from the malignant ascites of patients with advanced epithelial ovarian cancer. The same mRNA samples were used as in Figure 5A. mRNA levels were normalized for the expression of β -actin (*ACTB*) and ribosomal protein S18 (*RPS18*), and scaled based on the lowest expressing samples.

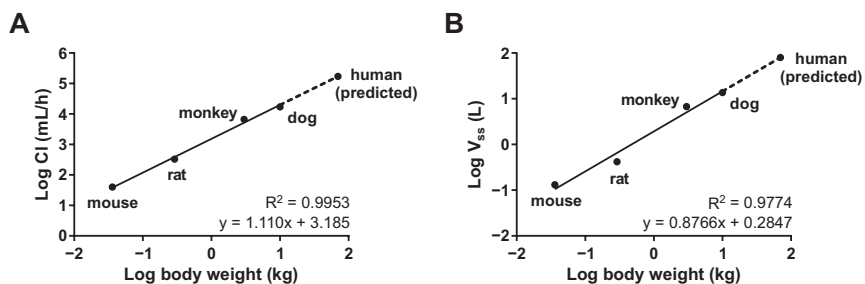


Supplementary Figure 3. Analysis of the tumor cell markers mucin-16 and EpCAM on five patient-derived cell samples by flow cytometry. The passage number (P) at the time of analysis is indicated. Grey-shaded peaks represent the staining with isotype control antibodies. Expression was quantified by determining the ratio of the median fluorescence intensity (MFI) of the peak corresponding to the surface marker and the peak corresponding to the isotype control antibody (Supplementary Table 2). The adenocarcinoma ovarian cancer cell line SK-OV-3 was included for reference.

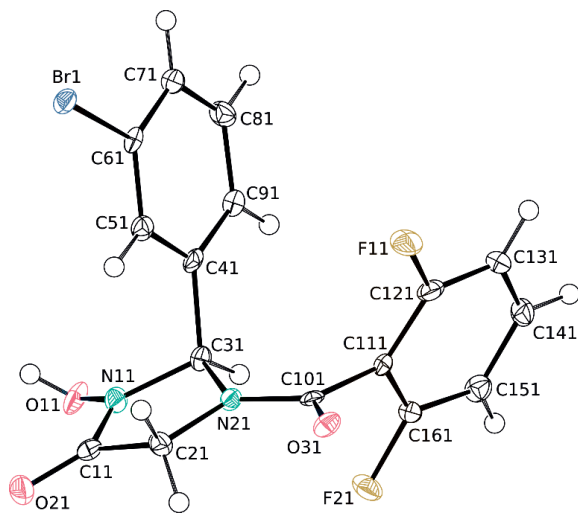
(Figure continued on next page)



Supplementary Figure 3. *Continued.*



Supplementary Figure 4. Allometric graphical plots for (A) clearance (Cl) and (B) volume of distribution at steady state (V_{ss}) of NTRC 3883-0 in mouse, rat, monkey and dog and predicted parameters for human based on extrapolation. Values for the individual parameters are listed in Supplementary Table 4.



Supplementary Figure 5. Crystal structure (ORTEP diagram) of NTRC 3883-0.

TDO



Chapter 7

Pharmacological validation of tryptophan 2,3-dioxygenase (TDO) as a target for Parkinson's disease

Paula Perez-Pardo¹, Yvonne Grobben², Nicole Willemsen-Seegers², Mitch Hartog¹, Michaela Tutone¹, Michelle Muller², Youri Adolfs³, R. Jeroen Pasterkamp³, Diep Vu-Pham², Antoon M. van Doornmalen², Freek van Cauter², Joeri de Wit², Jan Gerard Sterrenburg², Joost C. M. Uitdehaag², Jos de Man², Rogier C. Buijsman², Guido J. R. Zaman² and Aletta D. Kraneveld¹

¹ Division of Pharmacology, Utrecht Institute for Pharmaceutical Sciences, Faculty of Science, Utrecht University, Utrecht, The Netherlands

² Netherlands Translational Research Center B.V., Oss, The Netherlands

³ Department of Translational Neuroscience, UMC Utrecht Brain Center, University Medical Center Utrecht, Utrecht University, Utrecht, The Netherlands

***FEBS Journal* (2021) 288:4311–4331**

Abstract

Parkinson's disease patients suffer from both motor and non-motor impairments. There is currently no cure for Parkinson's disease, and the most commonly used treatment, levodopa, only functions as a temporary relief of motor symptoms. Inhibition of the expression of the L-tryptophan-catabolizing enzyme tryptophan 2,3-dioxygenase (TDO) has been shown to inhibit aging-related α -synuclein toxicity in *Caenorhabditis elegans*. To evaluate TDO inhibition as a potential therapeutic strategy for Parkinson's disease, a brain-penetrable, small molecule TDO inhibitor was developed, referred to as NTRC 3531-0. This compound potently inhibits human and mouse TDO in biochemical and cell-based assays, and is selective over IDO1, an evolutionarily unrelated enzyme that catalyzes the same reaction. In mice, NTRC 3531-0 increased plasma and brain L-tryptophan levels after oral administration, demonstrating inhibition of TDO activity *in vivo*. The effect on Parkinson's disease symptoms was evaluated in a rotenone-induced Parkinson's disease mouse model. A structurally dissimilar TDO inhibitor, LM10, was evaluated in parallel. Both inhibitors had beneficial effects on rotenone-induced motor and cognitive dysfunction as well as rotenone-induced dopaminergic cell loss and neuroinflammation in the *substantia nigra*. Moreover, both inhibitors improved intestinal transit and enhanced colon length, which indicates a reduction of the rotenone-induced intestinal dysfunction. Consistent with this, mice treated with TDO inhibitor showed decreased expression of rotenone-induced glial fibrillary acidic protein, which is a marker of enteric glial cells, and decreased α -synuclein accumulation in the *enteric plexus*. Our data support TDO inhibition as a potential therapeutic strategy to decrease motor, cognitive and gastrointestinal symptoms in Parkinson's disease.

Introduction

Parkinson's disease (PD) is a chronic, progressive neurodegenerative disease characterized by motor symptoms such as bradykinesia, resting tremor, rigidity and late postural instability. PD involves the degeneration of dopamine-generating neurons in the *substantia nigra* (SN).¹ Misfolding and aggregation of α -synuclein in the remaining dopaminergic neurons results in inclusions termed Lewy bodies.² This pathology is also found in the peripheral autonomic nervous system, where it affects the function of various organs, including the heart and the gut.^{2,3} Moreover, several studies have described a role for neuroinflammation in PD, the hallmark of which is microgliosis.⁴ In addition to the motor symptoms, PD patients often experience non-motor symptoms, including depression,⁵ cognitive decline⁶ and, most commonly, gastrointestinal disturbances.⁷ Gastrointestinal symptoms may precede the classical motor symptoms of PD by many years,⁸ and their occurrence in otherwise healthy people is associated with an increased risk of PD.^{8,9}

To date, PD remains incurable. The most commonly used treatment is levodopa, which induces an increase in the synthesis of dopamine in the termini of the remaining dopaminergic neurons in the brain and improves motor function. However, levodopa does not prevent neurodegeneration, and therefore acts only as a temporary remedy for motor symptoms.¹⁰ Levodopa has no effect on the non-motor symptoms of PD, which are major determinants for the quality of life of PD patients.¹¹ Furthermore, the long-term use of levodopa causes inter-dose dyskinesias.¹² Therefore, there is a need for new therapeutic strategies that alter the disease course or improve the treatment of both motor and non-motor symptoms of PD.

Van der Goot and coworkers¹³ identified the L-tryptophan (Trp)-catabolizing enzyme tryptophan 2,3-dioxygenase (TDO) (EC 1.13.11.11) as a potential drug target for PD in a genome-wide RNA interference screen for regulators of aging-related α -synuclein toxicity in *Caenorhabditis elegans*. Genetic and pharmacological experiments in *Drosophila melanogaster* models of Parkinson's, Huntington's and Alzheimer's disease confirmed that inhibition of TDO can ameliorate neurodegeneration.^{14,15}

TDO catalyzes the first, rate-limiting step of the catabolism of the amino acid Trp in the kynurenine pathway, an enzymatic cascade responsible for the synthesis of nicotinic adenine dinucleotide (NAD) and NAD phosphate (Figure 1).¹⁶ In the human brain, 95% of Trp is metabolized via the kynurenine pathway, while the remaining Trp is used for the synthesis of serotonin or proteins. The kynurenine pathway of Trp metabolism produces neuroprotective as well as neurotoxic metabolites (Figure 1). PD, like several other neurodegenerative diseases, has been associated with an imbalance between these

neuroactive metabolites.¹⁷⁻²¹ There is no genetic evidence for a direct role of TDO or other enzymes of the pathway in the development of PD. However, a locus in close proximity to the gene encoding aminocarboxymuconate semialdehyde decarboxylase (ACMSD), a downstream enzyme in the kynurenine pathway (Figure 1), is associated with an increased risk of sporadic PD, suggesting that ACMSD may influence the pathogenesis of PD.^{22,23}

Modulation of the kynurenine pathway with small molecule inhibitors has been explored already for more than two decades for neurodegenerative diseases.²¹ There have been several drug discovery programs on inhibitors of kynurenine-3-monooxygenase (KMO), the enzyme responsible for the generation of the neurotoxic metabolite 3-hydroxy-L-kynurenine (3-HK).²⁴ While none of these efforts have yet resulted in compounds investigated in the clinic due to lack of brain penetration,²⁵ a non-blood-brain barrier-penetrating KMO inhibitor was shown to significantly improve Alzheimer's disease symptoms and slow the disease progression.²⁴

To evaluate TDO inhibition as a potential therapeutic strategy for PD, a brain-penetrable, small molecule inhibitor of TDO was developed (NTRC 3531-0). To investigate the effects on symptoms associated with PD, the compound was evaluated in a rotenone-induced

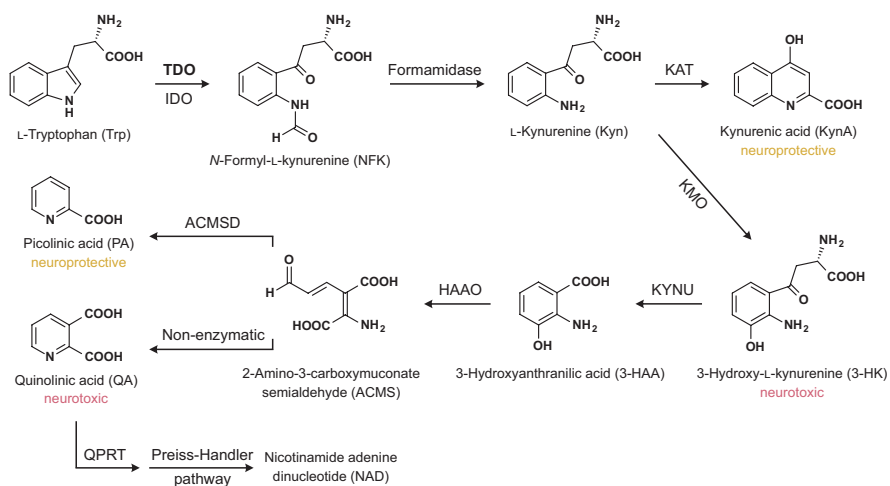


Figure 1. Diagram of the enzymes and metabolites of the kynurenine pathway. ACMSD, aminocarboxymuconate semialdehyde decarboxylase; HAAO, 3-hydroxyanthranilic acid oxygenase; IDO, indoleamine 2,3-dioxygenase; KAT, kynurenine aminotransferase; KMO, kynurenine 3-monooxygenase; KYNU, kynureninase; NAD, nicotinamide adenine dinucleotide; QPRT, quinolinatase phosphoribosyltransferase; TDO, tryptophan 2,3-dioxygenase.

mouse model of PD.^{26–28} The natural product rotenone is a pesticide that interferes with mitochondrial function.²⁶ Rotenone exposure is associated with an increased risk of PD in humans,²⁶ and many of the hallmarks of the disease in humans have been reproduced in the rotenone model. These include the loss of dopaminergic cell bodies in the SN and α -synuclein aggregation, but also gastrointestinal dysfunction, which is thought to arise from a bi-directional communication system between the central nervous system and the gastrointestinal tract, referred to as the gut-brain axis.^{26–28} In parallel with the evaluation of NTRC 3531-0, a chemically different TDO inhibitor, LM10, published by the Ludwig Cancer Center,^{29,30} was tested in the same animal model. LM10 was previously shown to effectively inhibit the growth of TDO-expressing tumors.³⁰ We observed that both TDO inhibitors inhibited the development of motor, cognitive and intestinal dysfunctions. Moreover, TDO inhibitor treatment was associated with a decreased loss of dopaminergic cells and decreased microglia activation in the SN, as well as with reduced glial cell marker expression and reduced accumulation of α -synuclein in the enteric nerves of the intestinal tract.

Results

***In vitro* characterization of a novel, selective TDO inhibitor**

TDO catalyzes the oxidation of Trp, resulting in the formation of *N*-formyl-L-kynurenine (NFK).¹⁶ To identify small molecule inhibitors of TDO, a library of 87,000 synthetic low molecular weight molecules was screened with a biochemical assay, making use of recombinant human TDO (hTDO) and a fluorescent probe that specifically binds to NFK.³¹ Hit compounds were tested for selectivity against human indoleamine 2,3-dioxygenase (hIDO1) (EC 1.13.11.42), an evolutionarily unrelated enzyme that catalyzes the same reaction, using a similar biochemical assay.³¹ Cellular activity was determined in cell lines derived from the human embryonic kidney cell line HEK-293, stably overexpressing the full-length human *TDO2* or *IDO1* cDNA.

Optimization of one of the screening hits resulted in NTRC 3531-0, a potent and selective TDO inhibitor with a 3-phenyl-1*H*-indole scaffold (Figure 2).³² NTRC 3531-0 inhibited hTDO with a half-maximal inhibitory concentration (IC_{50}) of 490 nM in the biochemical assay, and with an IC_{50} of 816 nM in *hTDO2*-overexpressing HEK-293 cells (HEK-hTDO) (Table 1). The compound also inhibited the conversion of Trp to NFK in the colon carcinoma cell line SW48 (Table 1), which constitutively expresses TDO.³¹

NTRC 3531-0 was inactive on hIDO1 in the biochemical assay at the highest tested concentration (*i.e.*, 31.6 μ M), and it inhibited Trp metabolism in human *IDO1*-overexpressing

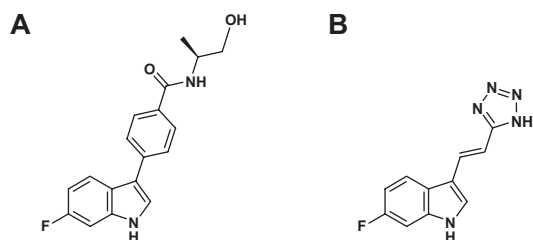


Figure 2. Chemical structure of (A) NTRC 3531-0 and (B) LM10.

HEK-293 cells (HEK-hIDO1) with an IC_{50} of 20.7 μ M (Table 1). In biochemical assays, NTRC 3531-0 is therefore more than 60 times selective for hTDO over hIDO1, and in the HEK-293 cell-based assays at least 25 times. NTRC 3531-0 also inhibited mouse TDO (mTDO) in a biochemical assay and in a cellular assay based on a mouse glioma GL-261 cell line stably overexpressing the full-length mouse *TDO2* cDNA (GL-261-mTDO) (Table 1). NTRC 3531-0 was slightly less potent on mTDO compared to hTDO in the biochemical assays (Table 1). Inhibitory potency in the GL-261-mTDO cellular assay was similar to that in the SW48 cells and was four times higher compared to the potency in HEK-hTDO cells (Table 1).

Since TDO contains a heme center, similar to cytochrome P450 (CYP) enzymes, we evaluated the selectivity of NTRC 3531-0 on a panel of seven CYP enzymes, that is, CYP1A2, CYP2B6, CYP2C8, CYP2C9, CYP2C19, CYP2D6 and CYP3A4. NTRC 3531-0 inhibited CYP2C8 with an IC_{50} of 16.3 μ M, and was inactive against all other CYPs (IC_{50} > 31.6 μ M). These data indicate that NTRC 3531-0 selectively interacts with the active site of TDO.

Table 1. Potency (IC_{50}) in nM of TDO inhibitors NTRC 3531-0 and LM10 in biochemical and cell-based assays for human (h) and mouse (m) TDO or IDO1.

Assay	NTRC 3531-0	LM10
hTDO	490 (461–520) ($n = 76$)	716 (491–1,040) ($n = 8$)
hIDO1	< 20% inhibition @ 31,600 ($n = 72$)	< 20% inhibition @ 31,600 ($n = 6$)
HEK-hTDO	816 ($n = 2$)	33% inhibition @ 31,600 ($n = 2$)
HEK-hIDO1	20,700 ($n = 2$)	< 20% inhibition @ 31,600 ($n = 2$)
SW48 (hTDO)	220 (184–262) ($n = 13$)	31,600 (22,800–43,800) ($n = 5$) ^a
mTDO	846 (728–983) ($n = 3$)	1,070 (732–1,570) ($n = 3$)
GL-261-mTDO	214 ($n = 2$)	42% inhibition @ 31,600 ($n = 2$)

^a Values are based on extrapolation above 31,600 nM for three out of five experiments. Confidence intervals and number of experimental replicates (n) are given within brackets.

In our biochemical assays, NTRC 3531-0 was slightly more potent on hTDO than LM10 (Table 1).²⁹ However, LM10 showed a considerably lower potency in our cellular assays, with respectively 33% and 50% inhibition at a concentration of 31.6 μM in the HEK-hTDO and SW48 cells (Table 1). In both the biochemical and cell-based assays, the activity of LM10 on mTDO was similar to that on hTDO (Table 1).

Pharmacokinetics and brain penetration

To determine whether NTRC 3531-0 could potentially enter the brain, a bi-directional transport assay was performed with Madin–Darby canine kidney (MDCK) cells overexpressing the human *ABCB1* gene-encoded MDR1 P-glycoprotein (MDCK-MDR1) at Cyprotex (Macclesfield, UK).³³ MDCK-MDR1 cells form a confluent monolayer in Transwell® cell culture plates (Corning) and express active MDR1 P-glycoprotein at the apical side. The cell model is a surrogate model of the brain capillary endothelial cell layer that constitutes the blood–brain barrier.³⁴ The transport of NTRC 3531-0 from the apical (A) to the basolateral (B) side of the monolayer ($P_{\text{app, A to B}}$), and from basolateral (B) to apical (A) ($P_{\text{app, B to A}}$), was determined by measuring compound levels in the two compartments of the Transwell plates by liquid chromatography–tandem mass spectrometry (LC-MS/MS) (Table 2). Transport assays were performed in the absence and presence of the P-glycoprotein inhibitor elacridar.

NTRC 3531-0 showed passage through the MDCK-MDR1 cell layer from A to B, indicating that it may cross the blood–brain barrier. However, efflux from B to A was higher ($P_{\text{app, B to A}} > P_{\text{app, A to B}}$), resulting in an efflux ratio of 3.32 (Table 2), indicating that NTRC 3531-0 could be a weak substrate of P-glycoprotein. In agreement with this, B-to-A transport and the efflux ratio strongly decreased in the presence of elacridar. In contrast, LM10 showed higher transport from A to B than from B to A (Table 2), which is indicative of an active uptake mechanism present in the MDCK cells. Elacridar had no effect on transport or efflux, indicating that LM10 is not a P-glycoprotein substrate (Table 2).

Table 2. Bi-directional transport through a monolayer of human MDR1 P-glycoprotein-overexpressing MDCK cells.

	elacridar	$P_{\text{app, A to B}}$ (10^{-6} cm/s)	$P_{\text{app, B to A}}$ (10^{-6} cm/s)	Efflux ratio
NTRC 3531-0	–	15.7	52.0	3.32
NTRC 3531-0	+	26.0	14.0	0.54
LM10	–	5.63	1.58	0.28
LM10	+	3.50	1.27	0.36

$P_{\text{app, A to B}}$, apparent permeability coefficient in apical-to-basolateral direction; $P_{\text{app, B to A}}$, apparent permeability coefficient in basolateral-to-apical direction.

In vivo pharmacokinetic (PK) properties and brain penetration of NTRC 3531-0 were determined in male C57BL/6NCrI mice (Figures 3A and 3B). Oral bioavailability (F) was determined by comparing plasma levels after a single per oral (p.o.) administration of 100 mg/kg inhibitor with the levels after a single intravenous (i.v.) dose of 10 mg/kg. Plasma and brain levels at steady state were determined after administration of 100 mg/kg inhibitor for five consecutive days. Compound concentrations in plasma samples and brain homogenates were measured by LC-MS/MS. Permeability across the blood–brain barrier was determined by calculation of the brain-to-blood partition coefficient (K_p),³⁵ based on the areas under the curves (AUCs) determined after 5 days dosing. NTRC 3531-0 had an oral bioavailability of 22% and a high C_{max} (Table 3). The K_p was 0.37 after repeated dosing. The unbound brain-to-plasma partition coefficient (K_{p,uu})³⁵ of NTRC 3531-0 was 0.067 (Table 3).

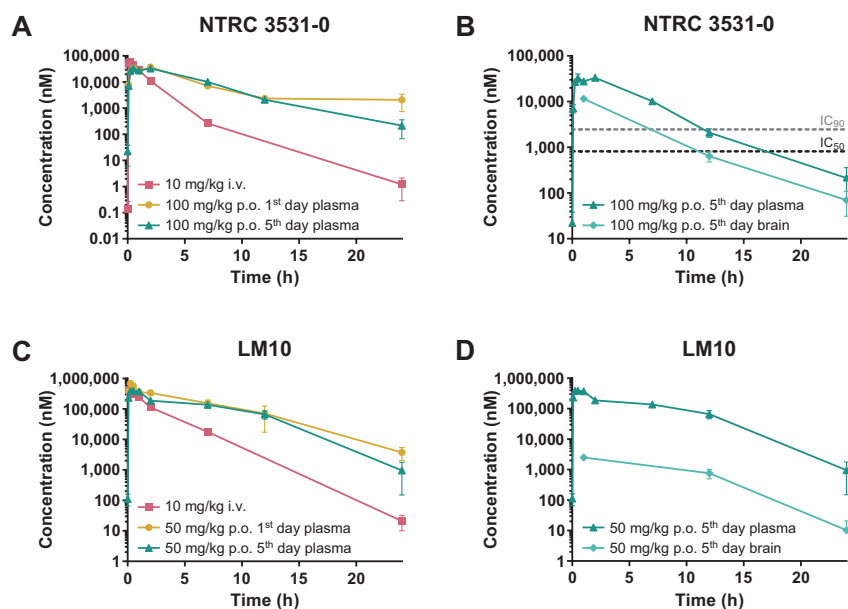


Figure 3. Pharmacokinetics of NTRC 3531-0 and LM10 in plasma and brain. (A) Plasma levels in time of NTRC 3531-0 measured after single intravenous (i.v.) administration of 10 mg/kg, single oral (p.o.) administration of 100 mg/kg, or after the 5th dose of a 5-day consecutive, once daily p.o. dosing of 100 mg/kg. (B) Levels of NTRC 3531-0 in plasma and brain after the 5th dose. The horizontal dashed lines correspond to the IC₅₀ and IC₉₀ concentrations of NTRC 3531-0 in the HEK-hTDO assay. (C) Plasma levels in time of LM10 measured after single i.v. administration of 10 mg/kg, single p.o. administration of 50 mg/kg, or after the 5th dose of a of 5-day consecutive, once daily p.o. dosing of 50 mg/kg. (D) Levels of LM10 in plasma and brain after the 5th dose. Plasma and brain levels are expressed as mean ± SEM of 3 mice per time point and dosing group.

An additional PK study was performed in C57BL/6NCrl mice for LM10, which was dosed at 50 mg/kg p.o. and 10 mg/kg i.v. (Figures 3C and 3D). LM10 had a good oral bioavailability of 63% and reached more than ten times higher plasma levels compared to NTRC 3531-0, at two times lower dose (Table 3). However, the Kp of LM10 was 0.010 after repeated dosing. The Kp_{uu} of LM10 was 0.020, indicating a considerably less efficient brain penetration than NTRC 3531-0.

To determine whether the inhibitors modulated TDO activity *in vivo*, the concentrations of Trp and L-kynurenine (Kyn) were measured in the plasma and brain samples of the PK studies using LC-MS/MS (Figure 4). Oral administration of NTRC 3531-0 resulted in an increase in the concentration of Trp in plasma (1 h, $p < 0.01$; 2 h, $p < 0.0001$; 7 h, $p < 0.01$) as well as in brain ($p < 0.0001$ at 1, 12 and 24 h) compared to mice treated with vehicle (Figures 4A and 4B), which conforms with the inhibition of TDO activity. Kyn levels were found to be slightly decreased in plasma at early timepoints (*i.e.*, 0.25 and 0.5 h), although no statistical significance was reached, while the levels subsequently increased in both plasma (1 and 2 h, $p < 0.05$) and brain (12 h, $p < 0.01$; 24 h, $p < 0.05$) (Figures 4C and 4D). In contrast, no increase in Trp levels was detected after administration of LM10 (Figures 4A and 4B), while the plasma Kyn levels showed a similar pattern as observed for NTRC 3531-0 treatment, but only the initial decrease in Kyn levels was found to be significant (0.25 h, $p < 0.01$; 0.5 h, $p < 0.05$) (Figure 4C).

Table 3. *In vivo* pharmacokinetic profile of the TDO inhibitors NTRC 3531-0 and LM10 in mice.

Administration route	NTRC 3531-0			LM10		
	i.v.	single p.o.	5-day p.o.	i.v.	single p.o.	5-day p.o.
Dose (mg/kg)	10	100	100	10	50	50
C _{max} (μmol/L)	56.5	37.5	33.2	427	688	391
t _{1/2} (h)	0.903	2.49	3.13	1.77	3.09	2.35
AUC _{plasma} (h·μmol/L)	93.2	207	210	985	3,100	2,360
AUC _{brain} (h·μmol/L)		84.5	77.0		18.5	23.8
Kp		0.41	0.37		0.006	0.010
Kp _{uu}		0.074	0.067		0.012	0.020
F (%)		22.3			63.1	

AUC, area under the curve; C_{max}, maximum plasma concentration; F, oral bioavailability; i.v., intravenous; Kp, brain-to-plasma partition coefficient; Kp_{uu}, unbound brain-to-plasma partition coefficient; p.o., oral administration; t_{1/2}, half-life.

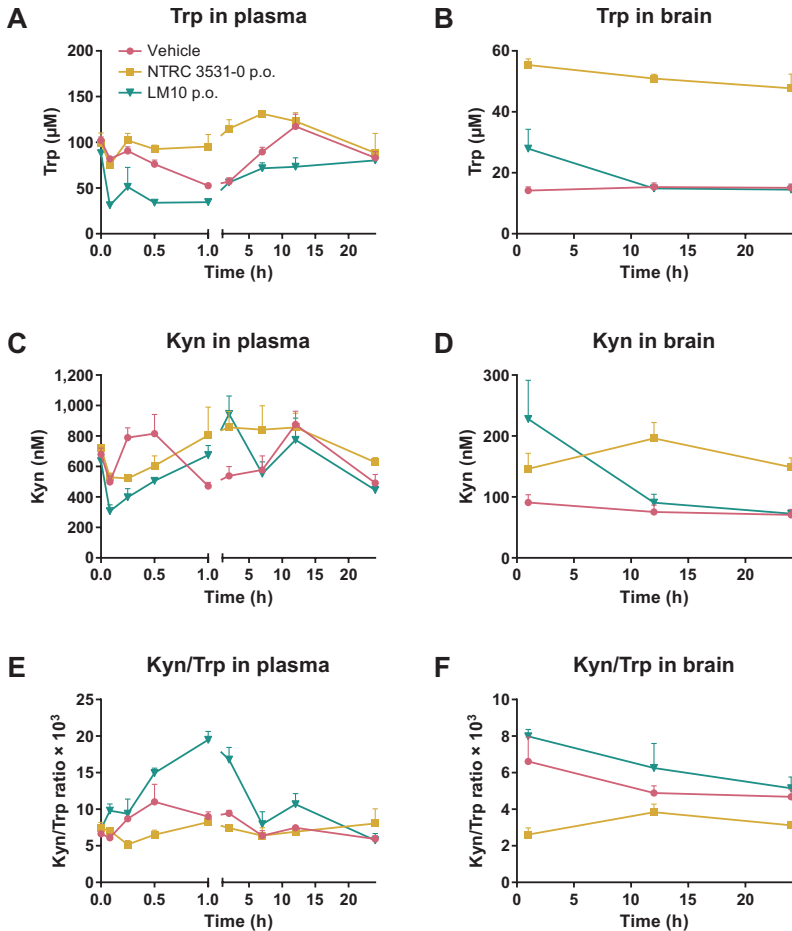


Figure 4. *In vivo* effect of NTRC 3531-0 on L-tryptophan (Trp) and L-kynurenine (Kyn) levels. (A,B) Plasma and brain levels in time of Trp after single p.o. administration of 100 mg/kg NTRC 3531-0 or 50 mg/kg LM10. Two-way ANOVA showed an overall effect of TDO inhibitor treatment on Trp levels in both plasma ($p < 0.0001$) and brain ($p < 0.0001$), an overall effect of time on Trp levels in plasma ($p < 0.0001$) and brain ($p < 0.001$), and an interaction effect between TDO inhibitor treatment and time in plasma ($p < 0.0001$). (C,D) Plasma and brain levels of Kyn. Two-way ANOVA showed an overall effect of TDO inhibitor treatment on Kyn levels in brain ($p < 0.01$), an overall effect of time on Kyn levels in plasma ($p < 0.0001$) and brain ($p < 0.01$), and an interaction effect between TDO inhibitor treatment and time in plasma ($p < 0.0001$) and brain ($p < 0.01$). Basal levels of Trp and Kyn were determined after treatment with vehicle. (E,F) Kyn/Trp ratio in plasma and brain. Levels after single treatment were determined in naive mice, which regained access to feed 2 h after dosing. Plasma and brain levels are expressed as mean \pm SEM of 3 mice per time point and dosing group.

Effects on motor and cognitive functions in rotenone model

To evaluate TDO inhibition as a potential therapeutic strategy for PD, NTRC 3531-0 and LM10 were evaluated in parallel in a rotenone-induced mouse model of PD.^{26–28} To investigate the effects of TDO inhibition, both compounds were orally administered once daily from day 7 after induction of the PD model (Figure 5A). To determine the effect of TDO inhibitor treatment on rotenone-induced motor dysfunction, the rotarod test was performed (Figures 5A and 5B). In this test, the time spent on an accelerating wheel was used to analyze motor function. Rotenone-infused, vehicle-treated mice demonstrated a significant motor dysfunction starting 21 days after surgery when compared to sham-operated, vehicle-treated animals ($p < 0.01$) (Figure 5B). The highest dose of both TDO inhibitors did not affect motor function in sham-operated mice (Figure 5B). However, both TDO inhibitors improved the motor function of rotenone-treated mice (Figure 5B). Specifically, treatment with NTRC 3531-0 at the two highest doses (50 mg/kg, $p < 0.01$ at day 35; 100 mg/kg, $p < 0.01$), and LM10 at the highest dose (50 mg/kg, $p < 0.05$) resulted in a significantly improved motor function (Figure 5B).

The cognitive function of the mice was evaluated in a spatial memory test.³⁶ In this test, the mice were placed in a cage where they were allowed to habituate to the configuration of a number of objects. Subsequently, the object exploration behavior of the mice was evaluated after relocation of two of the objects in the cage. Sham-operated, vehicle-treated mice were able to selectively react to a spatial change during the entire course of the animal experiment, that is, they selectively re-explored the displaced objects compared to the nondisplaced objects (Figure 5C). Both TDO inhibitors did not affect spatial memory in sham-operated mice (Figure 5C). The spatial recognition of animals infused with rotenone was significantly affected at 42 days after surgery when compared to sham-operated, vehicle-treated animals ($p < 0.0001$). At the same time point, however, there was significantly less rotenone-induced spatial recognition loss in mice treated with the highest dose of NTRC 3531-0 ($p < 0.001$). Results for mice treated with the highest dose of LM10 showed a similar trend, but were not statistically significant (Figure 5C).

To determine the effect of TDO inhibitor treatment on rotenone-induced dopaminergic cell loss, the number of dopaminergic cells in the SN of mice was quantified by immunolabeling of tyrosine hydroxylase (TH)-positive cells and 3D image analysis.³⁷ Infusion with rotenone resulted in a reduction of the number of TH-positive cell in the SN ($p < 0.0001$) when compared to sham-operated, vehicle-treated mice (Figures 6A and 6B). Both TDO inhibitors did not affect dopaminergic cell counts in the SN of sham-operated mice. NTRC 3531-0, at the highest dose, and LM10, at the two highest doses, decreased the rotenone-induced loss of TH-positive cells in the SN ($p < 0.01$ for both inhibitors) (Figures 6A and 6B). This demonstrates that TDO inhibitor treatment decreases neurodegeneration.

To evaluate the effect of TDO inhibitor treatment on rotenone-induced neuroinflammation, the volume of microglial cells and the space occupied by these cells in the SN was measured by immunolabeling of Iba1 followed by 3D image analysis. Microglia are morphologically and functionally dynamic cells and their activation is associated with an

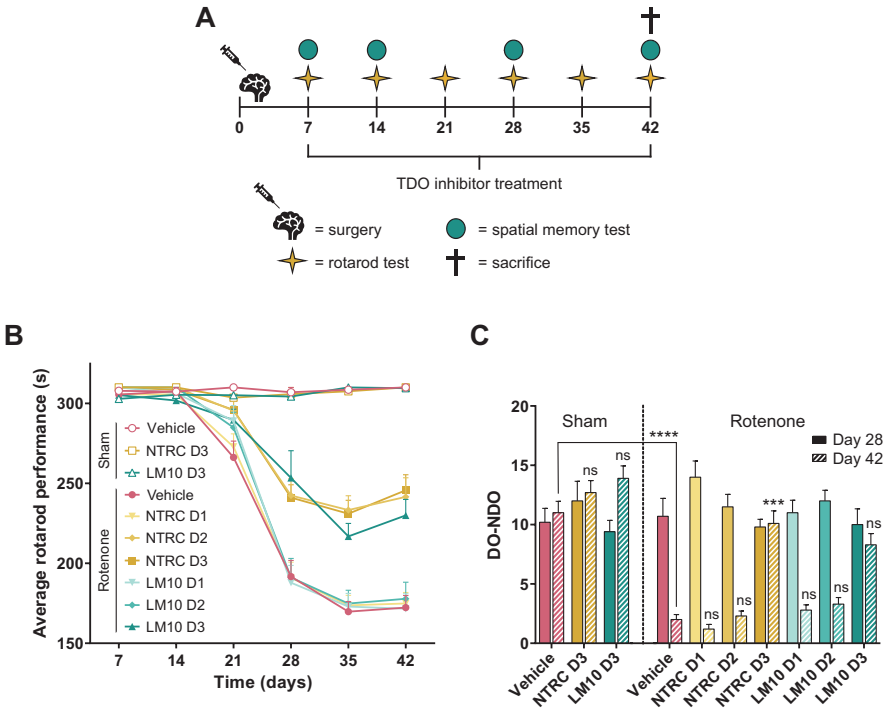


Figure 5. Evaluation of motor and cognitive function of mice treated with rotenone and TDO inhibitors. (A) Experimental set-up of the study with the numbers representing the days after surgery. PD was induced in mice by infusing rotenone in the striatum of the mice. Starting at day 7 after the operation, mice were treated once daily with an oral gavage of vehicle, NTRC 3531-0 (D1: 25 mg/kg; D2: 50 mg/kg; D3: 100 mg/kg) or LM10 (D1: 12.5 mg/kg; D2: 25 mg/kg; D3: 50 mg/kg). (B) Rotarod performance of mice treated with rotenone and TDO inhibitors. Two-way ANOVA showed an overall effect of rotenone injection on rotarod performance starting from day 21 ($p < 0.0001$). Repeated measures demonstrated that rotenone-treated mice developed motor problems with time when compared to sham-operated mice (interaction effect rotenone and time) ($p < 0.0001$). (C) Effect of TDO inhibitors on spatial memory at day 28 and day 42. Spatial discrimination is determined by comparing the time mice spent to explore a nondisplaced object (NDO) or a displaced object (DO), upon returning into a cage. Two-way ANOVA showed an overall effect of rotenone injection on day 42 ($p < 0.0001$). $N = 10$ mice per group for panels B and C. Results are expressed as mean \pm SEM. Indications of significance above individual bars represent the comparison to the respective vehicle control of the sham-operated or rotenone-injected groups. ns, not significant ($p > 0.05$); *** $p < 0.001$; **** $p < 0.0001$.

increased cell body size and decreased number of branches, reflecting the morphological transition from a ramified 'resting' to an activated phagocytic amoeboid-like phenotype.³⁸ Infusion with rotenone resulted in an increased mean volume of the microglia in the SN, which is indicative for microglia cell body enlargement, when compared to sham-operated, vehicle-treated mice ($p < 0.05$) (Figures 6C and 6E). Both TDO inhibitors did not affect the mean microglia volume in sham-operated mice. However, at the highest dose, both NTRC 3531-0 and LM10 reduced the mean microglia volume in rotenone-treated mice ($p < 0.05$ for both inhibitors) (Figure 6C). This indicates that TDO inhibitor treatment decreases the rotenone-induced neuroinflammation in the SN. Infusion of mice with rotenone additionally resulted in an increase of the total space occupied by microglia in the SN when compared to sham-operated, vehicle-treated mice ($p < 0.05$) (Figures 6D and 6E). Treatment with the TDO inhibitors resulted in a similar trend as observed for the microglia volume, although the effects were not statistically significant (Figure 6D).

Effects on intestinal phenotype in rotenone model

To evaluate the effect of TDO inhibitor treatment on rotenone-induced gastrointestinal dysfunction, the intestinal transit of a dye (Evans blue) was determined. The dye was injected intragastrically, thirty minutes before the sacrifice of the mice. Intestinal transit was measured as the distance travelled by the dye from the pylorus to the most distal part of the colon. Infusion with rotenone resulted in a significant delay of intestinal transit when compared to sham-operated, vehicle-treated mice ($p < 0.0001$) (Figure 7A). Both TDO inhibitors at the highest dose did not affect the intestinal transit time of sham-operated mice. Treatment with the highest dose of NTRC 3531-0, and the two highest doses of LM10 improved the intestinal transit of the PD mice ($p < 0.0001$ for all) (Figure 7A). This suggests that treatment with TDO inhibitor restores the PD-associated disturbed gastrointestinal function.

The effect of rotenone and inhibitor treatment on intestinal inflammation was determined by measuring the colon length of the mice. Infusion with rotenone resulted in a decreased colon length ($p < 0.0001$) when compared to sham-operated, vehicle-treated mice, which is indicative of an inflammatory response (Figure 7B). Treatment with the highest dose of NTRC 3531-0, and the two highest doses of LM10 reduced the rotenone-induced intestinal inflammatory response ($p < 0.05$ for all) (Figure 7B).

PD is associated with the activation of glial cells in the enteric nervous system.⁷ Furthermore, aggregates of α -synuclein have been observed in the enteric nervous system of PD patients.⁷ The expression of glial fibrillary acidic protein (GFAP), a marker of enteric glial cells, and of α -synuclein was determined by immunofluorescent staining of fixed sections of the colons of the sacrificed mice. Infusion with rotenone in the striatum

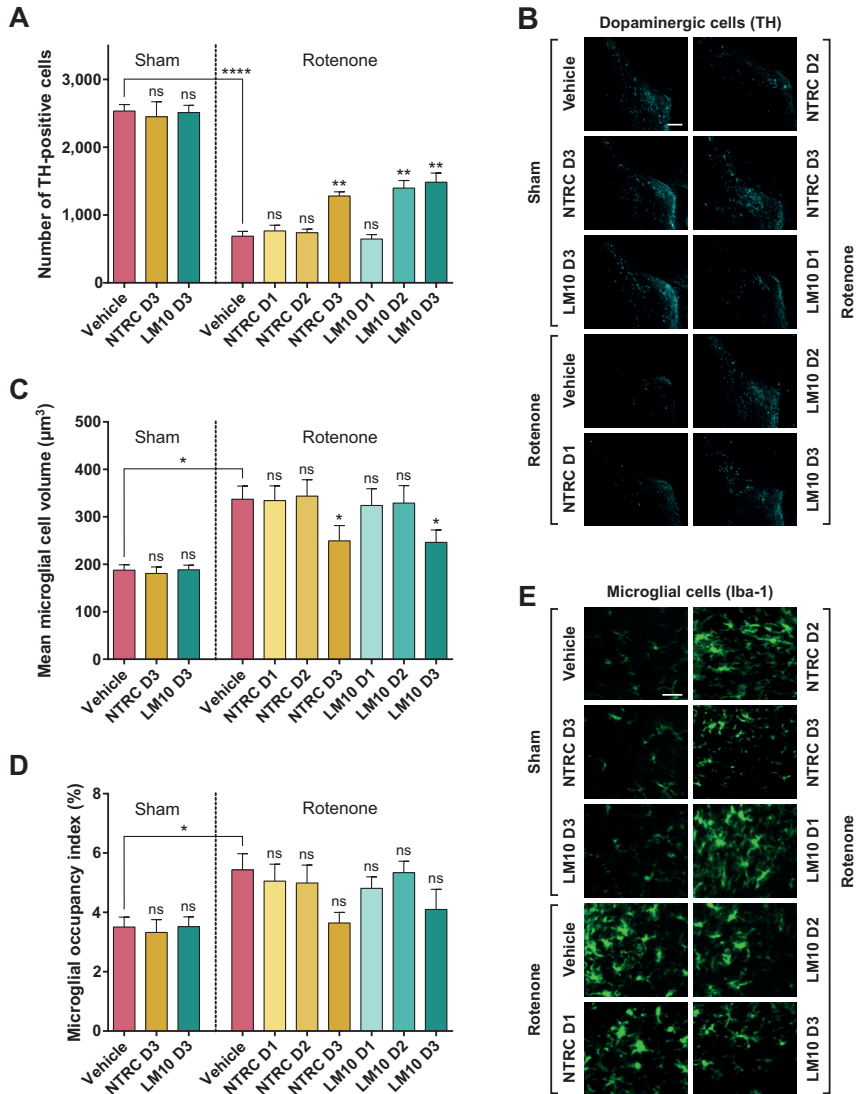


Figure 6. Evaluation of dopaminergic cell loss and neuroinflammation in mice treated with rotenone and TDO inhibitors. **(A)** Effect of rotenone and TDO inhibitors on the number of dopaminergic cells (tyrosine hydroxylase-positive cells) in the substantia nigra. Two-way ANOVA showed an overall effect of rotenone injection on the number of dopaminergic neurons in the substantia nigra ($p < 0.0001$). **(B)** Representative 2D images of anti-TH-labeled dopaminergic cells in the cleared brains of mice treated with rotenone and TDO inhibitors (scale bar: 250 μm). **(C)** Effect of rotenone and TDO inhibitors on the volume of microglia in the substantia nigra. Two-way ANOVA showed an overall effect of rotenone injection on the volume of the microglia ($p < 0.0001$). **(D)** Effect of rotenone and TDO (Legend continued on next page)

resulted in an increased expression of GFAP ($p < 0.0001$) (Figure 7C), and an increased accumulation of α -synuclein in the *enteric plexus* of the colon ($p < 0.05$) when compared to sham-operated, vehicle-treated mice (Figure 7D). Treatment with either NTRC 3531-0 or LM10 at the highest two doses resulted in a decrease of GFAP staining (NTRC 3531-0: $p < 0.0001$ for both doses; LM10: 25 mg/kg, $p < 0.001$; 50 mg/kg, $p < 0.0001$) (Figures 7C and 7E), and a decrease in the expression of α -synuclein in the *enteric plexus* of rotenone-treated mice at all inhibitor doses (NTRC 3531-0: 25 mg/kg, $p < 0.05$; 50 and 100 mg/kg, $p < 0.01$; LM10: 12.5 mg/kg, $p < 0.01$; 25 and 50 mg/kg, $p < 0.001$) (Figures 7D and 7E). These results are consistent with the restoration of the gastrointestinal function determined by measurement of the intestinal transit and the colon length. Moreover, the results demonstrate that the TDO inhibitors do not only have positive effects on central nervous system function, but also act peripherally on the intestinal phenotype in the rotenone model.

Discussion

PD has been associated with an imbalance of neurotoxic and neuroprotective metabolites in the kynurenine pathway.^{17–21} Previous studies have shown that downregulation of TDO expression by RNA interference techniques in the invertebrate model species *Caenorhabditis elegans* and *Drosophila melanogaster* reduced α -synuclein proteotoxicity.^{13,15} Formation of α -synuclein aggregates is one of the pathological hallmarks of PD in humans.² Here we show for the first time in a relevant mammalian model for PD that pharmacological inhibition of TDO decreases the development of motor and non-motor symptoms associated with the disease in humans. PD symptoms were induced by intrastriatal infusion of rotenone, and oral treatment with TDO inhibitors was started seven days after disease induction. Two chemically and pharmacologically distinct TDO inhibitors were used, NTRC 3531-0 and LM10, which induced similar positive

(Legend continued from previous page)

inhibitors on the space occupied by microglia in the substantia nigra. Rotenone injection decreased the space occupied by microglia compared to sham-operated mice. The labeling of the groups is the same as listed for Figure 5A. $N = 4$ mice per group for all groups in panels A, C and D, except for the sham/NTRC D3 and rotenone/LM10 D3 groups with $N = 3$, and the sham/LM10 D3 group with $N = 5$. Results are expressed as mean \pm SEM. Indications of significance above individual bars represent the comparison to the respective vehicle control of the sham-operated or rotenone-injected groups. ns, not significant ($p > 0.05$); * $p < 0.05$; ** $p < 0.01$; **** $p < 0.0001$. (E) Representative 2D images of anti-Iba1-labeled microglial cells in the cleared brains of mice treated with rotenone and TDO inhibitors (scale bar: 30 μ m).

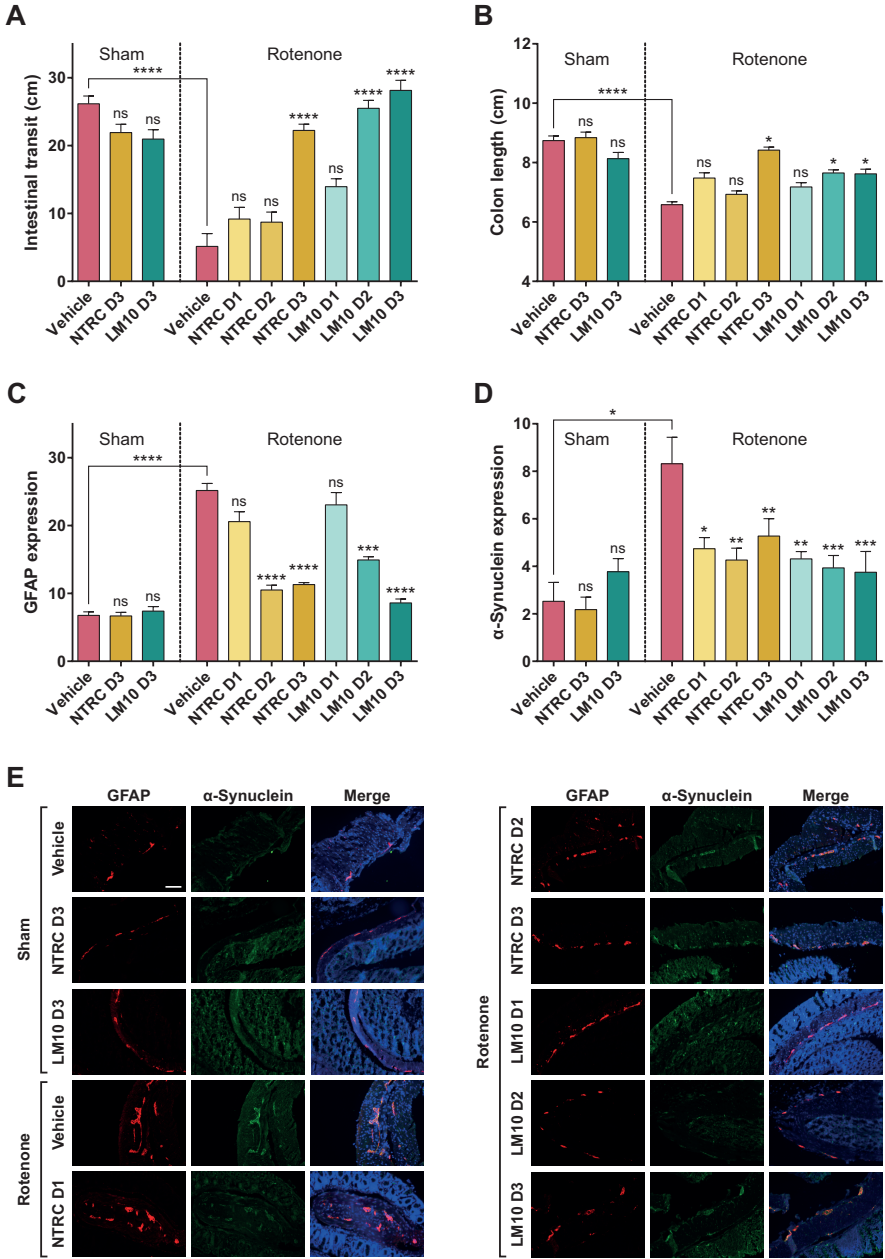


Figure 7. Gastrointestinal phenotype of mice treated with rotenone and TDO inhibitor. **(A)** Transit time. Two-way ANOVA showed an overall effect of rotenone injection on intestinal transit ($p < 0.0001$) and an interaction effect between rotenone and TDO inhibitor treatment ($p < 0.05$). **(B)** Colon length. (Legend continued on next page)

effects in the rotenone model. TDO inhibitor treatment was effective in reducing motor and cognitive deficits, as well as in reducing gastrointestinal dysfunction. Immunolabeling and 3D image analysis of TH-positive cells and Iba1-positive cells indicated that TDO inhibitor treatment decreased the rotenone-induced loss of dopaminergic neurons and the activation of microglia in the SN. Furthermore, immunofluorescent staining of colon tissue showed that TDO inhibitor treatment reduced glial cell activation and α -synuclein accumulation in the *enteric plexus*.

Though the restorative effects of both inhibitors were significant, they were partial. *In vivo* efficacy may have been limited by potency, or bioavailability. Assuming that at least 90% target inhibition is required for efficacy, the levels of NTRC 3531-0 were efficacious for only half of the time between the dose administrations. Suboptimal dosing may also provide an explanation for the saturating effect seen in the rotarod test, since the 50 and 100 mg/kg doses of NTRC 3531-0 were equally effective. To improve the *in vivo* efficacy, derivatives of NTRC 3531-0 are needed with significantly higher activity on TDO, and improved pharmacokinetic properties. For LM10, relationships between target occupancy and efficacy could not be determined because of its low cellular potency. Nevertheless, LM10 showed similar or even stronger effects than NTRC 3531-0 on most phenotypes in the rotenone model.

LM10 has previously been described to be effective in tumor models,³⁰ and was originally reported as a high-nanomolar potent inhibitor in hTDO-overexpressing HEK-293 cells.³⁰ Our cellular assays have indicated a considerably lower cellular potency of LM10, which is in agreement with a more recent publication reporting an IC_{50} of 24 μ M in the constitutively TDO-expressing human glioblastoma A172 cell line.³⁹ In the PK studies, we have observed that LM10, despite its high plasma levels, does not induce the expected increase in

(Legend continued from previous page)

Two-way ANOVA showed an overall effect of rotenone injection on colon length ($p < 0.0001$). **(C)** Expression of glial fibrillary acidic protein (GFAP) in enteric glial cells. Two-way ANOVA showed an overall effect of rotenone injection on GFAP expression ($p < 0.001$). **(D)** α -Synuclein expression in colonic tissue. The labeling of the groups is the same as listed for Figure 5A. $N = 10$ mice per group for all groups in panels A to D, except for the sham/LM10 D3 and rotenone/vehicle groups in panel A with $N = 9$, the rotenone/LM10 D1 and D2 groups in panel A with $N = 8$, and the rotenone/NTRC D3 group in panel C with $N = 9$. Results are expressed as mean \pm SEM. Indications of significance above individual bars represent the comparison to the respective vehicle control of the sham-operated or rotenone-injected groups. ns, not significant ($p > 0.05$); * $p < 0.05$; ** $p < 0.01$; *** $p < 0.001$; **** $p < 0.0001$. **(E)** Representative images of GFAP expression (red) as a marker for enteric glial cells, α -synuclein expression (green) and DAPI staining (blue) in the colonic tissue of mice treated with rotenone and TDO inhibitors (scale bar: 100 μ m).

plasma Trp levels, which may be correlated with the low cellular activity of LM10. A further lack of the modulation of Trp and Kyn levels in the brain can be explained by the poor brain penetration of LM10. Nonetheless, the plasma Kyn levels showed a relatively similar pattern in time as that observed upon treatment with NTRC 3531-0. While the initial decrease in Kyn levels would conform with the inhibition of TDO activity, the subsequent increase would seemingly contradict this. Nonetheless, this observation is in agreement with increased plasma Kyn levels observed in a TDO inhibitor-treated tumor mouse model and in *TDO2* knock-out mice.^{39,40} In the former study, plasma Trp and Kyn levels were studied at 2, 8 and 16 h after TDO inhibitor treatment.³⁹ The highest increase in Trp levels relative to vehicle-treated mice was found at 2 h, after which the levels decreased. For Kyn, increased levels were found at both 2 and 8 h, but not at 16 h.³⁹ These observations are both in agreement with the observed patterns for NTRC 3531-0. While the initial decrease in Kyn levels at the earlier timepoints may be attributed to inhibition of TDO activity, Schramme and coworkers suggested that increased Trp levels may induce IDO1 activity in peripheral IDO1-expressing cells,³⁹ resulting in increased Kyn levels in plasma at later timepoints. While increases in Kyn levels would expectedly nullify the effect of TDO inhibition, we believe that local changes in kynurenine pathway metabolite levels, for instance in specific cell types, or brain regions in which IDO1 is not expressed, may underlie the beneficial effects of TDO inhibitor treatment observed in the PD model, although this would require further study. Moreover, the mechanism by which LM10 induces the beneficial effect in the PD model in the absence of clear *in vivo* modulation of Kyn and Trp levels requires further understanding.

The mechanism through which TDO inhibitor treatment results in positive effects on rotenone-induced central and peripheral phenotypes remains to be elucidated. It is important to note the differences in *in vivo* PK properties of NTRC 3531-0 and LM10. LM10 reached very high levels in plasma after p.o. administration. Based on results obtained with an MDCK-MDR1 transporter assay, LM10 was expected to reach high levels in brain as well. However, the concentration of LM10 measured in the brain at steady state (*i.e.*, the AUC after 5-day p.o. dosing) was only 1% of the concentration in plasma. Although the amount of blood in the brain was reduced by exsanguination of the mice before isolation of the brains, it cannot be excluded that the low amount of LM10 measured in the brain samples originates from the blood instead of the brain tissue, since blood accounts for approximately 3 to 6% of the total brain volume in mice.^{41,42} The contribution of brain LM10 to its efficacy is therefore difficult to determine. Moreover, although the results with the MDCK-MDR1 assay indicate that LM10 is not a substrate of P-glycoprotein, passage across the blood–brain barrier may be impaired by another drug transporter, such as the breast cancer resistance protein (BCRP).⁴³ However, BCRP and P-glycoprotein have overlapping substrates, which implies that substrates of BCRP are

often also substrates of P-glycoprotein.⁴⁴ The presence of an acidic moiety in LM10 most likely precludes blood–brain barrier penetration due to the fact that it is mostly ionized in systemic circulation.³⁵

The total concentration of NTRC 3531-0 measured in brain at steady state was 37% of the concentration in plasma (K_p of 0.37). NTRC 3531-0 did show higher plasma protein and brain tissue binding compared to LM10, but the $K_{p_{uu}}$ was still higher compared to LM10. Therefore, NTRC 3531-0 is most suitable to be used as a pharmacological tool compound to study the functions of TDO both in the brain and in the periphery.

Since no compound or metabolite levels were measured in the efficacy study, it cannot be determined whether the disease-modifying effects were mediated through an effect on the TDO enzyme expressed in the brain or in peripheral tissues, such as the liver or intestine.¹⁶ Further studies are needed to determine to what extent the modulation of peripheral TDO activity can affect the central levels of Trp and its metabolites. Since Trp is actively transported over the blood–brain barrier,⁴⁵ and several metabolites formed in the kynurenine pathway can cross the blood–brain barrier as well,⁴⁶ modulation of central TDO activity may not be required. This could explain the beneficial effects observed for LM10 in the PD model in the absence of efficient brain penetration, although further understanding of the mechanism of LM10 is still required. Nonetheless, this could be in line with a study reporting that a non-blood–brain barrier-penetrating KMO inhibitor has beneficial effects on both peripheral and central phenotypes in an Alzheimer's disease mouse model.²⁴

Notably, the PK studies were carried out with healthy mice. Rotenone treatment is reported to have a negative impact on the integrity of the blood–brain barrier,⁴⁷ although contradicting data are also reported.⁴⁸ Therefore, it is possible that rotenone treatment in the efficacy model has resulted in a change of the blood-to-brain partition coefficients of the TDO inhibitors compared with those measured in the PK model.

There are several possible mechanisms through which TDO inhibition may ameliorate PD symptoms at the molecular or metabolic level. First of all, inhibition of TDO could lead to increased serotonin levels as a consequence of the increase in Trp, because Trp acts as a precursor in serotonin biosynthesis.⁴⁹ In the brains of PD patients, the concentration of serotonin is found to be decreased.⁵⁰ At neural synapses, increased serotonin levels as a consequence of TDO inhibition could have positive effects on cognitive function, thereby reducing depression,⁵¹ which is one of the most common non-motor symptoms in PD with an average prevalence of 40%.⁵² This concept was explored more than two decades ago by Madge and coworkers,⁵³ who synthesized TDO inhibitors and combined TDO/5-HT reuptake inhibitors.⁵³ Administration of these inhibitors to rats resulted in increased

cerebrospinal Trp and serotonin levels.⁴¹ Moreover, selective serotonin reuptake inhibitors (SSRIs) have been shown to significantly ameliorate depression in PD patients,⁵⁴ while administration of an SSRI to rotenone-treated rats resulted in improved motor function.⁵⁵ Secondly, TDO inhibition may decrease the levels of neurotoxic metabolites of Trp, more specifically, 3-HK and quinolinic acid (QA) (Figure 1). 3-HK causes neuronal cell death by generating free radicals,⁵⁶ while QA is a potent stimulant of the *N*-methyl-D-aspartate (NMDA) receptor.⁵⁷ Intracerebroventricular injection of QA causes seizure activity in mice.⁵⁸ Recent studies indicate that QA may also have a direct effect on the formation of α -synuclein inclusion bodies associated with PD. Tavassoly and coworkers showed that QA can form amyloid-like fibrillar assemblies that can induce the formation of α -synuclein aggregates in cells.⁵⁹ However, formation of these assemblies required high concentration of metabolite (at least 0.5 μ g/mL, *i.e.*, 3 mM) and heating to high temperature (90 °C).⁵⁹ Furthermore, the same investigators published that Trp can form similar structures, indicating that the effect is not specific for QA.^{59,60}

The availability of human genetic evidence is an important aspect in the selection of new targets for therapeutic intervention. Such evidence, although lacking for TDO, is available for ACMSD, an enzyme further downstream in the kynurenine pathway (Figure 1).^{22,23} ACMSD catalyzes the formation of the neuroprotective picolinic acid, thereby reducing QA cytotoxicity (Figure 1).⁶¹ Polymorphisms in the *ACMSD* locus are predicted to result in decreased ACMSD levels and increased QA levels.⁶² Moreover, there is a report of an individual with a missense mutation in *ACMSD* and late-onset PD.⁶³ Although the functional consequence of the mutation has not been characterized, computer-assisted structural studies indicate that it impairs ACMSD activity.⁶² Finally, a stop codon mutation in *ACMSD* is linked to an autosomal dominant neurological disease with epilepsy and features of parkinsonism, that is, familial cortical myoclonic tremor and epilepsy (FCMTE).⁶⁴ While this is a relatively mild disorder with no evidence of neurodegeneration, it provides strong genetic evidence for the involvement of a deregulated kynurenine pathway in aberrant motor function and neurological disease.

In conclusion, our study shows for the first time in a relevant animal model that TDO inhibition with small molecule drugs may be beneficial for treatment of PD symptoms. Whereas levodopa acts only as a temporary relief of motor symptoms, our preclinical study indicates that administration of TDO inhibitors has beneficial effects on both motor and non-motor symptoms of PD. The precise mechanism underlying the disease-modifying effects of TDO inhibition, and the relative contribution of peripheral *versus* brain TDO require further study.

Materials and methods

Compound library and TDO inhibitors

Human TDO was screened at the Pivot Park Screening Centre (PPSC; Oss, The Netherlands; www.ppscreeningcentre.com) using the NFK Green™ assay technology developed at Netherlands Translational Research Center B.V. (NTRC; www.residencetimer.com).³¹ The PPSC library consisted of a diverse set of 87,000 lead-like compounds purchased at Specs (Delft, The Netherlands). NTRC 3531-0 is derived from a TDO inhibitor identified in this screen with a unique 3-phenyl-1*H*-indole scaffold (Figure 2A). The synthesis of NTRC 3531-0 is described in patent application WO/2018/011227 A1.³² The compound is available for academic research under a Materials Transfer Agreement with NTRC. LM10 was synthesized according to the protocol described by Dolušić and coworkers.²⁹ The IDO1 inhibitor epacadostat, used as a reference inhibitor in the biochemical and cell-based assays for IDO1, was purchased at MedKoo (cat. no. 206461). Before testing in biochemical and cell-based assays, compounds were dissolved in dimethylsulfoxide (DMSO). For dose-response testing, the compound stock was diluted in $\sqrt{10}$ -fold steps in DMSO to obtain a 10-point dilution series, followed by further dilution in aqueous buffers, as specified below for the different assays.

TDO biochemical assay

Recombinant TDO was purified and its biochemical activity was measured with the NFK Green assay, as described.³¹ In short, compounds were diluted in DMSO and finally in TDO reaction buffer, consisting of 100 mM NaH₂PO₄, pH 7.0, supplemented with 0.01% Tween-20 (Sigma, cat. no. P7949). hTDO enzyme was diluted in reaction buffer supplemented with ascorbic acid, as described,³¹ and combined with inhibitor solution in a black 384-well plate (Corning, cat. no. 3537). The final concentration of hTDO in the assay was 50 nM. After incubation for 60 min at room temperature, the enzymatic reaction was initiated by the addition of Trp to a final concentration of 200 μ M. The reaction was stopped after incubation for 15 min at room temperature by the addition of NFK Green. Plates were read on an EnVision multimode reader (Perkin Elmer). For high-throughput screening, the assay was further miniaturized to 1536-well format and the compound library was screened at a single concentration of 10 μ M. For determination of IC₅₀ values, the effect of inhibitors was determined in 10-point duplicate dose-response curves. Graphs were fitted to a four-parameter logistics equation in XLfit (IDBS) from which IC₅₀ values were calculated. The same assay was performed for mTDO (final concentration of 100 nM), except that the preincubation with compound was performed for 30 min and, after addition of Trp to a final concentration of 400 μ M, the enzymatic reaction was allowed to proceed for 60 min.

IDO1 biochemical assay

Activity on recombinant hIDO1 was determined with the NFK Green assay as described above for TDO,³¹ except that the reaction buffer consisted of 50 mM NaH₂PO₄, pH 7.0, supplemented with 0.01% Tween-20 and 1% glycerol. In addition to ascorbic acid (final concentration of 10 mM), the enzyme solution contained catalase (10 µg/mL) and methylene blue (10 µM). The final hIDO1 enzyme concentration was 25 nM, and the final Trp concentration was 100 µM.³¹ The enzyme was preincubated with compound for 30 min, after which the enzymatic reaction with Trp was allowed to proceed for 60 min.

Cell lines and culture

The GripTite™ HEK-293 MSR cell line was purchased from Thermo Fisher (cat. no. R79507), the human colorectal carcinoma SW48 cell line (cat. no. CCL-231) from the American Type Culture Collection (ATCC), and the mouse glioma cell line GL-261 (cat. no. ACC 802) from the Deutsche Sammlung von Mikroorganismen und Zellkulturen (DSMZ). HEK-hTDO and HEK-hIDO1 cells were cultured in DMEM supplemented with 10% fetal bovine serum (FBS), 1% Penicillin/Streptomycin (P/S) solution, 1% MEM non-essential amino acids, 600 µg/mL geneticin and 10 µg/mL blasticidin. SW48 cells were cultured in RPMI 1640 supplemented with 10% bovine calf serum (BCS) and 1% P/S. GL-261-mTDO cells were cultured in DMEM supplemented with 10% BCS, 1% P/S and 10 µg/mL blasticidin. DMEM medium contains 78 µM Trp and RPMI 1640 contains 24.5 µM Trp.

Generation of *TDO2*- and *IDO1*-overexpressing cell lines

Full-length *hTDO2*, *mTDO2* and *hIDO1* cDNAs were synthesized and cloned in the expression vector pEF6v5 (Thermo Fisher, cat. no. V96120), harboring an ampicillin and blasticidin resistance marker gene, at BaseClear (Leiden, The Netherlands). Using these vectors, cell lines expressing *hTDO2* or *hIDO1* were generated by transfection of GripTite™ HEK-293 MSR cells. A cell line expressing *mTDO2* was generated by transfection of GL-261 cells. HEK-293 MSR and GL-261 cells lack endogenous expression of *TDO2* and *IDO1* as determined by quantitative real-time PCR (qPCR). The absence of TDO and IDO1 in HEK-293 MSR cells was further confirmed by immunoblot analysis. Cells were transfected with Lipofectamine 3000 (Thermo Fisher). Single cell clones were selected with blasticidin selection and limited dilution in 384-well culture plates. Trp-converting activity in the clones was tested with NFK Green or 4-dimethylaminobenzaldehyde (pDMAB).⁶⁵ To assess the stability of *TDO2* or *IDO1* expression, clones were cultured for four weeks in the absence of blasticidin, during which they were tested weekly for maintenance of the Trp-catabolizing activity. Afterward, the gene expression levels, the protein expression levels and the inhibitory activity of reference compounds were determined in the resulting sublines. Cell-based assays with the transfected cell lines were performed in the absence of blasticidin.

Gene expression analysis

Expression of *TDO2* and *IDO1* in human and mouse cell lines transfected with cDNA expression vectors was confirmed by qPCR, following standard protocols.⁶⁶ Sequences of DNA oligonucleotide primers used are provided in Supplementary Table 1. Expression of *TDO2* and *IDO1* was normalized using the expression of housekeeping genes. For the analysis of *hTDO2* and *hIDO1* gene expression, this was the gene for β -actin (*ACTB*). For the analysis of the expression of *mTDO2* or *mIDO1*, the control genes were mouse *ACTB* and glyceraldehyde-3-phosphate dehydrogenase (*GAPDH*).

Immunoblot analysis

The expression of hTDO and hIDO1 in cell lines was also confirmed by SDS-polyacrylamide gel electrophoresis (SDS-PAGE) and immunoblot analysis. hTDO was detected with mouse polyclonal anti-TDO antibody (Abcam, cat. no. ab76859), horseradish peroxidase (HRP) conjugated anti-mouse IgG (Cell Signaling, cat. no. 7076S), and enhanced chemiluminescence (ECL) using Clarity™ Western ECL substrate (Bio-Rad, cat. no. 170-5060). hIDO1 was detected with anti-IDO1 rabbit monoclonal antibody (Cell Signaling, cat. no. 86630), HRP-conjugated anti-rabbit IgG (Cell Signaling, cat. no. 7074) and ECL. To control for equal loading of the samples on SDS/PAGE gels, the blots were stripped using Restore™ Plus Western Blot Stripping Buffer (Thermo Fisher, cat. no. 46430) after which β -actin was detected using rabbit polyclonal anti- β -actin antibody (Cell Signaling, cat. no. 4967), HRP-conjugated anti-rabbit IgG (Cell Signaling) and ECL.

Cell-based assays for TDO and IDO1

Inhibition of Trp-to-NFK conversion in HEK-hTDO, HEK-hIDO1 and SW48 cells was measured with NFK Green, essentially as described previously for cancer cell lines.³¹ Cell density, incubation time and Trp concentrations were optimized. For the TDO assay with HEK-hTDO and SW48 cells, 200 μ M Trp was added to the culture medium. No additional Trp was added for the IDO1 assay with HEK-hIDO1 cells. The incubation time with compound was 42 h for the assays with HEK-hTDO and HEK-hIDO1 cells, and 18 h for the assay with SW48 cells.

Inhibition of Trp-metabolizing activity in GL-261-mTDO cells was measured with pDMAB.⁶⁵ The cells were incubated with compound for 1 h, after which 200 μ M Trp was added. After incubation for 42 h, 5% trichloroacetic acid (Fisher) in Milli-Q was added to each well and incubated for 1 h at 55 °C to hydrolyze NFK to Kyn. The plates were centrifuged for 10 min at 2,900 *g*. The supernatant was transferred to another plate and 2% pDMAB (Fisher Chemicals) dissolved in acetic acid (Acros) was added. After 10 min incubation at room temperature, the absorbance at 480 nm was measured to determine the production of Kyn.

In parallel with the cell-based NFK Green assays, the cytotoxicity of the compounds was determined in cell viability assays using ATPlite™ 1Step (PerkinElmer).⁶⁷ NTRC 3531-0 and LM10 were not cytotoxic to any cell line used in this study.

Pharmacokinetic analysis, brain penetration and quantification of Trp and Kyn

In vivo half-life and oral bioavailability of NTRC 3531-0 and LM10 were determined following single p.o. and i.v. administration to male CB57BL/6 mice at Aurigon (Dunakeszi, Hungary). In addition, plasma and brain levels after repeated dosing were determined by treating mice for five consecutive days p.o. daily (QD). Nine mice were used per dosing group. Plasma and brain samples were collected from three mice per dosing group at each time point. For plasma sampling, this enabled sampling at three time points (including pretreatment) from each mice. Formulations were prepared in DMSO, Kolliphor® EL, 5% D-mannitol in mineral water at a volume ratio of 1:1:8. Mice treated with a single dose of compound (i.v. or p.o.) and vehicle-treated mice were fasted for approximately 4 h prior to dosing, and regained access to feed 2 h after dosing. Mice treated for 5 days had free access to feed. Blood samples were collected in K3-EDTA tubes from the retro-orbital plexus of the mice at 0.083, 0.25, 0.5, 1, 2, 7, 12 and 24 h after i.v. or p.o. dosing. Plasma samples were obtained by cooling of the blood samples in ice-water followed by centrifugation at 2,000 g for 10 min at 4 °C, and collection of the supernatant, which were immediately frozen on dry-ice. Brains were collected immediately after the blood sampling at 1, 12 and 24 h after single and repeated p.o. dosing, after exsanguination of the animals to the standard extent, and were snap frozen in liquid nitrogen. Pharmacokinetic parameters (C_{max} , $t_{1/2}$ and AUC) were determined by LC-MS/MS analysis of the plasma samples after acetonitrile extraction. To determine brain penetration, compound levels were determined in homogenates prepared from the brains. The brain-to-plasma partition coefficient (K_p) was determined as AUC_{brain}/AUC_{plasma} . The unbound brain-to-plasma partition coefficient ($K_{p,u}$) was determined as $(AUC_{brain} \times \text{unbound fraction in brain tissue}) / (AUC_{plasma} \times \text{unbound fraction in plasma})$. Quantification of Trp and Kyn levels was additionally performed by LC-MS/MS in both the plasma samples and brain homogenates. The exact timepoints of blood sampling for these mice are listed in Supplementary Table 2.

Rotenone model, surgery, and administration of inhibitors

Seven week old male C57BL/6NCRl mice (Charles River, The Netherlands) were housed at room temperature under 12 h light/dark cycle. Animal procedures were approved by the Ethical Committee of Animal Research of Utrecht University, Utrecht, The Netherlands. Food and water was provided *ad libitum*. Mice underwent stereotaxic surgery under isoflurane anesthesia: a hole was drilled in the skull, a cannula inserted in the right striatum and 5.4 µg of freshly prepared rotenone (dissolved in DMSO) was infused. The

following stereotaxic coordinates were used: AP + 0.4, ML -2.0 from bregma and DV -3.3 below dura.

Two independent experiments were performed involving two cohorts of mice, with ten mice per dosing or control group in total. To control for the effect of rotenone treatment, sham-operated mice were injected with vehicle. TDO inhibitors were administered from seven days after surgery, once daily by oral gavage. Formulations were prepared in 5% DMSO, 5% Kolliphor® EL, 5% D-mannitol in water. Both inhibitors were administered at three different doses: NTRC 3531-0 at 25 mg/kg (D1), 50 mg/kg (D2) and 100 mg/kg (D3), and LM10 at 12.5 mg/kg (D1), 25 mg/kg (D2) and 50 mg/kg (D3). The highest dose of NTRC 3531-0 (*i.e.*, 100 mg/kg) was predicted to result in at least 90% TDO inhibition, lasting for approximately 12 h, based on the PK properties of NTRC 3531-0 after p.o. administration, and an IC_{90} of 2.5 μ M in the cell-based HEK-hTDO assay (Figure 3B). The effect of inhibitor treatment was determined by comparison to vehicle-treated mice. For ethical reasons it was not possible to dose the TDO inhibitors p.o. twice daily. Forty-two days after surgery, mice were euthanized by decapitation.

Motor symptoms assessment

Motor function was assessed in the rotarod test by placing mice on an accelerating rod with speeds starting at 2 rpm and gradually increasing to 20 rpm. The latency to fall was recorded for a maximum of 300 s. Baseline motor function was tested seven days after surgery, and subsequently, motor function was tested every seven days until day 42.

Spatial memory test

The spatial memory test measures the ability of the mice to react to a spatial novelty.³⁶ Mice were individually submitted to seven consecutive sessions of six minutes. During the first session, mice were placed in an empty cage. During the 2nd to 4th session, five objects were present and mice were placed into the cage to habituate to the configuration of the objects (habituation phase). During an interval of three minutes between two sessions, the animals were returned to a waiting cage. Before the 5th session, the spatial test session, the configuration of the objects was changed by moving two objects (displaced objects, DO) and leaving the other three objects at the same position (nondisplaced objects, NDO). In all sessions, the total activity of the animal was measured. From session 2 to session 5, object exploration was evaluated on the basis of the mean time spent by the animal in contact with the different objects. The ability of the animals to selectively react to the spatial change was analyzed by calculating the spatial re-exploration index ($DO[S5] - DO[S4] = DO$ and $NDO[S5] - NDO[S4] = NDO$). The time the animals interacted with the DO minus the time they interact with the NDO was used for the analysis. The raw data of the spatial memory test can be found in Supplementary Tables 3–6.

Intestinal transit and colon length

Thirty minutes before sacrificing the mice, 2.5% (v/v) Evans blue solution in 1.5% methylcellulose was administered intragastrically (0.3 mL per animal). Intestinal transit was measured as the distance from the pylorus to the most distal point of migration of the Evans blue dye. In addition, the length of the colon was determined as a sign of intestinal inflammation.²⁸

iDISCO

The number of TH-positive cells and the morphology of microglia (Iba1 immunolabeling) in the brains of mice was determined by immunolabeling-enabled three-dimensional imaging of solvent-cleared organs (iDISCO).³⁷ Brains were cut in hemispheres and dehydrated with a methanol/H₂O series: 20%, 40%, 60%, 80%, 100% and 100% for 1 h each. Samples were incubated overnight in 66% DCM/33% methanol at room temperature, with shaking. The next day, the samples were washed twice in 100% methanol at room temperature, and bleached in chilled fresh 5% H₂O₂ in methanol overnight at 4 °C. The samples were rehydrated with a methanol/H₂O series: 80%, 60%, 40%, 20% and phosphate-buffered saline (PBS) for 1 h each at room temperature. They were then washed twice in PTx.2 (PBS with 0.2% Triton X-100) at room temperature for 1 h.

For immunolabeling, samples were incubated in permeabilization buffer (400 mL PTx.2 supplemented with 11.5 g glycine and 100 mL of DMSO) for 2 days at 37 °C. After permeabilization, samples were blocked in blocking solution for 2 days at 37 °C. Primary antibodies (sheep anti-TH, Pel freez, cat. no. P60101; rabbit anti-Iba1, Thermo Fisher, cat. no. PA5-27436) diluted in PTwH/5% DMSO/3% donkey serum (PTwH being defined as PBS with 0.2% Triton X-100 and 10 µg/mL heparin) were then incubated with the tissue for 5 days at 37 °C. After incubation, samples were washed in PTwH for 4 to 5 times until the next day. Secondary antibodies (Alexa Fluor® 647-conjugated donkey anti-sheep and Alexa Fluor® 594-conjugated donkey anti-rabbit) were diluted in PTwH with 3% donkey serum and incubated with the samples for 5 days at 37 °C. Samples were washed with PTwH for 4 to 5 times until the next day.

Samples were dehydrated in a methanol/H₂O series: 20%, 40%, 60%, 80%, 100% and 100% for 1 h each. The hemispheres were subsequently put in 66% DCM/33% methanol for 3 h at room temperature. They were incubated twice in 100% dichloromethane for 15 min to wash away the methanol. Finally, samples were incubated in dibenzyl ether overnight. The tube was completely filled to prevent any oxidization.

Light sheet imaging

Samples were imaged in horizontal orientation with an UltraMicroscope II (LaVision BioTec) light sheet microscope equipped with Imspector software (LaVision BioTec, version 5.0285.0). Images were taken with a Neo sCMOS camera (Andor) (2,560 × 2,160 pixels; pixel size: 6.5 × 6.5 μm²). Samples were scanned with double-sided illumination, a sheet NA of 0.148348 and a step-size of 2.5 μm and 0.5 μm using the horizontal focusing light sheet scanning method with the optimal amount of steps and using the contrast blending algorithm. The effective magnification for all images was 1.36x (zoombody × objective + dipping lens = 0.63 × 2.152). A Coherent OBIS 647-120 LX with 676/29 filter and LS 561-100 laser was used. After image acquisition, full stained 3D brain images were obtained. TH-immunopositive neurons and Iba1-positive cells in the SN were analyzed using Bitplane Imaris 9.0. To measure TH-immunopositive neurons, the automatic 'spots' measurement function was used with a median diameter of 16.3 μm. For the Iba1-positive cells, the 'Imaris Surfaces' tool was used for measurement of the volume and the space occupied by these cells in the SN.

Immunofluorescent microscopy

Expression of GFAP and α-synuclein in colonic tissue was determined using confocal microscopy (Leica SP8). The colons of the mice were embedded in paraffin. Sections of 15 μm were cut and incubated with 0.3% (v/v) H₂O₂ for 30 min, rehydrated, and incubated with citrate buffer. Following blocking with serum, the sections were incubated overnight with rabbit anti-α-synuclein (Millipore, cat. no. AB5038) at a dilution of 1:1,000, or rabbit anti-GFAP (Dako, cat. no. Z0334), 1:1,000. After incubation with Alexa[®]488-labeled donkey anti-rabbit secondary antibody, the slides were mounted using Vectashield[®] medium for fluorescence with DAPI (Vector Laboratories, cat. no. H-1000).

Immunofluorescence images were made using a Keyence BZ-9000 microscope. GFAP and α-synuclein staining were quantified by calculation of the corrected total fluorescence (CTF) with the formula: integrated density - (area × mean fluorescence of background reading).

Statistical analyses

Experimental results of the PK study and the rotenone model are expressed as mean ± SEM. Differences in metabolite levels between the groups of the PK study were analyzed with a two-way ANOVA, followed by Dunnett's multiple comparison test. The effect of treatment with inhibitor was related to the effect of vehicle treatment. Differences between groups of the rotenone model were analyzed with a two-way ANOVA, followed by a Tukey's multiple comparison test. The effect of injection with rotenone (rotenone/vehicle) was related to the effect of the sham surgery (sham/vehicle). Furthermore, the effect

of treatment with inhibitor (rotenone/TDO inhibitor) was related to the effect of vehicle treatment (rotenone/vehicle). For the rotarod test, data were analyzed with a general linear model repeated measures ANOVA with the within-subjects factor 'time' and the between-subjects factors 'surgery' and 'TDO inhibitor treatment'. Results are considered statistically significant when $p < 0.05$. The individual p -values of the multiple comparisons presented in the bar charts are listed in Supplementary Table 7. Analyses were performed using SPSS (version 22.0; IBM Corp.) and GraphPad Prism (version 6.07; GraphPad Software).

References

1. Reich, S. G. & Savitt, J. M. Parkinson's disease. *Med. Clin. North Am.* **103**, 337–50 (2019).
2. Beach, T. G. *et al.* Multi-organ distribution of phosphorylated α -synuclein histopathology in subjects with Lewy body disorders. *Acta Neuropathol.* **119**, 689–702 (2010).
3. Poewe, W. Non-motor symptoms in Parkinson's disease. *Eur. J. Neurol.* **15 Suppl 1**, 14–20 (2008).
4. Tansey, M. G. & Goldberg, M. S. Neuroinflammation in Parkinson's disease: its role in neuronal death and implications for therapeutic intervention. *Neurobiol. Dis.* **37**, 510–8 (2010).
5. Goodarzi, Z. *et al.* Detecting depression in Parkinson disease: a systematic review and meta-analysis. *Neurology* **87**, 426–37 (2016).
6. Aarsland, D., Andersen, K., Larsen, J. P., Lolk, A. & Kragh-Sørensen, P. Prevalence and characteristics of dementia in Parkinson disease: an 8-year prospective study. *Arch. Neurol.* **60**, 387–92 (2003).
7. Pfeiffer, R. F. Gastrointestinal dysfunction in Parkinson's disease. *Curr. Treat. Options Neurol.* **20**, 54 (2018).
8. Abbott, R. D. *et al.* Frequency of bowel movements and the future risk of Parkinson's disease. *Neurology* **57**, 456–62 (2001).
9. Gao, X., Chen, H., Schwarzschild, M. A. & Ascherio, A. A prospective study of bowel movement frequency and risk of Parkinson's disease. *Am. J. Epidemiol.* **174**, 546–51 (2011).
10. LeWitt, P. A. & Fahn, S. Levodopa therapy for Parkinson disease: a look backward and forward. *Neurology* **86**, S3–12 (2016).
11. Santos García, D. *et al.* Non-motor symptoms burden, mood, and gait problems are the most significant factors contributing to a poor quality of life in non-demented Parkinson's disease patients: results from the COPPADIS Study Cohort. *Parkinsonism Relat. Disord.* **66**, 151–7 (2019).
12. Colzi, A., Turner, K. & Lees, A. J. Continuous subcutaneous waking day apomorphine in the long term treatment of levodopa induced interdose dyskinesias in Parkinson's disease. *J. Neurol. Neurosurg. Psychiatry* **64**, 573–6 (1998).
13. van der Goot, A. T. *et al.* Delaying aging and the aging-associated decline in protein homeostasis by inhibition of tryptophan degradation. *Proc. Natl. Acad. Sci. U. S. A.* **109**, 14912–7 (2012).
14. Campesan, S. *et al.* The kynurenine pathway modulates neurodegeneration in a *Drosophila* model of Huntington's disease. *Curr. Biol.* **21**, 961–6 (2011).
15. Breda, C. *et al.* Tryptophan-2,3-dioxygenase (TDO) inhibition ameliorates neurodegeneration by modulation of kynurenine pathway metabolites. *Proc. Natl. Acad. Sci. U. S. A.* **113**, 5435–40 (2016).
16. Schutz, G. & Feigelson, P. Purification and properties of rat liver tryptophan oxygenase. *J. Biol. Chem.* **247**, 5327–32 (1972).
17. Chen, Y. & Guillemin, G. J. Kynurenine pathway metabolites in humans: disease and healthy states. *Int. J. Tryptophan Res.* **2**, 1–19 (2009).
18. Szabó, N., Kincses, Z. T., Toldi, J. & Vécsei, L. Altered tryptophan metabolism in Parkinson's disease: a possible novel therapeutic approach. *J. Neurol. Sci.* **310**, 256–60 (2011).
19. Schwarcz, R., Bruno, J. P., Muchowski, P. J. & Wu, H.-Q. Kynurenines in the mammalian brain: when physiology meets pathology. *Nat. Rev. Neurosci.* **13**, 465–77 (2012).
20. Lim, C. K. *et al.* Involvement of the kynurenine pathway in the pathogenesis of Parkinson's disease. *Prog. Neurobiol.* **155**, 76–95 (2017).
21. Platten, M., Nollen, E. A. A., Röhrig, U. F., Fallarino, F. & Opitz, C. A. Tryptophan metabolism as a common therapeutic target in cancer, neurodegeneration and beyond. *Nat. Rev. Drug Discov.* **18**, 379–401 (2019).

22. Bandrés-Ciga, S. *et al.* Genome-wide assessment of Parkinson's disease in a Southern Spanish population. *Neurobiol. Aging* **45**, 213.e3–e9 (2016).
23. Tejera-Parrado, C. *et al.* A replication study of GWAS-genetic risk variants associated with Parkinson's disease in a Spanish population. *Neurosci. Lett.* **712**, 134425 (2019).
24. Zwillig, D. *et al.* Kynurenine 3-monooxygenase inhibition in blood ameliorates neurodegeneration. *Cell* **145**, 863–74 (2011).
25. Smith, J. R., Jamie, J. F. & Guillemin, G. J. Kynurenine-3-monooxygenase: a review of structure, mechanism, and inhibitors. *Drug Discov. Today* **21**, 315–24 (2016).
26. Betarbet, R. *et al.* Chronic systemic pesticide exposure reproduces features of Parkinson's disease. *Nat. Neurosci.* **3**, 1301–6 (2000).
27. Perez-Pardo, P. *et al.* Promising effects of neurorestorative diets on motor, cognitive, and gastrointestinal dysfunction after symptom development in a mouse model of Parkinson's disease. *Front. Aging Neurosci.* **9**, 57 (2017).
28. Perez-Pardo, P. *et al.* Gut-brain and brain-gut axis in Parkinson's disease models: effects of a uridine and fish oil diet. *Nutr. Neurosci.* **21**, 391–402 (2018).
29. Dolusić, E. *et al.* Tryptophan 2,3-dioxygenase (TDO) inhibitors. 3-(2-(Pyridyl) ethenyl)indoles as potential anticancer immunomodulators. *J. Med. Chem.* **54**, 5320–34 (2011).
30. Pilotte, L. *et al.* Reversal of tumoral immune resistance by inhibition of tryptophan 2,3-dioxygenase. *Proc. Natl. Acad. Sci. U. S. A.* **109**, 2497–502 (2012).
31. Seegers, N. *et al.* High-throughput fluorescence-based screening assays for tryptophan-catabolizing enzymes. *J. Biomol. Screen.* **19**, 1266–74 (2014).
32. de Man, A. P. A. *et al.* Inhibitors of tryptophan 2,3-dioxygenase. Patent WO/2018/011227 (2018).
33. Horio, M. *et al.* Transepithelial transport of drugs by the multidrug transporter in cultured Madin-Darby canine kidney cell epithelia. *J. Biol. Chem.* **264**, 14880–4 (1989).
34. Hellinger, E. *et al.* Comparison of brain capillary endothelial cell-based and epithelial (MDCK-MDR1, Caco-2, and VB-Caco-2) cell-based surrogate blood-brain barrier penetration models. *Eur. J. Pharm. Biopharm.* **82**, 340–51 (2012).
35. Di, L., Rong, H. & Feng, B. Demystifying brain penetration in central nervous system drug discovery. *J. Med. Chem.* **56**, 2–12 (2013).
36. De Leonibus, E. *et al.* Spatial deficits in a mouse model of Parkinson disease. *Psychopharmacology (Berl.)* **194**, 517–25 (2007).
37. Renier, N. *et al.* iDISCO: a simple, rapid method to immunolabel large tissue samples for volume imaging. *Cell* **159**, 896–910 (2014).
38. Joers, V., Tansey, M. G., Mulas, G. & Carta, A. R. Microglial phenotypes in Parkinson's disease and animal models of the disease. *Prog. Neurobiol.* **155**, 57–75 (2017).
39. Schramme, F. *et al.* Inhibition of tryptophan-dioxygenase activity increases the antitumor efficacy of immune checkpoint inhibitors. *Cancer Immunol. Res.* **8**, 32–45 (2020).
40. Kanai, M. *et al.* Tryptophan 2,3-dioxygenase is a key modulator of physiological neurogenesis and anxiety-related behavior in mice. *Mol. Brain* **2**, 8 (2009).
41. Chugh, B. P. *et al.* Measurement of cerebral blood volume in mouse brain regions using micro-computed tomography. *Neuroimage* **47**, 1312–8 (2009).
42. Pathak, A. P., Kim, E., Zhang, J. & Jones, M. V. Three-dimensional imaging of the mouse neurovasculature with magnetic resonance microscopy. *PLoS One* **6**, e22643 (2011).

43. Agarwal, S., Hartz, A. M. S., Elmquist, W. F. & Bauer, B. Breast cancer resistance protein and P-glycoprotein in brain cancer: two gatekeepers team up. *Curr. Pharm. Des.* **17**, 2793–802 (2011).
44. Sarkadi, B., Ozvegy-Laczka, C., Németh, K. & Váradi, A. ABCG2 – a transporter for all seasons. *FEBS Lett.* **567**, 116–20 (2004).
45. Hargreaves, K. M. & Pardridge, W. M. Neutral amino acid transport at the human blood-brain barrier. *J. Biol. Chem.* **263**, 19392–7 (1988).
46. Fukui, S., Schwarcz, R., Rapoport, S. I., Takada, Y. & Smith, Q. R. Blood-brain barrier transport of kynurenines: implications for brain synthesis and metabolism. *J. Neurochem.* **56**, 2007–17 (1991).
47. Doll, D. N. *et al.* Mitochondrial crisis in cerebrovascular endothelial cells opens the blood-brain barrier. *Stroke* **46**, 1681–9 (2015).
48. Ravenstijn, P. G. M. *et al.* The exploration of rotenone as a toxin for inducing Parkinson's disease in rats, for application in BBB transport and PK-PD experiments. *J. Pharmacol. Toxicol. Methods* **57**, 114–30 (2008).
49. Grahame-Smith, D. G. Tryptophan hydroxylation in brain. *Biochem. Biophys. Res. Commun.* **16**, 586–92 (1964).
50. Tohgi, H., Abe, T., Takahashi, S., Takahashi, J. & Hamato, H. Concentrations of serotonin and its related substances in the cerebrospinal fluid of parkinsonian patients and their relations to the severity of symptoms. *Neurosci. Lett.* **150**, 71–4 (1993).
51. Xie, Y., Liu, P.-P., Lian, Y.-J., Liu, H.-B. & Kang, J.-S. The effect of selective serotonin reuptake inhibitors on cognitive function in patients with Alzheimer's disease and vascular dementia: focusing on fluoxetine with long follow-up periods. *Signal Transduct. Target. Ther.* **4**, 30 (2019).
52. Slaughter, J. R., Slaughter, K. A., Nichols, D., Holmes, S. E. & Martens, M. P. Prevalence, clinical manifestations, etiology, and treatment of depression in Parkinson's disease. *J. Neuropsychiatry Clin. Neurosci.* **13**, 187–96 (2001).
53. Madge, D. J., Hazelwood, R., Iyer, R., Jones, H. T. & Salter, M. Novel tryptophan dioxygenase inhibitors and combined tryptophan dioxygenase/5-HT reuptake inhibitors. *Bioorg. Med. Chem. Lett.* **6**, 857–60 (1996).
54. Bomasang-Layno, E., Fadlon, I., Murray, A. N. & Himelhoch, S. Antidepressive treatments for Parkinson's disease: a systematic review and meta-analysis. *Parkinsonism Relat. Disord.* **21**, 833–42 (2015).
55. Sharma, N., Jamwal, S. & Kumar, P. Beneficial effect of antidepressants against rotenone induced Parkinsonism like symptoms in rats. *Pathophysiol. Off. J. Int. Soc. Pathophysiol.* **23**, 123–34 (2016).
56. Okuda, S., Nishiyama, N., Saito, H. & Katsuki, H. Hydrogen peroxide-mediated neuronal cell death induced by an endogenous neurotoxin, 3-hydroxykynurenine. *Proc. Natl. Acad. Sci. U. S. A.* **93**, 12553–8 (1996).
57. Stone, T. W. & Perkins, M. N. Quinolinic acid: a potent endogenous excitant at amino acid receptors in CNS. *Eur. J. Pharmacol.* **72**, 411–2 (1981).
58. Lapin, I. P. Stimulant and convulsive effects of kynurenines injected into brain ventricles in mice. *J. Neural Transm.* **42**, 37–43 (1978).
59. Tavassoly, O. *et al.* Quinolinic acid amyloid-like fibrillar assemblies seed α -synuclein aggregation. *J. Mol. Biol.* **430**, 3847–62 (2018).
60. Shaham-Niv, S. *et al.* Formation of apoptosis-inducing amyloid fibrils by tryptophan. *Isr. J. Chem.* **57**, 729–37 (2017).
61. Jhamandas, K. H., Boegman, R. J., Beninger, R. J., Miranda, A. F. & Lipic, K. A. Excitotoxicity of quinolinic acid: modulation by endogenous antagonists. *Neurotox. Res.* **2**, 139–55 (2000).
62. Thirtamara-Rajamani, K. *et al.* Is the enzyme ACMSD a novel therapeutic target in Parkinson's disease? *J. Parkinsons Dis.* **7**, 577–87 (2017).

63. Vilas, D. *et al.* A novel p.Glu298Lys mutation in the ACMSD gene in sporadic Parkinson's disease. *J. Parkinsons Dis.* **7**, 459–63 (2017).
64. Martí-Massó, J. F. *et al.* The ACMSD gene, involved in tryptophan metabolism, is mutated in a family with cortical myoclonus, epilepsy, and parkinsonism. *J. Mol. Med. (Berl.)* **91**, 1399–406 (2013).
65. Matin, A., Streete, I. M., Jamie, I. M., Truscott, R. J. W. & Jamie, J. F. A fluorescence-based assay for indoleamine 2,3-dioxygenase. *Anal. Biochem.* **349**, 96–102 (2006).
66. Libouban, M. A. A. *et al.* Stable aneuploid tumors cells are more sensitive to TTK inhibition than chromosomally unstable cell lines. *Oncotarget* **8**, 38309–25 (2017).
67. Uitdehaag, J. C. M. *et al.* Comparison of the cancer gene targeting and biochemical selectivities of all targeted kinase inhibitors approved for clinical use. *PLoS One* **9**, e92146 (2014).

Supplementary data

Supplementary Table 1. DNA sequences of oligonucleotide primers used for quantitative real-time PCR analysis of *TDO2* and *IDO1* gene expression in cell lines.

Gene	Species	Direction	Sequence
<i>TDO2</i>	human	forward	CTTAGTAAAGGTGAAAGACGG
	human	reverse	GTCCATAAGAGAAGTCAGCA
<i>TDO2</i>	mouse	forward	ATGAGTGGGTGCCCGTTT
	mouse	reverse	GGCTCTGTTTACACCAGTTTGAG
<i>IDO1</i>	human	forward	TTAGAGTCAAATCCCTCAGTCC
	human	reverse	TGCAGATGGTAGCTCCTC
<i>IDO1</i>	mouse	forward	GGCTTTGCTCTACCACATCCAC
	mouse	reverse	TAGCCACAAGGACCCAGGG
<i>ACTB</i>	human	forward	CAAGAGATGGCCACGGCTGCTTCCA
	human	reverse	GCATGGAGTTGAAGGTAGTTTCG
<i>ACTB</i>	mouse	forward	GGCTGTATTCCTCCATCG
	mouse	reverse	CCAGTTGGTAACAATGCCATGT
<i>RPS18</i>	human	forward	GACAACAAGCTCCGTGAAGA
	human	reverse	AGAAGTGAGCGAGCCCTCTA
<i>GAPDH</i>	mouse	forward	ACGGATTTGGTCGTATTGGG
	mouse	reverse	CGCTCCTGGAAGATGGTGAT
<i>RPL37</i>	mouse	forward	TCTGTGGCAAGACCAAGATG
	mouse	reverse	GACAGCAGGCTTCTACTGG

Supplementary Table 2. Time (hh:mm) of treatment and blood sampling of the mice analyzed for plasma Trp and Kyn levels in Figure 4. The treatment and sampling within the subgroups of three mice (indicated by 1–3, 4–6 and 7–9) was performed with three-minute intervals, of which the time of the first treatment or sampling per subgroup is listed in the table.

Mouse	Vehicle			NTRC 3531-0			LM10		
	1–3	4–6	7–9	1–3	4–6	7–9	1–3	4–6	7–9
Treatment	11:15	10:00	10:18	10:00	09:15	10:20	11:06	10:09	10:57
5 min	11:20			10:05			11:11		
15 min		10:15				10:35		10:24	
30 min			10:48		09:45				11:27
1 h	12:15			11:00			12:06		
2 h			12:18			12:20			12:57
7 h		17:00			16:15			17:09	
12 h		22:00			21:15			22:09	
24 h			10:18			10:25			10:57

Supplementary Table 3. Raw data of the spatial memory test at day 7.

	Sham			Rotenone						
	Vehicle	NTRC D3	LM10 D3	Vehicle	NTRC D1	NTRC D2	NTRC D3	LM10 D1	LM10 D2	LM10 D3
DO	29	13	18	23	14	15	10	20	19	13
	15	23	20	18	19	25	24	7	14	19
	13	23	20	19	15	26	17	18	20	18
	19	19	20	18	14	13	15	18	19	10
	15	19	17	17	24	9	19	15	18	17
	13	12	9	16	19	23	10	21	14	22
	21	24	23	17	12	13	17	12	10	14
	15	19	15	19	16	14	15	18	20	16
	17	20	21	18	19	19	9	23	21	24
	10	15	15	17	20	16	11	13	10	19
NDO	9	7	9	7	6	5	2	4	7	5
	4	3	5	10	8	11	9	1	6	5
	4	11	7	6	4	6	6	10	6	4
	3	5	4	4	6	3	6	3	5	7
	4	5	4	8	6	3	4	8	7	5
	7	3	3	3	3	12	3	6	7	7
	7	9	6	4	4	4	2	4	1	5
	5	8	3	10	7	5	2	6	2	4
	9	3	6	3	4	5	3	7	9	9
	2	3	6	9	9	8	6	6	3	11
DO - NDO	20	6	9	16	8	10	8	16	12	8
	11	20	15	8	11	14	15	6	8	14
	9	12	13	13	11	20	11	8	14	14
	16	14	16	14	8	10	9	15	14	3
	11	14	13	9	18	6	15	7	11	12
	6	9	6	13	16	11	7	15	7	15
	14	15	17	13	8	9	15	8	9	9
	10	11	12	9	9	9	13	12	18	12
	18	17	15	15	15	14	6	16	12	15
	8	12	9	8	11	8	5	7	7	8

The data are reported as the time the animals interacted with the displaced objects (DO; calculated as DO[S5] - DO[S4]), the time they interacted with the non-displaced objects (NDO; calculated as NDO[S5] - NDO[S4]), and the difference between DO and NDO.

Supplementary Table 4. Raw data of the spatial memory test at day 14.

	Sham			Rotenone						
	Vehicle	NTRC D3	LM10 D3	Vehicle	NTRC D1	NTRC D2	NTRC D3	LM10 D1	LM10 D2	LM10 D3
DO	21	13	13	15	20	20	17	21	15	21
	9	14	13	20	20	13	21	21	19	27
	17	13	21	14	20	19	10	15	21	18
	23	18	16	25	10	16	7	12	14	14
	16	15	10	19	14	19	18	11	12	12
	19	10	14	16	13	20	15	20	16	17
	19	11	16	15	11	12	12	16	18	18
	14	22	20	17	17	12	13	13	17	11
	18	17	17	20	19	21	17	16	17	17
	15	24	15	22	16	16	16	20	15	18
NDO	3	5	7	8	7	6	2	10	4	10
	3	3	7	3	4	5	6	5	3	11
	10	7	2	10	10	6	5	1	7	4
	4	6	5	4	3	8	4	3	5	5
	5	5	2	8	6	4	8	6	7	7
	7	1	4	5	5	6	3	8	4	5
	9	1	9	3	4	4	2	6	8	8
	7	10	8	9	5	4	2	5	9	3
	5	9	6	8	8	7	6	5	6	6
	4	12	4	10	5	6	8	8	3	6
DO - NDO	18	8	6	6	13	14	15	11	11	11
	6	11	6	17	16	8	15	16	16	16
	7	6	19	4	10	13	5	14	14	14
	19	12	11	21	7	8	3	9	9	9
	11	10	8	11	8	15	10	5	5	5
	12	9	10	11	8	14	12	12	12	12
	10	10	7	12	7	8	10	10	10	10
	7	12	12	8	12	8	11	8	8	8
	13	8	11	12	11	12	11	11	11	11
	11	12	11	12	11	10	8	12	12	12

The data are reported as the time the animals interacted with the displaced objects (DO; calculated as DO[S5] - DO[S4]), the time they interacted with the non-displaced objects (NDO; calculated as NDO[S5] - NDO[S4]), and the difference between DO and NDO.

Supplementary Table 5. Raw data of the spatial memory test at day 28.

	Sham			Rotenone						
	Vehicle	NTRC D3	LM10 D3	Vehicle	NTRC D1	NTRC D2	NTRC D3	LM10 D1	LM10 D2	LM10 D3
DO	15	16	19	18	23	17	14	15	18	16
	15	24	16	11	16	16	18	14	18	13
	21	8	14	12	20	14	14	19	20	16
	10	15	16	15	18	20	12	23	17	25
	12	21	18	20	23	20	11	16	21	11
	20	24	16	22	21	10	22	16	19	12
	18	23	13	18	11	17	16	10	14	20
	17	10	10	18	21	16	14	17	21	13
	19	13	14	11	19	22	14	20	14	22
	18	18	16	12	25	19	10	19	15	15
NDO	6	4	8	7	6	8	3	9	3	6
	3	4	3	9	10	7	6	4	9	3
	3	2	9	7	6	5	8	6	6	10
	5	8	6	1	4	3	1	7	10	7
	6	4	10	4	4	7	2	6	6	5
	9	9	1	5	6	3	9	8	6	4
	10	6	6	5	3	7	6	2	3	8
	5	3	3	5	9	5	6	2	7	5
	7	7	6	5	3	7	5	6	5	6
9	5	6	3	6	4	1	9	2	9	
DO - NDO	9	12	11	11	17	9	11	6	15	10
	12	20	13	3	6	9	12	10	9	10
	18	6	5	5	14	9	6	13	14	6
	5	7	10	14	14	17	11	16	7	18
	6	17	8	16	19	13	9	10	15	6
	11	15	15	17	15	7	13	8	13	8
	8	17	7	13	8	10	10	8	11	12
	12	7	7	13	12	11	8	15	14	8
	12	6	8	6	16	15	9	14	9	16
9	13	10	9	19	15	9	10	13	6	

The data are reported as the time the animals interacted with the displaced objects (DO; calculated as DO[S5] - DO[S4]), the time they interacted with the non-displaced objects (NDO; calculated as NDO[S5] - NDO[S4]), and the difference between DO and NDO. The data reported for DO - NDO is used for the statistical analysis and is shown in Figure 5C.

Supplementary Table 6. Raw data of the spatial memory test at day 42.

	Sham			Rotenone						
	Vehicle	NTRC D3	LM10 D3	Vehicle	NTRC D1	NTRC D2	NTRC D3	LM10 D1	LM10 D2	LM10 D3
DO	13	18	18	4	0	4	12	8	8	20
	18	15	14	8	3	3	25	10	9	9
	16	16	17	10	10	9	11	7	6	16
	18	15	14	5	5	3	14	6	1	6
	12	14	21	2	3	2	14	9	2	13
	20	18	18	4	4	4	13	4	10	15
	19	16	18	4	6	7	15	5	11	12
	21	11	13	2	3	9	14	4	7	13
	15	16	15	6	2	6	14	6	4	12
	14	17	20	3	6	5	16	2	7	15
NDO	5	0	4	3	1	1	8	4	2	7
	2	2	0	4	0	0	9	6	5	5
	3	3	8	8	8	5	2	3	1	5
	7	4	1	2	4	2	5	5	0	2
	5	6	1	3	2	2	1	7	0	4
	10	2	2	2	4	2	5	1	6	7
	5	1	6	2	4	3	2	0	6	4
	10	1	2	0	1	7	4	2	5	7
	2	7	3	3	0	3	6	4	3	1
	7	3	2	1	0	4	5	1	4	6
DO - NDO	8	18	14	1	-1	3	4	4	6	13
	16	13	14	4	3	3	16	4	4	4
	13	13	9	2	2	4	9	4	5	11
	11	11	13	3	1	1	9	1	1	4
	7	8	20	-1	1	0	13	2	2	9
	10	16	16	2	0	2	8	3	4	8
	14	15	12	2	2	4	13	5	5	8
	11	10	11	2	2	2	10	2	2	6
	13	9	12	3	2	3	8	2	1	11
	7	14	18	2	0	1	11	1	3	9

The data are reported as the time the animals interacted with the displaced objects (DO; calculated as DO[S5] - DO[S4]), the time they interacted with the non-displaced objects (NDO; calculated as NDO[S5] - NDO[S4]), and the difference between DO and NDO. The data reported for DO - NDO is used for the statistical analysis and is shown in Figure 5C.

Supplementary Table 7. Overview of the *p*-values of the multiple comparisons presented in the denoted bar charts.

	Sham			Rotenone						
	Vehicle	NTRC D3	LM10 D3	Vehicle	NTRC D1	NTRC D2	NTRC D3	LM10 D1	LM10 D2	LM10 D3
<i>Spatial memory at day 42 (Figure 5C)</i>										
Sham	Vehicle	ns	ns	< 0.0001	< 0.0001	< 0.0001	ns	< 0.0001	< 0.0001	ns
	NTRC D3		ns	< 0.0001	< 0.0001	< 0.0001	ns	< 0.0001	< 0.0001	ns
	LM10 D3			< 0.0001	< 0.0001	< 0.0001	ns	< 0.0001	< 0.0001	ns
Rotenone	Vehicle			ns	ns	ns	< 0.001	ns	ns	ns
	NTRC D1					ns	< 0.001	ns	ns	ns
	NTRC D2						< 0.001	ns	ns	ns
	NTRC D3							< 0.0001	< 0.0001	ns
	LM10 D1								ns	ns
LM10 D2									ns	
LM10 D3										ns
<i>TH-positive cells (Figure 6A)</i>										
Sham	Vehicle	ns	ns	< 0.0001	< 0.0001	< 0.0001	< 0.0001	< 0.0001	< 0.0001	< 0.0001
	NTRC D3		ns	< 0.0001	< 0.0001	< 0.0001	< 0.0001	< 0.0001	< 0.0001	< 0.0001
	LM10 D3			< 0.0001	< 0.0001	< 0.0001	< 0.0001	< 0.0001	< 0.0001	< 0.0001
Rotenone	Vehicle			ns	ns	ns	< 0.01	ns	< 0.01	< 0.01
	NTRC D1					ns	< 0.05	ns	< 0.01	< 0.01
	NTRC D2						< 0.05	ns	< 0.01	< 0.01
	NTRC D3							< 0.01	< 0.01	< 0.001
	LM10 D1								< 0.01	< 0.001
LM10 D2								< 0.001	< 0.001	
LM10 D3									ns	

Supplementary Table 7. Continued.

	Sham			Rotenone						
	Vehicle	NTRC D3	LM10 D3	Vehicle	NTRC D1	NTRC D2	NTRC D3	LM10 D1	LM10 D2	LM10 D3
<i>Microglial cell volume (Figure 6C)</i>										
Sham	Vehicle	ns	ns	< 0.05	< 0.05	< 0.05	< 0.05	< 0.05	< 0.05	< 0.05
	NTRC D3		ns	< 0.05	< 0.05	< 0.05	< 0.05	< 0.05	< 0.05	< 0.05
	LM10 D3			< 0.05	< 0.05	< 0.05	< 0.05	< 0.05	< 0.05	< 0.05
Rotenone	Vehicle			ns	ns	ns	< 0.05	ns	< 0.05	< 0.05
	NTRC D1					ns	< 0.05	ns	ns	< 0.05
	NTRC D2						< 0.05	ns	ns	< 0.05
	NTRC D3							< 0.05	< 0.05	ns
	LM10 D1								ns	< 0.05
	LM10 D2									< 0.05
	LM10 D3									< 0.05
<i>Microglial occupancy index (Figure 6D)</i>										
Sham	Vehicle	ns	ns	< 0.05	ns	ns	ns	ns	ns	ns
	NTRC D3		ns	< 0.05	ns	ns	ns	ns	ns	ns
	LM10 D3			< 0.05	ns	ns	ns	ns	ns	ns
Rotenone	Vehicle			ns	ns	ns	ns	ns	ns	ns
	NTRC D1					ns	ns	ns	ns	ns
	NTRC D2						ns	ns	ns	ns
	NTRC D3							ns	ns	ns
	LM10 D1								ns	ns
	LM10 D2									ns
	LM10 D3									ns

Supplementary Table 7. Continued.

	Sham				Rotenone					
	Vehicle	NTRC D3	LM10 D3	Vehicle	NTRC D1	NTRC D2	NTRC D3	LM10 D1	LM10 D2	LM10 D3
<i>Intestinal transit (Figure 7A)</i>										
Sham	Vehicle	ns	ns	< 0.0001	ns	< 0.001	ns	ns	ns	ns
	NTRC D3		ns	< 0.001	ns	< 0.01	ns	ns	ns	ns
	LM10 D3			< 0.001	ns	< 0.001	ns	ns	ns	ns
Rotenone	Vehicle				ns	ns	< 0.0001	ns	< 0.0001	< 0.0001
	NTRC D1					ns	ns	ns	ns	ns
	NTRC D2						< 0.0001	ns	< 0.0001	< 0.0001
	NTRC D3							ns	ns	ns
	LM10 D3								ns	ns
<i>Colon length (Figure 7B)</i>										
Sham	Vehicle	ns	ns	< 0.0001	ns	ns	ns	ns	ns	ns
	NTRC D3		< 0.05	< 0.0001	< 0.01	< 0.01	ns	< 0.01	< 0.01	< 0.01
	LM10 D3			< 0.001	ns	ns	ns	ns	ns	ns
Rotenone	Vehicle				ns	ns	< 0.05	ns	< 0.05	< 0.05
	NTRC D1					ns	ns	ns	ns	ns
	NTRC D2						ns	ns	ns	ns
	NTRC D3							ns	ns	ns
	LM10 D1								ns	ns
LM10 D2									ns	
LM10 D3										ns

Supplementary Table 7. Continued.

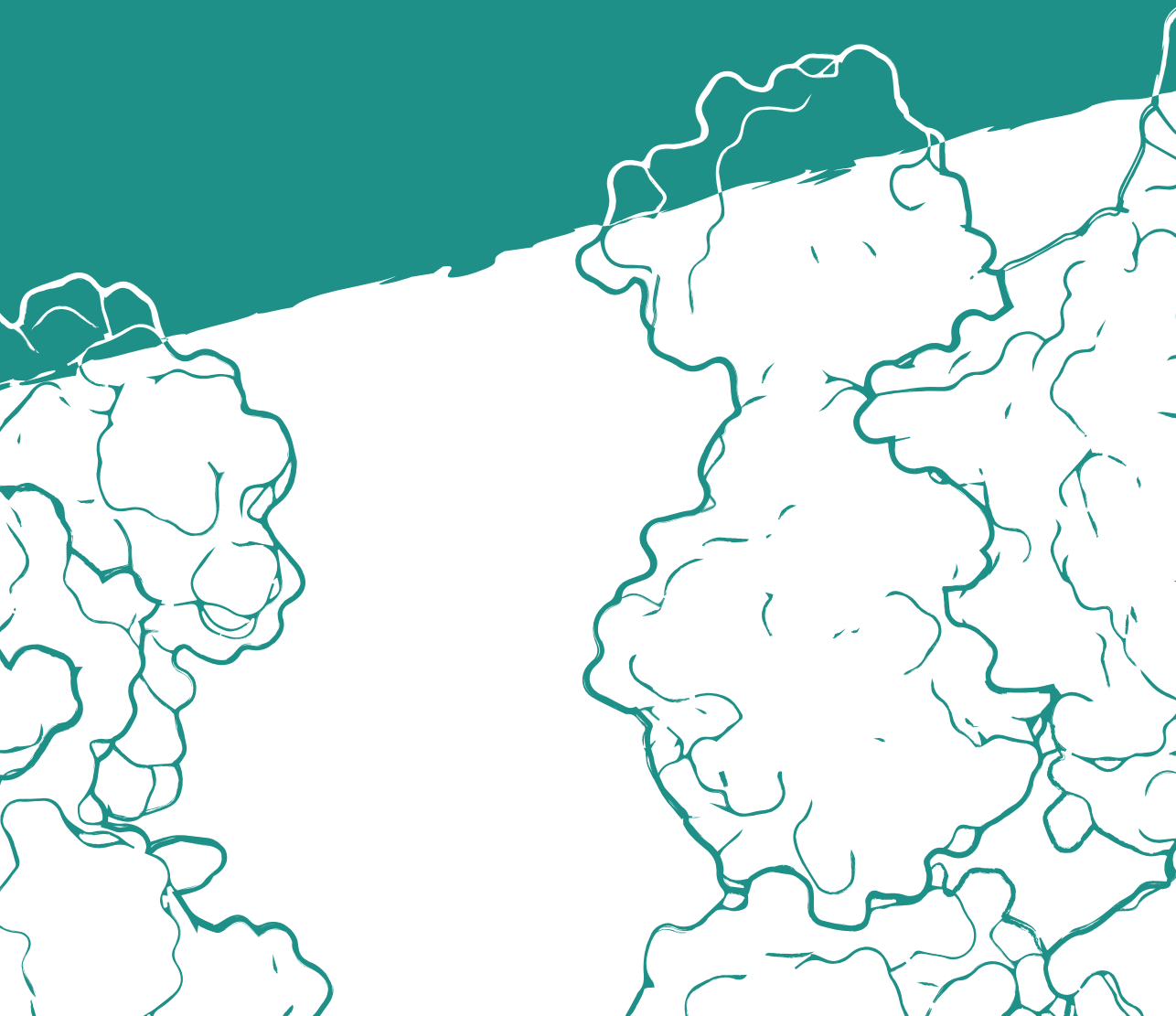
	Sham			Rotenone						
	Vehicle	NTRC D3	LM10 D3	Vehicle	NTRC D1	NTRC D2	NTRC D3	LM10 D1	LM10 D2	LM10 D3
<i>GFAP expression (Figure 7C)</i>										
Sham	Vehicle	ns	ns	<0.0001	<0.0001	ns	ns	<0.0001	<0.0001	ns
	NTRC D3		ns	<0.0001	<0.0001	ns	ns	<0.0001	<0.0001	ns
	LM10 D3			<0.0001	<0.0001	ns	ns	<0.0001	<0.0001	ns
Rotenone	Vehicle			ns	ns	<0.0001	<0.0001	ns	<0.001	<0.0001
	NTRC D1					ns	ns	ns	ns	ns
	NTRC D2						ns	<0.01	ns	ns
	NTRC D3							<0.01	ns	ns
	LM10 D1							<0.01	<0.01	<0.001
	LM10 D2									ns
	LM10 D3									ns
<i>α-Synuclein expression (Figure 7D)</i>										
Sham	Vehicle	ns	ns	<0.05	ns	ns	ns	ns	ns	ns
	NTRC D3		ns	<0.05	ns	ns	ns	ns	ns	ns
	LM10 D3			<0.05	ns	ns	ns	ns	ns	ns
Rotenone	Vehicle			<0.05	<0.05	<0.01	<0.01	<0.01	<0.001	<0.001
	NTRC D1					ns	ns	ns	ns	ns
	NTRC D2						ns	ns	ns	ns
	NTRC D3						ns	ns	ns	ns
	LM10 D1							ns	ns	ns
	LM10 D2								ns	ns
	LM10 D3									ns

ns, not significant.



Chapter 8

Summarizing discussion





Metabolic homeostasis of amino acids is fundamental to human health and development. Accordingly, altered amino acid metabolism has been found to contribute to the pathogenesis of a variety of diseases (introduced in **chapter 1**). In cancer, different amino acid-metabolizing enzymes are often aberrantly expressed, which promotes tumor growth and metastasis through suppression of the anti-tumor immune response (reviewed in **chapter 2**). These enzymes therefore serve as promising immunotherapeutic targets for the treatment of various cancer types. To date, however, clinical successes of amino acid-metabolizing enzyme inhibitors are still limited, and no inhibitor has yet been approved for clinical use in cancer treatment. For this reason, **chapters 3, 4, 5 and 6** of this thesis were aimed at contributing to the drug discovery process of inhibitors targeting these enzymes. In addition to cancer, dysregulated amino acid metabolism has also been implicated in the pathogenesis of neurodegenerative disorders. More specifically, an imbalance in tryptophan metabolism has been associated with Parkinson's disease, and **chapter 7** of this thesis was therefore aimed at exploring the inhibition of a tryptophan-metabolizing enzyme as a potential therapeutic strategy for its treatment. In the current chapter, the main findings of this thesis are summarized, discussed in light of the current literature, and supplemented with recommendations for extension and broadening of the described research.

Amino acid-metabolizing enzymes as targets for cancer immunotherapy

The emergence of cancer immunotherapy (introduced in **chapter 2**) has revolutionized the landscape of cancer treatment, with unprecedented clinical responses being observed in a subset of cancer patients.^{1,2} However, a variety of resistance mechanisms restricts the broader application of currently approved immunotherapies such as immune checkpoint inhibitors,^{3,4} urging for the development and implementation of innovative strategies to improve patient outcomes. As mentioned above, amino acid-metabolizing enzymes represent attractive targets for such strategies, and inhibitors of these enzymes are actively being developed and investigated in both preclinical and clinical settings. In **chapter 2**, the role of amino acid-metabolizing enzymes in cancer immune escape and the advances made in their therapeutic targeting was investigated through in-depth review of the available literature. Here, six amino acid-metabolizing enzymes were recognized for their potential contribution to immunosuppression in different cancer types, *i.e.*, glutaminase 1 (GLS1), arginase 1 (ARG1), inducible nitric oxide synthase (iNOS), indoleamine 2,3-dioxygenase 1 (IDO1), tryptophan 2,3-dioxygenase (TDO) and interleukin 4 induced 1 (IL4I1).

Among these enzymes, IDO1 and ARG1 have most comprehensively been investigated for their role in cancer immune escape. However, while extensive prognostic, preclinical and early-phase clinical evidence has been presented that supports a potential beneficial effect of IDO1 inhibition for cancer treatment, the most advanced IDO1 inhibitor, epacadostat, has failed in a large phase III clinical trial in patients with advanced melanoma. Regrettably, this has dampened the interest in this field of research, although efforts are also still being made to explore ways forward from this unforeseen predicament. This includes the development of inhibitors targeting both IDO1 and TDO, or compounds targeting downstream mediators, such as the aryl hydrocarbon receptor (AhR). Contrary to the vast amount of structurally diverse IDO1 inhibitors reported in the literature, the chemical space covered by reported ARG1 inhibitors is limited. Nonetheless, two distinctively-acting ARG1 inhibitors have already entered clinical evaluation, which should contribute to our understanding of the optimal mode of ARG1 inhibition as well as the translatability of this therapeutic strategy from mice to men. Distinctive from both ARG1 and IDO1, the enzymes GLS1 and iNOS have primarily been studied as targets for targeted anti-cancer therapies, rather than immunotherapy, based on their direct effect on cancer cells. However, both enzymes are also found to be capable of inducing immunosuppression. Therefore, further exploration of the consequences of GLS1 and iNOS inhibition on the immune cell compartment, both in preclinical models and cancer patients, is warranted to substantiate the promise of these enzymes as immunotherapeutic targets. Finally, IL411 has most recently been identified as a promising target for cancer immunotherapy. As exploration of the effects of IL411 inhibition in tumor models has only just commenced, it will be exciting to see where this immunotherapeutic target will take us in the future.

Role of amino acid-metabolizing enzymes in high-grade serous ovarian cancer

Although **chapter 2** has indicated that amino acid-metabolizing enzymes are promising targets for cancer treatment, cancer is a tremendously diverse disease, and therapeutic approaches that may work for some cancer types, may not yield the same effect in others. Therefore, involvement of the different amino acid-metabolizing enzymes in cancer immune escape must be evaluated on a per-cancer type basis. In **chapter 3**, it was explored which of the discussed amino acid-metabolizing enzymes may be aberrantly active and thereby serve a role in high-grade serous ovarian cancer. This cancer type is of particular interest, as it is characterized by a highly immunosuppressive tumor microenvironment⁵ that has allowed for insufficient modulation by immunotherapies previously approved for other cancer types.⁶

A targeted metabolomics approach was developed that enabled the determination of amino acid and corresponding metabolite levels as indirect measures of enzyme activity in liquid biopsies of high-grade serous ovarian cancer patients and healthy donors. This approach revealed an elevated metabolism of tryptophan in the cancer patients, for which metabolite levels in ascites provided a stronger indicator than those in plasma. Based on gene expression data and enzyme–substrate affinities,^{7,8} IDO1, rather than TDO, was suggested to serve as the major contributor to this metabolism. Contrarily, amino acid and metabolite levels in neither plasma nor ascites provided an indication for enhanced GLS1, ARG1 or iNOS activity in high-grade serous ovarian cancer patients. Instead, high levels of phenylalanine- and tyrosine-derived metabolites associated with IL4I1 activity were found in the ascites samples. These levels significantly correlated with those of the IL4I1 enzyme as well as with disease stage, suggesting a potential role for IL4I1 in disease progression.

The apparent absence of enhanced GLS1, ARG1 and iNOS activity in the patient samples suggests that inhibitors of these enzymes may not be beneficial for treatment of high-grade serous ovarian cancer. Importantly, however, it should be considered that amino acid and metabolite levels in liquid biopsies may not be the ideal indicator for aberrant activity of these enzymes. Nonetheless, analyses of amino acid and metabolite levels in epithelial ovarian tumor and normal ovary tissue biopsies confirm our findings.⁹ However, to truly rule out a contribution of GLS1, ARG1 or iNOS to this disease, this field of study would benefit from the immunohistochemical evaluation of expression of these enzymes in tumor tissue biopsies. On the other hand, it would be recommended to instead focus on IDO1 and IL4I1, which may both potentially serve as therapeutic targets for high-grade serous ovarian cancer based on the **chapter 3** findings.

Interestingly, IDO1 and IL4I1 share tryptophan as a common substrate, and tryptophan-derived metabolites produced by IDO1 and IL4I1 can act through similar immunosuppressive mechanisms.^{8,10} However, the apparent absence of elevated IL4I1-associated tryptophan metabolites in the patient samples suggests that IL4I1 may not be able to compete with IDO1 for this particular substrate, in line with their dissimilar tryptophan affinities.^{7,11} Instead, IL4I1 may serve a role in high-grade serous ovarian cancer through its metabolism of phenylalanine and/or tyrosine, although the immunosuppressive (or other) effects of these metabolisms still require further exploration. An elevated IL4I1 expression and activity in high-grade serous ovarian cancer may additionally cause IDO1 inhibition to be ineffective for restoration of anti-tumor immunity, since inhibition of IDO1 would restore tryptophan availability for generation of immunosuppressive metabolites by IL4I1. This would be in line with the general hypothesis that IL4I1 can serve as a potential resistance mechanism for IDO1 inhibition in different cancer types.⁸

The findings reported in **chapter 3** urge for their validation in a larger patient cohort, which should preferably be supplemented with patients harboring benign tumors and presenting with ascites. This should allow confirmation of the malignant nature of the observed IL4I1 expression and activity in high-grade serous ovarian cancer. Moreover, since metabolites associated with IDO1 and IL4I1 activity have previously been found elevated in epithelial ovarian tumor biopsies compared to normal ovary tissues,⁹ comparison of paired ascites and tumor biopsy samples could substantiate the use of ascites over tumor biopsies for biomarker evaluation. Finally, it will be interesting to explore the role of IL4I1 in other cancer types as well, as gene expression data indicate that IL4I1 is expressed in many different cancers.⁸ In the presented study, pleural effusions from non-small cell lung cancer patients have already hinted towards IL4I1 having an elevated activity in a subset of these patients, but it remains to be determined for which other cancer types the inhibition of IL4I1 may present a new avenue for disease treatment.

ARG1 inhibitors for cancer immunotherapy: exploring characteristics and creating new opportunities

While ARG1 activity does not appear elevated in high-grade serous ovarian cancer patients based on **chapter 3** results, this enzyme is still considered relevant for other cancer types. Accordingly, and as mentioned above, two ARG1 inhibitors have already entered clinical development for patients with different solid tumors.^{12,13} Notably, although CB-1158 (INCB001158; numidargistat) has been studied in the clinic since 2016, only very limited biochemical (and no biophysical) data was reported for this inhibitor, and a crystal structure of its binding to ARG1 had also not been revealed.¹² For this reason, **chapter 4** of this thesis was aimed at studying the mechanism of ARG1 inhibition by CB-1158, side-by-side with other well-known ARG1 inhibitors, from a biochemical, biophysical and structural perspective. The knowledge gained from this study is anticipated to support other drug discovery initiatives for small molecule ARG1 inhibitors.

ARG1 is a granulocyte-expressed arginine-metabolizing enzyme that, despite having a remarkably alkaline pH optimum (*i.e.*, pH 9 to 10),^{14,15} presumably exerts most of its tumor-associated activity at near-physiological pH. However, since it cannot be excluded that alkaline pH may at least have some relevance for the physiological function of ARG1 based on the alkaline pH levels observed during granulocyte function,¹⁶ ARG1 inhibition and binding by inhibitors was studied at both physiological pH 7.4 and alkaline pH 9.5 (or pH 7.0 and 9.0, respectively, in the case of structural studies). Characterization of the inhibitors ABH, nor-NOHA and CB-1158 in ARG1 biochemical inhibition, thermal shift and surface plasmon resonance assays revealed that the potency and/or binding strength of

each inhibitor was pH-dependent, albeit in varying directions. Furthermore, at physiological pH, likely being closest to the relevant pH for ARG1 function in tumor immunology, CB-1158 demonstrated the strongest effect among the inhibitors in all three assay types (*i.e.*, based on potency, thermal stabilization and binding affinity). CB-1158 additionally showed a considerably longer target residence time compared to the other inhibitors at this pH, which should favorably contribute to its pharmacokinetics. Together, these data have highlighted the superior biochemical and biophysical properties of CB-1158 compared to ABH and nor-NOHA, thereby backing its ongoing clinical development.

Several crystal structures of ARG1 in complex with inhibitors were also revealed in **chapter 4**. These structures indicated that the binding of boron-containing inhibitors (such as CB-1158 and ABH) can involve sodium-binding in the active site, which was not detected in previously published structures. Moreover, comparison of crystal structures at pH 7.0 and 9.0 suggested that a more symmetrical coordination structure of the active site manganese cluster may contribute to the increased activity of ARG1 at alkaline pH. Finally, the binding mode of the clinical-stage inhibitor CB-1158 in the ARG1 active site was visualized for the first time. Together with the slow association and dissociation kinetics observed for this inhibitor by surface plasmon resonance, the ARG1/CB-1158 crystal structure suggested that active site conformational plasticity may be involved in CB-1158 binding. Moreover, additional hydrogen-bond interactions to the ARG1 active site and an increased rigidity of the inhibitor compared to ABH were presumed to underly its favorable biochemical and biophysical characteristics.

Only recently, the chemical structure of a second ARG1 inhibitor under clinical evaluation, OATD-02, was disclosed,¹³ allowing investigators to now also include this inhibitor in any future ARG1-focused study. Although this disclosure was too late for inclusion of OATD-02 in the **chapter 4** study, the biochemical, biophysical and structural data shared upon its disclosure¹³ still enable comparison to the **chapter 4** results. Important to consider here, however, is that biochemical and biophysical data from different publications cannot always directly be compared. This is demonstrated by the discrepancies found in reported potencies and binding affinities for different ARG1 inhibitors (also when compared to the **chapter 4** data),^{12,17–21} indicating that assay conditions (and perhaps other factors) certainly matter. This underscores the importance of side-by-side comparison of inhibitors with relevant reference compounds, rather than sole comparison to literature values, which should only be allowed in the case of (near-)identical assay conditions.

In the case of OATD-02 and CB-1158, a direct comparison of biochemical potencies was already made in an earlier publication, revealing OATD-02 as the more potent ARG1 inhibitor.²¹ Comparison of the newly published data¹³ and the **chapter 4** results now

additionally demonstrates that OATD-02 has a higher affinity and longer target residence time compared to CB-1158 (under very similar assay conditions). Finally, comparison of the crystal structures of these inhibitors bound to ARG1 reveals both the overlapping and distinctive binding features of OATD-02¹³ and CB-1158 (**chapter 4**). Since there is always room for improvement, even when inhibitors for promising targets are already being evaluated in clinical trials, these crystal structures can serve as inspiration for the future rational design of small molecule ARG1 inhibitors with even further improved characteristics.

An alternative approach to drug discovery, however, is to unbiasedly screen large compound libraries for novel chemical starting points, which can potentially be optimized into inhibitors with unique characteristics. For ARG1, the largest portion of published inhibitors contains a boronic acid warhead that elegantly coordinates to the manganese cluster in the ARG1 active site (such as shown for CB-1158 and ABH in **chapter 4**).²² However, boronic acid derivatives are frequently associated with toxicity and stability issues.²³ Potent non-boronic acid-containing ARG1 inhibitors, on the other hand, are currently still scarce, with most of them remaining stuck at supra-micromolar potencies.^{24,25} Nonetheless, the relatively potent activity of nor-NOHA demonstrated in **chapter 4** indicates that potent ARG1 inhibitors without a boronic acid warhead can in fact be developed but may require the discovery of innovative scaffolds that are in general most readily obtained by high-throughput screening (HTS).

Since an HTS-compatible assay for biochemical ARG1 inhibition was not available yet, **chapter 5** was aimed at developing and optimizing such an assay and applying it in an HTS campaign to determine whether promising hits could be obtained. The novel, proprietary ARG1 activity assay was developed to have a homogeneous format and fluorescent read-out, and was extensively optimized with respect to various parameters. The assay pharmacology was validated by comparison of inhibitor potencies with those measured in an established, non-HTS-compatible assay, and its applicability for HTS was investigated by screening a 93,000-compound library of the Pivot Park Screening Centre on a fully automated robotic system. This demonstrated that the assay was sensitive, robust, and suitable for HTS. Unfortunately, the screen did not generate any hits that were worth pursuing for medicinal chemistry optimization.

Since publication of **chapter 5**, a second HTS campaign was also performed. During this campaign, the ESCulab compound collection of the European Lead Factory, comprising over 500,000 compounds,²⁶ was screened. However, while the ARG1 activity assay again demonstrated favorable performance statistics, no auspicious hits were obtained from this screen either (data not reported). Overall, the results from the two screens underline

the difficulty of targeting ARG1 with non-boronic acid-containing compounds (which likely comprise most, if not all, compounds in the libraries). Importantly, however, the hope for finding novel ARG1 inhibitors with unique chemotypes should not be lost, although it will evidently not be an easy pursuit. Beyond the screening of other large compound libraries with the reported assay, novel chemical starting points for ARG1 inhibitors may additionally be discovered from virtual or fragment-based screening, or by use of functional cell-based assays. Once optimization of such hits eventually succeeds, this may open up new perspectives for cancer treatment through ARG1 inhibition.

Advancing research on IDO1 inhibition: new inhibitor scaffold and pharmacological models

For IDO1, intense efforts have already been devoted to the development of small molecule inhibitors with diverse chemotypes and characteristics,²⁷ which is mainly owed to IDO1 having been considered a “hot target” for cancer immunotherapy during several years. Among those efforts are those described in **chapter 6** of this thesis, which were focused on the development and pharmacological characterization of a potent, selective and orally bioavailable IDO1 inhibitor, termed NTRC 3883-0, that was structurally distinct from priorly existing inhibitors.

NTRC 3883-0 was developed from an HTS hit towards a nanomolar-potent IDO1 inhibitor that, compared to epacadostat, demonstrated a higher biochemical selectivity over TDO. Moreover, in co-cultures of IDO1-overexpressing cells and lymphocytes, NTRC 3883-0 was found capable of abolishing the IDO1-induced suppression of cytotoxic T-cell proliferation. Syngeneic mouse studies were subsequently set out to determine whether this observation could be translated to the *in vivo* setting, *i.e.*, whether IDO1 inhibition by NTRC 3883-0 could inhibit tumor growth through reinvigoration of the anti-tumor immune response. Two different models were employed for this purpose, one with reported endogenous expression of *IDO1* upon colon tumor cell (CT26) engraftment²⁸ and another utilizing murine IDO1-overexpressing melanoma cells (B16F10-mIDO1) for tumor initiation.²⁹ Unfortunately, however, for neither model the effects of IDO1 expression and/or inhibition reported in the literature^{28,29} could be reproduced. Although the exact reasons for this are unclear, this indicates the lack of robustness of these models, which regrettably does not easily come to light in the literature due to the stigma on publishing negative results. Importantly, though, these results should be considered in light of the failure of the phase III clinical trial of epacadostat,³⁰ as they indicate that the progression towards human studies may not have been adequately supported by reproducible, preclinical *in vivo* data.

Although both murine models described in **chapter 6** failed as reproducible efficacy disease models, the B16F10-mIDO1-induced model was nonetheless found suitable for studying *in vivo* target modulation. These studies demonstrated that both NTRC 3883-0 and epacadostat were capable of significantly increasing intratumoral tryptophan levels and reducing intratumoral kynurenine levels, of which particularly the latter effect was also mirrored by changes in plasma levels. Notably, at equal dose and treatment interval, NTRC 3883-0 reached lower levels in both plasma and tumor compared to epacadostat, but still induced a stronger effect on kynurenine levels. While NTRC 3883-0 was not pursued for further clinical development, its favorable characteristics for targeting murine IDO1 compared to those of epacadostat suggest that it may instead serve as a useful tool compound for studying the role of IDO1 in murine disease models. Aside from epacadostat, the clinical candidate indoximod (1-methyl-D-tryptophan; D-1-MT) or its racemate (1-MT) is also often used to probe the role of IDO1 in different models. However, although indoximod is still occasionally being referred to as an IDO1 inhibitor, it in fact acts downstream of IDO1 through restoration of mTORC1 activity,³¹ and therefore opposes not only the effects of aberrantly expressed IDO1, but also those of TDO (and IDO2).

NTRC 3883-0 was also studied in *ex vivo* primary cancer cell cultures established from the malignant ascites of ovarian cancer patients. In **chapter 3**, as discussed earlier, IDO1 had been implicated in high-grade serous ovarian cancer based on the elevated metabolism of tryptophan into kynurenine observed in patient plasma and ascites. However, whereas that study was solely focused on cell-depleted samples, in **chapter 6**, cancer cells isolated from ovarian cancer ascites were studied for IDO1 expression, activity and inhibition. This was done to evaluate whether minimally-invasively collected ascites could be utilized for the identification of patients that may benefit from IDO1 inhibitor treatment, since other strategies applied in the clinic generally involve invasive surgical biopsy.³⁰ Although relatively low basal *IDO1* gene expression could be detected in most cell cultures, IDO1 expression and activity tremendously increased upon stimulation with IFN γ , an important effector molecule in the tumor microenvironment.³² Moreover, this tryptophan-metabolizing activity could successfully be inhibited by NTRC 3883-0 and epacadostat, suggesting that IDO1 inhibitors, when optimized and dosed appropriately, should have the same effect in the patients from which these cultures were derived.

Although the phase III failure of epacadostat (discussed in **chapter 2**) has meant a significant setback for the clinical development of IDO1 inhibitors, the modulation of tryptophan metabolism still holds promise as an immunotherapeutic approach for cancer treatment. In **chapter 2**, an elaborate perspective was already provided on how to move forward in this field, which included recommendations to extend preclinical research efforts, thoroughly investigate clinical samples, and improve the design of future clinical

trials. Based on **chapter 6** results, the first of these recommendations could benefit from the use of NTRC 3883-0 as a tool compound for murine studies, whereas the last recommendation may include the application of functional cell-based assays for the *a priori* selection of patients most likely to derive benefit from IDO1 inhibition. The innovative scaffold of NTRC 3883-0 and the described pharmacological models may additionally serve useful for future drug discovery initiatives, which are expected to regain focus if and when positive news from ongoing or future clinical trials emerges.

Targeting TDO in Parkinson's disease

Aside from cancer, imbalances in tryptophan metabolism have been implicated in the pathogenesis of Parkinson's disease, a currently incurable, progressive neurodegenerative disorder. Patients suffering from this disease have shown enhanced metabolism of tryptophan and an elevated ratio of neurotoxic to neuroprotective metabolites along the IDO1- and TDO-initiated kynurenine pathway.^{33–36} In invertebrate models, genetic or pharmacological inhibition of TDO has been demonstrated to ameliorate α -synuclein toxicity and neurodegeneration.^{37–39} Therefore, inhibition of TDO holds promise for the treatment of Parkinson's disease. In **chapter 7**, this therapeutic strategy was investigated in a rotenone-induced murine model of the disease, which allows assessment of the therapeutic effects not only on Parkinson's disease pathologies, but also on both motor and non-motor symptoms.^{40,41}

A brain-penetrable, small molecule TDO inhibitor (NTRC 3531-0) was developed by optimization of an HTS hit and was studied alongside the previously reported TDO inhibitor LM10^{42,43} in various *in vitro* assays. Moreover, pharmacokinetic and pharmacodynamic properties of both inhibitors were characterized *in vivo*, together demonstrating the superior character of NTRC 3531-0 compared to LM10 with respect to cellular potency, brain penetration and target modulation. In the murine rotenone model of Parkinson's disease, both inhibitors effectively reduced motor and cognitive dysfunction, and decreased rotenone-induced dopaminergic cell loss and neuroinflammation in the *substantia nigra*. Furthermore, treatment with either inhibitor reduced intestinal dysfunction, which was consistently accompanied by decreased glial cell marker expression and α -synuclein accumulation in the enteric nerves of the intestinal tract. Overall, the findings in this chapter have demonstrated the beneficial effects of TDO inhibition in a relevant animal model of Parkinson's disease.

Shortly after publication of **chapter 7**, another study also reported on the *in vivo* efficacy of TDO inhibition for treatment of Parkinson's disease, although in this case through

use of a dual IDO1/TDO inhibitor and a different murine model.⁴⁴ Notably, although IDO1 has not (yet) directly been implicated in Parkinson's disease, its expression has been found increased in the hippocampus of Alzheimer's disease patients,^{45,46} and IDO1 inhibition in models of this disease improved cognitive and behavioral symptoms.^{47,48} In a 1-methyl-4-phenyl-1,2,3,6-tetrahydropyridine (MPTP)-induced model of Parkinson's disease, the dual IDO1/TDO inhibitor reduced motor impairments, neurodegeneration and neuroinflammation.⁴⁴ Although it remains to be determined whether these beneficial effects mostly derive from inhibition of TDO or IDO1, these results underline the promise of targeting tryptophan metabolism for the treatment of Parkinson's disease.

To further substantiate the role of TDO in Parkinson's disease and its potential as a therapeutic target, follow-up studies are required in which pharmacological and/or genetic TDO inhibition is evaluated in other models of the disease, such as transgenic mouse models with α -synuclein overexpression or disease-associated mutations.⁴⁹ Such studies would also benefit from the use of TDO inhibitors with further improved characteristics, as there is still room for improvement in terms of potency, unbound brain concentration and other pharmacokinetic properties. Furthermore, it will be interesting to determine whether brain penetration is in fact required for TDO inhibitor efficacy, as the inhibitors described in **chapter 7** have shown clear effects on Parkinson's disease symptoms, despite displaying suboptimal or poor brain penetration. Similarly, in another study, a non-brain-penetrable inhibitor of a downstream kynurenine pathway enzyme (*i.e.*, kynurenine 3-monooxygenase) demonstrated efficacy in models of both Alzheimer's and Huntington's disease.⁵⁰ In this context, however, it is imperative to consider the integrity of the blood–brain barrier in the studied models, and to monitor both the central and peripheral levels of tryptophan and its metabolites in TDO inhibitor-treated mice. Importantly, studying the latter may additionally provide clues on the mechanism through which TDO inhibitor treatment positively affects both central and peripheral phenotypes of Parkinson's disease.

Beyond Parkinson's disease, dysregulated tryptophan metabolism has also been described for other neurodegenerative diseases, including Alzheimer's and Huntington's disease.⁵¹ Therefore, it will be of interest to explore TDO inhibition as therapeutic strategy for these diseases as well. Moreover, the fact that TDO and IDO1 present potential common therapeutic targets in cancer and neurodegenerative disease raises the question whether this may also be the case for the other amino acid-metabolizing enzymes described in this thesis. Interestingly, though, both arginine and ARG1 are suggested to protect, rather than damage, neurons in models of Parkinson's disease and amyotrophic lateral sclerosis (ALS),^{52–54} which may be related to the synthesis of neuroprotective polyamines downstream of ARG1 activity.⁵² Similarly, IL4I1 expression may be protective against multiple sclerosis,⁵⁵ although evidence is still scarce. In contrast, GLS and glutamate levels

are found to be increased in the brain and cerebrospinal fluid, respectively, of Alzheimer's disease patients,^{56,57} and inhibition of GLS inhibits glutamate excitotoxicity, thereby promoting neuronal survival.^{58,59} However, GLS1 is also critical for neurogenesis, which questions the desirability of GLS inhibition in patients with neurodegenerative disease.⁶⁰ Finally, excessive production of nitric oxide by iNOS-expressing activated glial cells is reported to induce neuronal death through different mechanisms, and has been implicated in a variety of neurodegenerative diseases.^{61,62} Therefore, inhibition of iNOS or downstream pathways could also serve as a valuable strategy for treatment of these diseases.

Concluding remarks

In conclusion, targeting amino acid-metabolizing enzymes holds considerable promise as a therapeutic strategy for treatment of both cancer and Parkinson's disease. Further drug discovery and development efforts are, however, needed to fully elucidate the therapeutic potential of these approaches. In this thesis, research has been described that aims at supporting both ongoing and future drug discovery initiatives within these fields of study. Highlights from this research include the identification of IDO1 and IL4I1 as potential targets for high-grade serous ovarian cancer and the pharmacological validation of TDO as a target for Parkinson's disease. A detailed characterization of both existing and novel inhibitors of ARG1, IDO1 and TDO was additionally provided in this thesis, which, together with a novel HTS-compatible assay and the described pharmacological models, should contribute to prospective pharmaceutical pursuits. Important to reiterate, though, is that there remains a strong need for continued research into the described therapeutic strategies, since only through continued efforts can these approaches be translated into effective treatments for patients.

References

1. Pardoll, D. M. The blockade of immune checkpoints in cancer immunotherapy. *Nat. Rev. Cancer* **12**, 252–64 (2012).
2. Chen, D. S. & Mellman, I. Elements of cancer immunity and the cancer-immune set point. *Nature* **541**, 321–30 (2017).
3. Sharma, P., Hu-Lieskovan, S., Wargo, J. A. & Ribas, A. Primary, adaptive, and acquired resistance to cancer immunotherapy. *Cell* **168**, 707–23 (2017).
4. O'Donnell, J. S., Teng, M. W. L. & Smyth, M. J. Cancer immunoediting and resistance to T cell-based immunotherapy. *Nat. Rev. Clin. Oncol.* **16**, 151–67 (2019).
5. Rodriguez, G. M., Galpin, K. J. C., McCloskey, C. W. & Vanderhyden, B. C. The tumor microenvironment of epithelial ovarian cancer and its influence on response to immunotherapy. *Cancers (Basel)* **10**, 242 (2018).
6. Gaillard, S. L., Secord, A. A. & Monk, B. The role of immune checkpoint inhibition in the treatment of ovarian cancer. *Gynecol. Oncol. Res. Pract.* **3**, 11 (2016).
7. Seegers, N. *et al.* High-throughput fluorescence-based screening assays for tryptophan-catabolizing enzymes. *J. Biomol. Screen.* **19**, 1266–74 (2014).
8. Sadik, A. *et al.* IL411 Is a metabolic immune checkpoint that activates the AHR and promotes tumor progression. *Cell* **182**, 1252–70.e34 (2020).
9. Fong, M. Y., McDunn, J. & Kakar, S. S. Identification of metabolites in the normal ovary and their transformation in primary and metastatic ovarian cancer. *PLoS One* **6**, e19963 (2011).
10. Opitz, C. A. *et al.* The therapeutic potential of targeting tryptophan catabolism in cancer. *Br. J. Cancer* **122**, 30–44 (2020).
11. Castellano, F., Prevost-Blondel, A., Cohen, J. L. & Molinier-Frenkel, V. What role for AHR activation in IL411-mediated immunosuppression? *Oncoimmunology* **10**, 1924500 (2021).
12. Steggerda, S. M. *et al.* Inhibition of arginase by CB-1158 blocks myeloid cell-mediated immune suppression in the tumor microenvironment. *J. Immunother. Cancer* **5**, 101 (2017).
13. Borek, B. *et al.* Arginase 1/2 inhibitor OATD-02: from discovery to first-in-man setup in cancer immunotherapy. *Mol. Cancer Ther.* **22**, 807–17 (2023).
14. Jenkinson, C. P., Grody, W. W. & Cederbaum, S. D. Comparative properties of arginases. *Comp. Biochem. Physiol. B. Biochem. Mol. Biol.* **114**, 107–32 (1996).
15. Zakalskiy, A. E. *et al.* Overexpression of (His)₆-tagged human arginase I in *Saccharomyces cerevisiae* and enzyme purification using metal affinity chromatography. *Protein Expr. Purif.* **81**, 63–8 (2012).
16. Levine, A. P., Duchon, M. R., de Villiers, S., Rich, P. R. & Segal, A. W. Alkalinity of neutrophil phagocytic vacuoles is modulated by HVCN1 and has consequences for myeloperoxidase activity. *PLoS One* **10**, e0125906 (2015).
17. Colleluori, D. M. & Ash, D. E. Classical and slow-binding inhibitors of human type II arginase. *Biochemistry* **40**, 9356–62 (2001).
18. Di Costanzo, L., Ilies, M., Thorn, K. J. & Christianson, D. W. Inhibition of human arginase I by substrate and product analogues. *Arch. Biochem. Biophys.* **496**, 101–8 (2010).
19. Golebiowski, A. *et al.* 2-Substituted-2-amino-6-boronohexanoic acids as arginase inhibitors. *Bioorg. Med. Chem. Lett.* **23**, 2027–30 (2013).
20. Van Zandt, M. C. *et al.* Discovery of *N*-substituted 3-amino-4-(3-boronopropyl)pyrrolidine-3-carboxylic acids as highly potent third-generation inhibitors of human arginase I and II. *J. Med. Chem.* **62**, 8164–77 (2019).
21. Grzybowski, M. M. *et al.* OATD-02 validates the benefits of pharmacological inhibition of arginase 1 and 2 in cancer. *Cancers (Basel)* **14**, 3967 (2022).

22. Borek, B., Gajda, T., Golebiowski, A. & Blaszczyk, R. Boronic acid-based arginase inhibitors in cancer immunotherapy. *Bioorg. Med. Chem.* **28**, 115658 (2020).
23. Ivanenkov, Y. A. & Chufarova, N. V. Small-molecule arginase inhibitors. *Pharm. Pat. Anal.* **3**, 65–85 (2014).
24. Ilies, M., Di Costanzo, L., North, M. L., Scott, J. A. & Christianson, D. W. 2-Aminoimidazole amino acids as inhibitors of the binuclear manganese metalloenzyme human arginase I. *J. Med. Chem.* **53**, 4266–76 (2010).
25. Gathiaka, S. *et al.* Discovery of non-boronic acid Arginase 1 inhibitors through virtual screening and biophysical methods. *Bioorg. Med. Chem. Lett.* **84**, 129193 (2023).
26. van Vlijmen, H., Ortholand, J.-Y., Li, V. M.-J. & de Vlieger, J. S. B. The European Lead Factory: an updated HTS compound library for innovative drug discovery. *Drug Discov. Today* **26**, 2406–13 (2021).
27. Cheong, J. E., Ekkati, A. & Sun, L. A patent review of IDO1 inhibitors for cancer. *Expert Opin. Ther. Pat.* **28**, 317–30 (2018).
28. Koblisch, H. K. *et al.* Hydroxyamide inhibitors of indoleamine-2,3-dioxygenase potently suppress systemic tryptophan catabolism and the growth of IDO-expressing tumors. *Mol. Cancer Ther.* **9**, 489–98 (2010).
29. Holmgaard, R. B. *et al.* Tumor-expressed IDO recruits and activates MDSCs in a Treg-dependent manner. *Cell Rep.* **13**, 412–24 (2015).
30. Long, G. V. *et al.* Epcadostat plus pembrolizumab versus placebo plus pembrolizumab in patients with unresectable or metastatic melanoma (ECHO-301/KEYNOTE-252): a phase 3, randomised, double-blind study. *Lancet. Oncol.* **20**, 1083–97 (2019).
31. Metz, R. *et al.* IDO inhibits a tryptophan sufficiency signal that stimulates mTOR: a novel IDO effector pathway targeted by D-1-methyl-tryptophan. *Oncoimmunology* **1**, 1460–8 (2012).
32. Gocher, A. M., Workman, C. J. & Vignali, D. A. A. Interferon- γ : teammate or opponent in the tumour microenvironment? *Nat. Rev. Immunol.* **22**, 158–72 (2022).
33. Ogawa, T. *et al.* Kynurenine pathway abnormalities in Parkinson's disease. *Neurology* **42**, 1702–6 (1992).
34. Widner, B., Leblhuber, F. & Fuchs, D. Increased neopterin production and tryptophan degradation in advanced Parkinson's disease. *J. Neural Transm.* **109**, 181–9 (2002).
35. Sorgdrager, F. J. H. *et al.* Age- and disease-specific changes of the kynurenine pathway in Parkinson's and Alzheimer's disease. *J. Neurochem.* **151**, 656–68 (2019).
36. Iwaoka, K. *et al.* Impaired metabolism of kynurenine and its metabolites in CSF of Parkinson's disease. *Neurosci. Lett.* **714**, 134576 (2020).
37. Campesan, S. *et al.* The kynurenine pathway modulates neurodegeneration in a *Drosophila* model of Huntington's disease. *Curr. Biol.* **21**, 961–6 (2011).
38. van der Goot, A. T. *et al.* Delaying aging and the aging-associated decline in protein homeostasis by inhibition of tryptophan degradation. *Proc. Natl. Acad. Sci. U. S. A.* **109**, 14912–7 (2012).
39. Breda, C. *et al.* Tryptophan-2,3-dioxygenase (TDO) inhibition ameliorates neurodegeneration by modulation of kynurenine pathway metabolites. *Proc. Natl. Acad. Sci. U. S. A.* **113**, 5435–40 (2016).
40. Betarbet, R. *et al.* Chronic systemic pesticide exposure reproduces features of Parkinson's disease. *Nat. Neurosci.* **3**, 1301–6 (2000).
41. Perez-Pardo, P. *et al.* Gut-brain and brain-gut axis in Parkinson's disease models: effects of a uridine and fish oil diet. *Nutr. Neurosci.* **21**, 391–402 (2018).
42. Dolusić, E. *et al.* Tryptophan 2,3-dioxygenase (TDO) inhibitors. 3-(2-(Pyridyl)ethenyl) indoles as potential anticancer immunomodulators. *J. Med. Chem.* **54**, 5320–34 (2011).
43. Pilotte, L. *et al.* Reversal of tumoral immune resistance by inhibition of tryptophan 2,3-dioxygenase. *Proc. Natl. Acad. Sci. U. S. A.* **109**, 2497–502 (2012).

44. Ning, X.-L. *et al.* X-ray structure-guided discovery of a potent, orally bioavailable, dual human indoleamine/tryptophan 2,3-dioxygenase (hIDO/hTDO) inhibitor that shows activity in a mouse model of Parkinson's disease. *J. Med. Chem.* **64**, 8303–32 (2021).
45. Guillemin, G. J., Brew, B. J., Noonan, C. E., Takikawa, O. & Cullen, K. M. Indoleamine 2,3 dioxygenase and quinolinic acid immunoreactivity in Alzheimer's disease hippocampus. *Neuropathol. Appl. Neurobiol.* **31**, 395–404 (2005).
46. Wu, W. *et al.* Expression of tryptophan 2,3-dioxygenase and production of kynurenine pathway metabolites in triple transgenic mice and human Alzheimer's disease brain. *PLoS One* **8**, e59749 (2013).
47. Yu, D. *et al.* The IDO inhibitor coptisine ameliorates cognitive impairment in a mouse model of Alzheimer's disease. *J. Alzheimers. Dis.* **43**, 291–302 (2015).
48. Fertan, E. *et al.* Effects of the novel IDO inhibitor DWG-1036 on the behavior of male and female 3xTg-AD mice. *Front. Pharmacol.* **10**, 1044 (2019).
49. Chesselet, M.-F. & Richter, F. Modelling of Parkinson's disease in mice. *Lancet. Neurol.* **10**, 1108–18 (2011).
50. Zwilling, D. *et al.* Kynurenine 3-monooxygenase inhibition in blood ameliorates neurodegeneration. *Cell* **145**, 863–74 (2011).
51. Maddison, D. C. & Giorgini, F. The kynurenine pathway and neurodegenerative disease. *Semin. Cell Dev. Biol.* **40**, 134–41 (2015).
52. Lee, J., Ryu, H. & Kowall, N. W. Motor neuronal protection by L-arginine prolongs survival of mutant SOD1 (G93A) ALS mice. *Biochem. Biophys. Res. Commun.* **384**, 524–9 (2009).
53. Lewis, K. E. *et al.* Microglia and motor neurons during disease progression in the SOD1G93A mouse model of amyotrophic lateral sclerosis: changes in arginase1 and inducible nitric oxide synthase. *J. Neuroinflammation* **11**, 55 (2014).
54. Hami, J. *et al.* Beneficial effects of L-arginine on 1-methyl-4-phenyl-1,2,3,6-tetrahydropyridine-induced neuronal degeneration in substantia nigra of Balb/c mice. *Adv. Biomed. Res.* **5**, 140 (2016).
55. Psachoulia, K. *et al.* IL41 augments CNS remyelination and axonal protection by modulating T cell driven inflammation. *Brain* **139**, 3121–36 (2016).
56. Burbaeva, G. S. *et al.* Glutamate metabolizing enzymes in prefrontal cortex of Alzheimer's disease patients. *Neurochem. Res.* **30**, 1443–51 (2005).
57. Madeira, C. *et al.* Elevated glutamate and glutamine levels in the cerebrospinal fluid of patients with probable Alzheimer's disease and depression. *Front. Psychiatry* **9**, 561 (2018).
58. Thomas, A. G. *et al.* Small molecule glutaminase inhibitors block glutamate release from stimulated microglia. *Biochem. Biophys. Res. Commun.* **443**, 32–6 (2014).
59. Fuchsberger, T. *et al.* A β induces excitotoxicity mediated by APC/C-Cdh1 depletion that can be prevented by glutaminase inhibition promoting neuronal survival. *Sci. Rep.* **6**, 31158 (2016).
60. Wang, Y., Huang, Y., Zhao, L., Li, Y. & Zheng, J. Glutaminase 1 is essential for the differentiation, proliferation, and survival of human neural progenitor cells. *Stem Cells Dev.* **23**, 2782–90 (2014).
61. Yuste, J. E., Tarragon, E., Campuzano, C. M. & Ros-Bernal, F. Implications of glial nitric oxide in neurodegenerative diseases. *Front. Cell. Neurosci.* **9**, 322 (2015).
62. Tewari, D. *et al.* Role of nitric oxide in neurodegeneration: function, regulation, and inhibition. *Curr. Neuropharmacol.* **19**, 114–26 (2021).





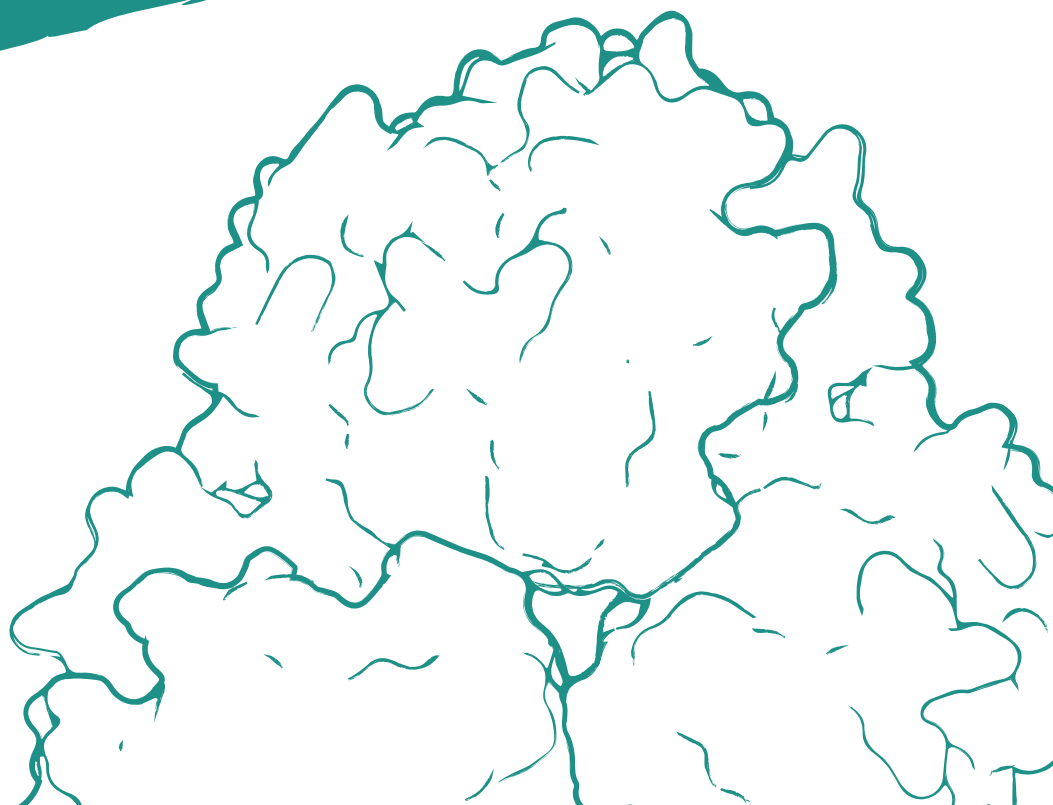
Appendices

Nederlandse samenvatting

Curriculum vitae

List of publications

Dankwoord



Nederlandse samenvatting

*Dit hoofdstuk geeft een vereenvoudigde Nederlandse samenvatting van het onderzoek dat in dit proefschrift beschreven is. Voor een meer gedetailleerde Engelse samenvatting en een uitgebreide discussie van de onderzoeksresultaten, zie **hoofdstuk 8** van dit proefschrift.*

In alle levende wezens wordt continu gestreefd naar een stabiel evenwicht van alle activiteiten die inwendig plaatsvinden. Het behoud van dit evenwicht, genaamd *homeostase*, is essentieel voor een normaal functioneren en verhoogt de overlevingskans. Homeostase wordt gereguleerd door een complex netwerk van uiteenlopende processen en vindt plaats binnen alle niveaus van het organisme—van cel tot orgaan tot organisme als geheel. Verscheidene invloeden kunnen deze homeostase verstoren, waaronder veroudering, een tekort aan voedingsstoffen en blootstelling aan gifstoffen. Wanneer een dergelijke verstoring van de homeostase voor een langere periode aanhoudt, kan dit uiteindelijk leiden tot ziekte.

Eén van de cruciale aspecten van homeostase is de evenwichtige aanmaak en omzetting van aminozuren, ook wel het *aminozuur metabolisme* genoemd. Aminozuren zijn de primaire bouwstenen van alle eiwitten in het lichaam en dienen daarnaast als grondstoffen voor een tal van andere belangrijke moleculen, zoals signaalstoffen, energiedragers en bouwstenen van het DNA. Om de niveaus van deze moleculen op pijl te houden, dient er ten alle tijden voldoende omzetting van aminozuren plaats te vinden. Tegelijkertijd is het echter van belang dat er geen overproductie van dergelijke moleculen plaatsvindt, aangezien dit ook nadelige gevolgen kan hebben.

Verstoringen in het aminozuur metabolisme kunnen een rol spelen bij de ontwikkeling van verschillende aandoeningen, waaronder kanker, ziekten van het zenuwstelsel, harten- en vaatziekten, en auto-immuunziekten. In dit proefschrift worden twee van deze ziekten onderzocht, namelijk *kanker* en *de ziekte van Parkinson*.¹ Hoewel deze ziekten ogenschijnlijk niets met elkaar te maken hebben, hebben ze wel degelijk een aantal overeenkomsten. Beide zijn leeftijd gerelateerde ziekten en hebben vaak te maken met een ontregeling van het immuunsysteem. Daarnaast kunnen beide ziekten mogelijk behandeld worden met medicijnen die aangrijpen op eiwitten die betrokken zijn bij de omzetting van aminozuren. Deze eiwitten worden *aminozuur-metaboliserende enzymen* genoemd,² en vormen de rode draad in dit proefschrift.

¹ *De ziekte van Parkinson* behoort tot de ziekten van het zenuwstelsel, of nog specifieker tot de zogeheten neurodegeneratieve ziekten.

² *Enzymen* vormen een klasse van eiwitten die chemische reacties in lichaam mogelijk maken of versnellen. In het geval van *aminozuur-metaboliserende enzymen* gaat het daarbij om de chemische omzetting van aminozuren in andere moleculen.

In het vervolg van deze samenvatting wordt eerst de rol van aminozuur-metaboliserende enzymen in kanker uitgelegd, wat gevolgd wordt door een samenvatting van de onderzoeksresultaten die in het kader hiervan zijn verkregen. Daarna wordt ingegaan op het verband tussen aminozuur-metaboliserende enzymen en de ziekte van Parkinson, en op het onderzoek dat hiernaar is uitgevoerd.

Aminozuur-metaboliserende enzymen als aangrijpingspunten voor kankerimmunotherapie

Met ongeveer tien miljoen sterfgevallen per jaar is kanker één van de belangrijkste doodsoorzaken wereldwijd. Kanker is een gevarieerde en dynamische ziekte waar een complexe wisselwerking van verschillende factoren aan ten grondslag ligt, resulterend in een ongeremde groei van abnormale cellen. Eén van de belangrijkste kenmerken van kankercellen is dat zij vaak in staat zijn om het immuunsysteem te omzeilen, welke normaliter de kwaadaardige cellen herkent en vernietigt. Hoewel dit een kwalijke eigenschap van kanker is, aangezien het de kankercellen vrije baan geeft om te vermenigvuldigen, geeft dit echter ook een mogelijke strategie om deze ziekte te behandelen. Deze innovatieve strategie staat bekend als *kankerimmunotherapie*, en heeft als doel om het immuunsysteem te stimuleren tot het aanvallen van de ongewenste cellen. Dit in tegenstelling tot andere kankertherapieën, die doorgaans direct op de kankercellen zelf zijn gericht.

Bij de omzeiling van het immuunsysteem kunnen verschillende factoren betrokken zijn, die allen een mogelijk aangrijpingspunt vormen voor de ontwikkeling van nieuwe medicijnen. Hiertoe behoren onder meer verschillende aminozuur-metaboliserende enzymen, waaronder enzymen die de aminozuren *glutamine*, *arginine* of *tryptofaan* omzetten in andere moleculen, ook wel *metabolieten* genoemd. Deze enzymen worden regelmatig in (sterk) verhoogde mate door tumoren geproduceerd, met als gevolg een abnormaal hoge omzetting van de betrokken aminozuren. Hier kan een tumor vaak direct van profiteren, aangezien hierbij geproduceerde metabolieten de groei en verspreiding van kankercellen kunnen bevorderen. Daarnaast kan dit ingrijpende gevolgen hebben voor nabijgelegen cellen van het immuunsysteem, ofwel *immuuncellen*. Deze cellen kunnen hierdoor namelijk een tekort aan bovengenoemde aminozuren ervaren, waardoor de groei en functionaliteit van de cellen wordt geremd. Daarnaast kunnen ze ook bloot worden gesteld aan grote hoeveelheden van gevormde metabolieten, die weer op andere wijze de immuuncellen kunnen remmen. Het resultaat van beide effecten is dus hetzelfde: een slecht- of niet-functionerend immuunsysteem, dat vaak een snelle tumorgroei tot gevolg heeft.

Gezien de rol van aminozuur-metaboliserende enzymen in de onderdrukking van immuunreacties tegen tumoren, is de remming van dit soort enzymen een veelbelovende benadering voor kankerimmunotherapie. Door de jaren heen is er daarom al veel

onderzoek gedaan naar deze enzymen, maar tot op heden heeft dit nog niet geleid tot een goedgekeurd medicijn voor kankerpatiënten. Dit geeft aan dat er nog een weg te gaan is in de ontwikkeling van effectieve therapieën. In dit proefschrift, en specifiek in **hoofdstukken 2, 3, 4, 5 en 6**, is daarom beoogd om aan deze ontwikkeling bij te dragen.

Op dit moment is van zes aminozuur-metaboliserende enzymen bekend dat ze in verhoogde mate aanwezig kunnen zijn in tumoren én een onderdrukking van het immuunsysteem kunnen veroorzaken. Dit betreft:

- een glutamine-metaboliserend enzym:
 - *glutaminase 1 (GLS1)*
- twee arginine-metaboliserende enzymen:
 - *arginase 1 (ARG1)*
 - *induceerbaar stikstofmonoxide synthase (Eng: inducible nitric oxide synthase; iNOS)*
- drie tryptofaan-metaboliserende enzymen:
 - *indoleamine 2,3-dioxygenase (IDO1)*
 - *tryptofaan 2,3-dioxygenase (TDO)*
 - *interleukine 4 geïnduceerd 1 (Eng: interleukin 4 induced 1; IL4I1)*

In **hoofdstuk 2** van dit proefschrift is literatuuronderzoek gedaan naar wat er al bekend is over deze enzymen, specifiek met betrekking tot kanker. Hierbij is onder meer gekeken naar de wijze waarop de enzymen op molecuul-, cel- en organismeniveau het immuunsysteem en de groei van tumoren kunnen beïnvloeden, en naar de stappen die al zijn gemaakt in de ontwikkeling van hierop aangrijpende medicijnen.

Uit bovengenoemd literatuuronderzoek blijkt dat aminozuur-metaboliserende enzymen inderdaad veelbelovende aangrijpingspunten zijn voor kankertherapieën. Het is echter van belang om te realiseren dat kanker een gevarieerde en dynamische ziekte is, en dat een bepaalde therapie daarom vaak maar voor een (klein) deel van de kankervormen effectief is. Daarom is het essentieel dat er per kankervorm wordt onderzocht welke potentiële aangrijpingspunten wel óf niet relevant zijn, zodat medicijnontwikkeling gericht en effectief uitgevoerd kan worden. In **hoofdstuk 3** is om deze reden onderzocht welke van de zes eerdergenoemde enzymen een verhoogde activiteit laat zien in *eierstokkanker*, en daarmee een potentieel doelwit voor behandeling kan zijn. Onderzoek naar dit type kanker is van groot belang, omdat de behandelopties hiervoor momenteel nog erg beperkt zijn. Gedurende de studie zijn van verschillende eierstokkankerpatiënten bloed- en buikvochtmonsters afgenomen, waarin vervolgens de niveaus van relevante aminozuren en hieruit gevormde metabolieten zijn bepaald. Hierbij is gevonden dat de metabolieten van sommige aminozuren verhoogd aanwezig zijn in het buikvocht van patiënten ten opzichte van hun bloed. Dit geeft aan dat het gebruik van buikvochtmonsters voor dit type onderzoek van verhoogde waarde kan zijn ten opzichte van het gebruik van bloedmonsters.

De meetwaarden zijn vervolgens gecombineerd met de medische data van de patiënten, waaruit naar voren is gekomen dat de enzymen IDO1 en IL4I1 waarschijnlijk betrokken zijn bij het ziekteproces. Zo is de omzetting van tryptofaan door IDO1 verhoogd in monsters van patiënten ten opzichte van gezonde donoren, en nemen de niveaus van metaboliëten gevormd door IL4I1 toe naar mate de ziekte verergert. Het remmen van deze enzymen zou daarom een effectieve strategie kunnen zijn voor behandeling van patiënten met eierstokkanker, en dient in vervolgstudies uitgebreider onderzocht te worden.

Voor het enzym ARG1, evenals de enzymen GLS1, iNOS en TDO, is er geen duidelijke aanwijzing gevonden voor een betrokkenheid bij de ontwikkeling van eierstokkanker. Andere gepubliceerde onderzoeken geven echter aan dat deze enzymen wél relevant kunnen zijn voor andere kankervormen. In **hoofdstuk 4** van dit proefschrift is gericht onderzoek gedaan naar ARG1. Door de jaren heen zijn er al een aantal verschillende *remmers* ontwikkeld voor dit enzym,³ waarvan één al enkele jaren in een breed scala aan kankerpatiënten wordt getest, en een ander pas sinds kort in een eerste patiëntenstudie wordt onderzocht. Opvallend hierbij is dat er voor de eerstgenoemde remmer, genaamd *CB-1158*, vóór aanvang van dit onderzoek slechts beperkte informatie beschikbaar was over de wijze waarop deze op molecuulniveau het enzym remt. Hierbij kan gedacht worden aan informatie over hoe efficiënt het enzym wordt geremd, hoe sterk de remmer aan het enzym bindt, en op welke manier de remmer zich vasthecht aan het enzym. In dit hoofdstuk is daarom beoogd om meer inzicht in deze zaken te krijgen, om andere initiatieven voor het ontwikkelen van ARG1-remmers te ondersteunen. Ondanks dat er inmiddels al twee ARG1-remmers op patiënten wordt getest, is er namelijk altijd nog ruimte voor verbetering, zoals verhoging van effectiviteit en vermindering van bijwerkingen. In verschillende typen experimenten is de remmer CB-1158 vergeleken met andere bekende remmers van het enzym, waarbij ook nadrukkelijk rekening is gehouden met de pH, ofwel zuurgraad, tijdens de experimenten. ARG1 is namelijk het meest actief bij een verhoogde pH, maar deze pH komt slechts op specifieke plekken in het lichaam voor. Om deze reden zijn de karakteristieken van CB-1158 en de andere remmers onderzocht bij zowel een neutrale als verhoogde pH. Hieruit is gebleken dat CB-1158 over het algemeen een uitstekende remmer van het enzym is, wat daarmee steun biedt voor de lopende klinische ontwikkeling van deze remmer. Daarnaast is voor het eerst een ruimtelijke (of driedimensionale) weergave van het remmer-gebonden enzym gepubliceerd, dat waardevolle inzichten geeft in de factoren die verantwoordelijk zijn het gunstige karakter van de remmer.

³ *Remmers* zijn moleculen die in staat zijn om de activiteit van een bepaald enzym te verlagen of stil te leggen. Voor elk enzym kunnen er veel verschillende remmers bestaan, al is vaak slechts een fractie hiervan geschikt om uiteindelijk als medicijn te dienen.

Hoewel bestaande remmers van ARG1 veel inspiratie kunnen bieden voor de ontwikkeling van nieuwe remmers met verbeterde eigenschappen, is er ook een andere strategie om tot innovatieve medicijnen te komen. Dit gebeurt door middel van *geautomatiseerde screening* van omvangrijke bibliotheken van kleine, synthetische moleculen.⁴ Hierbij wordt onderzocht welke moleculen in staat zijn om een enzym van interesse te remmen. Het resultaat hiervan is een verzameling van *kandidaat-moleculen*, ofwel *hits*, die allen een remmende werking hebben. Deze moleculen zijn nog niet direct geschikt om aan patiënten toe te dienen, maar vormen wel een mogelijk startpunt voor de ontwikkeling van remmers die uiteindelijk wél gebruikt zouden kunnen worden voor therapieën. Voor het uitvoeren van een screeningstudie is er echter wel een test nodig die compatibel is met het systeem waarop zo'n studie uitgevoerd wordt, en voor ARG1 was deze nog niet beschikbaar. Om deze reden is er in het onderzoek beschreven in **hoofdstuk 5** een nieuwe test ontwikkeld die geschikt is voor deze toepassing. Deze test is eerst uitgebreid geoptimaliseerd, waarna bevestigd is dat de test vergelijkbare resultaten oplevert als een andere, veelgebruikte test die niet geschikt is voor screening-studies. Vervolgens is de test gebruikt om een bibliotheek van 93.000 stoffen te screenen op moleculen die ARG1 remmen. Dit heeft aangetoond dat de test ook tijdens een omvangrijke studie zijn gevoeligheid en betrouwbaarheid behoudt. Desondanks heeft de studie geen kandidaat-moleculen opgeleverd die geschikt zijn voor verdere ontwikkeling tot nieuwe medicijnen, waarschijnlijk omdat er maar weinig moleculen bestaan die goed aan dit enzym kunnen binden. De geteste 93.000 moleculen vormen echter maar een minuscule fractie van de geschatte 10^{60} (ofwel een miljoen triljoen triljoen triljoen) moleculen die over geneesmiddelachtige eigenschappen beschikken. Daarom brengt de test alsnog nieuwe mogelijkheden met zich mee om in toekomstige studies, bij voorkeur met grotere molecuul bibliotheken, nieuwe startpunten te vinden die succesvol vertaald kunnen worden naar effectieve kankermedicatie.

In tegenstelling tot ARG1 zijn er voor het enzym IDO1 al heel veel verschillende remmers ontwikkeld en gepubliceerd. Deze remmers zijn veelal van diverse chemische opbouw, en kunnen ook sterk verschillen in hun eigenschappen. De reden dat er al veel remmers voor IDO1 zijn ontwikkeld, is dat dit enzym gedurende meerdere jaren als één van de belangrijkste aangrijpingspunten voor kankerimmunotherapie is gezien. In lijn met deze visie, is in het onderzoek beschreven in **hoofdstuk 6** ook een nieuwe remmer van IDO1 ontwikkeld en uitgebreid gekarakteriseerd. Hierbij is beoogd om een remmer te ontwikkelen die krachtig is, geen andere vergelijkbare eiwitten remt, goed door het lichaam opgenomen kan worden, en niet te snel afgebroken wordt. Het startpunt van dit

⁴ *Geautomatiseerde screening* van chemische bibliotheken wordt uitgevoerd met behulp van geavanceerde robotsystemen, waarmee elk van de duizenden tot miljoenen moleculen in een bibliotheek individueel getest kan worden. De verwerkingssnelheid van een geautomatiseerde screen ligt meestal op tien- tot honderdduizenden moleculen per dag.

proces was een eerder uitgevoerde screening-studie, waarvan een gevonden kandidaat-molecuul heeft geleid tot de bouw van een reeks verschillende moleculen. Na toetsing van deze moleculen op efficiënte remming van IDO1, is er één hiervan geselecteerd voor uitgebreidere karakterisering, namelijk *NTRC 3883-0*. Deze remmer is in verschillende testen vergeleken met de veelbeschreven IDO1-remmer *epacadostat*, welke één van de meest ver ontwikkelde remmers van het enzym is. Hieruit is gebleken dat *NTRC 3883-0* zich voornamelijk gunstig onderscheidt van *epacadostat* door een veel lagere remming te geven van TDO, een eerdergenoemd enzym dat veel overeenkomsten vertoont met IDO1. Verder is aangetoond dat *NTRC 3883-0* de onderdrukking van geïsoleerde immuuncellen door IDO1 teniet kan doen, en dat het de activiteit van IDO1 ook in een muizenmodel van huidkanker kan remmen. Tot slot is de remmer ook op kankercellen afkomstig van eierstokkankerpatiënten getest. Dit heeft een efficiënte remming van het enzym in de cellen laten zien. Over het algemeen is *NTRC 3883-0* dus een goede remmer van IDO1, al is dit op zichzelf nog niet voldoende om geschikt te zijn als medicijn voor patiënten. Ondanks dat de remmer in muizen relatief langzame afbraak laat zien, geven voorspellingen aan dat de remmer in mensen waarschijnlijk te snel afgebroken zal worden. Om die reden moet *NTRC 3883-0* op dit moment dan ook vooral gezien worden als een innovatief chemisch molecuul dat, samen met de beschreven experimentele modellen, bij kan dragen aan de ontwikkeling van IDO1-remmers die wél alle gewenste eigenschappen hebben.

Tryptofaan metabolisme in de ziekte van Parkinson

Vergeleken met kanker treedt de ziekte van Parkinson wereldwijd minder vaak op. Toch zijn er ruim zes miljoen mensen die met deze ziekte leven. De ziekte van Parkinson is een ernstige *neurodegeneratieve ziekte*, oftewel een ziekte aan het zenuwstelsel waarbij in de loop der jaren steeds meer zenuwcellen afsterven. Patiënten met deze ziekte ervaren verschillende bewegingsklachten, maar kunnen daarnaast ook last hebben van onder meer depressie, achteruitgang van het leervermogen en verstoring van de maag-darmfunctie. Tot op heden is de ziekte van Parkinson ongeneeslijk, en zorgt de meest gebruikte medicatie slechts voor een onderdrukking van de bewegingsklachten. Om deze reden is er een dringende behoefte aan de ontwikkeling van nieuwe medicijnen die het ziekteverloop kunnen veranderen, of die zowel de bewegingsklachten als de andere symptomen kunnen aanpakken.

De oorzaak van de ziekte van Parkinson ligt vaak bij een complex samenspel van genetische aanleg, veroudering en omgevingsinvloeden, dat op molecuul- en celniveau resulteert in een aantal typerende kenmerken. Hiertoe behoren onder meer de samenklontering van het eiwit *α -synucleïne*, een afname in het aantal zenuwcellen, en een ontsteking van het zenuwweefsel. Daarnaast wordt gedacht dat een onbalans in het metabolisme van tryptofaan bij kan dragen aan ontwikkeling van de ziekte. Een argument hiervoor is dat er

in patiënten afwijkende niveaus worden aangetroffen van metabolieten afkomstig van dit aminozuur. Daarnaast leidt remming of complete uitschakeling van betrokken enzymen, waaronder het eerdergenoemde TDO, tot gunstige effecten in ongewervelde organismen (wormen en fruitvliegjes) waarin de ziekte van Parkinson wordt nagebootst. Om deze redenen zou medicatie die aangrijpt op het metabolisme van tryptofaan, en daarmee de onbalans tegen kan gaan, dus potentieel van grote waarde kunnen zijn voor patiënten die met deze ziekte leven.

In **hoofdstuk 7** van dit proefschrift is specifiek het remmen van TDO geëvalueerd als een strategie voor de behandeling van de ziekte van Parkinson. Hiervoor is een nieuwe remmer van TDO ontwikkeld, genaamd *NTRC 3531-0*, die als eigenschap heeft dat deze in de hersenen door kan dringen. Dit is van belang, omdat de ziekte zich voor een groot deel in de hersenen afspeelt. Net als de eerder beschreven IDO1-remmer, is de TDO-remmer ontwikkeld vanuit een kandidaat-molecuul verkregen door middel van screening. Vervolgens is de remmer, samen met een eerder gerapporteerde TDO-remmer (*LM10*), bestudeerd in een reeks verschillende testen. Hiermee is onder andere bepaald hoe efficiënt de remmers de activiteit van TDO verlagen, en of de remmers geen andere belangrijke eiwitten remmen. Ook is voorspeld hoe goed de remmers in de hersenen kunnen komen. Vervolgens zijn de remmers aan gezonde muizen toegediend, om te bepalen of dezelfde bevindingen ook in een complex organisme konden worden gedaan. Het resultaat van deze experimenten is dat *NTRC 3531-0* ten opzichte van *LM10* een krachtigere remming van TDO laat zien, beter in de hersenen door kan dringen en een groter effect heeft op het metabolisme van tryptofaan. Gezien dit gunstige karakter van *NTRC 3531-0*, is deze remmer daaropvolgend getest in een muizenmodel van de ziekte van Parkinson, waarbij *LM10* ter vergelijking parallel is meegenomen. Dit laat zien dat beide remmers niet alleen zorgen voor een vermindering van de bewegingsproblemen, maar ook voor een verbetering van het leervermogen. Daarnaast wordt op celniveau een lagere afsterving van zenuwcellen en een verminderde ontsteking van het zenuwweefsel waargenomen. Ook leidt toediening van de remmers tot een verbeterde maag-darmfunctie van de muizen, dat gepaard gaat met een lager aantal geactiveerde immuuncellen en verminderde samenklontering van het eiwit α -synucleïne in het zenuwstelsel van de darmen. De remming van TDO zorgt in dit model dus voor verschillende gunstige effecten. Daarom dienen remmers van TDO ook in andere modellen van de ziekte getest te worden, zodat patiënten met de ziekte van Parkinson in de toekomst mogelijk een beter perspectief hebben dan vandaag.

Slotbeschouwing

In dit proefschrift is duidelijk geworden dat aminozuur-metaboliserende enzymen veelbelovende aangrijpingspunten zijn voor de behandeling van zowel kanker als de ziekte van Parkinson. Aanhoudende inspanningen op het gebied van medicijnontwikkeling zijn

echter onmisbaar om de therapeutische waarde van deze strategieën op te helderen. Het onderzoek beschreven in dit proefschrift is gericht op het ondersteunen van zowel lopende als toekomstige initiatieven op dit gebied. Hoogtepunten van dit onderzoek zijn onder andere de identificatie van IDO1 en IL4I1 als potentiële aangrijpingspunten voor de behandeling van eierstokkanker, en de bevestiging van TDO als een veelbelovend aangrijpingspunt voor de behandeling van de ziekte van Parkinson. Daarnaast zijn zowel bekende als nieuwe remmers van ARG1, IDO1 en TDO uitgebreid gekarakteriseerd. Samen met de nieuwe test voor ARG1-remming en de verschillende experimentele modellen beschreven in dit proefschrift, zal dit bijdragen aan toekomstige farmaceutische ontwikkelingen op het gebied van kanker en de ziekte van Parkinson.

Curriculum vitae

Yvonne Grobбен was born on September 20th, 1994 in Nieuwegein, the Netherlands. In 2012, after completing her secondary education at the Koningin Wilhelmina College in Culemborg with a Gymnasium degree (*cum laude*), she started the bachelor's program in Chemistry at Utrecht University. Here, her fascination for biochemistry and drug discovery was born, and she graduated with a bachelor's degree (*cum laude*) after completion of an internship at the NMR Spectroscopy group of the Bijvoet Center for Biomolecular Research. In 2015, she continued her education with a master's program in Chemistry (specialization: 'Chemistry for Life') at the Radboud University in Nijmegen. In pursuit of her master's degree, she completed two internships, of which the first was performed at the department of Biomolecular Chemistry and the Synthetic Organic Chemistry group of the Institute for Molecules and Materials of the Radboud University. During this internship, she worked on two separate projects focused on different aspects of the chromatin and nucleosome structure. Her second internship was performed at the Netherlands Translational Research Center B.V. (NTRC), a biotechnology company focused on drug discovery for cancer treatment. Here, she developed several drug discovery tools for the enzyme arginase 1, a promising target for cancer immunotherapy. After receiving her master's degree in 2017 with the distinction *cum laude*, she started her PhD research at NTRC, in collaboration with the division of Pharmacology of the Utrecht Institute for Pharmaceutical Sciences (UIPS), Utrecht University. Under the supervision of Dr. Guido Zaman, the research described in this thesis was performed at NTRC and, since 2021, at Oncolines B.V., a spin-off company of NTRC. Part of this research was performed in collaboration with and in the group of Prof. Dr. Aletta Kraneveld and Dr. Paula Perez-Pardo at UIPS. After completion of her PhD research, Yvonne continued her work at Oncolines in the role of Investigator.

List of publications

Included in this thesis

Grobben, Y. Targeting amino acid-metabolizing enzymes for cancer immunotherapy. [Manuscript in preparation]

Grobben, Y., den Ouden, J. E., Aguado, C., van Altena, A. M., Kraneveld, A. D. & Zaman, G. J. R. Amino acid-metabolizing enzymes in advanced high-grade serous ovarian cancer patients: value of ascites as biomarker source and role for IL4I1 and IDO1. *Cancers* 15, 893 (2023).

Perez-Pardo, P., **Grobben, Y.**, Willemsen-Seegers, N., Hartog, M., Tutone, M., Muller, M., Adolfs, Y., Pasterkamp, R. J., Vu-Pham, D., van Doornmalen, A. M., van Cauter, F., de Wit, J., Sterrenburg, J. G., Uitdehaag, J. C. M., de Man, J., Buijsman, R. C., Zaman, G. J. R. & Kraneveld, A. D. Pharmacological validation of TDO as a target for Parkinson's disease. *FEBS J.* 288, 4311–4331 (2021).

Grobben, Y., de Man, J., van Doornmalen, A. M., Muller, M., Willemsen-Seegers, N., Vu-Pham, D., Mulder, W. R., Prinsen, M. B. W., de Wit, J., Sterrenburg, J. G., van Cauter, F., den Ouden, J. E., van Altena, A. M., Massuger, L. F., Uitdehaag, J. C. M., Buijsman, R. C. & Zaman, G. J. R. Targeting indoleamine 2,3-dioxygenase in cancer models using the novel small molecule inhibitor NTRC 3883-0. *Front. Immunol.* 11, 609490 (2020).

Grobben, Y., Willemsen-Seegers, N., Uitdehaag, J. C. M., de Man, J., van Groningen, J., Friesen, J., van den Hurk, H., Buijsman, R. C. & Zaman, G. J. R. High-throughput fluorescence-based activity assay for arginase-1. *SLAS Discov.* 25, 1018–1025 (2020).

Grobben, Y., Uitdehaag, J. C. M., Willemsen-Seegers, N., Tabak, W. W. A., de Man, J., Buijsman, R. C. & Zaman, G. J. R. Structural insights into human Arginase-1 pH dependence and its inhibition by the small molecule inhibitor CB-1158. *J. Struct. Biol.: X* 4, 100014 (2020).

Other publications

de Man, A. P. A., Buijsman, R. C., Sterrenburg, J. G., De Wit, J. J. P., Van Cauter, F., Van Gemert, S. P. W., Prinsen, M. B. W., Mulder, W. R., Muller, M., Vu-Pham, D., **Grobbe**, Y., Simons-van Riel, W. E. & van Mil, Y. G. T. H. Macrocyclic BTK inhibitors. Patent WO/2023/110970 (2023).

Kooijman, J. J., van Riel, W. E., Dylus, J., Prinsen, M. B. W., **Grobbe**, Y., de Bitter, T. J. J., van Doornmalen, A. M., Melis, J. J. T. M., Uitdehaag, J. C. M., Narumi, Y., Kawase, Y., de Roos, J. A. D. M., Willemsen-Seegers, N. & Zaman, G. J. R. Comparative kinase and cancer cell panel profiling of kinase inhibitors approved for clinical use from 2018 to 2020. *Front. Oncol.* 12, 953013 (2022).

den Ouden, J. E., Zaman, G. J. R., Dylus, J., van Doornmalen, A. M., Mulder, W. R., **Grobbe**, Y., van Riel, W. E., de Hullu, J. A., Buijsman, R. C. & van Altena, A. M. Chemotherapy sensitivity testing on ovarian cancer cells isolated from malignant ascites. *Oncotarget* 11, 4570–4581 (2020).

Pieters, B. J. G. E., Hintzen, J. C. J., **Grobbe**, Y., Al Temimi, A. H. K., Kamps, J. J. A. G. & Mecinović, J. Installation of trimethyllysine analogs on intact histones via cysteine alkylation. *Bioconjug. Chem.* 30, 952–958 (2019).



Dankwoord

Dit proefschrift markeert het einde van een waardevolle, intensieve, en bovenal leerzame reis waarin ik mij heb mogen verdiepen in een fascinerend en belangrijk onderzoeksveld. Tijdens deze periode heb ik samen mogen werken met veel inspirerende collega's en samenwerkingspartners, zonder wie dit proefschrift niet tot stand had kunnen komen. Daarnaast is de onvoorwaardelijke steun en liefde die ik van familie en vrienden heb gekregen onmisbaar geweest om de eindbestemming van deze reis te bereiken. Daarom wil ik iedereen bedanken die enigerwijs een bijdrage—groot of klein, en direct of indirect—aan dit proefschrift heeft geleverd. Een aantal hiervan wil ik daarnaast in het bijzonder bedanken voor hun bijdrage.

Allereerst gaat mijn dank uit naar **Guido**, die mij de unieke kans heeft gegeven om binnen een toegewijd en ambitieus bedrijf mijn promotieonderzoek uit te voeren. Ik heb veel bewondering voor je gedrevenheid en de passie die je hebt voor dit vakgebied. Ik heb veel van je mogen leren in de afgelopen jaren, en geloof dat ik daardoor zowel als onderzoeker en als persoon veel heb kunnen groeien. Ik wil je bedanken voor de vrijheid en het vertrouwen die je mij hebt gegeven, en voor je aanhoudende steun, geduld en enthousiasme gedurende mijn promotietraject.

Ik wil **Aletta** bedanken voor de hartelijke ontvangst bij de farmacologie divisie van het UIPS. Bedankt voor je enthousiasme, opbouwende feedback en vele geïnteresseerde vragen. Ook wil ik je bedanken voor de flexibiliteit die je hebt getoond in de vormgeving van mijn promotietraject, en de ruimte die je mij hebt gegeven om hierin mijn eigen weg te vinden.

Mijn dank gaat ook uit naar **Rogier**, die het mogelijk heeft gemaakt voor mij om mee te werken aan inspirerende projecten, zowel als onderdeel van dit proefschrift, als ook daarbuiten. Bedankt voor je betrokkenheid, expertise en positieve instelling. Ik ben er zeker van dat *Crossfire Oncology* mooie dingen gaat bereiken in de toekomst.

Johan, bedankt dat je de rol van tweede promotor op je hebt willen nemen. Ik heb je enthousiaste reactie op mijn proefschrift erg kunnen waarderen.

Daarnaast gaat mijn dank uit naar prof. dr. **Jos Beijnen**, prof. dr. **Celia Berkers**, prof. dr. **René Medema**, dr. **Monique Slijper** en prof. dr. **Guus Smit** voor het lezen en beoordelen van mijn proefschrift.

Bedankt aan alle mede-auteurs van de publicaties die de basis van dit proefschrift vormen. Allereerst mijn (oud)-collega's, met wie ik nauw heb mogen samenwerken. **Joost en Nicole**, ik heb tijdens mijn stage, maar zeker ook daarna, veel van jullie mogen leren en heb graag met jullie samengewerkt. **Jos, Jan Gerard, Freek en Joeri**, bedankt dat jullie mij altijd een kijkje bleven geven in de wonderde wereld van de chemie. **Diep**, ik heb erg genoten van samenwerken met jou en heb met veel plezier een kantoor met je gedeeld. **Martine**, bedankt voor je bereidheid om altijd mee te denken op het lab, en voor je gezelligheid zowel op als buiten het lab. **Antoon**, ik heb jouw kennis en expertise, maar bovenal je enthousiasme hierover, erg kunnen waarderen; bedankt ook voor alle mooie verhalen die je altijd wist te vertellen. **Michelle**, ik bewonder de vrolijkheid die jij altijd met je meebrengt. **Winfried**, bedankt voor de interesse die je altijd hebt getoond in de voortgang van mijn onderzoek en proefschrift.

Ook wil ik de samenwerkingspartners bedanken die een (grote) bijdrage hebben geleverd aan de verschillende onderzoeksprojecten. **Paula**, *muchas gracias* voor de prettige samenwerking die we hebben gehad rondom het TDO project. **Anne en Judith**, bedankt voor jullie inspanningen en expertise binnen het eierstokkankeronderzoek, en de bereidheid om steeds maar mijn vragen te blijven beantwoorden. **Helma, Jan, Johan en Els**, bedankt voor jullie deskundigheid bij het uitvoeren van de screening campagnes; ik heb veel geleerd door dit proces van dichtbij mee te mogen maken. **Cristina and Miguel**, thank you for your openness and willingness to share valuable samples with us.

Mijn dank gaat daarnaast uit naar mijn plezierige (oud)-collega's bij Oncolines. **Jeffrey en Jelle**, mijn kantoorgenootjes van het eerste uur; bedankt voor de gezelligheid, en Jeffrey, bedankt voor alle goede adviezen die je in de afgelopen jaren hebt gegeven. **Mandy**, ook al zag jouw promotietraject er heel anders uit dan die van mij, jouw komst bij Oncolines heeft ervoor gezorgd dat ik mij als PhD-er minder alleen heb gevoeld (net als **Tessa** overigens); ik ben heel blij dat jij mijn paranime wilt zijn, en kijk er ook naar uit om jouw verdediging mee te maken. **Helma**, bedankt dat jij altijd paraat stond met goede adviezen, en dat ik bij jou terecht kon wanneer dat even nodig was. **Jeroen**, bedankt voor alle leuke gesprekken de afgelopen jaren. **Janneke**, ik vind het gezellig om jou als kantoorbuur te hebben, en heb erg genoten van de mooie reis die we samen met Mandy en Jelle hebben gemaakt. Daarnaast wil ik **alle andere (oud)-collega's van Oncolines en voormalig NTRC** (inmiddels *Crossfire Oncology*) bedanken voor de gezelligheid en fijne tijd die ik met jullie heb gehad (en met de meeste nog steeds heb).

Ik wil ook **Rieke, Twan en Laurence** bedanken, die ik met plezier tijdens hun stages heb mogen begeleiden. Naast dat jullie hopelijk veel van mij hebben mogen leren tijdens jullie stage, heb ik zeker ook veel geleerd van jullie begeleiden.

Lieve **Pieter, Marianne, Elske, JP, Roeland, Bram, Michiel** en **Thijs**, bedankt dat ik bij jullie altijd terecht kan voor de nodig ontspanning, vele spelletjes en sportieve activiteiten. Ik heb genoten van alle mooie avonturen die we tot nu toe al hebben beleefd, van Embrun tot Noorwegen tot het huisje in de heuvels. Pieter, veel dank ook voor de kritische blik die je op mijn Nederlandse samenvatting hebt geworpen.

Lieve **Hans** en **Willy**, en **Geurt** en **Hetty**, bedankt voor jullie steun tijdens dit intensieve traject, en voor de gezelligheid die altijd bij jullie te vinden is. Jullie vormen de basis van een prachtige familie, waar ik met veel plezier deel van mag uitmaken.

Lieve **Marloes**, ik ben heel dankbaar dat jij al mijn hele leven naast mij staat. Ik geniet altijd erg van onze leuke uitstapjes en urenlange spelletjesmarathons, en ben ook heel trots op wat jij door de jaren heen allemaal hebt bereikt. Ik vind het onwijs leuk dat jij straks als mijn paranimf naast mij zal staan, en kan ook niet wachten tot de rollen volgend jaar omgedraaid zijn! **Douwe**, mijn aanstaande zwager, ik vind het erg leuk dat jij al jarenlang deel uitmaakt van ons gezin, en wens jou ook alle succes toe met de laatste loodjes van jouw promotieonderzoek.

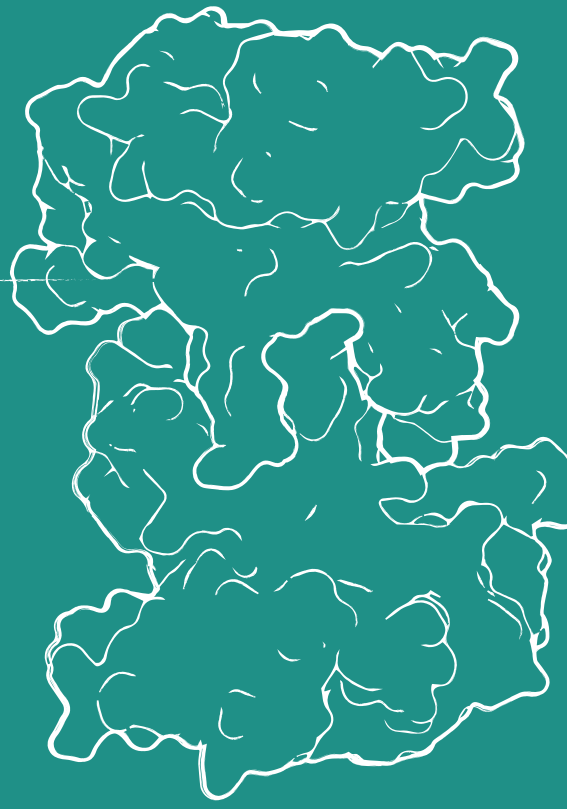
Liefste **pap** en **mam**, laat ik vooropstellen dat ik zonder jullie onvoorwaardelijke steun en liefde nooit alles had kunnen bereiken wat ik tot nu toe bereikt heb. Bedankt dat jullie altijd in mij geloofd hebben, mij gemotiveerd hebben om het beste uit mezelf te halen, en mij geholpen hebben om door te zetten wanneer het niet altijd even makkelijk was. Ik had me geen fijnere ouders kunnen wensen.

Tot slot een zee van dank aan mijn lieve **Joris**, die tijdens dit hele proces aan mijn zijde heeft gestaan. Bedankt voor alle liefde die je mij al hebt gegeven, en voor je onmisbare geduld, zorgzaamheid en aanmoedigingen bij alles wat ik ondernomen heb. Ik kan niet wachten om te ontdekken wat voor mooie avonturen wij nog allemaal samen gaan beleven!

Yvonne



IL4I1



iNOS



GLS1